

NASA Conference Publication 3125

Space Electrochemical Research and Technology

(NASA-CR-79-102) SPACE ELECTROCHEMICAL
RESEARCH AND TECHNOLOGY (NASA) 244 D

CSCL 10A

N91-32547

--THRU--

N91-32567

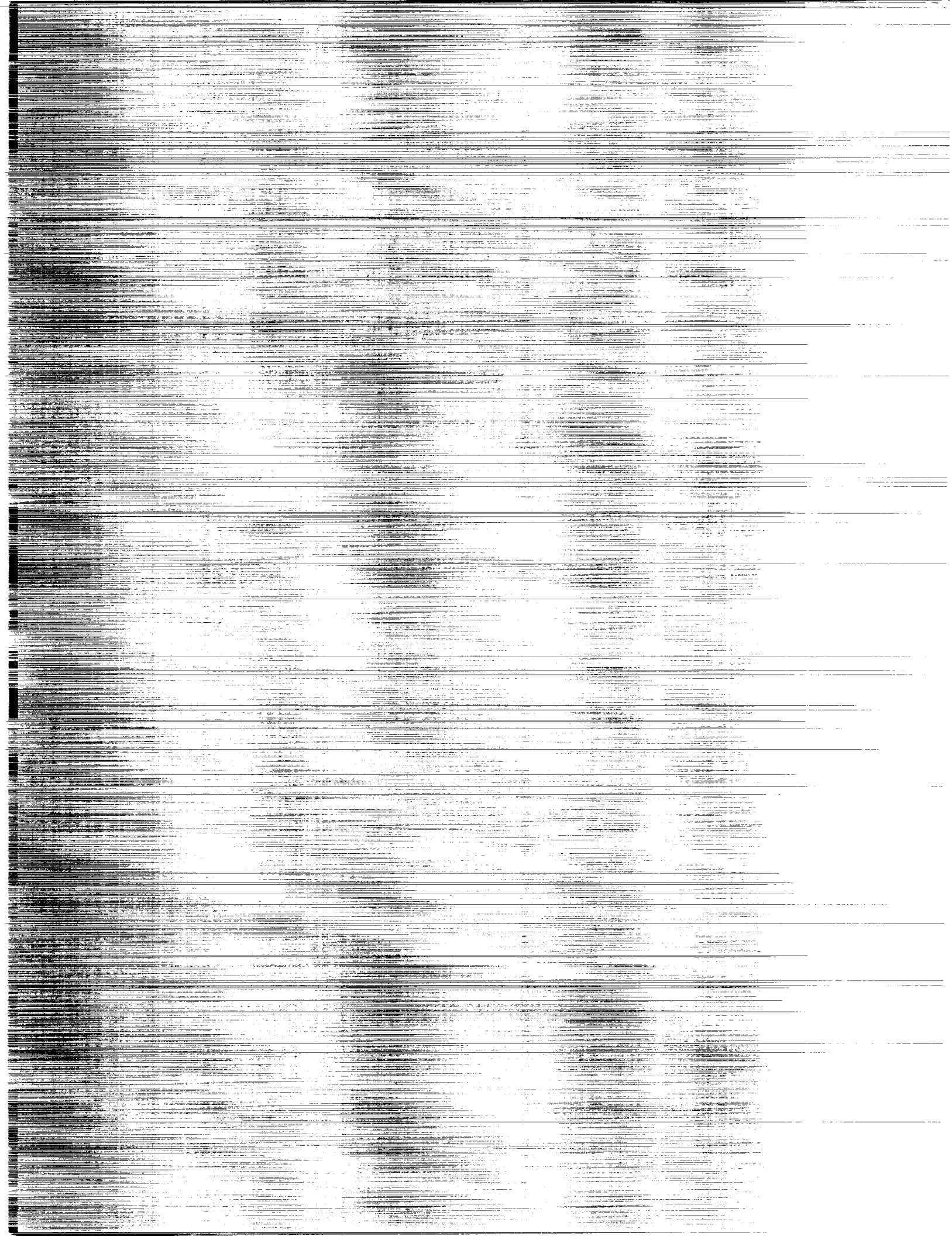
Unclas

H1/44

0039625

NASA Johnson Space Center

NASA



NASA Conference Publication 3125

Space Electrochemical Research and Technology

*Lewis Research Center
Cleveland, Ohio*

Proceedings of a conference held at
NASA Lewis Research Center
April 9-10, 1991

NASA

National Aeronautics and
Space Administration

Office of Management

Scientific and Technical
Information Program

1991

Trade names or manufacturers' names are used in this report for identification only. This usage does not constitute an official endorsement, either expressed or implied, by the National Aeronautics and Space Administration.

TABLE OF CONTENTS

| | Page |
|--|------|
| <i>Electrolytic Production of Oxygen from Lunar Resources</i> R. Keller, EMEC Consultants | 1 |
| <i>The Au Cathode in the System Li_2CO_3-CO_2-CO at 800 to 900 °C</i> N.H. Hagedorn, NASA Lewis Research Center | 7 |
| <i>SPE Water Electrolyzers in Support of Mission from Planet Earth</i> J.F. McElroy, United Technologies Corp. Hamilton Standard Division | 23 |
| <i>Space Water Electrolysis: Space Station Through Advanced Missions</i> R.J. Davenport, F.H. Schubert, and D.J. Grigger, Life Systems, Inc. | 37 |
| <i>The Effects of Platinum on Nickel Electrodes in the Nickel Hydrogen Cell</i> A. Zimmerman, The Aerospace Corp. | 57 |
| <i>Physical and Chemical Analysis of a Ni/H₂ Cell</i> H. Vaidyanathan, M.W. Earl, and T.D. Kirkendall, Comsat Laboratories | 73 |
| <i>Raman Spectral Observation of a "New Phase" Observed in Nickel Electrodes Cycled to Failure</i> P.L. Loyselle, X. Shan, and B.C. Cornilsen, Michigan Technological University, and M.A. Reid, NASA Lewis Research Center | 81 |
| <i>Impedances of Nickel Electrodes Cycled in Various KOH Concentrations</i> M.A. Reid and P.L. Loyselle, NASA Lewis Research Center | 89 |
| <i>High Energy Efficiency and High Power Density Proton Exchange Membrane Fuel Cells – Electrode Kinetics and Mass Transport</i> S. Srinivasan, O.A. Velez, A. Parthasarathy, D.J. Manko, and A.J. Appleby, Texas A & M University | 101 |
| <i>I-BIEM Calculations of the Frequency Dispersion and AC Current Distribution at Disk and Ring-Disk Electrodes</i> B.D.Cahan, Case Western Reserve University | 123 |
| <i>Regenerative Fuel Cell and Architectures for Lunar Surface Power</i> D.W. Harris, S.P. Gill, T.M. Nguyen, and J.J. Vrolyk, Rockwell International | 147 |
| <i>Oxygen Electrodes for Rechargeable Alkaline Fuel Cells – III</i> L. Swette, N. Kackley, and S.A. McCatty, Giner, Inc. | 155 |
| <i>Some Recent Studies with the Solid-Ionomer Electrochemical Capacitor</i> S. Sarangapani, J. Forchione, A. Griffith, and A.B. LaConti, Giner, Inc., and R. Baldwin, NASA Lewis Research Center | 175 |

| | |
|---|-----|
| <i>Performance of a Dual Anode Nickel-Hydrogen Cell</i> R.F. Gahn, NASA Lewis Research Center | 195 |
| <i>Multiple Cell Common Pressure Vessel Nickel Hydrogen Battery</i> J.P. Zagrodnik and K.R. Jones, Johnson Controls Battery Group, Inc. | 209 |
| <i>Small Capacity, Low Cost (Ni-H₂) Design Concept for Commercial, Military and Higher-Volume Aerospace Applications</i> J.R. Wheeler, W.D. Cook, and R. Smith, Eagle-Picher Industries, Inc. | 221 |
| <i>Sodium - Metal Chloride Battery Research at JPL</i> B.V. Ratnakumar, A.I. Attia, and G. Halpert, Jet Propulsion Laboratory | 227 |
| <i>Advances in Li-TiS₂ Cell Technology</i> S. Surampudi, D.H. Shen, C.-K. Huang, F. Deligiannis, A. Attia, and G. Halpert, Jet Propulsion Laboratory | 235 |

ELECTROLYTIC PRODUCTION OF OXYGEN FROM LUNAR RESOURCES

Rudolf Keller
EMEC Consultants
Export, PA 15632

Abstract

Oxygen is a valuable commodity in space. Substantial savings have been projected for future missions if oxygen could be produced on the moon from local resources.

Some of the most promising approaches to extract oxygen from lunar resources involve electrochemical oxygen generation. In a straight-forward concept called "magma electrolysis", suitable oxides (silicates) are molten at 1300-1500 °C and the melt electrolyzed. Residual melt can be discarded after partial electrolysis. Alternatively, lunar soil may be dissolved in a molten salt and electrolyzed. In this approach, temperatures are lower and melt conductances higher, but electrolyte constituents need to be preserved. Both possibilities are being studied in the laboratory.

In a different approach, ilmenite is reduced by hydrogen and the resulting water electrolyzed (Carbotek Process TM).

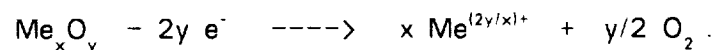
Although know-how from terrestrial technology can be applied, the process task is unconventional and requires many innovative solutions. Time and effort needed for successful development should not be underestimated.

Oxygen from Lunar Resources

Due to the effort necessary to transport it there from Earth, oxygen is a precious commodity in space. Oxygen is needed for life support and, in larger amounts, also for propulsion. In situ preparation of oxygen from local resources in space can reduce costs for future missions in space. The lunar surface is an appropriate site to establish an oxygen manufacturing capability.

Molecular oxygen may be prepared from oxides by electrolysis. In the absence of volatile oxides, solid oxides may be used. Such oxides are readily available on the lunar surface, mainly as silicates of various compositions. Lunar soil may be regarded as an already adequately comminuted raw material. Highland soils are anorthositic, feldspar-like, with compositions similar to the one given as an example in Table 1. Soils of the mare region have a more basaltic character and are represented in Table 1 by a composition indicated by Washington University authors [1] as representative.

In the electrolytic decomposition of the oxides, oxygen gas is produced at the positive electrode, the anode. The reaction may be formulated as follows:



Metallic components, meanwhile, are reduced at the cathode:

Table 1. Compositions of Lunar Soils

| | Anorthositic Soil [2] | Basaltic Soil [1] |
|--------------------------------|-----------------------|-------------------|
| SiO ₂ | 44.9 wt% | 46.2 wt% |
| Al ₂ O ₃ | 27.6 wt% | 12.6 wt% |
| FeO | 5.03 wt% | 17.4 wt% |
| TiO ₂ | 0.55 wt% | 2.8 wt% |
| MgO | 5.35 wt% | 10.4 wt% |
| CaO | 15.8 wt% | 10.5 wt% |
| Na ₂ O | 0.39 wt% | |
| K ₂ O | 0.10 wt% | |



Various metals are reduced with different ease. Theoretical decomposition potentials for the oxides can be calculated from thermodynamic data, but they are modified as the oxides combine to mixed oxide compounds. For the major components of the oxides discussed, the following order of decreasing (more negative) cathodic deposition potential appears to exist:



The cathodic products may be of no substantial interest and may even be discarded. Silicon and aluminum, on the other hand, may be the products of major interest. Depending on the desirability to produce and collect the metals, the process may be refined to various degree [3], as illustrated by Figure 1.

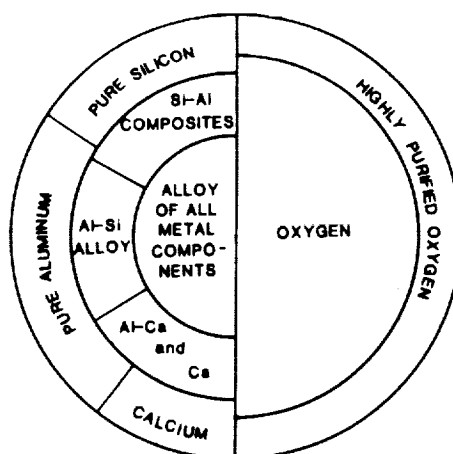


Figure 1. Refinement of Lunar Molten Salt Electrolysis Depending on Metallic Products Desired

Two major approaches to the electrolysis of lunar oxides are being explored: (1) a molten silicate electrolysis in which the oxides are melted and the melt electrolyzed, and (2) a fused salt electrolysis in which the oxides are dissolved in a molten salt (flux) and electrolyzed.

Electrolysis of Molten Silicates

Lunar raw material may be molten and electrolyzed at temperatures of 1400 - 1500 °C. This can be accomplished in a batch mode, whereby the electrolyte composition changes during the course of electrolysis; at a certain point, the residual melt is discarded. Such an approach was discussed in an earlier publication by Washington University authors [1].

Alternatively, the electrolysis may be conducted in a quasi-continuous mode. Fresh ore is added to an electrolyte which represents partially electrolyzed raw material. While components that reduce most easily are continuously electrolyzed, electrolyte is gradually removed from the system. This approach is represented in Figure 2.

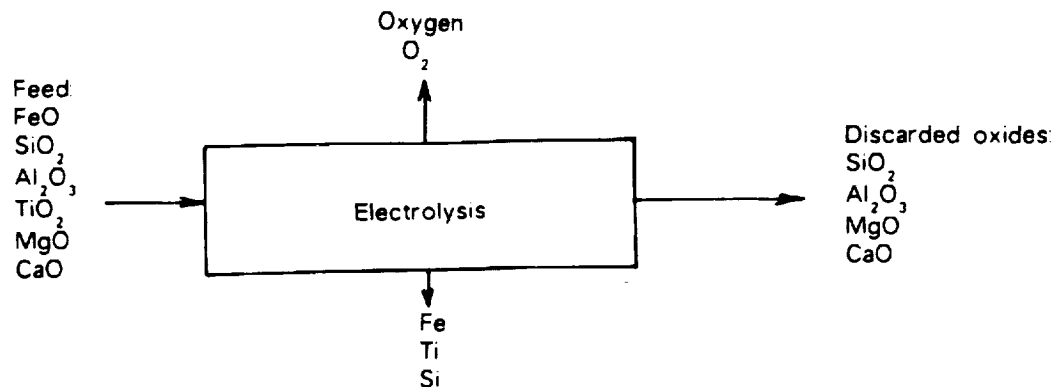


Figure 2. Continuous Electrolysis of Molten Oxides

A cell design for such an electrolysis, with a molten silicon-iron cathode, has been suggested by McCullough and Mariz [4].

Electrolyte conductivities vary significantly with composition. Haskin et al [1] give the following regression equation (for 1425 °C):

$$\ln \lambda = 5.738 - 12.6[\text{SiO}_2] - 10.0[\text{AlO}_{1.5}] - 3.7[\text{TiO}_2] + 1.89[\text{FeO}] + 0.07[\text{MgO}] - 1.25[\text{CaO}]$$

(λ in $\text{ohm}^{-1}\text{cm}^{-1}$; symbols for oxides stand for mole fractions).

High iron oxide contents obviously lead to relatively high conductances. Excessive silicon contents result in low conductivities. In practice, one may expect to be operating with electrolytes of specific conductivities of about $0.3 \text{ ohm}^{-1}\text{cm}^{-1}$.

So-called "magma electrolysis" experiments have been conducted by L. A. Haskin and his co-

workers at Washington University. They gathered essential basic data on the electrolyte properties and electrolyzed small molten charges suspended in platinum wire loops. Recently, experiments were conducted in small spinel crucibles. EMEC Consultants started investigations using alumina crucibles, a platinum anode and a graphite cathode. Cathodic deposits will be examined and several anode candidates and other materials tested in future work.

Electrolysis in Molten Salt

Lunar soil may be dissolved in a suitable electrolyte of molten fluorides and electrolyzed at temperatures of about 1000 °C. It is important that all components added to the electrolyte are removed again from the system. In the approach envisioned by EMEC Consultants, this is accomplished by complete electrolysis (separation of some components as undecomposed oxides would also be possible). Electrolysis conditions are such that the component most difficult to decompose reacts. As this component is calcium, a cathode potential, therefore, is maintained which permits reduction of calcium; the other metals are co-reduced at the rate they reach the cathode, i.e. at the mass transport limited rate. This approach has, thus, been called a "calcium-plus electrolysis".

Calcium fluoride, with a very high theoretical decomposition voltage, would be a desirable electrolyte, but its melting point is high. Also metal solubilities leading to current efficiency losses would be excessive. A mixture of calcium fluoride and lithium fluoride is preferable as electrolyte, as added lithium fluoride reduces operating temperatures. The presence of lithium fluoride, however, leads to a cathodic co-deposition of lithium which has to be recovered in an auxiliary metal separation step, presumably by vacuum distillation.

Oxygen is evolved at the anode as a gas. Some electrolyte components will evaporate into this gas but may be retained by process feed through which the off-gases are bled, similar to the recovery of fluorine values in the fume treatment of commercial aluminum production. Traces of sulfur dioxide may remain with the oxygen and should not affect the performance of the oxygen as propellant. It may be possible to obtain oxygen feasible for life support by simple reevaporation of liquefied oxygen.

The envisioned molten salt electrolysis process to produce oxygen is summarized in Figure 3

The development of this process actually started with work on a concept to produce silicon and aluminum from lunar resources [5]. In a stepwise reduction process, silicon of the anorthite feed is reduced chemically by aluminum metal. Aluminum oxide and calcium oxide are electrolyzed in a second major process step. Auxiliary process steps involve the beneficiation of lunar soil by magnetic separation to yield a good-quality anorthite ($\text{CaAl}_2\text{Si}_2\text{O}_8$) feed, the separation of silicon from a hypereutectic Si-Al alloy, the purification of oxygen by exposing the cell gases to feed ore, and the separation of lithium from the cathode metal.

Other Approaches

Ilmenite reduction with hydrogen is practiced in the Carbotek process [6]. This process includes an electrochemical step, as the water produced by the reaction of hydrogen with ferrous oxide is electrolyzed. An electrolysis at high temperatures is proposed but has not been explored in Carbotek's experimental work.

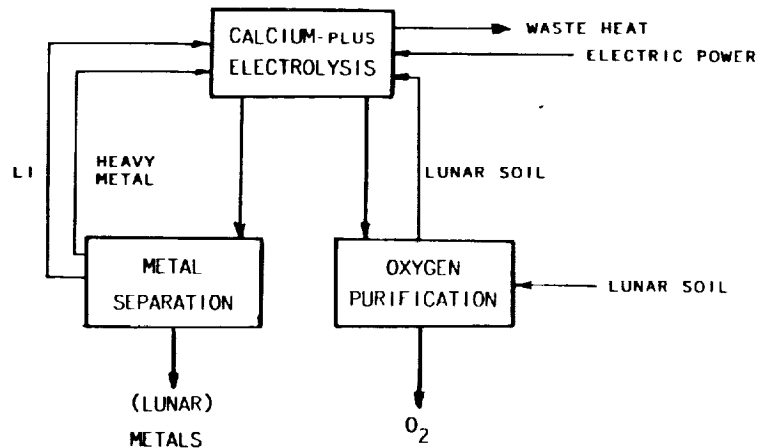


Figure 3 "Calcium-plus Electrolysis" to Produce Oxygen From Lunar Soil

Concluding Remarks

There does not appear to be a clearly favored process to produce lunar oxygen at this time. All approaches discussed above include unconventional process elements with various degree of uncertainty regarding their technical feasibility [7]. Additional research is required. Materials stability problems need to be addressed. In particular, a suitable anode for the evolution of oxygen needs to be identified. Such work is in progress at EMEC Consultants.

After investigating the chemistry of individual process steps, processes shall be demonstrated on the bench scale. It is estimated that 8 to 12 years of additional work will be required before a successful pilot demonstration may be undertaken [8]. Time periods for the development of new processes or process variants in terrestrial extractive metallurgy, which is directly related to the discussed approaches, are considerable. Time and effort necessary to develop a lunar oxygen extraction process should not be underestimated.

Acknowledgements

The author gratefully acknowledges the contributions of his co-workers and associates D. L. Anthony, C. N. Cochran, W. C. Cochran, W. E. Haupin, and K. T. Larimer. Thanks also to Prof L. A. Haskin and Dr. R. O. Colson of Washington University for fruitful discussions.

EMEC appreciates the support of the NASA Johnson Space Center through the SBIR program, of the University of Arizona's Space Engineering Research Center for Utilization of Local Planetary Resources, and of the Space Studies Institute. Particular thanks to Dr. David S. McKay for his interest and support.

References

- [1] L. A. Haskin, R. O. Colson, D. J. Lindstrom, R. H. Lewis, and K. W. Semkow .
Electrolytic Smelting of Lunar Rock for Oxygen, Iron, and Silicon .
Revised Manuscript , 1989 .
- [2] R. J. Williams and J. J. Jadwick, editors .
Handbook of Lunar Materials .
NASA Reference Publication 1057 , 1980 .
- [3] D. L. Anthony, C. N. Cochran, W. C. Cochran, W. E. Haupin, R. Keller, and K. T. Larimer .
Products from Lunar Anorthite .
Space Manufacturing 7; Proceedings of the Ninth Princeton/AIAA/SSI Conference 86-89
 , 1989 .
- [4] E. McCullough and C. Mariz .
Lunar Oxygen Production Via Magma Electrolysis .
In *Proceedings of Engineering, Construction and Operations in Space II, Space 90, Al-
buquerque NM* . April , 1990 .
- [5] D. L. Anthony, W. C. Cochran, W. E. Haupin, R. Keller, K. T. Larimer .
Dry Extraction of Silicon and Aluminum from Lunar Ores .
Lunar Bases & Space Activities in the 21st Century Paper No. LBS-88-066 : , 1988 .
- [6] M. A. Gibson and C. W. Knudsen .
Development of the Carbotek Process for Lunar Oxygen Production .
In *Proceedings of Engineering, Construction and Operations in Space II, Space 90, Al-
buquerque NM* . April , 1990 .
- [7] R. Keller .
Lunar Production of Aluminum, Silicon and Oxygen .
*Metallurgical Processes for the Year 2000 and Beyond, edited by H. Y. Sohn and
E. S. Geskin, published by The Minerals, Metals & Materials Society* 551-562 .
1989 .
- [8] EMEC Consultants .
Production of Oxygen by Electrolysis of Lunar Soil in Molten Salt
NASA Phase II Proposal , 1990 .

THE Au CATHODE IN THE SYSTEM $\text{Li}_2\text{CO}_3\text{-CO}_2\text{-CO}$ AT 800 TO 900 °C

Norman H. Hagedorn
NASA Lewis Research Center
Cleveland, Ohio 44135

SUMMARY

The lithium- CO_2 battery has recently been proposed as an advanced concept for missions to Mars or Venus, planets with carbon dioxide atmospheres. This article discusses the initial evaluation of gold as a catalyst for the cathodic reduction of carbon dioxide in molten lithium carbonate. An attempt is then made to rationalize the experimental results by proposing a phenomenological model for the sequence of reactions at and around the electrode. Finally, inferences are made as to the viability of gold as a cathode catalyst for the proposed battery.

INTRODUCTION

The possibility of missions such as a manned outpost on Mars, or a probe to the surface of Venus, has motivated researchers to consider developing electrochemical devices which might utilize the carbon dioxide atmosphere common to both planets. One such device is an alkali metal - carbon dioxide battery in which the carbon dioxide serves as the cathodic reactant. As presently envisioned, the device would utilize lithium as the anodic reactant, and the cell reaction product would be lithium carbonate, from which the lithium anode would be shielded by an as-yet hypothetical lithium-ion-conducting solid. The battery could be treated as a primary device, serving only until its supply of stored lithium was exhausted; as a secondary device, recharged chemically by resupply with lithium transported from Earth (which would, because of the low mass of lithium, be quite efficient); or, for the Mars mission, as a secondary device recharged electrochemically from an available nuclear central station power supply to regenerate the lithium. The last possibility is quite unlikely, since it would require a very high potential, evolving not only carbon dioxide at the anode, but oxygen as well. However, if energy were abundant and a premium were placed on the availability of an oxygen-containing process stream, perhaps an argument could be made for this option.

The following presents current results of experimental work to evaluate gold as a possible catalyst for the cathodic reduction of carbon dioxide. An attempt is then made to rationalize the experimental results by proposing a phenomenological model for the sequence of reactions at and around the electrode. Finally, inferences are made as to the viability of gold as a cathode catalyst for the proposed battery.

EXPERIMENTAL

Apparatus

The test cell used in this experiment is shown in figure 1. The 5-cm-diameter gold-plated nickel cup which served as the counter electrode was supported by a nickel disk suspended by nickel tie rods from a water-cooled cell cover. The cup was insulated electrically from the support disk by an intervening alumina disk. Alumina baffles were spaced above the cup to minimize thermal gradients due to radiation and convection. The water-cooled cell cover made possible the use of O-ring compression fittings, enabling the vertical positioning of cell components such as the working

and reference electrodes, reactant gas feed tubes, and the cell thermocouple. The cell was enclosed in an alumina sheath and suspended in an Inconel 600 container which was, in turn, positioned vertically in a tubular furnace. The portion of the Inconel container that extended above the furnace was also water-cooled, ensuring the integrity of the rubber O-ring flange seal between the cell cover and the container, as well as that of those in the fittings in the cell cover. The use of O-ring seals made operation possible at pressures greater than one atmosphere.

The working electrode was 99.985 wt% gold foil (Johnson Matthey, Inc.), 1 cm by 1 cm by 0.5 mm. After several configurations were tried, the reference electrode was modeled after Borucka (ref. 1). When this electrode was lowered to the bottom of the cell, it trapped a portion of the carbonate melt and isolated it from the reaction products of the working and counter electrodes in the bulk melt. The reference electrode consisted of an outer 6.35-mm-diameter tube and an inner 3.18-mm-diameter tube, both of 99.8 wt% alumina (Coors); 0.813-mm-diameter, 99.9 wt% gold wire (Johnson Matthey); and assorted plastic fittings for sealing the electrode and connecting it to the gas supply system. The reference gas entered the electrode via the annulus between the gold wire and the inner tube, and exited between the inner and outer tubes. The outer tube, as described above, rested flush on the bottom of the counter electrode cup, trapping melt yet providing a thin-film high-impedance path for continuity between the trapped melt and the bulk melt of the cell. The inner tube extended about halfway down from the cell cover, and the gold wire continued to about 1 mm from the bottom of the counter electrode cup. Gold wire leads to the external circuit from the working and counter electrodes were enclosed in 3.18-mm-diameter alumina tubes and were externally sealed at the tube ends with epoxy resin. Prior to cell assembly, all gold electrode surfaces were washed in acetone, isopropyl alcohol, and deionized water.

The chromel-alumel (type K, ± 6 °C accuracy) thermocouple was sheathed in a 3.18-mm-diameter Inconel 600 tube with the lower 7.5 cm gold-plated. During the experiment, the thermocouple was positioned above the melt except when the melt temperature was being measured. The reactant gas feed was a 3.18-mm-diameter, 99.8% alumina tube that could be positioned to bubble the gas through the melt. The melt depth was 2.5 cm, and the working electrode was vertically centered in the melt and horizontally centered in the counter electrode cup.

Two reactant gases were used in the experiment: 99.99 mol% CO₂, and an equimolar mixture (± 1 percent mixing accuracy) of 99.99 mol% CO₂ and 99.3 mol% CO. In use, the gases were dried in a molecular sieve column (type 4A, Union Carbide) and purified over copper turnings in an in-line tube furnace. Flows were set by hand and monitored with rotameters (Cole-Parmer, ± 2 percent accuracy). The Li₂CO₃ electrolyte (Fischer Certified ACS grade) was used as purchased.

Power to the cell furnace was regulated by a zero-firing solid-state relay actuated by a digital, solid-state microprocessor (Therm-Pro, Inc.). Stability was ± 2 °C. A model 273 potentiostat (EG&G Princeton Applied Research Corp.) was used for the electrochemical experiments, and that company's Electrochemistry Demonstration Program, Vol. I, in conjunction with an Apple IIe personal computer, was used to control transient tests and for the associated acquisition and presentation of data.

Procedure. - The reference electrode was designed to permit the use of a separate reference gas, isolated from the working electrode reactant. However, for the experiments being reported, the composition of the reference gas was identical to that of the reactant gas stream, and cell potentials are reported as polarizations

away from the rest potential. In practice, the reference electrode quickly became blocked, probably because the carbonate melt crept up the annular flow passages to a location cool enough for it to solidify. It thus became standard procedure to occasionally raise the reference electrode above the melt so that the gas in the outer tube of the electrode could become representative of the reactant stream, and then to return it to its operating position. Stability of the reference under this stagnant flow condition presented no difficulty during the short duration of the linear potential sweeps used as the standard technique to monitor the working electrode. Such stability could not be assumed during the acquisition of steady-state polarization data, when one data point could require half an hour or more. It was fortuitous under these conditions that the counter electrode, having a much greater active area than the working electrode, polarized only a few millivolts anodically under load and quickly returned to its rest potential when current flow ceased. In effect, it became a "reference for the reference" and made it possible to sort out the recorded data.

As mentioned above, linear sweep voltammetry was used to evaluate the performance of the working electrode in response to changes in pressure, temperature, and reactant gas composition, and to the presence or absence of bubbling through the melt. Generally, cathodic sweeps were made at 20, 40, and 80 mV/sec to a polarization of -100 mV from the rest potential. The test parameters were total pressures of 1.2×10^5 and 2.1×10^5 N/m²; melt temperatures of 800, 850, and 900 °C; reactant feeds of CO₂ and an equimolar CO₂-CO mixture; and a bubble rate, when used, of about 30 ml/min. Because of the cell configuration and the high conductance of the molten Li₂CO₃, about 5 (Ω-cm)⁻¹ at 850 °C (ref. 2), IR-corrections have not been applied to the measured currents. Because of the nonuniform current distribution on a flag working electrode surrounded by its counter electrode, currents are presented simply in milliamperes and not as current densities.

When switching from one reactant gas to the other, a laboratory vacuum pump (Leybold, Inc., Model D1.6B) was used to exhaust the existing gas from the cell, and the cell was then repressurized with the replacement gas. In order to avoid bulk dissociation of the carbonate melt according to

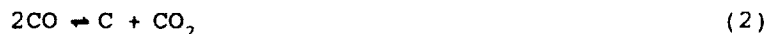


it was necessary first to cool the melt below its solidification temperature of 723 °C. When switching from pure CO₂ to the mixture, it was sufficient to carry out only one or two vacuum/repressurization cycles. However, going in the other direction, in order to completely remove the CO component from the cell, four of the cycles were executed, theoretically reducing the gas phase CO concentration to the order of 10 N/m².

To avoid melt dissociation according to equation (1) while at operating temperatures, it is necessary to maintain the partial pressure of CO₂ in the gas above the melt at values greater than the equilibrium dissociation pressure at the existing temperature. Some dissociation pressure data for Li₂CO₃ are presented by Janz et al. (ref. 2), but their results contain some uncertainties and extend only to about 850 °C. No data have been discovered relating the dissociation rate of the molten carbonate to the deficit between the existing CO₂ partial pressure and the equilibrium dissociation pressure, but it has been reported that the corresponding recombination rate for the ternary eutectic carbonate melt is generally quite slow (ref. 3). In the light of the uncertainties, it is possible that, when operating at 900 °C and 1.2×10^5 N/m² with an equimolar mixture of CO and CO₂, melt dissociation

was occurring. However, there is no experimental evidence for this, and no straightforward way to estimate possible effects if melt dissociation were occurring.

Another chemical process that one must be cognizant of is the Boudouard reaction for the partitioning of CO (ref. 1):



The reaction is favored thermodynamically by high CO pressure and low temperature. It has been pointed out (ref. 1) that, regardless of the cover gas composition, an electrochemical reaction at the surface of an electrode, by consuming CO_2 and generating CO, could create local conditions for carbon deposition. To estimate the "worst case" scenario for the present experiment, a calculation based on data from the Joint Army-Navy-Air Force (JANAF) tables (ref. 4) for an equimolar mixture of CO and CO_2 at 827 °C and $2.1 \times 10^5 \text{ N/m}^2$ total pressure indicates that a cathodic polarization of -150 mV from the rest potential could result in carbon deposition. This assumes very fast kinetics and negligible resistive loss, so that total polarization is Nernstian. Later discussion will argue that the reaction at the electrode surface does not produce the situation proposed above.

The working electrode surface was examined before and after its 9-day exposure to the carbonate melt at temperatures of 800 °C or greater. Scanning electron microscopy, with both secondary and backscattered electron imaging, along with energy dispersive x-ray spectroscopy, were used in the analyses.

RESULTS AND DISCUSSION

Experimental results

Figure 2 presents linear sweep voltammograms for the gold cathode in Li_2CO_3 at 800, 850, and 900 °C, under an equimolar atmosphere of CO and CO_2 at a total pressure of about $1.2 \times 10^5 \text{ N/m}^2$ (1.2 atm). These data represent a baseline for the effects of other parameters, including aging at cell temperature. Some of these effects were quite surprising, in light of the original assumption that the cathodic process would reduce dissolved CO_2 diffusing from the melt. In the simplest case, the linear sweep voltammograms for such a process would have shown a current peak as the diffusional gradients developed, then a fall off to a steady limiting current until the potential became adequate to promote some new reaction (ref. 5). However, the potential sweeps in figure 2 indicate no approach to a limiting current. Rather, the inflection of the curves toward the ends of the sweeps shows an increasing gradient of current with applied polarization. At much greater cathodic polarizations, one can expect the deposition of carbon, or even alkali metal, with very rapid reaction kinetics (ref. 6). But, at the cathodic limit of -100 mV adhered to for the cathodic sweeps in this experiment, it is assumed that such depositions have not occurred, and that the overall thermodynamic process can be represented as



However, the actual sequence of physical, chemical, and electrochemical steps comprising this process becomes a matter of conjecture.

The most arresting result of this work was that electrode performance was very poor in the presence of CO_2 alone, but quite good when the reactant gas was a mixture

of CO₂ and CO. Figure 3 presents cathodic potential sweeps at -40 mV/sec before and after changes in the reactant gas, and reveals several salient characteristics:

- (1) A loss in performance (e.g., from -18 to -7.5 mA at a polarization of -100 mV) after switching from the CO₂-CO mixture to CO₂ alone
- (2) A further loss in performance, from -7.5 to -2 mA, during six days of evaluation of the Au cathode in CO₂
- (3) A recovery, from -2 to -4 mA, due to return to the CO-CO₂ mixture
- (4) A subsequent additional recovery to -12 mA following several hours of quasi-steady-state operation under the CO-CO₂ mixture, during which steady-state polarization data were acquired

This last characteristic, an improvement engendered by extended periods under load, was consistently observed when working with the CO-CO₂ gas mixture, as shown in figure 4. The two curves at each temperature indicate performance, at a sweep rate of -40 mV/sec, before (upper curve) and after (lower curve) the collection of steady-state polarization data. This improvement was not consistently in evidence when operating with CO₂ alone. Rather, in that case, the time spent under quasi-steady load conditions resulted almost equally in small gains or losses in sweep performance and seemed to be more affected by other aspects of electrode history, such as prior time at the existing temperature, time at open circuit, or time raised from the melt.

The results of steady-state polarization measurements are shown in figure 5 for the CO-CO₂ mixture. Figure 5 shows excellent steady-state performance of the gold cathode when CO is present equally with the CO₂. In the same figure, single data points at 800 and 900 °C indicate the effect when the reactant gas stops bubbling. Also, the data for 900 °C include measurements at 2.1×10^5 N/m², and unexpectedly show no pressure effect. Furthermore, it can be seen in figure 6 that increasing pressure actually inhibited sweep voltammograms, whereas one would anticipate, on the basis of equation (3), that increased total pressure would enhance performance.

Both systems were slow to equilibrate after load changes. With the CO-CO₂ gas mixture, tens of minutes could be required for the rate of change of potential under load to diminish to 1 mV/2 to 3 min, at which time data would be recorded; and up to $\frac{1}{2}$ hr was required to return to a stable open circuit value. With CO₂ alone, attainable currents were at least an order of magnitude less than with the gas mixture, and polarizations were greater. Response was so slow in both directions that a considerable degree of uncertainty exists for the recorded data. For this reason, figure 7 simply shows envelopes encompassing the data at a given temperature, without attempting to distinguish between the effects of total pressure or bubbling of the gas through the melt.

A phenomenological model. - In order to rationalize the performance characteristics exhibited by the gold cathode in this experiment, it is hypothesized that the primary source of CO₂ being reduced at the cathode surface is not diffusion from the melt, but the dissociation reaction:



At the electrode surface, reaction (1) would be promoted by the initial electrochemical consumption of any dissolved CO₂ at, or near, the electrode. (Note that

reaction (1) would be retarded by an increase in total pressure or in CO₂ partial pressure, with the inhibiting effect noted in fig. 6.)

It is also hypothesized that the buildup of the oxide ion at the electrode surface can strongly impede cathodic performance. Reaction (1) is an example of a Lux-Flood (refs. 7 and 8) acid-base system in which the carbonate ion (the oxide ion donor) is the base, and carbon dioxide is its conjugate acid. Depending on the operating conditions and the processes occurring locally, the melt can become extremely basic near the electrode. This could significantly affect the overall reaction path by influencing the variety of electrochemically active species that could be present, including carboxy-ion intermediates such as CO⁺ and CO₂⁻ (ref. 9).

The two systems (CO₂/Au and CO₂,CO/Au) in the molten ternary eutectic mixture of alkali carbonates were evaluated by Borucka (ref. 10) with regard to their suitability as reference electrodes in molten carbonates. Micropolarization was measured anodically and cathodically, with current densities of the order of 1 to 10 μA/cm². Exchange currents were estimated, and possible electrode processes were suggested. It was determined that the CO₂/Au electrode was extremely irreversible, with an overall process thermodynamically equivalent to a very dilute oxygen electrode,



governed by a very slow activation step possibly involving interaction between the gold surface and oxygen, a 200 ppm impurity in the CO₂. The exchange current for this electrode was shown to be about 1/30th that of CO₂,CO/Au.

Although the stability of gold oxides at the temperatures and potentials under consideration is difficult to defend thermodynamically, the observed behavior of CO₂ on the gold cathode supports the hypothesis of a process that is at least generically similar to that described. Therefore, for the sake of the present argument, it is simply assumed that oxide ions are preferentially adsorbed on the gold surface, presenting a physical impediment for access of CO₃⁻ to the electrode and for the charge transfer process.

The preference for this explanation is partly based on the extreme slowness of the return to open circuit potential, especially in the presence of CO₂ alone, after sustaining a quasi-steady-state cathodic load. The timeframe appears more typical of relaxations associated with chemisorption bonds than of the diffusional dispersal of concentrated species in solution, especially when the melt is agitated because the reactant gas is bubbling.

The remainder of the proposed reaction model draws heavily on the work of Borucka (ref. 3) and Borucka and Appleby (ref. 9), in which the CO₂,CO/Au/CO₃⁻ system was examined in relation to the oxidation of CO, as in a molten carbonate fuel cell anode. In particular, the CO₂⁻ ion, proposed in reference 3 and strongly supported by experiment and thermodynamic and kinetic arguments (ref. 9), is invoked here.

The CO_2^- ion was shown to be formed by the rapid reaction of CO and the O^- ion:



The CO_2^- was further shown to be quite soluble in the molten carbonate, with solubility comparable to that of CO_2 , about 3 times greater than that of CO (ref. 6). Thus, equation (5) presents the process by which CO is able to depolarize the cathode of O^- ions, promoting the supply of CO_2 reactant via equation (1). CO_2^- is also produced in the cathodic charge transfer sequence, which can be indicated by the overall process



the reverse of which represented the "second wave" in the oxidation of CO (ref. 3).

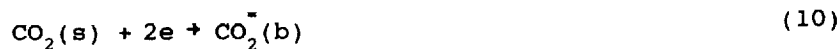
Finally, the reaction sequence is completed a short distance from the electrode by



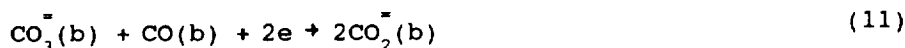
producing the expected products of the overall reaction and regenerating the CO for a continuation of the depolarization process at the cathode.

Obviously, equations (1), (5), and (7), when simply added, cancel each other. However, they convey a picture of the CO molecule functioning over a short distance, transporting O^- ions from the cathode surface into the bulk melt via the CO_2^- ion, and there being regenerated for return to the cathode. Thus, in spite of its relatively low solubility in the melt, the flux of CO to the cathode can be sufficient to depolarize the cathode because of the short distance the CO must diffuse from the saturated bulk melt.

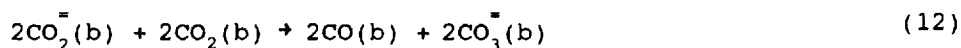
In summary, the proposed cathodic sequence for the $\text{CO}_2, \text{CO}/\text{Au}/\text{CO}_3^-$ system, with (s) denoting the cathode surface and (b) the bulk melt, is, near the electrode,



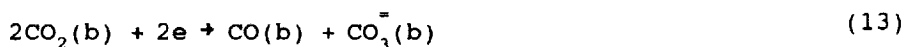
Summing,



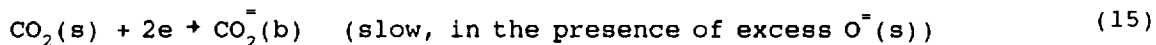
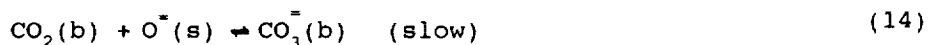
In the melt,



and overall,



In the absence of CO to effectively depolarize the cathode, the cathode must be depolarized via the slow (refs. 3, 6, and 9) acid-base equilibrium (equation (1)) by CO_2 diffusing from the melt. A possible sequence might be

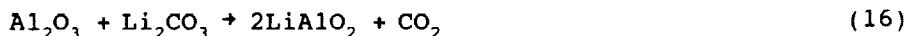


with equations (14) and/or (15) controlling.

Electrode morphology. - Figure 8 is a secondary electron image of the gold cathode surface after about 240 hr at temperatures between 800 and 900 °C, during most of which the electrode was immersed in the molten Li_2CO_3 . The large grains visible in the micrograph were not present at the beginning of the test. Figure 9 is an optical image of a cross section of a similar electrode that had not been at temperature as long but had been used as both an anode and a cathode. The picture reveals that the large gold grains can extend the full thickness of the 0.5-mm electrode flag. (Borucka (ref. 10) notes that after 6000 hr at 800 °C in a ternary alkali carbonate eutectic, a gold electrode remained "perfectly bright," developed very large surface grains, and did not dissolve, according to a spectroscopic analysis of the melt to a detection limit of 0.05 ppm.)

The Au flag working electrode had fused to it a 6-cm-long, 0.813-mm-diameter Au wire at the other end of which, above the melt, was fused another Au flag for connection to the external circuit. The upper flag was never immersed and does not visibly appear to have undergone grain development, as did the working electrode. Thus, the grain development is not simply the result of exposure to high temperature, but is due to some combination of temperature, exposure to the molten carbonate, and electrochemical usage.

Another indication of the reordering of the gold electrode surface during testing is seen in figure 10, a scanning electron microscope image which shows a region with a large population of small crystals in the process of being "swallowed up," as indicated by the contour lines encompassing each crystal. X-ray analysis of the crystals reveals aluminum and oxygen. Based on the bipyramid structure, it is assumed that the crystals are $\gamma\text{-LiAlO}_2$, since lithium is not detectable by the analysis and the γ -form is stable above 750 °C (ref. 6). This material would be formed by surface disintegration of the alumina tubes of the reference electrode and the reactant gas bubbler, followed by the reaction



CONCLUSIONS

In regards to the suitability of gold as a catalyst for the CO_2 cathode of a lithium- CO_2 battery, the results of the experiment reported here are generally encouraging. The most significant result is the evidence that CO must be present in the gaseous reactant feed stream of CO_2 to the battery cathode. In a functioning system this does not represent a problem, since CO is a product of the cathodic reaction and would be continuously rejected into the reactant gas stream. It would be a simple matter to recycle a portion of the effluent stream to build up the desired CO content. This is analogous to the recycling done in hydrogen-oxygen fuel cells to humidify a reactant inlet stream. The relationship between the amount of CO present and the activity of the gold electrode has not been established.

Of equal importance is the fact that, given the presence of CO in the reactant feed, gold allows the reduction of CO_2 to proceed at a high rate with moderate polarization. There was some loss of electrode activity during the 9-day experiment, but it is not clear whether this was due to an intrinsic characteristic of the electrode or was an artifact of the experiment. It was shown that the gold undergoes considerable morphological change at the test conditions and in a molten alkali carbonate environment. How this would manifest itself in a practical electrode design is open to conjecture. One can envision a finely divided gold catalyst dispersed on an appropriate current collector in such a way that the effect of the morphological changes would not be detrimental.

The conclusion from the experiment, that the primary cathodic reactant is, in a mechanistic sense, the carbonate melt, itself, has significance with regard to the design of a practical electrode. The electrode would not be subject to the traditional fuel cell electrode requirement of the "three-phase interface," with its vulnerability to flooding and drying, for example, thus giving the electrode designer considerably more flexibility in approach. Nonetheless, access of the CO_2 and CO to and from the near-electrode region must be quite unrestricted. Considerable conceptual, experimental, and modeling efforts will be required for development of a practical electrode.

The observed sluggishness in reaching steady-state operation after a change in load also requires mentioning. It may be that this is merely an artifact of the test cell geometry. If so, it must be resolved in the design of a practical electrode. If the problem is not so tractable, perhaps it can be resolved in a complete system by adequate power conditioning. This points out the need for some degree of system analysis early in the development of a defined mission.

ACKNOWLEDGMENTS

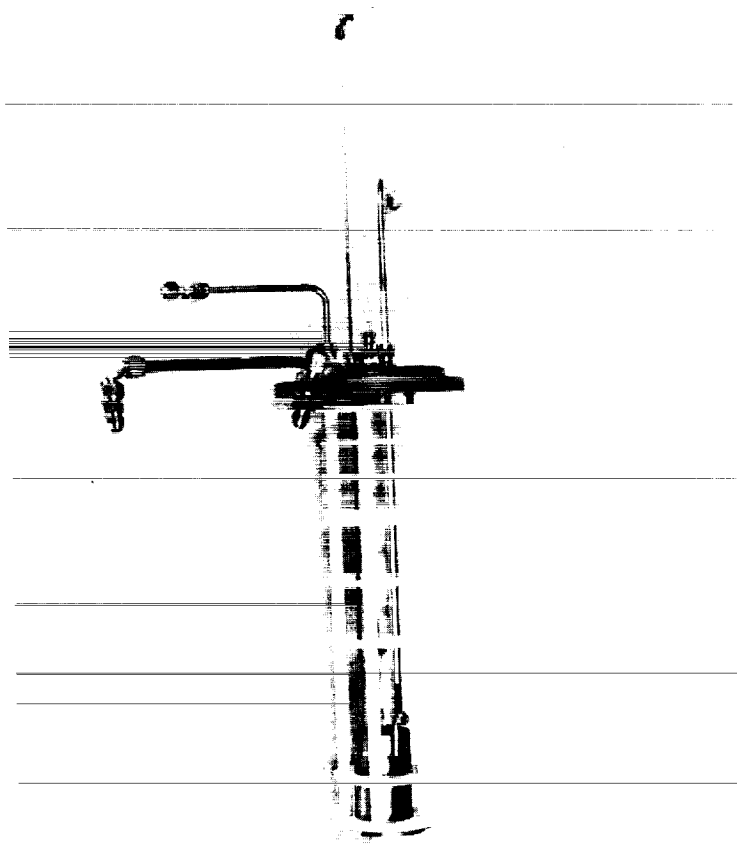
The author would like to thank Russel Gemeiner for his assistance and valuable design suggestions which made it possible to reposition cell components while at operating temperature, and Patricia Book for the microscopic and spectrographic analyses of the test electrode.

REFERENCES

1. Borucka, A.: Electrochemical Behaviour of CO/CO_2 Gas Electrode in Molten Alkali Carbonates. *Electrochimica Acta*, vol. 13, no. 3, Mar. 1968, pp. 295-307.

2. Janz, G.J., et al.: Physical Properties Data Compilations Relevant to Energy Storage-II, Molten Salts: Data on Single and Multi-Component Salt Systems. NSRDS-NBS-61-PT-2, U.S. Government Printing Office, Washington, 1979, pp. 102-112.
3. Borucka, A.: Evidence for the Existence of Stable CO_2^- Ion and Response Time of Gas Electrodes in Molten Alkali Carbonates. J. Electrochem. Soc., vol. 124, no. 7, July 1977, pp. 972-976.
4. JANAF Thermochemical Tables. 3rd ed., American Chemical Society, 1985.
5. Bard, A.J.; and Faulkner, L.R.: Electrochemical Methods, Wiley, 1980, pp. 213-248.
6. Selman, J.R.; and Maru, H.C.: Physical Chemistry and Electrochemistry of Alkali Carbonate Melts with Special Reference to the Molten-Carbonate Fuel Cell. Advances in Molten Salt Chemistry, Vol. 4, G. Mamantou and J. Braunstein, eds., Plenum, 1981, pp. 159-390.
7. Lux, H.: "Acids" and "Bases" in a Fused Salt Bath: The Determination of Oxygen-Ion Concentration. Z. Elektrochem., vol. 45, 1939, pp. 303-309.
8. Flood, H.; and Forland, T.: The Acidic and Basic Properties of Oxides. Acta Chem. Scand., vol. 1, 1947, pp. 592-604.
9. Borucka, A.; and Appleby, A.J.: Kinetics and Mechanism of Electrochemical Oxidation of Carbon Monoxide in Molten Carbonates. Confirmation of the Existence of the Carbon Dioxide Dianion. J. Chem. Soc. Faraday Trans. 1, 73, vol. no. 9, 1977, pp. 1420-1435.
10. Borucka, A.: Single Gas Electrodes in Molten Carbonates. Fuel Cell Systems II (Advances in Chemistry, Vol. 90), American Chemical Society, 1969, pp. 242-268.

ORIGINAL PAGE
BLACK AND WHITE PHOTOGRAPH



C-90-05657

Figure 1.—Experimental cell showing water-cooled cover, tie rod suspension, thermal baffles, thermocouple, reactant feed, and electrodes.

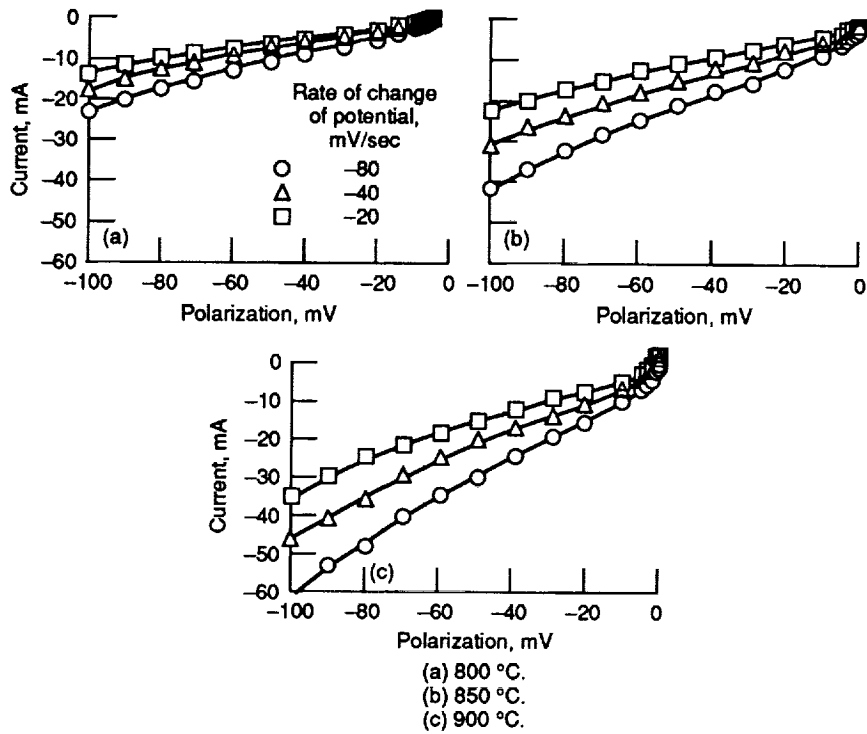


Figure 2.—Baseline linear sweep voltammograms. Gold electrode with Li_2CO_3 melt; gas feed, CO/CO_2 ; pressure, 1.2 atm; with bubbling.

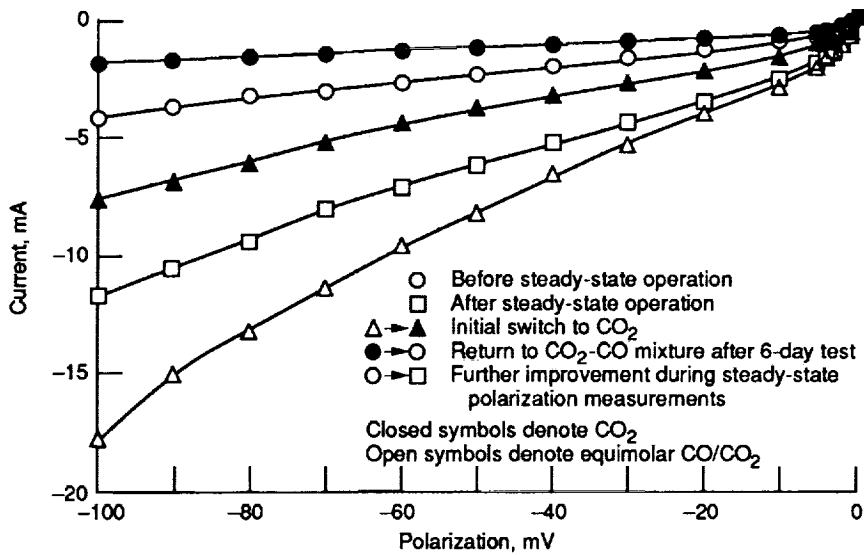


Figure 3.—Effect of reactant composition on performance, Gold electrode with Li_2CO_3 melt; potential sweep rate, -40 mV/sec; temperature, 800 °C; pressure, 1.2 atm.

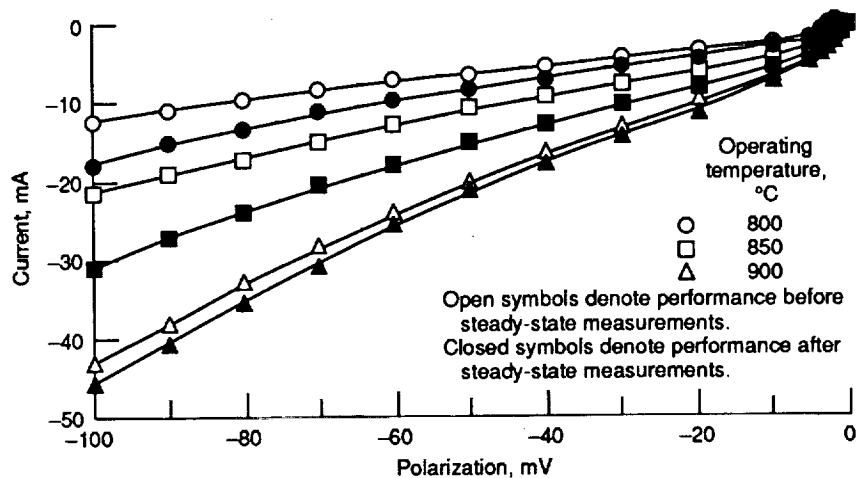


Figure 4.—Performance before (upper curve) and after (lower curve) acquisition of steady-state data at 800, 850, and 900 °C. Gold electrode with Li_2CO_3 melt; potential sweep rate, -40 mV/sec; gas feed, CO/CO_2 ; pressure, 1.2 atm.

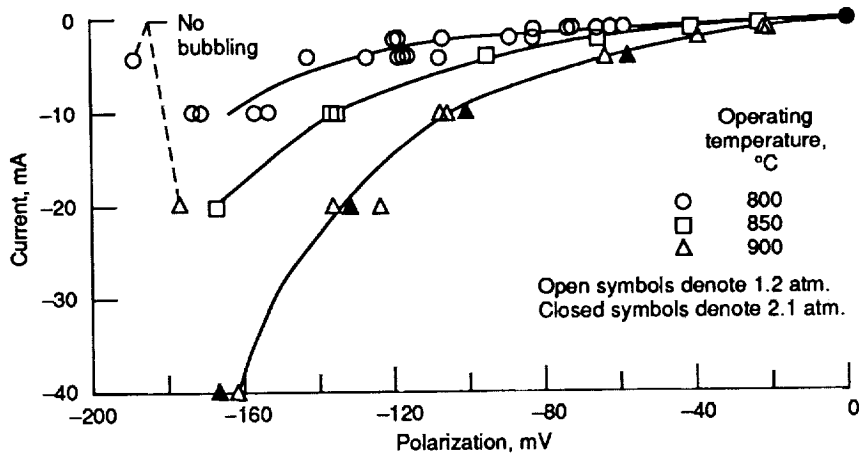


Figure 5.—Steady-state polarization data for equimolar CO/CO_2 mixture. Gold electrode with Li_2CO_3 melt.

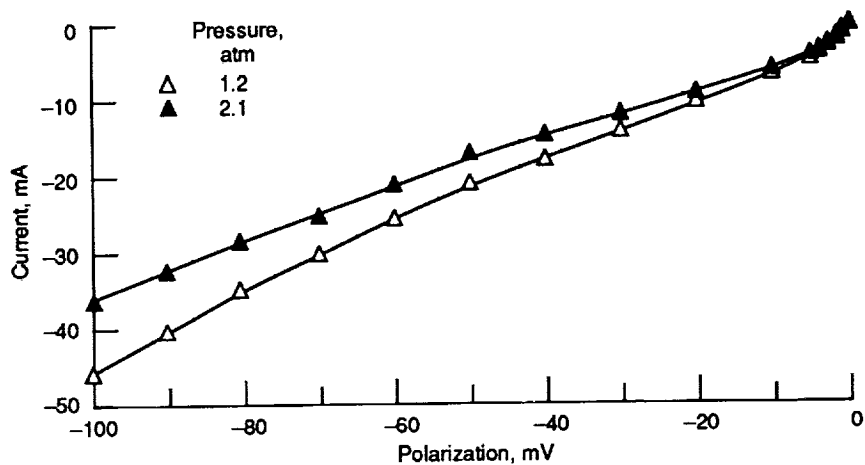


Figure 6.—Effect of total pressure on electrode performance. Gold electrode with Li_2CO_3 melt; potential sweep rate, -40 mV/sec; temperature, 900°C ; gas feed, CO/CO_2 .

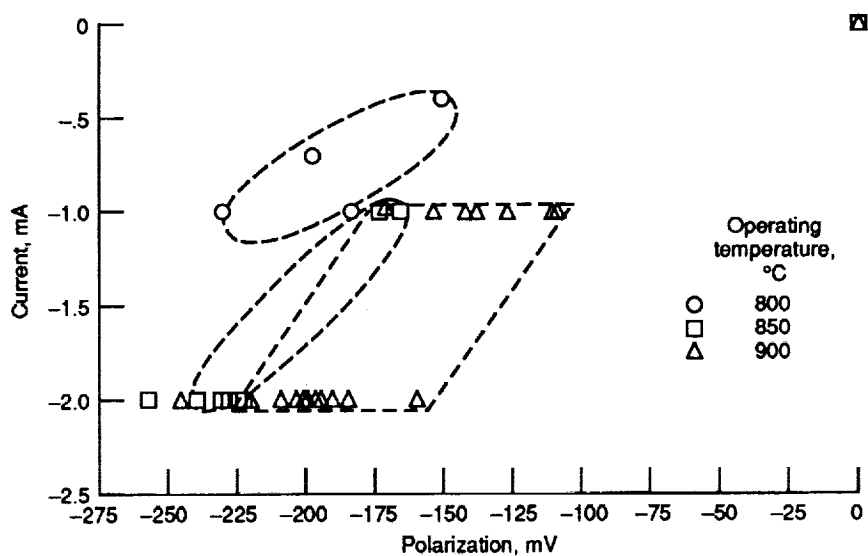


Figure 7.—Steady-state polarization data for CO_2 alone. Gold electrode with Li_2CO_3 melt; pressure, 1 to 2.1 atm; with and without bubbling.

ORIGINAL PAGE
BLACK AND WHITE PHOTOGRAPH

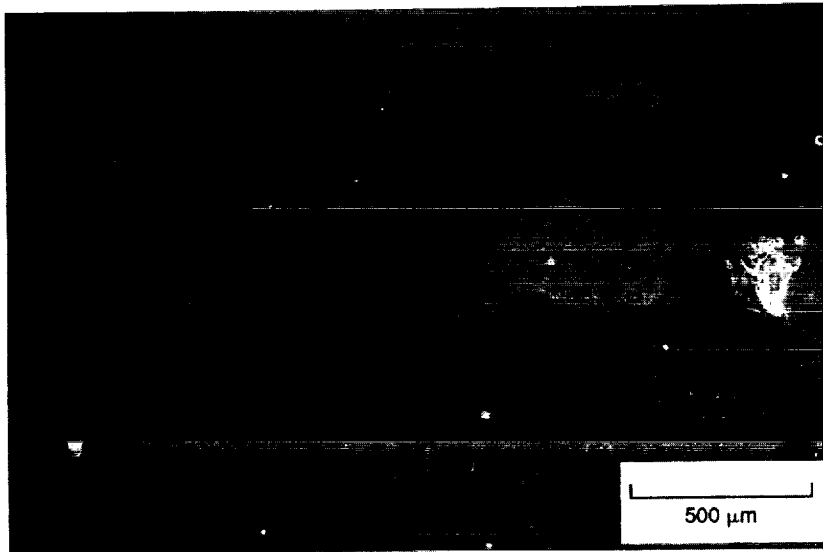


Figure 8.—Scanning electron microscope image of gold cathode surface after experiment showing development of large grains.

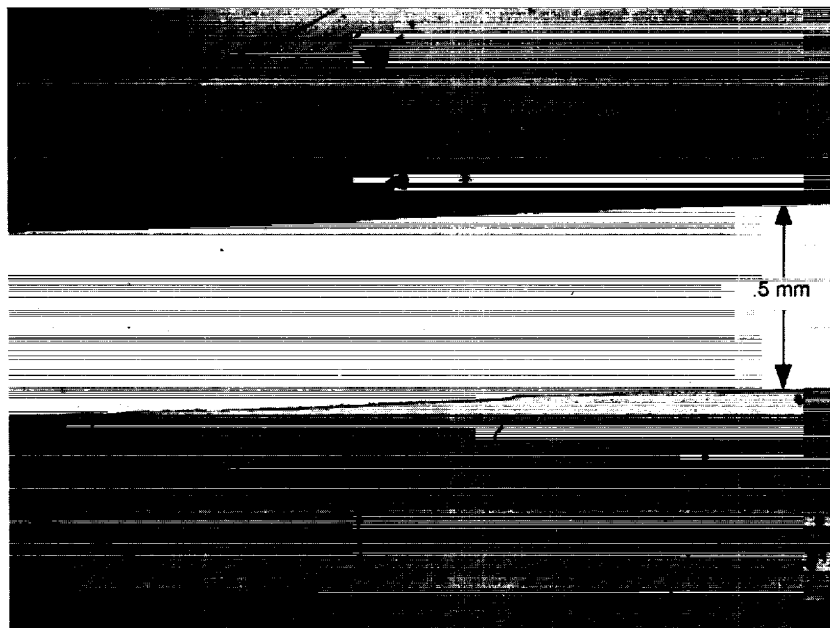


Figure 9.—Optical microscope image of cross section of gold electrode (lighter central segment) showing grain development to full depth.

ORIGINAL PAGE
BLACK AND WHITE PHOTOGRAPH

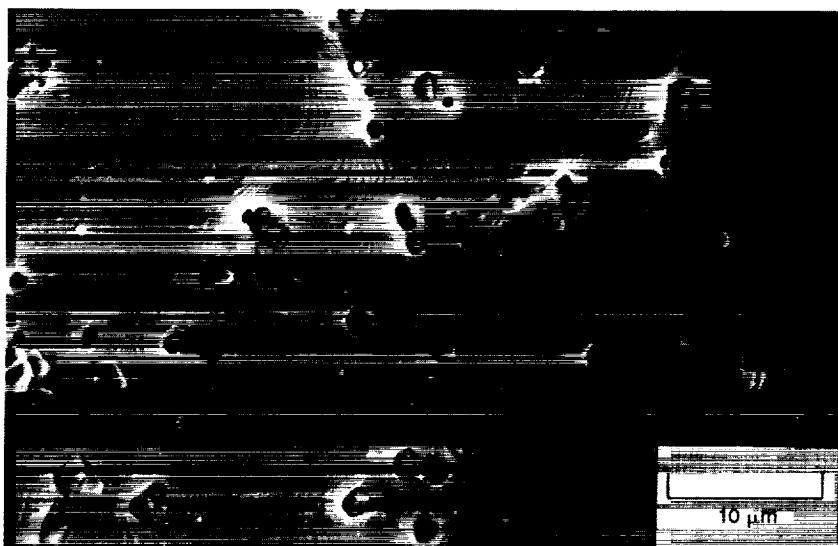


Figure 10.—Scanning electron microscope image of gold cathode surface after experiment showing encapsulation of ceramic crystals.

SPE® WATER ELECTROLYZERS IN SUPPORT OF MISSION FROM PLANET EARTH

J.F. McElroy
United Technologies Corp.
Hamilton Standard Division
Windsor Locks, Connecticut 06096

ABSTRACT

During the 1970's, the SPE water electrolyzer, which uses ion exchange membranes as its sole electrolyte, was developed for nuclear submarine metabolic oxygen production. These developments included SPE water electrolyzer operation at up to 3,000 psia and at current densities in excess of 1,000 amps per square foot. The SPE water electrolyzer system is now fully qualified for both the U.S. and U.K. Navies with tens of thousands of system hours accumulated at sea.

During the 1980's, the basic SPE water electrolyzer cell structure developed for the Navies was incorporated into several demonstrators for NASA's Space Station Program. Among these were:

- The SPE regenerative fuel cell for electrical energy storage
- The SPE water electrolyzer for metabolic oxygen production
- The high pressure SPE water electrolyzer for reboost propellant production

In the 1990's, the emphasis will be the development of SPE water electrolyzers for Mission from Planet Earth. Currently defined potential applications for the SPE water electrolyzer include:

- SPE water electrolyzers operating at high pressure as part of a regenerative fuel cell extraterrestrial surface energy storage system

SPE® is a Registered Trademark of Hamilton Standard Division, United Technologies Corporation

- SPE water electrolyzers for propellant production from extraterrestrial indigenous materials
- SPE water electrolyzers for metabolic oxygen and potable water production from reclaimed water

SPE WATER ELECTROLYSIS TECHNOLOGY OVERVIEW

The heart of the SPE water electrolyzer is the electrolysis cell which consists of an ion exchange membrane with teflon bonded, finely divided metal electrodes. Figure 1 shows this arrangement along with the water electrolysis reactions. Since the fixed acid ion exchange membrane has neither a traditional bubble point nor free electrolyte, operating pressures and hydrogen-oxygen differentials are limited only by the surrounding structures. This affords a significant safety factor in maintaining positive separation of the hydrogen and oxygen products.

The introduction of the perfluorocarbon cation exchange membrane in the late 1960's enabled the development of the SPE electrolyzer. In prior years, water electrolyzers made with existing ion exchange membranes had useful lifetimes of only a few hundred hours. With the use of perfluorocarbon ion exchange membranes, the SPE water electrolyzer cell life has been demonstrated to be in excess of 12 years and projected to over 30 years depending on operating conditions. Figure 2 displays the longest lifetime SPE water electrolyzer cell at its 100,000 hour milestone in 1989. This cell and two others have now accumulated in excess of 100,000 operational hours without disassembly or modification. These three cells continue to accumulate additional operational hours.

In most practical applications, a number of cells are stacked in a filter press arrangement with as many as 100 or more cells electrically connected in series while the fluids are passed through the cells in parallel. Figure 3 displays a pair of SPE water electrolyzers, each with 81 cells, in a filter press arrangement. Without any free electrolyte, the parallel fluid flows can be conducted without fear of shunt currents inducing stray water electrolysis and its potentially deleterious result of product gas mixing. The purity of the product gases from SPE water electrolyzers is typically greater than 99.99%.

NUCLEAR SUBMARINE OXYGEN GENERATORS

Both the U.S. Navy and the U.K. Royal Navy have sponsored the development of SPE water electrolyzers for oxygen generation in nuclear submarines. In the case of the U.K. Royal Navy, the SPE water electrolyzer system is fully qualified with more than 30 systems delivered to date. The SPE water electrolyzer module equipment is supplied by Hamilton Standard and the supporting system equipment supplied by CJB Developments of Portsmouth, England. The modules previously shown in Figure 3 are the type used in the U.K. Royal Navy system and the overall oxygen generation system itself is depicted in Figure 4. The operational experience of the SPE water electrolyzer has been exceptional with over 41,000 operational system hours without a single malfunction. The longest operational service for any single 150 psia SPE electrolyzer module is 8,539 hours as of December 31, 1990.

The U.S. Navy SPE water electrolyzer system, which operates at pressures up to 3000 psia, has passed all qualification testing, including shock, vibration and sea trials. The U.S. Navy SPE water electrolyzer modules and overall oxygen generation plant are shown in Figures 5 and 6 respectively.

During the course of developing the two Naval oxygen generation systems and the subsequent operation in the U.K. Royal Navy, over 8 million cell hours have been accumulated on the basic 0.23 ft² cell design. This high level of maturity is further described in Table 1.

SPACE STATION DEMONSTRATORS

During the decade of the eighties, a series of demonstrators were fashioned, delivered and tested at NASA. Each of these demonstrators made use of the identical 0.23 ft² SPE water electrolyzer design with its naval maturity.

SPE Regenerative Fuel Cell

The SPE regenerative fuel cell for electrical energy storage was the first of the demonstrators to be delivered to NASA in support of Space Station Freedom. Figure 7 shows the three subsystems making up the demonstrator as follows:

- SPE fuel cell subsystem
- SPE water electrolyzer subsystem
- Microprocessor controller

The SPE fuel cell module consists of eight cells, each of an active area of 1.1 ft². The SPE water electrolyzer module contains 22 cells, each of the 0.23 ft² design.

The SPE regenerative fuel cell demonstrator, with its 1 to 2 kW rating, underwent parametric testing at the factory prior to its delivery to NASA/JSC. NASA/JSC conducted extensive testing of the system accumulating 1,630 simulated low earth orbit charge/discharge cycles [1]. Including the pre-delivery factory cycles, over 2,000 cycles were accumulated on the combined SPE water electrolyzer and SPE fuel cell.

Other demonstrated features included:

- Closed system fluid cycle balance
- Direct solar array/electrolyzer voltage/current control compatibility (i.e., no power conditioning required)
- An electric energy storage efficiency of 48% recorded with the SPE water electrolyzer at ambient temperature

At the successful conclusion of the SPE regenerative fuel cell demonstration, the SPE fuel cell was replaced with a Space Shuttle alkaline development fuel cell subsystem. This hybrid of alkaline fuel cell and acid SPE water electrolyzer was operated by NASA through an additional 100 low earth orbit charge/discharge cycles [2]. Both subsystems displayed stable performance throughout the 100 cycles and proved the compatibility of the hybrid approach.

The most recent activity with the SPE water electrolyzer subsystem was to retrofit two random cells of the 22 cell SPE water electrolyzer module with high performance cells using a membrane manufactured by Dow Chemical. Following the factory modifications, the SPE water electrolyzer module with 20 standard 0.23 ft² cells and the two high performance 0.23 ft² cells underwent parametric testing at NASA/JSC [3]. The testing at various temperatures and pressures showed a significant performance improvement with the Dow membrane cells, especially at the higher current densities. The curves in Figure 8 are typical of the improvement.

SPE Metabolic Oxygen Generator

Under contract to the Boeing Aerospace and Electronics Company, an oxygen generator assembly technology demonstrator was constructed and is being evaluated. The heart of the oxygen generator is a 12 cell SPE water electrolyzer module of the identical 0.23 ft² SPE

cell configuration used on the Navy programs. Figure 9 displays the oxygen generator assembly technology demonstrator with its SPE electrolyzer module. The operating pressure, temperature and current density of the technology demonstrator are well within the technology maturity established by the Navy experiences. Where this technology demonstrator differs from the Navy data base is in the need to operate in a microgravity environment and to use processed hygiene water as the feedstock.

In the normal operation of the SPE water electrolyzer, liquid water is circulated through the oxygen anode. This loop requires a phase separator as an oxygen/water mix is discharged from the module. Also, as hydrogen protons pass through the cell membranes, water is carried to the hydrogen cathode and thus a phase separator for hydrogen/water is required.

In the microgravity situation, the functions of gravity type pressure vessel phase separators must be accomplished by other means in order to make use of the high performance SPE water electrolyzer. Prior designs have performed the microgravity function of the one gravity pressure vessel phase separator with a combination of bellows accumulators and motor driven centrifugal devices. Although this arrangement has been used successfully, the drawbacks include lower reliability and higher power consumption. The approach taken in the Boeing Technology Demonstrator utilizes two membrane static phase separators to replace the pressure vessel phase separators. This arrangement is displayed in Figure 10.

Three basic types of membranes are used in the construction of the membrane phase separators:

- **Hydrophilic Membrane** - This membrane easily passes liquid water with a small differential pressure but blocks the passage of gas up to the bubble point of the membrane. The chosen material for the Boeing Technology Demonstrator is Supor[®], having a bubble pressure of approximately 25 psi differential.

- **Hydrophobic Membrane** - This membrane easily passes gas with a small differential pressure but blocks the passage of liquid water up to the water intrusion pressure of the membrane. The chosen material for the Boeing Technology Demonstrator is Gore-Tex[®], having a water intrusion pressure of approximately 75 psi differential.
- **Ion Exchange Membrane** - Nafion[®] membrane with attached electrodes is a very efficient hydrogen compressor. With an applied voltage of between 0.5 and 1.0 volt, hydrogen is rapidly transferred through the membrane at a rate proportional to the electrical current draw.

The Technology Demonstrator was activated at NASA/MSFC in November 1990 and, in operating for 529 hours, exceeded the test objective of 450 hours. The water electrolysis was conducted at an eight-man rate, with both deionized water and shower water processed through an ultrafiltration/reverse osmosis subsystem. Throughout the operation of the Technology Demonstrator, the microgravity phase separators worked in a very satisfactory manner. The electrical performance of the Technology Demonstrator is shown in Figure 11. Continuing tests and evaluations are in process to improve the SPE cell voltage performance on processed hygiene water.

SPE Propellant Generator

Under contract to NASA/JSC, a 3,000 psi hydrogen-oxygen generator based on the Naval 0.23 ft² SPE water electrolyzer cell configuration was designed and delivered. The purpose was to demonstrate the feasibility of producing 3,000 psi hydrogen and oxygen on orbit for periodic rocket motor firing to maintain Space Station Freedom orbital altitude.

Supor[®] is a registered trademark of Gelman Sciences, Inc.

Gore-Tex[®] is a registered trademark of W. L. Gore & Associates, Inc.

Nafion[®] is a registered trademark of E. I. DuPont DeNemours & Co.

In high pressure SPE electrolyzers, a pressure vessel is used to enclose the module. Filling this pressure vessel with high pressure nitrogen precludes the necessity of designing cell seals to withstand the high pressure differential.

To reduce the mass and decrease the volume, as compared to the U.S. Navy design, several configuration changes were made to the supporting pressure vessel and fluid manifold. The resultant SPE propellant generator demonstrator is significantly smaller and lighter.

In the SPE propellant generator demonstrator, the pressure vessel is two torispherical domes opposed on either side of a central fluid plate. This configuration is shown in Figure 12. The domed design allows for a wall thickness of as low as one quarter of an inch when using Inconel or other high strength materials.

The fluid plate manifold is pressure balanced between the two pneumatic domes, eliminating the need for a thick plate to resist the pneumatic load, as is used in the U.S. Navy hardware. The demonstrator fluid manifold is only one inch thick. In the demonstrator, the cell stack is located on one side of the fluid plate within the volume of one dome.

Compression springs are located in the volume of the opposing dome. Volume is available for incorporation of gas/water phase separators and/or other system ancillaries, allowing for additional savings in system weight and volume. In addition, the cell stack incorporated edge electrical connections to a low profile positive terminal plate instead of using a plate and post assembly for additional mass and volume savings.

The SPE propellant generator demonstrator is shown in Figures 13 and 14. The dimensions of the demonstrator are 13 inches across the domes and 13 inches in diameter at the dome flanges. The total weight of the cell stack for space station propulsion is 193 lbs or 20% of the naval version. The volume is reduced 70% from the naval stack.

The demonstrator is designed to produce 2pph normal rate/4pph emergency rate of propellant (i.e., oxygen and hydrogen) gas at 3000 psia, 120°F at an efficiency of greater than 70%. Performance is shown in Figure 15 for conditions of 3100 psia, 120°F. This performance was established at the factory prior to delivery to NASA/JSC in 1990.

This demonstrator has been set up and operated intermittently at NASA/JSC over the

last few months. NASA personnel have expressed a high degree of satisfaction with the current performance.

MISSION FROM PLANET EARTH APPLICATIONS

The technology maturity gained from the 8 million cell hours of operation of the 0.23 ft² hardware, combined with the experience obtained from the Space Station Freedom demonstrators has placed the SPE water electrolyzer in position to support Mission from Planet Earth. Three potential applications for the SPE water electrolyzer are described in the following sections:

Extraterrestrial Surface Energy Storage

Recent studies have shown that, short of nuclear power, solar energy combined with an oxygen-hydrogen regenerative fuel cell is a mission enabling and preferred technology for Lunar and Mars bases [4]. Figure 16 displays the relative mass of three leading candidates for electrical energy storage as presented by NASA Lewis Research Center. The long occult periods, 14 days and 12 hours, respectively, make the separation of power and energy in the oxygen-hydrogen regenerative fuel cell decisive. In Figure 17, showing an overall power plant schematic, energy storage mass is related to the tankage and stored fluids whereas the power rating mass is related to the modules and thermal management. The electrolysis and fuel cell modules can be of either the alkaline or acid type; however, the acid SPE water electrolyzer, of the Naval 0.23 ft² configuration in particular, has demonstrated the life, stability, reliability and high pressure capability required of an extraterrestrial surface energy storage system.

The schematic for 3000 psi SPE water electrolysis is much the same as the low pressure schematic except that the electrolyzer module is enclosed in the nitrogen filled pressure vessel. Figure 18 displays the overall SPE water electrolyzer efficiency at various temperatures. The 1000 amps per square foot (ASF) current density, which is below the Naval design point of 1300 ASF, will provide an efficiency in excess of 70% at the 20,000 hour end-of-mission point.

A fuel cell operating at 70% overall fuel cell efficiency will require approximately 21.6 pounds per hour of hydrogen-oxygen reactants in a 1 to 8 weight ratio to produce 25 kW direct current. If one assumes an equal charge discharge time for either the lunar or Mars application, the electrolyzer will have to convert

a maximum of 21.6 pounds per hour of water into hydrogen and oxygen. The mass of the SPE water electrolyzer subsystem with 138 cells would be about 200 kg using the proven cell structure with DuPont's Nafion® 120 ion exchange membrane. Figure 19 shows that a decreased mass can be obtained by the use of higher performance membranes and/or advanced cell structures. However, the low mass is gained at the expense of design maturity.

A single SPE water electrolyzer subsystem would probably not be considered because of reliability aspects. Over a five-year period, the loss of a pump or gas regulator is predicted. These difficulties can be overcome by redundancy within the subsystem at a small weight penalty. Reliability is further enhanced by having multiple SPE water electrolyzer subsystems. Preliminary estimates show that three subsystems, each with selected component redundancies, would be highly reliable for a multiple year mission.

Propellant Production

In any round trip to Mars, the propellant for the return trip is a most significant mass factor when the propellant is brought from Earth. For manned missions to Mars, multiple launches with Earth orbital vehicle assembly will be required in mission architectures which bring the return propellant to Mars from Earth. By contrast, the use of in-situ propellant production can greatly reduce mission mass and, together with a heavy lift launch vehicle, can eliminate the need for on-orbit assembly.

A system which combines a SPE water electrolyzer with Sabatier and carbon formation reactors can produce methane and oxygen from carbon dioxide in the Martian atmosphere and hydrogen delivered from Earth [5]. This arrangement can increase the Earth return propulsive reactant mass leverage by up to 18 fold. Each of the required subsystems have been demonstrated individually with high confidence that they can be combined to produce the desired results.

A top level schematic with subsystem reactions is shown in Figure 20. In this mission architecture, liquid hydrogen is transported from the Earth directly to the Martian surface. This hydrogen is reacted with atmospheric carbon dioxide to produce methane and water in the exothermic Sabatier reactor. The water is delivered to the SPE water electrolyzer and the methane is liquified and stored. Hydrogen and

oxygen are produced within the SPE water electrolyzer with the oxygen being liquified and stored and the hydrogen returned to the Sabatier for the formation of more methane and water. With these two subsystems alone, a 12 to 1 propellant mass leverage is obtained.

The combined Sabatier and SPE water electrolyzer produce the oxygen and methane at a 2 to 1 mass ratio. Burning this mixture provides a specific impulse of about 340 S at a nozzle expansion ratio of 100. However, an optimum oxygen to methane combustion mixture ratio is about 3.5 to 1. This mixture would provide a specific impulse of 353 S. To obtain the 3.5 to 1 ratio, which increases the propellant to hydrogen mass leveraging to 18 to 1, additional oxygen must be obtained. The carbon formation reactor provides this opportunity.

Referring back to Figure 20, a portion of the methane produced in the Sabatier is borrowed and delivered to the carbon formation reactor. In the reactor, the methane is endothermically converted to solid carbon and hydrogen. The hydrogen is returned to the Sabatier/SPE water electrolyzer combination to replace the borrowed methane and produce the additional oxygen. By continuing this process, any desired level of excess oxygen can be produced. However, the 36 extra tonnes of excess oxygen needed for a manned mission would require a huge carbon formation reactor to hold all the solid carbon produced. This difficulty is overcome by having two carbon formation reactors which alternately cycle between carbon formation and an endothermic regeneration reaction with carbon dioxide.

Preliminary mass estimates for the required subsystems have been made for a Mars Sample Return Mission and a Mars Manned Mission. Table 2 provides these estimates. Since the subsystems, once on the Martian surface, will have to produce propellants for up to one year, a degree of redundancy is required. The mass estimates assume two complete units each with 100% mission capacity for the system used in the Mars Sample Return Mission and three units each with 50% capacity for the system employed on the manned Mars mission.

Metabolic Oxygen and Potable Water Production

The production of metabolic oxygen for space applications has been under investigation for a number of years. Recently, water feedstock with various organic contaminants have been tested with the SPE water electrolyzer to assess the impact on the voltage stability. In these tests, the

contaminated water feedstock has been introduced into the oxygen anode chamber in the same fashion as the Naval SPE water electrolyzers. As discussed earlier, continuing tests and evaluations are in process to improve the SPE cell voltage performance on water feedstock with organic contaminants.

Tests conducted on the quality of the water at various points in the system indicated that organic species were being oxidized within the oxygen chamber and that the proton pumped water was free of any detectable organics. These observations have led to the speculation that the SPE water electrolyzer can be configured to produce potable water as well as metabolic oxygen. Figure 21 displays the metabolic oxygen generator schematic as modified to show delivery of potable water. The rate of protonically pumped water is such that up to eight pounds of potable water can be delivered for each pound of oxygen produced. For manned Lunar and Mars bases and the Lunar and Mars manned transportation vehicles a combined oxygen generator and potable water processor could have significant mass advantages.

SUMMARY

Although the Mission From Planet Earth is still in the early planning stage, several unique and

potentially enabling uses of the SPE water electrolyzer have been identified. The maturity of the SPE water electrolyzer cells gained from the Naval applications should give mission planners the confidence to take advantage of the leveraging effects of the SPE cell technology. Although the inherent capabilities of this technology have been proven, significant development effort remains to package these cells for the Mission From Planet Earth applications.

REFERENCES

- [1]: NASA/JSC Internal Note
Document No. JSC-22044, dated 4/28/86
- [2]: NASA/JSC Internal Note
Document No. JSC-22632, dated 9/30/87
- [3]: NASA/JSC Internal Note
Document No. JSC-24411, dated 7/25/90
- [4]: NASA Conference Publication 3016;
September 12-13, 1988, p. 206
- [5]: Zubrin, R. et al: "*Mars Direct: A Simple, Robust and Cost Effective Exploration Initiative*" (AIAA 91-0326), 29th Aerospace Sciences Meeting, January 7-10, 1991

**TABLE 1
 DEMONSTRATED MATURITY-NUCLEAR SUBMARINE SPE WATER ELECTROLYZERS
 AS OF DECEMBER 31, 1990**

| Type of Service/Product Description Navy Electrolyzers | Electrolysis Rate lbs/hr H ₂ O | Cell Area ft ² | Operating Pressure PSI | Number of Stacks | Number of Cells Per Stack | Total Number Of Cells | System Hours | Stack Hours | Cell Hours |
|---|--|------------------------------|---------------------------|------------------|---------------------------|-----------------------|----------------|----------------|------------------|
| U.S. Navy: | | | | | | | | | |
| Nuclear Submarine O₂ Generation | | | | | | | | | |
| 3000 psi System Qualification Unit (OGP#2) | 21 | 0.23 | 300 to 3000 | 2 | 100 | 200 | 5,000 | 5,000 | 500,000 |
| 3000 psi System Preprototype (OGP#1) | 21 | 0.23 | 300 to 3000 | 2 | 100/83 | 183 | 10,000 | 13,000 | 1,181,000 |
| Development System (Breadboard) | 21 | 0.23 | 300 to 3000 | 2 | 100 | 200 | 14,000 | 28,000 | 2,800,000 |
| Development Stack OGP Program | 1 | 0.23 | 300 to 3000 | 1 | 5 | 5 | 1,900 | 1,900 | 9,500 |
| Development Stack OGP Program | 2 | 0.23 | 300 to 3000 | 1 | 10 | 10 | 1,500 | 1,500 | 15,000 |
| Development Stack OGP Program | 4 | 0.23 | 300 to 3000 | 1 | 20 | 20 | 2,500 | 2,500 | 50,000 |
| Development Stack OGP Program | 7.4 | 0.23 | 300 to 3000 | 1 | 35 | 35 | 3,900 | 3,900 | 136,500 |
| Development Stack NSSC 4 | 0.2 | 0.23 | ambient | 1 | 1 | 1 | 107,100 | 107,100 | 107,100 |
| Development Stack NSSC 7 | 0.2 | 0.23 | ambient | 1 | 1 | 1 | 103,200 | 103,200 | 103,200 |
| Development Stack NSSC 9 | 0.2 | 0.23 | ambient | 1 | 1 | 1 | 108,500 | 108,500 | 108,500 |
| United Kingdom Navy | | | | | | | | | |
| Nuclear Submarine O₂ Generation | | | | | | | | | |
| Development Stack S/N#1 | 12.5 | 0.23 | 150 | 1 | 58 | 58 | 3,000 | 3,000 | 174,000 |
| Development Stack S/N#2 | 15 | 0.23 | 150 | 1 | 70 | 70 | 6,000 | 6,000 | 420,000 |
| Production Stacks: | | | | | | | | | |
| Various Production | 15 to 17 | 0.23 | 150 | 35 | 70 or 81 | 2700 | 41,632 | 41,632 | 3,122,400 |
| Longest Life UK Stack | 15 to 17 | 0.23 | 150 | 1 | 81 | 81 | 8,539 | 8,539 | 691,659 |
| TOTAL | | | | 50 | | 3474 | 408,239 | 425,239 | 8,727,200 |

With over 8 million cell hours of successful operation, the SPE 0.23 ft² cell design is well established

**TABLE 2
 MASS ESTIMATES FOR CH₄/O₂ PLANT**

| REACTOR | MARS SAMPLE RETURN | MANNED MARS |
|-----------------------------------|--------------------|-------------|
| Sabatier | 36 kg | 164 kg |
| Electrolysis | 90 kg | 477 kg |
| Carbon Reactor | 105 kg | 450 kg |
| TOTAL | 231 kg | 1,091 kg |
| Propellant Generation Requirement | 3.6 kg/day | 360 kg/day |
| Capability | 7.2 kg/day | 540 kg/day |

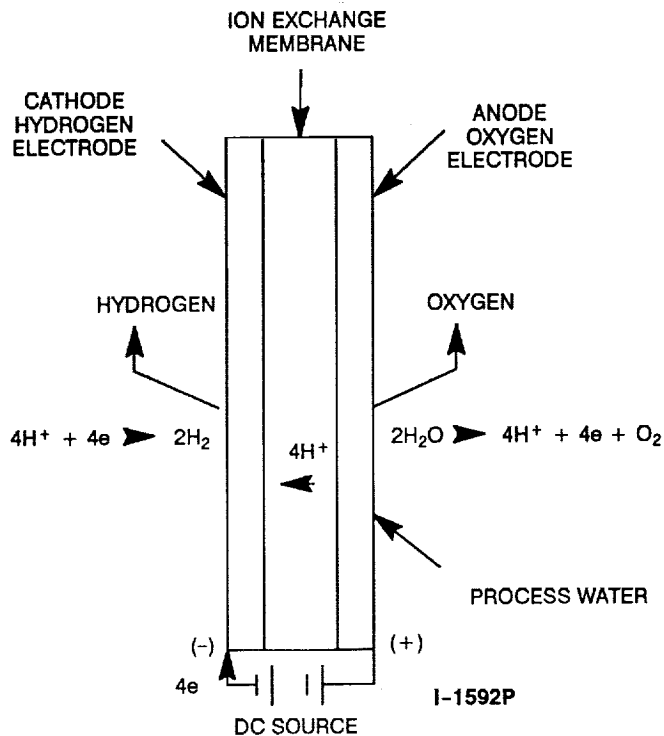


FIGURE 1. SPE WATER ELECTROLYZER REACTIONS

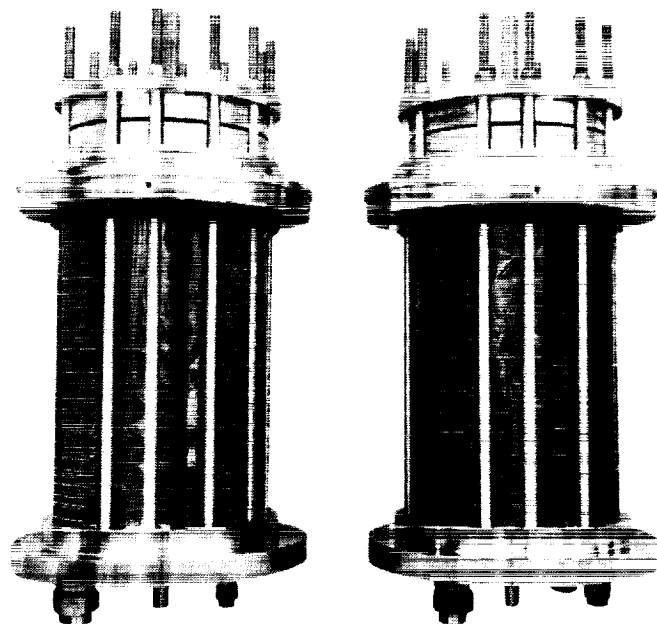


FIGURE 3. SPE WATER ELECTROLYZER MODULES

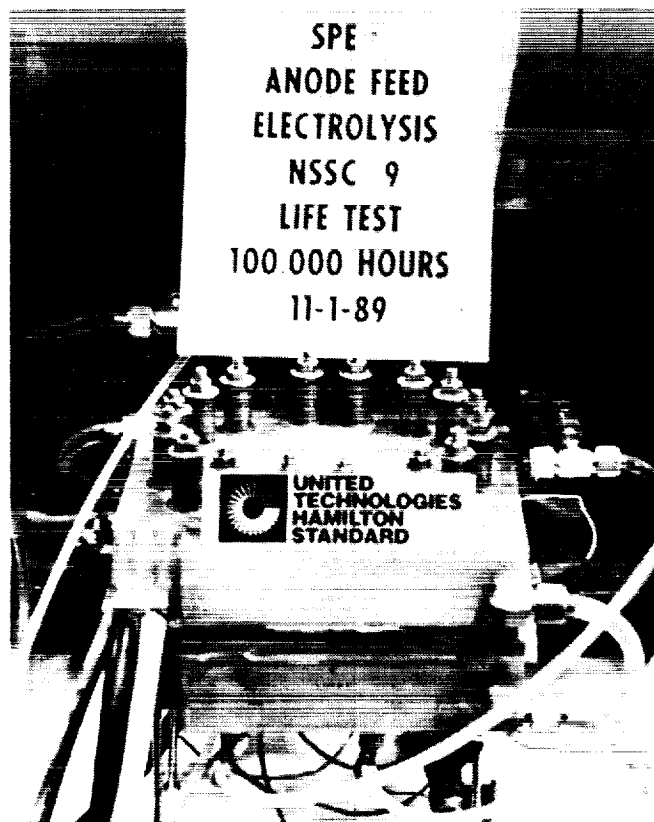


FIGURE 2. SPE ELECTROLYZER LIFE TEST

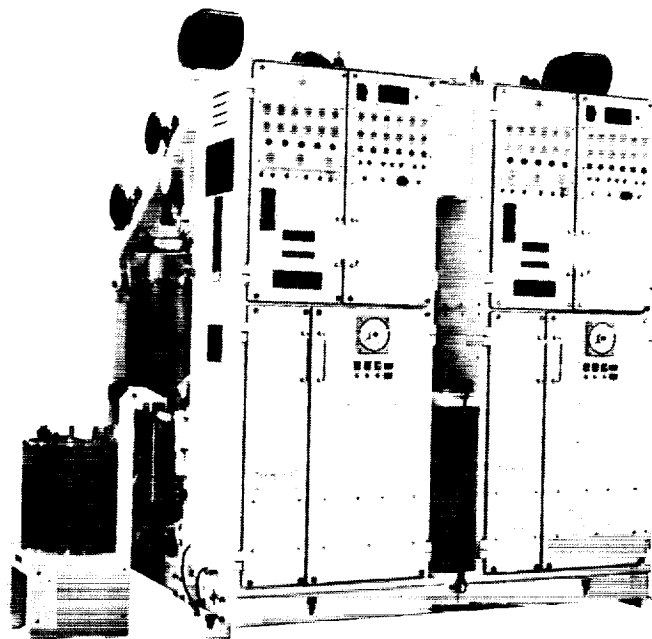


FIGURE 4. A DUPLEX LOW PRESSURE ELECTROLYZER (LPS) OXYGEN GENERATING SYSTEM FOR NAVAL USE

ORIGINAL PAGE
BLACK AND WHITE PHOTOGRAPH

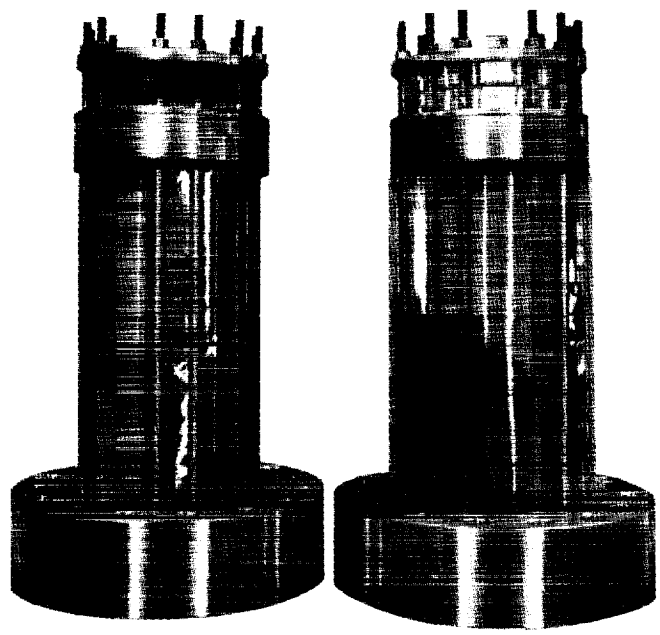


FIGURE 5. 225 SCFH U.S. NAVY SPE OXYGEN GENERATOR MODULES

ORIGINAL PAGE
BLACK AND WHITE PHOTOGRAPH

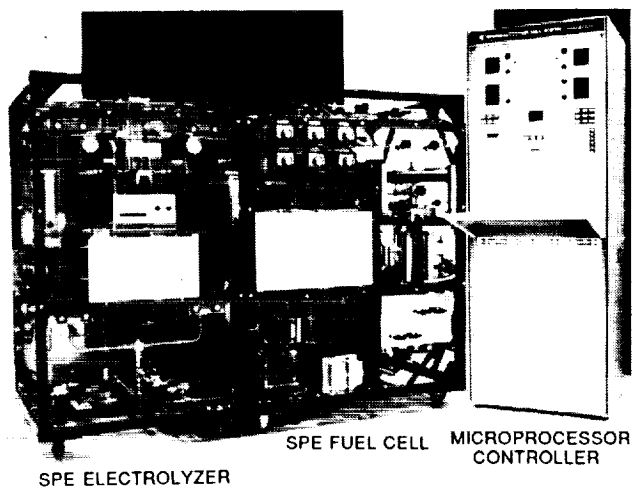


FIGURE 7. SPE REGENERATIVE FUEL CELL DEMONSTRATOR

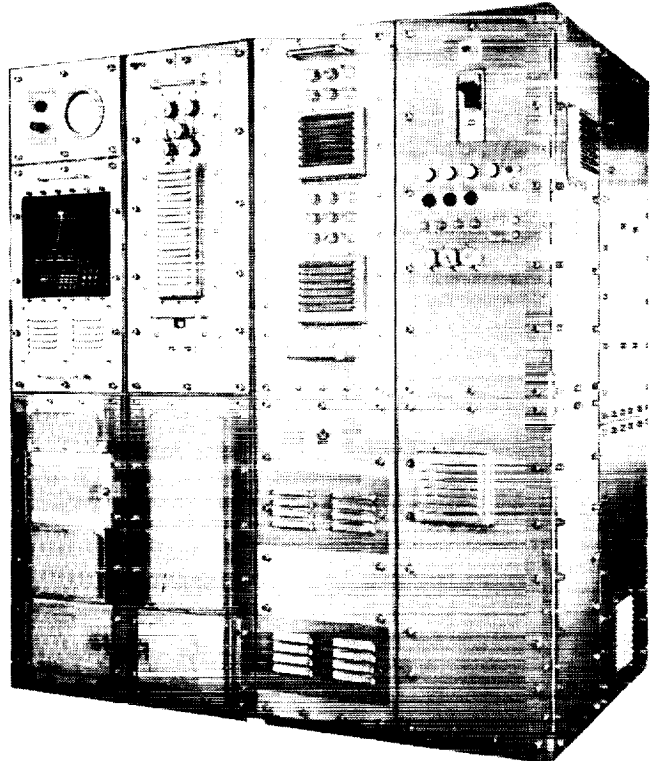


FIGURE 6. HIGH PRESSURE OXYGEN GENERATING PLANT (OGP) FOR NAVAL USE

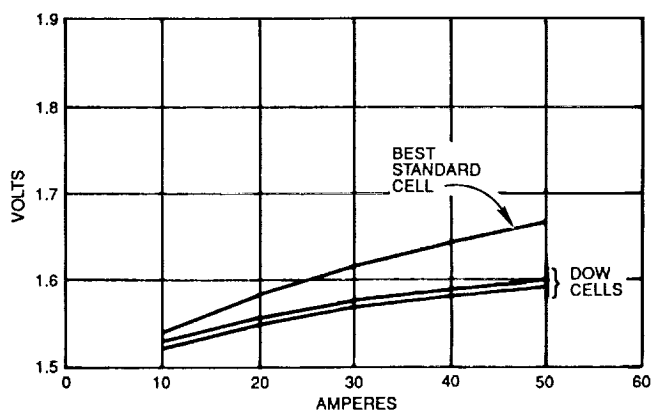


FIGURE 8. COMPARISON OF CELLS AT 150 PSI AND 105°F

OXYGEN GENERATOR ASSEMBLY

SPE ELECTROLYZER MODULE

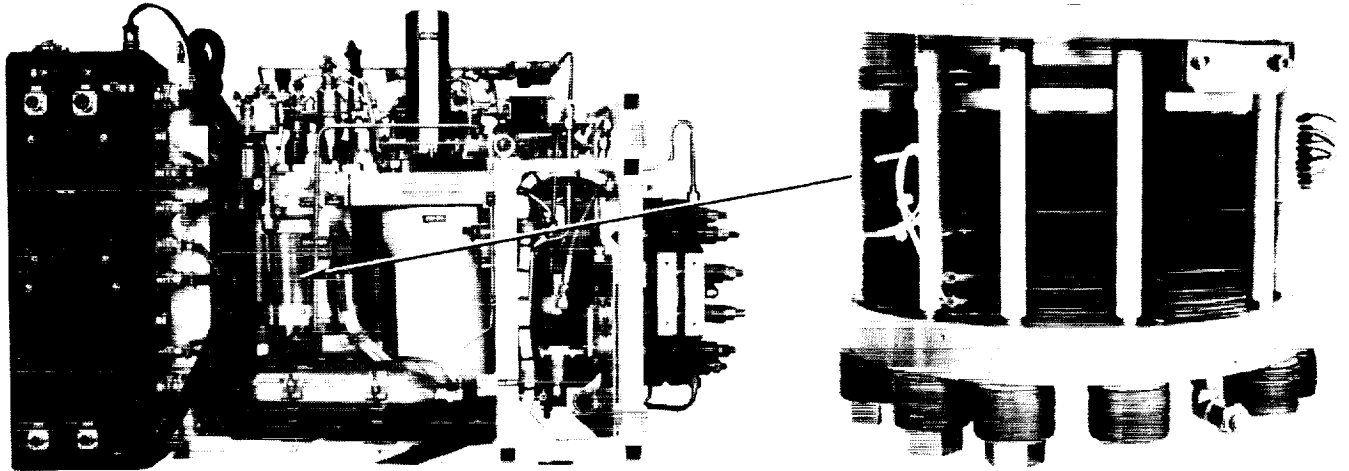


FIGURE 9. OXYGEN GENERATOR ASSEMBLY TECHNOLOGY DEMONSTRATOR

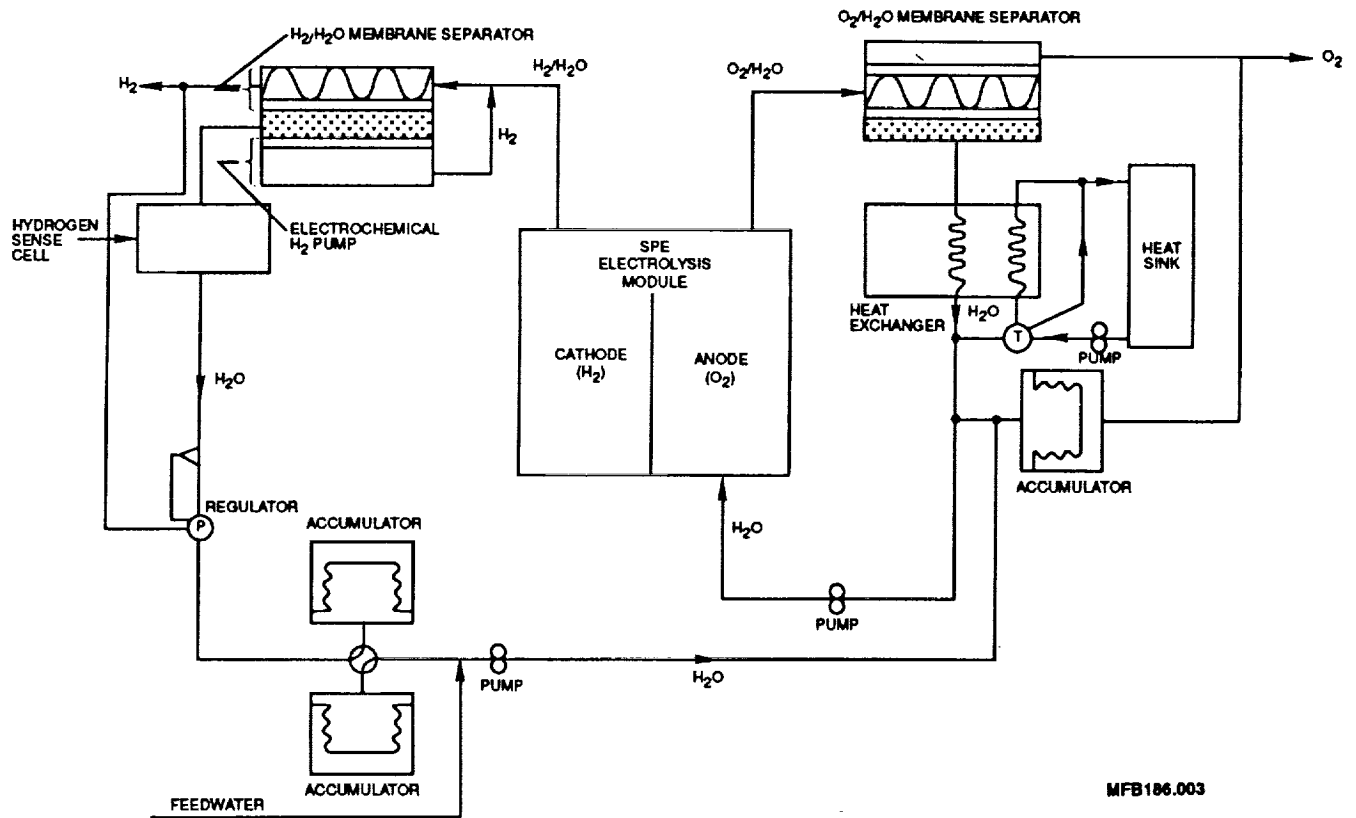


FIGURE 10. SIMPLIFIED MICROGRAVITY FLUID SCHEMATIC (SPE ELECTROLYZER SYSTEM)

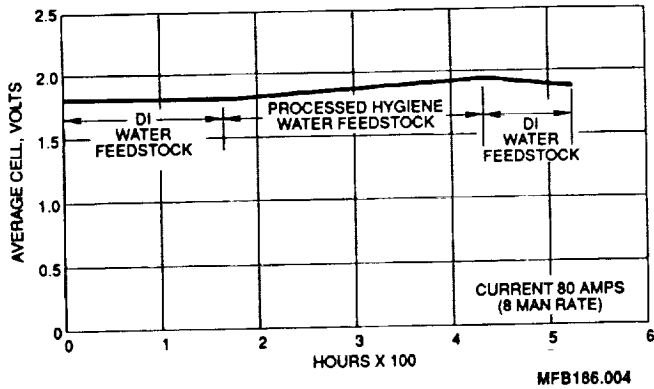


FIGURE 11. SPE ELECTROLYZER TECHNOLOGY DEMONSTRATOR PERFORMANCE

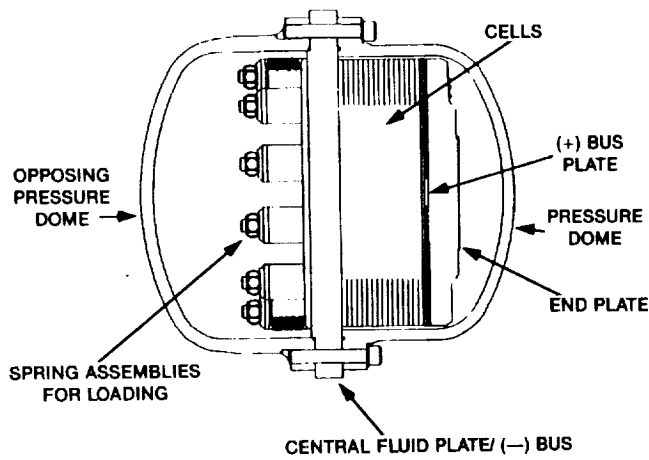


FIGURE 12. CROSS-SECTION, SPE PROPELLANT GENERATOR DEMONSTRATOR

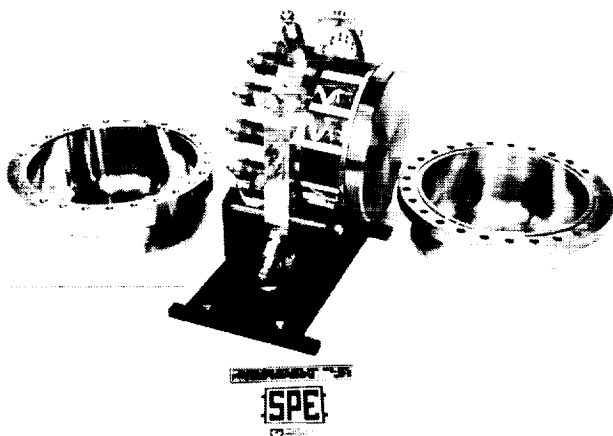


FIGURE 13. SPE PROPELLANT GENERATOR, DOMES REMOVED

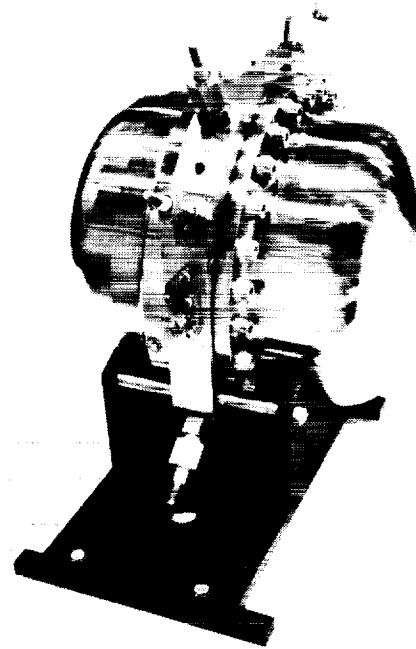


FIGURE 14. ASSEMBLED SPE PROPELLANT GENERATOR

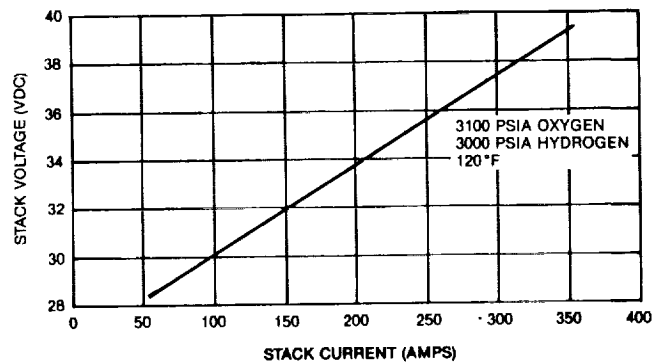


FIGURE 15. SPE PROPELLANT GENERATOR PERFORMANCE (STACK VOLTS VS. AMPS)

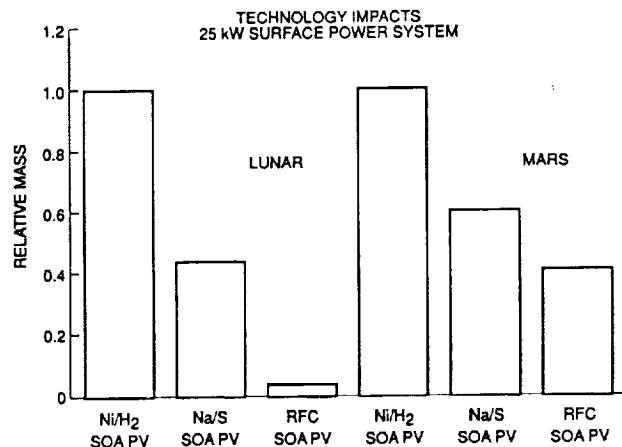


FIGURE 16. RELATIVE MASS OF ENERGY STORAGE TECHNOLOGIES

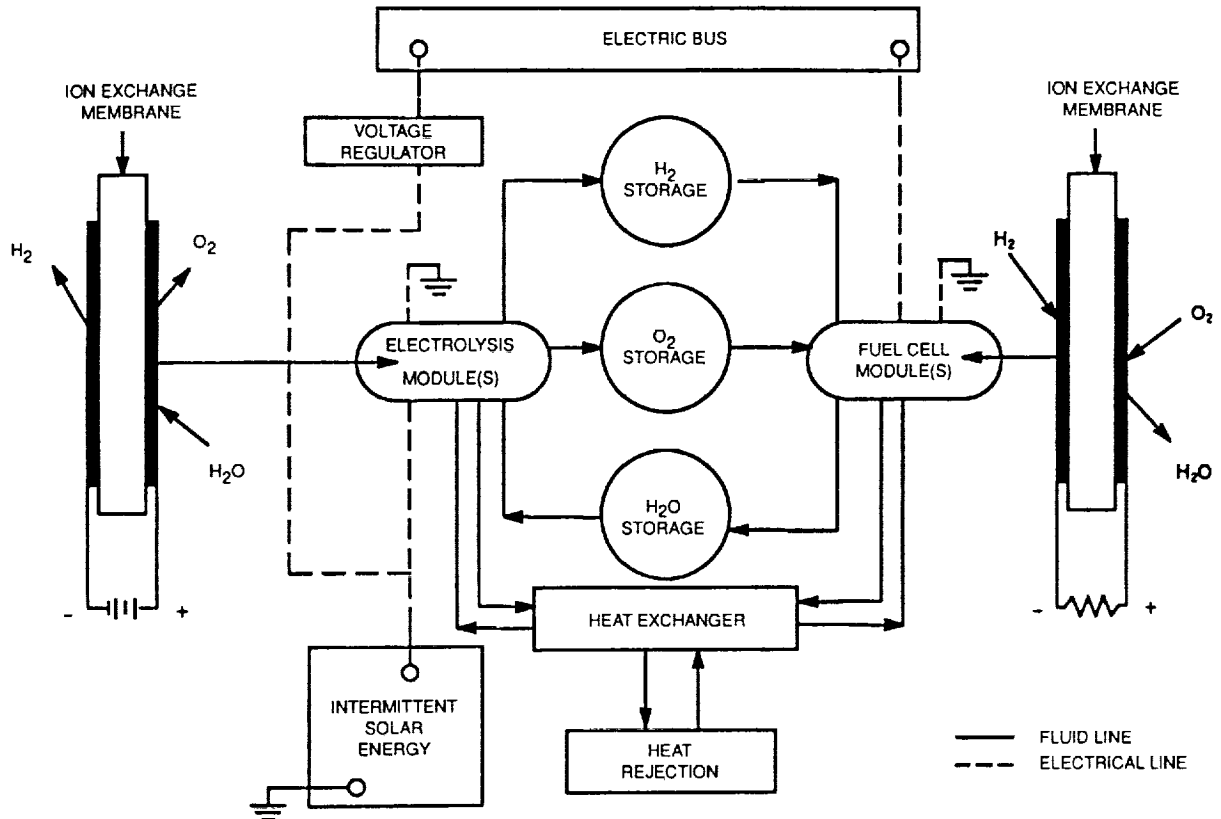


FIGURE 17. POWER PLANT SCHEMATIC INCLUDING HYDROGEN/OXYGEN REGENERATIVE FUEL CELL ENERGY STORAGE SYSTEM

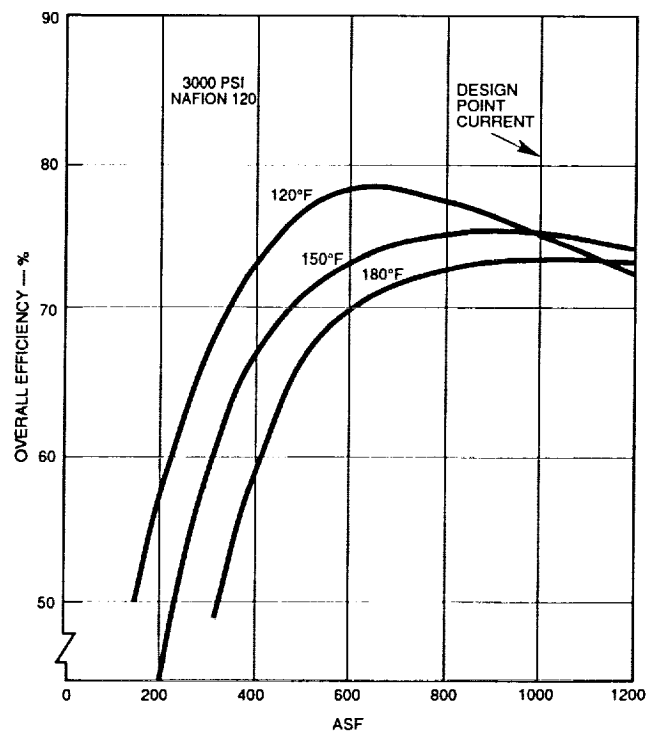


FIGURE 18. OVERALL SPE WATER ELECTROLYZER EFFICIENCY AT 3000 PSI

| ELECTROLYZER SUBSYSTEM DESCRIPTION | NAFION 120 MEMBRANE | NAFION 125/117 MEMBRANE | ADVANCED MEMBRANE |
|---|---------------------|-------------------------|-------------------|
| | LBS | LBS | LBS |
| | KG | KG | KG |
| "STATE OF THE ART" WITH STATIC SEPARATORS | 439 | 363 | 324 |
| | 200 | 165 | 147 |
| ADVANCED DESIGN WITH STATIC SEPARATORS | 347 | 316 | 301 |
| | 158 | 144 | 137 |

- BASED ON:
- 21.6 HR IF WATER ELECTROLYZED
 - 70% THERMAL EFFICIENCY FOR 20,000 HRS
 - 3,000 PSIA GAS GENERATION PRESSURE
 - THERMAL VACUUM COMPATIBLE
 - EQUAL CHARGE/DISCHARGE TIMES

- NOTES:
- ONLY NAFION 120 HAS THE PEDIGREE
 - ADVANCED DESIGN NEEDS DEVELOPMENT VERIFICATION

FIGURE 19. SPE WATER ELECTROLYZER SUBSYSTEM MASS SUMMARY FOR 25 KW SYSTEM

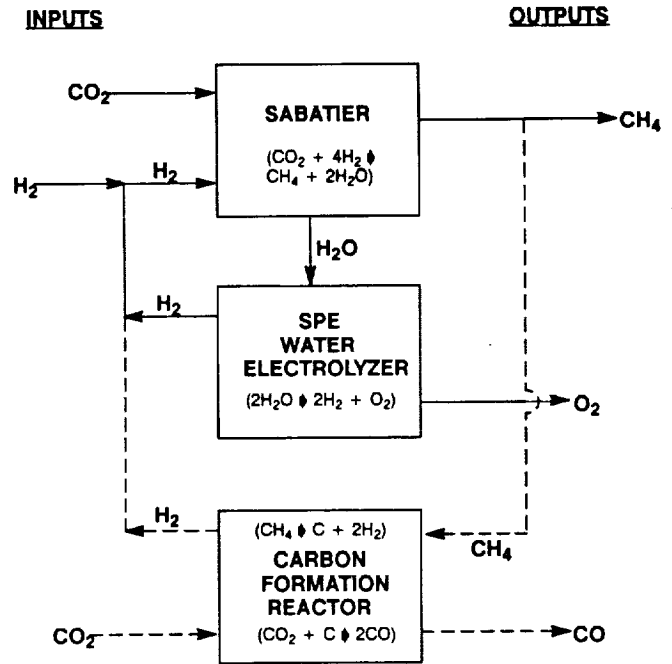


FIGURE 20. TOP LEVEL SCHEMATIC OF MARTIAN FUEL AND OXYGEN GENERATOR

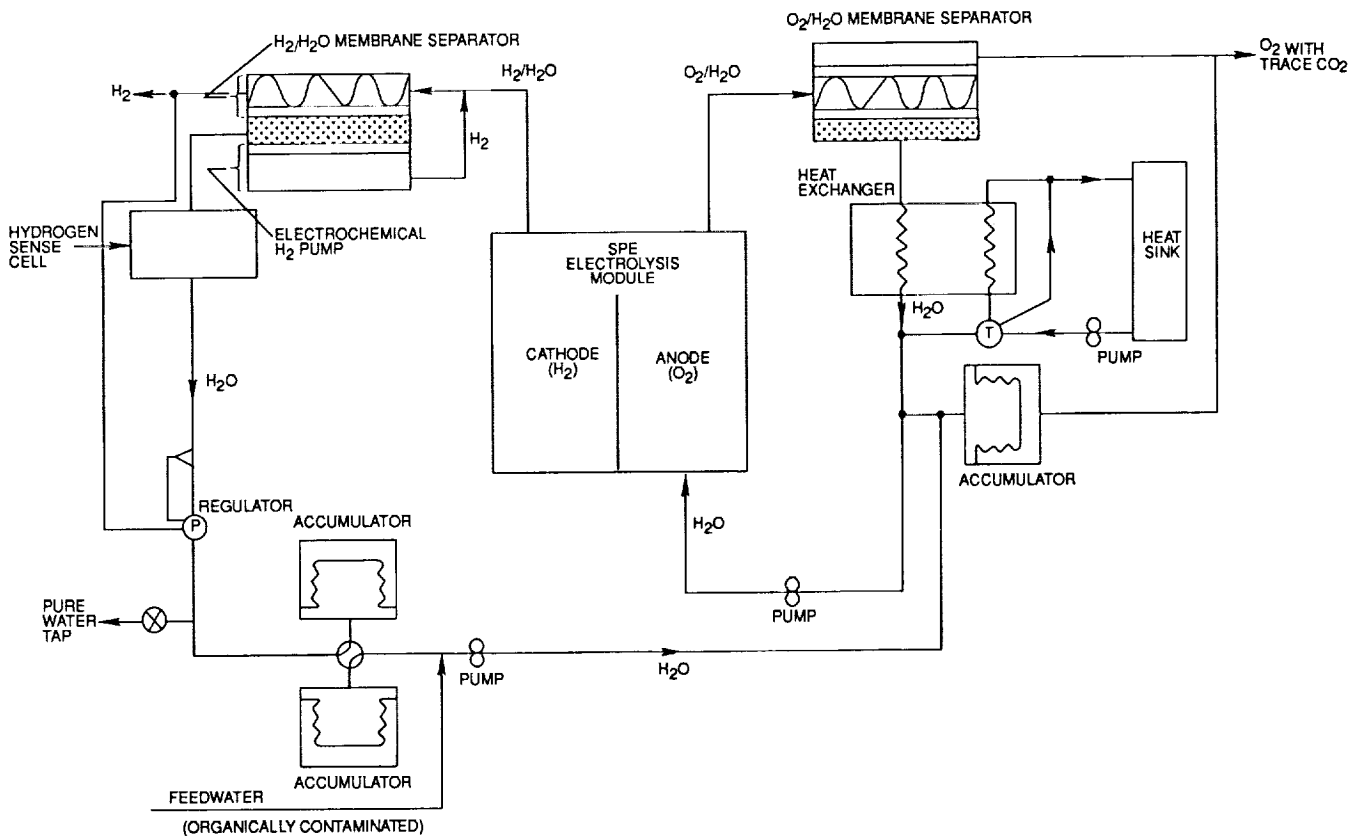


FIGURE 21. METABOLIC OXYGEN/POTABLE WATER GENERATOR



SPACE WATER ELECTROLYSIS:
SPACE STATION THROUGH ADVANCE MISSIONS

Ronald J. Davenport*, Franz H. Schubert, and David J. Grigger
Life Systems, Inc.
Cleveland, Ohio 44122

Static Feed Electrolysis technology has long been recognized as being important in meeting the National Aeronautics and Space Administration's requirements for life support within the Space Station Freedom Program and future, advanced missions. The Static Feed Electrolysis technology makes it possible to very efficiently generate oxygen to sustain the crew, and hydrogen for the efficient and economical operation of other space systems.

More recently, additional applications for the Static Feed Electrolysis technology have been evaluated and tested. This paper summarizes the results of those studies. The applications addressed here are those involving energy storage, propulsion, extravehicular activity and other, specialized applications, such as providing support for experimentation and manufacturing. The Environmental Control and Life Support System application is included for comparison.

INTRODUCTION

This paper summarizes how Static Feed Electrolyzer (SFE) technology can satisfy the need for oxygen (O_2) and hydrogen (H_2) in the Space Station Freedom and future, advanced missions. These applications are identified in Fig. 1. The efficiency with which the SFE technology can be used to generate O_2 and H_2 is one of its major advantages. In fact, the SFE is baselined for the Oxygen Generation Assembly (OGA) within the Space Station Freedom's Environmental Control and Life Support System (ECLSS).

Figure 2 shows the conventional SFE process. An alkaline electrolyte is contained within the matrix and is sandwiched between two porous electrodes. The electrodes and matrix make up a unitized cell core. The electrolyte provides the necessary path for the transport of water and ions between the electrodes, and forms a barrier to the diffusion of O_2 and H_2 .

A hydrophobic, microporous membrane permits water vapor to diffuse from the feed water to the cell core. This membrane separates the liquid feed water from the product H_2 , and, therefore, avoids direct contact of the electrodes by the feed water. This eliminates the possibility of catalyst poisoning by contaminants in the feed water. The feed water is also circulated through an external heat exchanger to control the temperature of the cell.

Electrical power, when applied to the electrodes, consumes water within the cell core. This increases the difference between the water vapor pressures in the

* Author to whom correspondence should be addressed.

electrolyte in the cell core, and in the liquid in the feed compartment. As a result, water vapor diffuses from the feed water compartment into the cell core. An external water supply tank replenishes water consumed from the feed compartment. The operation and performance of the SFE have been previously described in greater detail [1-3].

In a typical SFE subsystem, the electrochemical cells are combined to form an electrolysis module. The cells are arranged electrically in series, but the fluids flow through the cells in parallel. In addition to the module, the other mechanical components within the subsystem consist of the Thermal Control Assembly (TCA), a Fluids Control Assembly (FCA) and a Pressure Control Assembly (PCA).

The TCA supplies a constant flow rate of feed water to the electrochemical module. The temperature of this water is varied to maintain the module at the desired temperature. Temperature control is achieved by proportioning the flow of the feed water between a bypass and a heat exchanger.

The FCA controls and monitors the flow of feed water and purge gas into the SFE subsystem. The PCA maintains the absolute and differential pressures in the subsystem and controls pressurization of the system during startup and shutdown.

The TCA, FCA and PCA are mechanically integrated assemblies, made up of valves, pumps, pressure regulators and sensors which monitor and control the subsystem. These components were developed and refined by Life Systems as part of SFE subsystem development efforts performed during the last 20 years. The integrated design of these components offers significant savings in volume and weight, compared to the use of discrete components [4]. Equally important, the use of integrated components enhances the maintainability of SFE subsystems [5].

The operation of the SFE subsystem is controlled and monitored by microprocessor-based instrumentation. The instrumentation performs process control, automatic mode transition, fault diagnostics and data acquisition functions.

APPLICATIONS

This section discusses the application of the SFE technology to the energy storage, ECLSS, propulsion, extravehicular activity (EVA) and other, special applications. Typical O_2 and H_2 production and delivery requirements for some of these applications are listed in Table 1. This table shows the diversity of the requirements that be accommodated by SFE technology.

This section also addresses future studies that are planned to demonstrate the performance of SFE water electrolyzers under low-g conditions.

Energy Storage

The energy storage application requires the SFE to provide O_2 and H_2 for use in a Regenerative Fuel Cell Subsystem (RFCS) [6]. Electrical power is converted by the SFE into O_2 and H_2 , which the fuel cells use later to generate electrical power when there is a power demand.

A process schematic for the SFE in this application is shown in Fig. 3. The O_2 and H_2 product gases are stored in tanks at 2,172 kPa (315 psia), ready to be consumed by the fuel cell. The fuel cell provides feed water to the SFE. An advantage of using the SFE in this application is that H_2 from the fuel cell, dissolved in the feed water, is not a problem.

To demonstrate the readiness of the SFE technology for this application, endurance tests of SFE single cells and modules were performed [7]. A total test time of 238,616 cell-hr were accumulated (Table 2). Part of this testing (160,710 cell-hr) was performed in a continuous-operation mode, but an additional 77,906 cell-hr were obtained under cyclic operation to simulate the operation of the SFE in orbit. The SFE hardware was operated 54 min with current on, and 36 min with current off.

An integrated Breadboard RFCS (Fig. 4) was assembled, using a 2.12 kW Shuttle Orbiter fuel cell power plant (X708)[8]. The SFE contained a 6-cell, 1.0 ft² water electrolysis module, which is sized for operation at 3 kW. The SFE in this subsystem was operated for 635 hr at Life Systems, including 602 hr of cyclic operation. A light cycle time (SFE current on) of 56 min was used, with a dark cycle time (SFE current off) of 36 min. Figure 5 shows the cell voltage performance and the variation of O_2 -to-System and H_2 -to-System pressure differentials during this cyclic operation.

The projected configuration of a SFE subsystem, sized to produce 3.9 kg (8.5 lb) O_2 /hr is shown in Fig. 6. The characteristics of this subsystem are summarized in Table 3. Utilization of cells having an active area of 0.69 m² (1.0 ft²) achieves the high production rates required for this application.

ECLSS

Extensive development has been performed during the past 20 years to use SFE technology to generate O_2 for life support. The space station ECLSS requires O_2 for the crew, pressurization of the air lock and to replenish other external leakage. Hydrogen is required for the efficient operation of other subsystems.

A process schematic of the SFE is shown in Fig. 7. Low pressure water and electricity are used to produce the O_2 and H_2 . Feed water is circulated through an external heat exchanger in the TCA to control the temperature of the module. During normal operation, coolant is used to remove waste heat produced by the electrolysis reaction, and a small amount of nitrogen (N_2) is used during startup to pressurize the water tank. The dew point of the product gases, after expansion to ambient pressure is within the range of 278 to 289 K (40 to 60 F), so a dryer or condenser/separator is unnecessary for removal of moisture from the product gases.

Technology Demonstration hardware has been produced (Fig. 8) to support the development of the OGA for Space Station Freedom. The Technology Demonstration hardware is being tested at the National Aeronautics and Space Administration (NASA) George C. Marshall Space Flight Center (MSFC) and at Life Systems. One unit is undergoing endurance testing at Life Systems, and on 03/04/91 it surpassed 2,500 operating hours.

Life Systems also initiated other tests before the Technology Demonstrator hardware was available for testing. For example, a module that contains cells identical to those to be used in the OGA also has been under endurance test, and more than 10,190 operating hours have been accumulated as of 03/04/91.

Based on this experience and other design data, the OGA is projected to have the characteristics listed in Table 4. The baseline operating level for the OGA is production of O_2 at a four-person rate (plus O_2 to make up for leakage and air lock repressurization) of 4.12 kg/day (9.09 lb/day). By adjusting the current density and operating temperature, the OGA can increase production by 73% to a 45-day emergency level of 7.14 kg/day (15.75 lb/day).

Propulsion

The SFE is currently being evaluated for use in the Space Station Freedom's Propulsion System. In this application O_2 and H_2 propellants must be generated at a pressure of 20,680 kPa (3,000 psia).

A schematic of the SFE for propulsion is shown in Fig. 9. The module is contained within a pressure containment vessel. Inert fluid within the pressure containment vessel is pressurized with N_2 to the same pressure as the product gases, so the module experiences a minimal internal-to-external pressure differential. A pressure intensifier, external to the pressure containment vessel, pumps low pressure feed water into the water tank to make up for water electrolyzed by the module. The feed water in the pressure vessel is then pressurized by the inert fluid. Because of the low temperatures to be experienced by the Propulsion System, the product gases must be dried prior to storage.

The SFE₂ for propulsion is projected to have circular cells with an active area of 0.046 m² (0.5 ft²). The major objective of the current evaluation is to demonstrate the performance of a 15-cell SFE module having cells of this size (Fig. 10), and operating at 20,680 kPa (3,000 psia). The normal operating pressure of previous SFE subsystems is 1,241 kPa (180 psia), although one subsystem has operated for nearly 1,200 hr at 2,172 kPa (315 psia) in tests at Life Systems and NASA MSFC. Tests of SFE single cells have been performed at higher pressures. For example, Fig. 11 illustrates the voltage characteristics of one of these cells, operating at ambient temperature and 20,857 kPa (3,025 psia). Its performance has been projected to that which would be achieved at a normal operating temperature of 355 K (180 F).

The characteristics projected for a prototype-level SFE for propulsion are listed in Table 5.

EVA

In the EVA application, production of O_2 at 41,369 kPa (6,000 psia) is necessary to recharge the O_2 bottle in the Extravehicular Mobility Unit (EMU). To achieve this, Life Systems has modified the original SFE concept to incorporate a solid metal cathode (SMC) (Fig. 12). The SMC serves as a solid separator between the O_2 and H_2 compartments, and is capable of safely withstanding very large pressure differentials, with 41,369 kPa (6,000 psid) actually demonstrated.

The SMC is constructed of a proprietary alloy which only allows transmission of H_2 . As a result, the SMC electrolyzer has the unique ability to simultaneously generate O_2 at 41,369 kPa (6,000 psia) and generate ultra-high purity H_2 at low pressure. These characteristics make the SMC SFE ideally suited for use in the EVA application.

Feasibility tests were conducted in a high pressure electrolysis cell test vessel shown in Fig. 13. These tests indicated that it is possible to simultaneously generate O_2 at 41,369 kPa (6,000 psia) and H_2 at ambient pressure with a current efficiency at 93.7%. Life Systems used a proprietary electrode catalyst, which produces a nominal cell voltage of 1.865 V at 358 K (184 F) at a current density of 47.8 mA/cm^2 (44.4 ASF) (Fig. 14). Subsequent testing at NASA Lyndon B. Johnson Space Center (JSC) has confirmed these results.

A schematic of the SFE for the EVA application is shown in Fig. 15. The schematic is nearly identical to that for the propulsion application, with the exception that the H_2 gas dryer is not required because the H_2 product contains no water. Projected characteristics of the SMC SFE for EVA are listed in Table 6.

The SMC SFE also might be the technology of the future for the energy storage, propulsion and life support applications. It is potentially highly reliable and tolerant of hardware failures downstream of the SFE, since it can withstand the loss pressure in either the O_2 or H_2 streams without being damaged by the resulting pressure differential, up to at least 41,369 kPa (6,000 psid). More effort is required to assess the SMC SFE for these applications.

Special Applications

Future space habitats, such as the Lunar Base, will have all the applications and requirements discussed above. In addition, scientific and manufacturing requirements for O_2 and H_2 that will arise aboard Space Station Freedom are likely to be expanded and diversified within these habitats. The development of new emergency systems (e.g., O_2 for emergency atmosphere repressurization) will probably introduce additional requirements.

These requirements will doubtless necessitate both small-scale and large-scale hardware. The SFE has already demonstrated its ability to efficiently accommodate both needs. For example, evaluations of SFE technology for large-scale H_2 generation applications addressed the capability of the SFE to electrolyze impure water without costly purification equipment and expendables. In those evaluations [9] SFE modules electrolyzed Cleveland, Ohio tap water for 1,750 hr without any pretreatment and no adverse effects. Simulated sea water was also electrolyzed 1,100 hr, and real sea water was electrolyzed for 1,550 hr without adverse effects on the module.

The above discussion has shown that the SFE can be used to generate O_2 and H_2 at a variety of pressures and production rates. Therefore, nearly all experimentation and manufacturing needs can be satisfied by the SFE technology. In addition, a special capability exists within the SMC SFE for the generation of ultra-high purity, dry H_2 and O_2 at very high pressures. Special needs can be satisfied with this technology.

Electrolysis Performance Improvement Concepts Studies

An effort is being planned for the testing of three integrated SFE units aboard the Shuttle Orbiter. The objectives of the Electrolysis Performance Improvement Concepts Studies (EPICS) is to investigate the ways that a low-g environment may improve SFE performance by increasing the uniformity of thermal gradients and mass transport within the cells.

Each integrated electrolysis unit in the EPICS consists of an electrolysis cell, a thermal control plate, and accumulators for H_2 and O_2 (Fig. 16). Each unit will contain electrodes with a different catalyst microstructure. By comparing the performance of each unit, it is expected that knowledge will be gained on how to optimize the electrodes for a low-g environment, to result in decreased cell voltage and increased operational current densities (Fig. 17).

Figure 18 shows the EPICS packaging concept, consisting of the three integrated electrolysis units contained in a pressure control enclosure with external control/monitor instrumentation.

CONCLUDING REMARKS

Static Feed Water Electrolysis technology has been demonstrated to satisfy the O_2 and H_2 generation requirements of energy storage, life support, propulsion, EVA and other applications. Prototype and preprototype SFE subsystems have shown that SFE technology efficiently satisfies both small- and large-scale requirements. In addition to low power consumption, compact dimensions and low weight, these subsystems have demonstrated the ability to operate using impure water sources. Without the need for special water purification equipment, gas/liquid separators and other components, the SFE subsystems have the benefits of simplicity and reliability. Additional efficiency improvements are envisioned as a result of the planned low-g Electrolysis Performance Improvement Concepts Studies. Finally, applications requiring ultra-high pressure O_2 and/or ultra-high purity H_2 at low pressure, such as the extravehicular activity application, can be satisfied by the Solid Metal Cathode Static Feed Electrolyzer. An evaluation of the Solid Metal Cathode for energy storage, propulsion and life support applications is also recommended to evaluate how its ability to withstand large O_2 -to- H_2 pressure differentials could improve the reliability of those systems.

ACKNOWLEDGMENTS

The authors wish to acknowledge NASA Lewis Research Center, NASA MSFC, NASA JSC, Boeing, the Department of Energy and Life Systems, Inc. in the development of SFE subsystems. In addition, the authors wish to acknowledge the assistance of Dr. B-j Chang and Andrew J. Kovach in the preparation of this paper.

REFERENCES

1. F.H. Schubert, R.A. Wynveen and F.C. Jensen, "Development of an Advanced Static Feed Water Electrolysis Module," Paper No. 75-ENAs-30, Intersociety Conference on Environmental Systems; San Francisco, CA; July 21-24, 1975.

2. F.H. Schubert, M.K. Lee, R.J. Davenport and P.D. Quattrone, "Water Electrolysis Systems: H₂ and O₂ Generation," Paper No. 78-ENAs-03, Intersociety Conference on Environmental Systems; San Diego, CA; July 10-13, 1978.
3. J.T. Larkins and A.J. Kovach, "Static Feed Water Electrolysis System for Space Station O₂ and H₂ Generation," Paper No. 851339, Intersociety Conference on Environmental Systems; San Francisco, CA; July 16-17, 1985.
4. P.D. Quattrone, F.H. Schubert and D.B. Heppner, "Air Revitalization System Integration," Paper No. 840959, Intersociety Conference on Environmental Systems; San Diego, CA; July 16-19, 1984.
5. F.A. Fortunato, A.J. Kovach and L.E. Wolfe, "Static Feed Water Electrolysis System for Space Station Oxygen and Hydrogen Generation," Paper No. 880994, Intersociety Conference on Environmental Systems; San Francisco, CA; July 11-13, 1988.
6. B.J. Chang, F.H. Schubert, A.J. Kovach and R.A. Wynveen, "Engineering Model System Study for a Regenerative Fuel Cell," Study Report, Contract NAS 3-21287, NASA CR-174801, TR-376-30; Life Systems, Inc., Cleveland, OH; September, 1984.
7. A.J. Kovach, F.H. Schubert and B.J. Chang, "Endurance Test and Evaluation of Alkaline Water Electrolysis Cells," Final Report, Contract NAS3-21287, TR-614-3; Life Systems, Inc., Cleveland, OH; April, 1987.
8. B.J. Chang, A.J. Kovach, F.H. Schubert and J.T. Larkins, "Water Electrolysis Subsystem for a Regenerative Fuel Cell System Breadboard for Orbital Energy Storage," Final Report, Contract NAS9-16659, TR-529-4; Life Systems, Inc., Cleveland, OH; March, 1986.
9. Life Systems, Inc., "Development of Static Feed Water Electrolysis for Large Scale Hydrogen Production," Final Report, Contract 522723-S, BNL 51578, TR-470-4; Life Systems, Inc., Cleveland, OH; July, 1982.

TABLE 1
Typical application requirements

| Application | Gas Delivery Pressure, kPa (psia) | O ₂ Gas Production, kg/hr (lb/hr) | H ₂ Gas Production, kg/hr (lb/hr) |
|---|-----------------------------------|--|--|
| ECLSS ^(a) | 138 (20) | 0.17 (0.38) | 0.02 (0.04) ^(b) |
| Energy Storage (Regen. Fuel Cell) ^(c) | 2,172 (315) | 18.64 (41.09) | 2.35 (5.19) |
| Propulsion ^(d) | 20,685 (3,000) | 0.81 (1.78) | 0.101 (0.22) |
| EVA O ₂ Bottle Recharge ^(e) | 41,370 (6,000) | 0.11 (0.24) | — |

(a) Based on four-person crew: Metabolic O₂ at 0.83 kg (1.84 lb) O₂/person-day,
Air lock pressurization at 0.54 kg (1.20 lb) O₂/day,
Station leakage at 0.24 kg (0.52 lb) O₂/day,
O₂ Delivery Pressure 138 kPa (20 psia),
H₂ Delivery Pressure 172 kPa (25 psia).

(b) Required for CO₂ reduction.

(c) For 75 kW nominal bus power to user.

(d) Nominal rate of 0.91 kg (2.0 lb) water/hr.

(e) Nominal rate of 3.0 kg (6.5 lb) water/day.

TABLE 2
Static feed water electrolysis endurance test summary

| Cell No. | Electrode Type | Continuous | | | Cyclic | | | Total Current "On" Time, cell-hr |
|--|---------------------|--------------------------|--------------------|---|--------------------|---|----------------|----------------------------------|
| | | Total Test Time, cell-hr | Test Time, cell-hr | Current Density, mA/cm ² (ASF) | Test Time, cell-hr | Current Density, mA/cm ² (ASF) | | |
| 105A | Advanced | 16,856 | 8,578 8,278 | 323.0 (300) 161.5 (150) | — | — | 16,856 | |
| 105B | Advanced | 45,197 | 6,300 | 161.5 (150) | 38,897 | 161.5 (150) | 29,638 | |
| 105C | Super | 46,251 | 11,313 34,938 | 323.0 (300) 161.5 (150) | — | — | 46,251 | |
| 105D | Super | 44,269 | 5,260 | 161.5 (150) | 39,009 | 161.5 (150) | 28,665 | |
| 127-SWEC | Advanced | 6,900 | 6,900 | 161.5 (150) | — | — | 6,900 | |
| 127 Six-Cell Module | Super Unitized Core | 63,936 | 63,936 | 161.5 (150) | — | — | 63,936 | |
| 128 Three-Cell (1.0 ft ²) Module | Advanced | 2,535 | 2,535 | 21.5 – 107.6 (20 – 100) | — | — | 2,535 | |
| WS-6 Six-Cell (1.0 ft ²) Module | Advanced | 12,672 | 12,672 | — | — | — | 12,672 | |
| Total | | <u>238,616</u> | <u>160,710</u> | — | <u>77,906</u> | — | <u>207,453</u> | |

TABLE 3
 Projected SFE energy storage electrolysis subsystem
 characteristics for a 91 kW RFCS^(a)

| | |
|--|-------------|
| Number of Cells | 107 |
| Oxygen Generation, kg/day (lb/day) | 112.1 (247) |
| Current Density, mA/cm ² (ASF) | 157 (146) |
| Cell Area, m ² (ft ²) | 0.09 (1.0) |
| Operating Temperature, K (F) | 339 (150) |
| Operating Pressure, kPa (psia) | 2,172 (315) |
| Subsystem Weight, kg (lb) | 247 (544) |
| Subsystem Volume, ^(b) m ³ (ft ³) | 0.3 (10.6) |
| Subsystem Power, ^(c) kW | 22.7 |

-
- (a) Four units are required, for 75 kW nominal bus power to user.
 (b) Includes mechanical and electrical subassemblies (cables excluded).
 (c) Nominal level for electrolysis only (excludes ancillary components).

TABLE 4
 ECLSS subsystem characteristics

| | |
|--|--------------|
| Number of Cells | 20 |
| Oxygen Generation, kg/day (lb/day) | 4.12 (9.08) |
| Current Density, mA/cm ² (ASF) | 124 (115) |
| Cell Area, m ² (ft ²) | 0.023 (0.25) |
| Operating Temperature, K (F) | 339 (150) |
| Operating Pressure, kPa (psia) | 1,241 (180) |
| Subsystem Weight, ^(a) kg (lb) | 56.8 (125.0) |
| Subsystem Volume, ^(b) m ³ (ft ³) | 0.094 (3.32) |
| Subsystem Power, ^(c) W | 876 |

-
- (a) Design goal. Current weight is 86.6 kg (190.7 lb).
 (b) Includes mechanical subassembly (electrical subassembly and cables excluded).
 (c) Nominal level for electrolysis only (excludes ancillary components).

TABLE 5
Projected propulsion electrolysis subsystem characteristics

| | |
|---|----------------|
| Number of Cells | 45 |
| Oxygen Generation, kg/day (lb/day) | 19.4 (42.7) |
| Current Density, mA/cm ² (ASF) | 134 (124) |
| Cell Area, m ² (ft ²) | 0.046 (0.5) |
| Operating Temperature, K (F) | 356 (180) |
| Operating Pressure, kPa (psia) | 20,685 (3,000) |
| Subsystem Weight, ^(a, b) kg (lb) | 487 (1,072) |
| Subsystem Volume, ^(a, b) m ³ (ft ³) | 0.26 (9.1) |
| Subsystem Power, ^(c) kW | 4.28 |

(a) Design goal.

(b) Includes mechanical and electrical subassemblies (gas dryers and cables excluded).

(c) Nominal level for electrolysis only (excludes ancillary components).

TABLE 6
Projected SMC electrolysis subsystem characteristics
for the EVA application

| | |
|--|----------------|
| Number of Cells | 7 |
| Oxygen Generation, kg/day (lb/day) | 2.6 (5.8) |
| Current Density, mA/cm ² (ASF) | 53.8 (50) |
| Cell Area (Cathode), m ² (ft ²) | 0.058 (0.63) |
| Operating Temperature, K (F) | 383 (230) |
| Operating Pressure, kPa (psia) | 41,370 (6,000) |
| Subsystem Weight, kg (lb) | 272 (600) |
| Subsystem Volume, m ³ (ft ³) | 0.078 (2.74) |
| Subsystem Power, W | 537 |

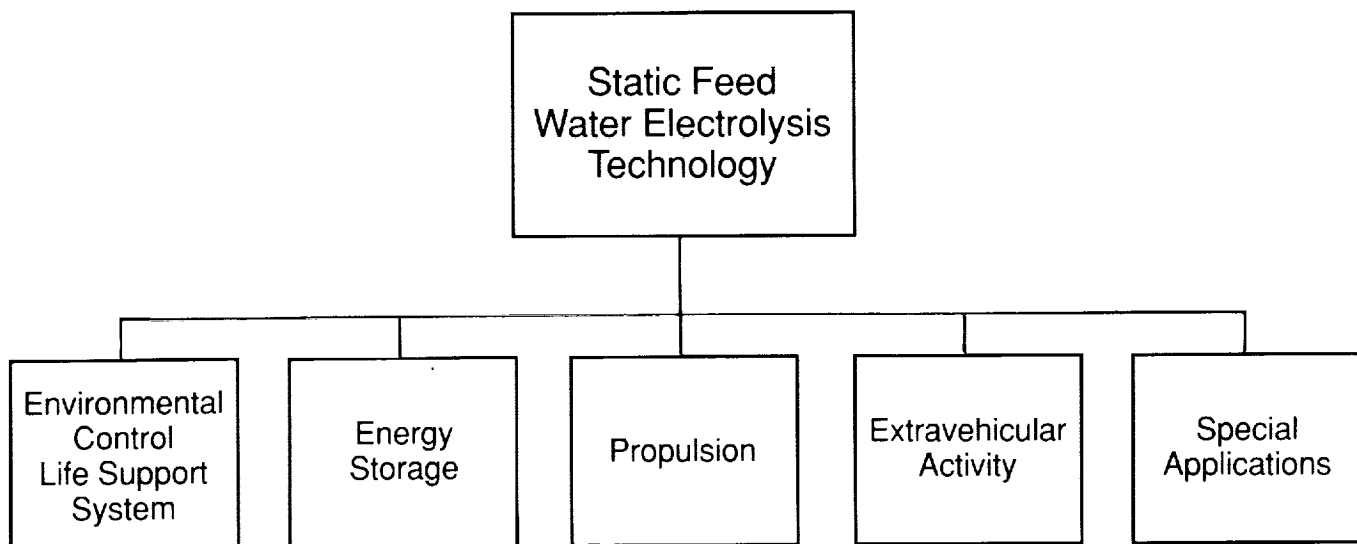


Fig. 1. Major SFE technology development applications

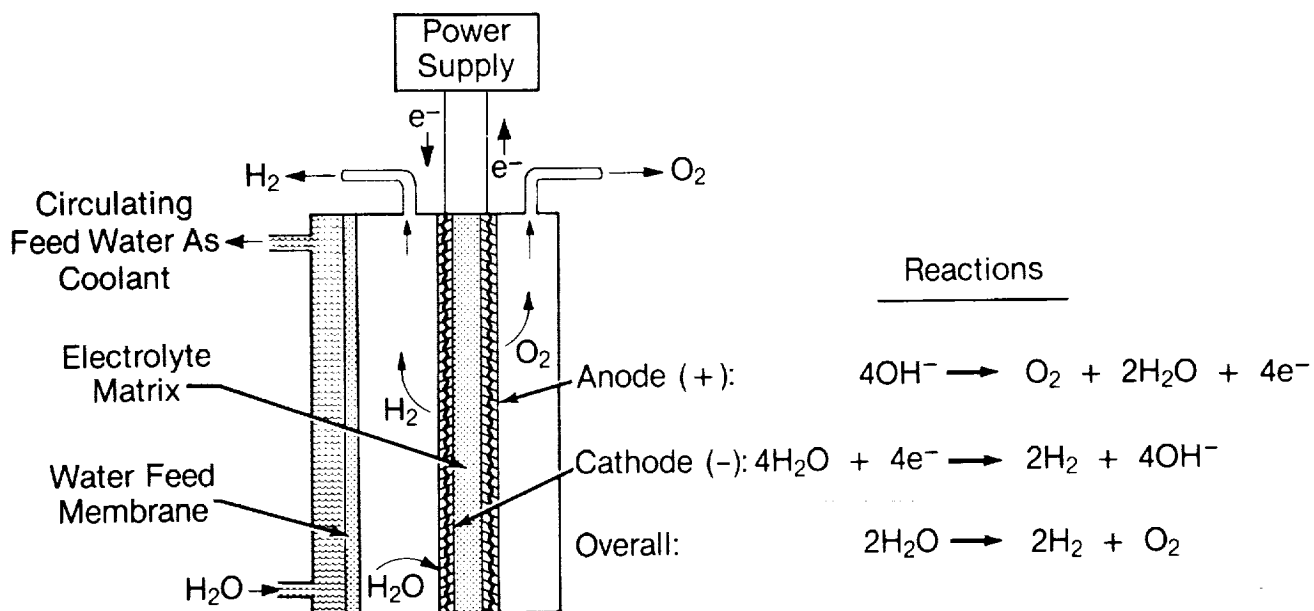


Fig. 2. Conventional static feed electrolysis process

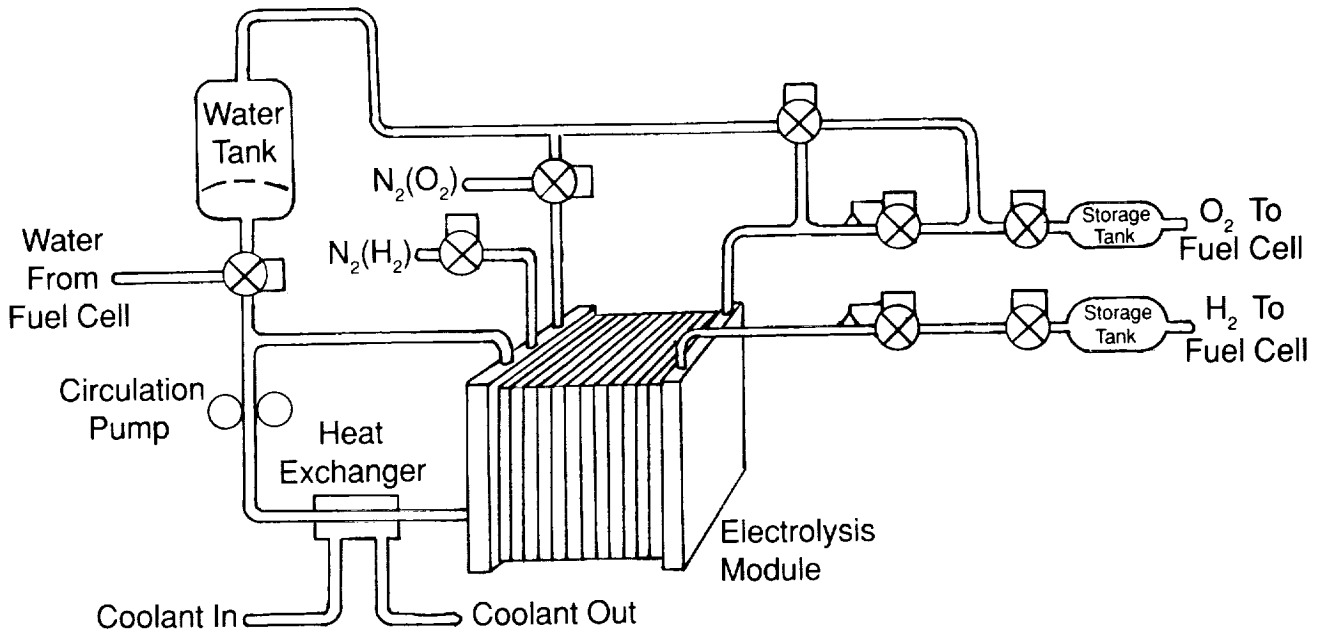


Fig. 3. SFE process schematic for the energy storage application

ORIGINAL PAGE
BLACK AND WHITE PHOTOGRAPH

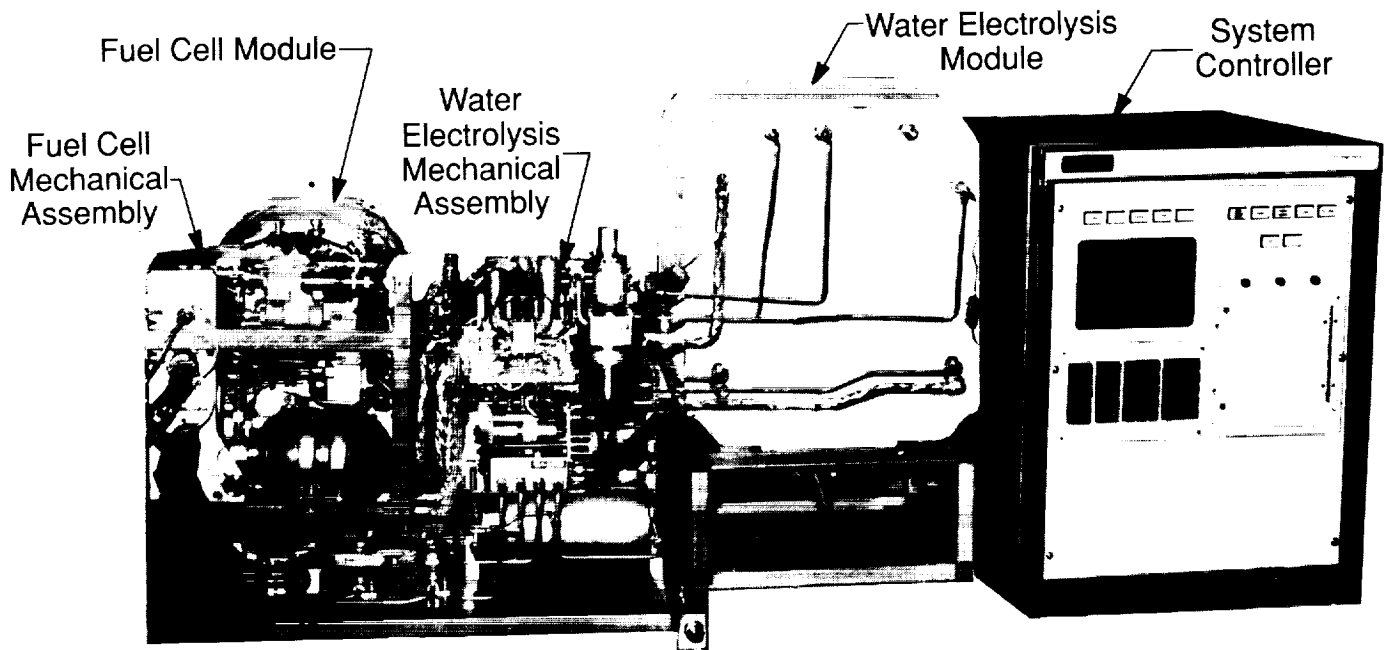


Fig. 4. 3kW regenerative fuel cell system breadboard

ORIGINAL PAGE
BLACK AND WHITE PHOTOGRAPH

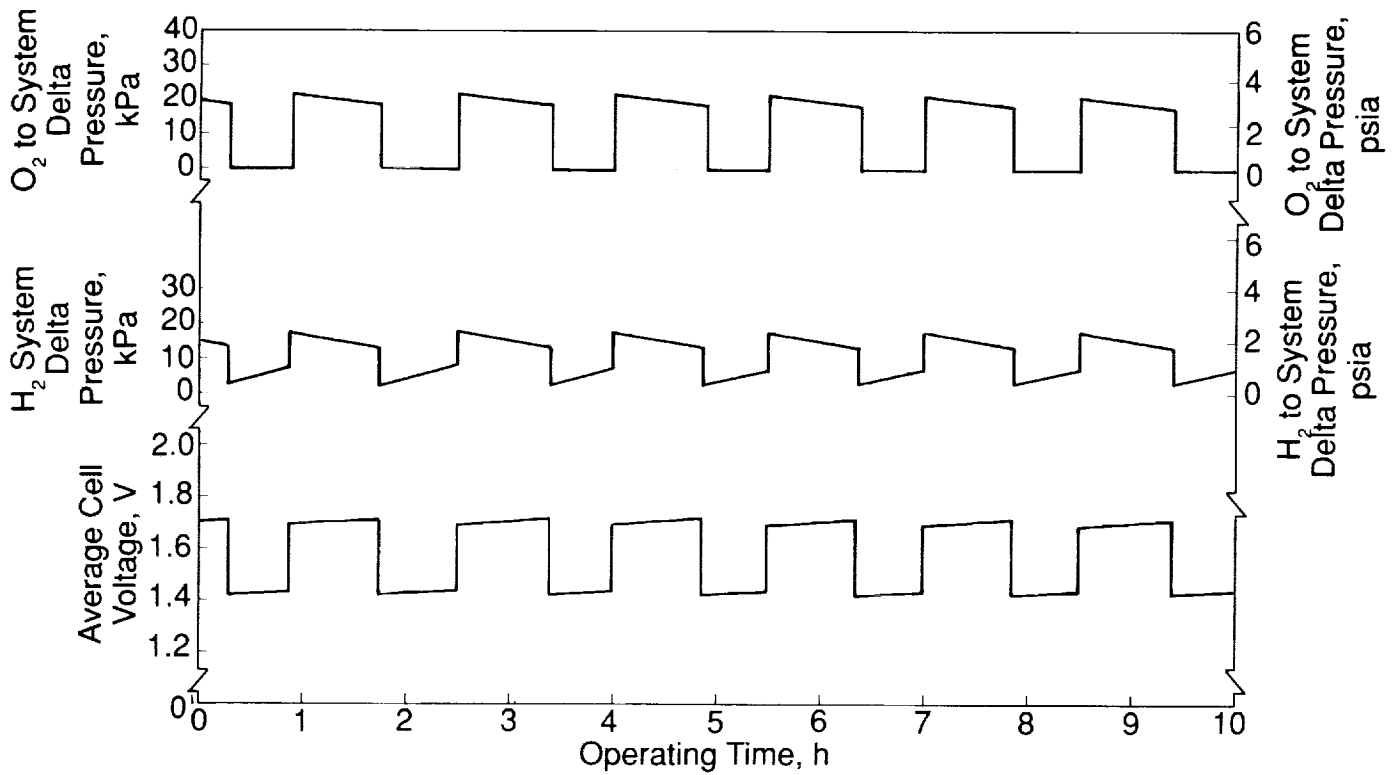


Fig. 5. WES cyclic performance versus operating time in RFCS normal mode

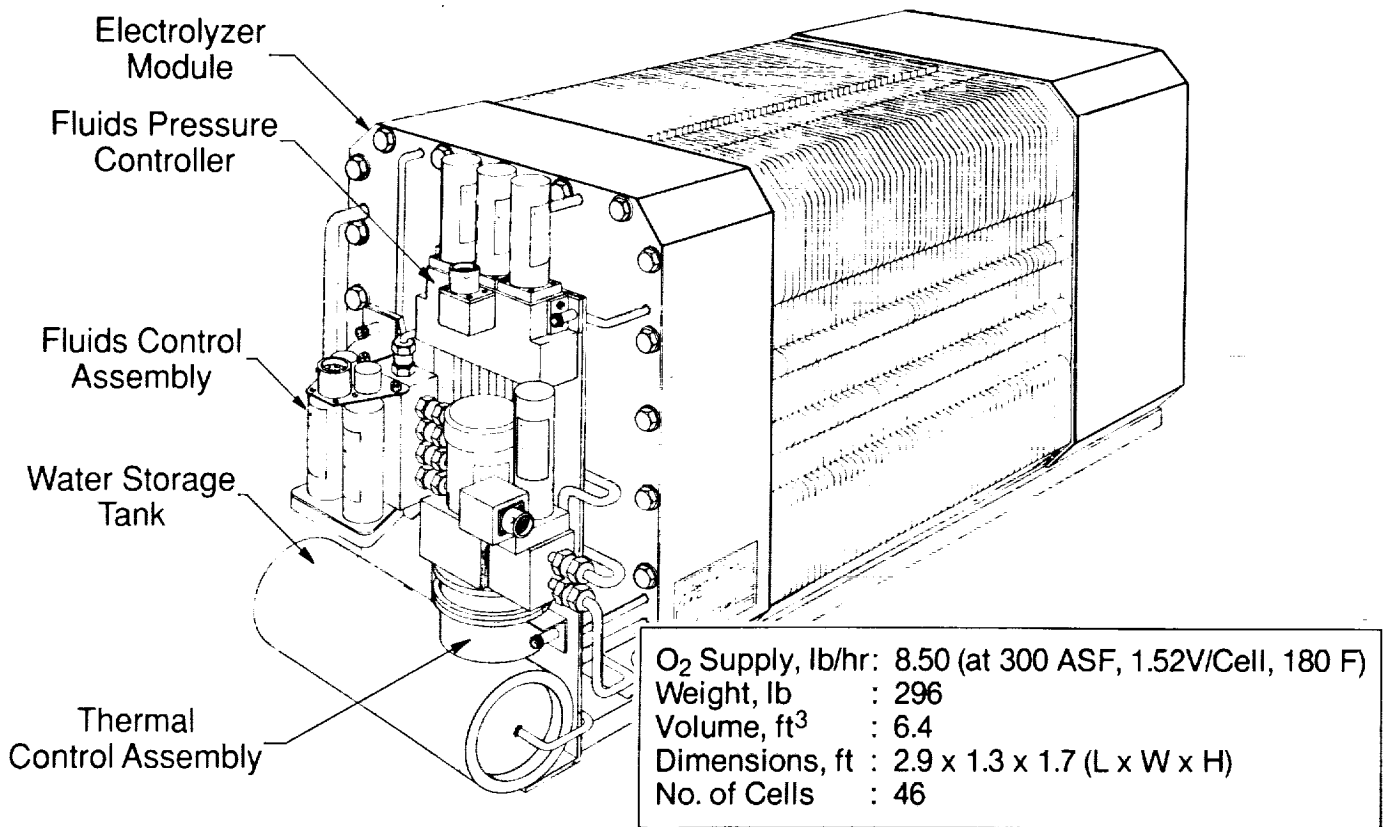


Fig. 6. Conceptual representation of a large production electrolysis subsystem

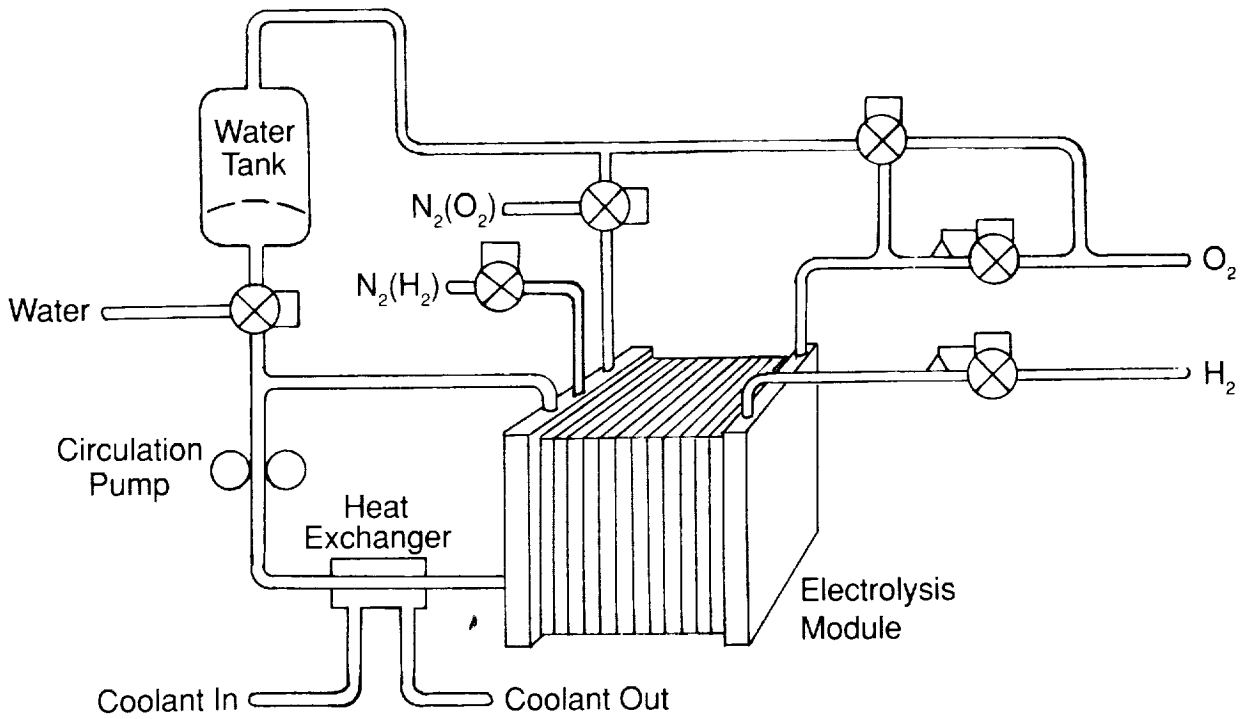


Fig. 7. SFE process schematic for the ECLSS application

ORIGINAL PAGE
BLACK AND WHITE PHOTOGRAPH

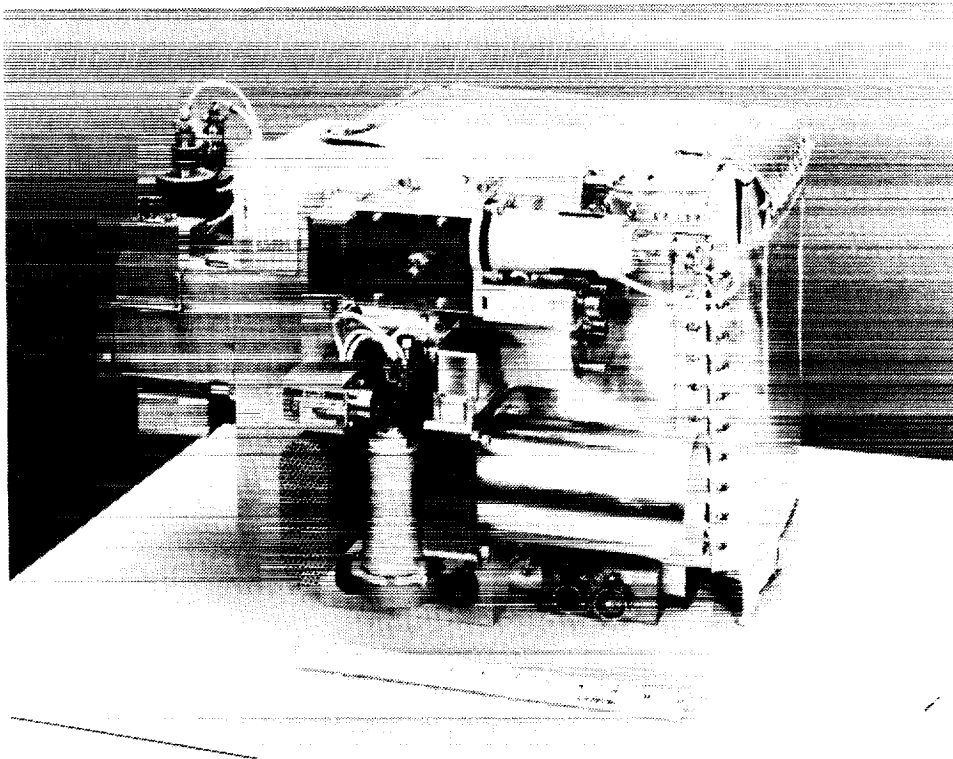


Fig. 8. SFE technology demonstration hardware

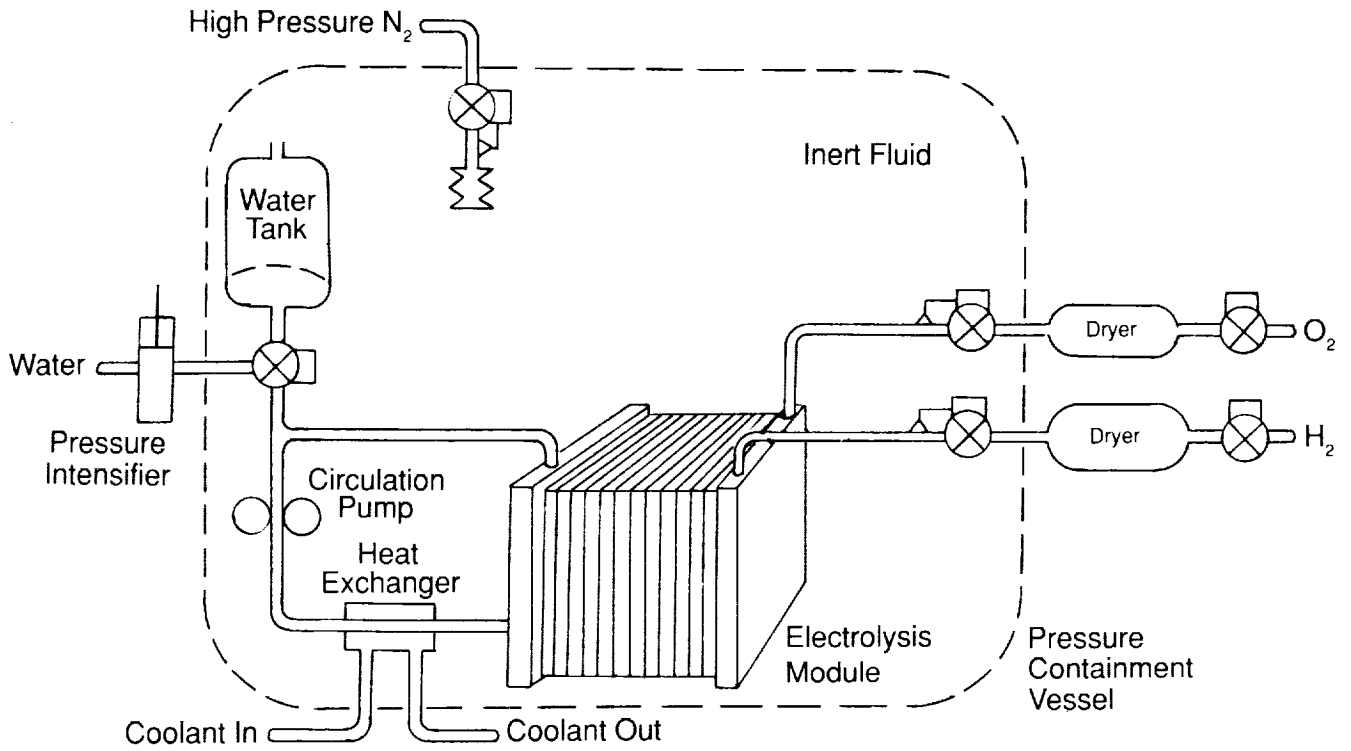


Fig. 9. SFE process schematic for the propulsion application

ORIGINAL PAGE
BLACK AND WHITE PHOTOGRAPH

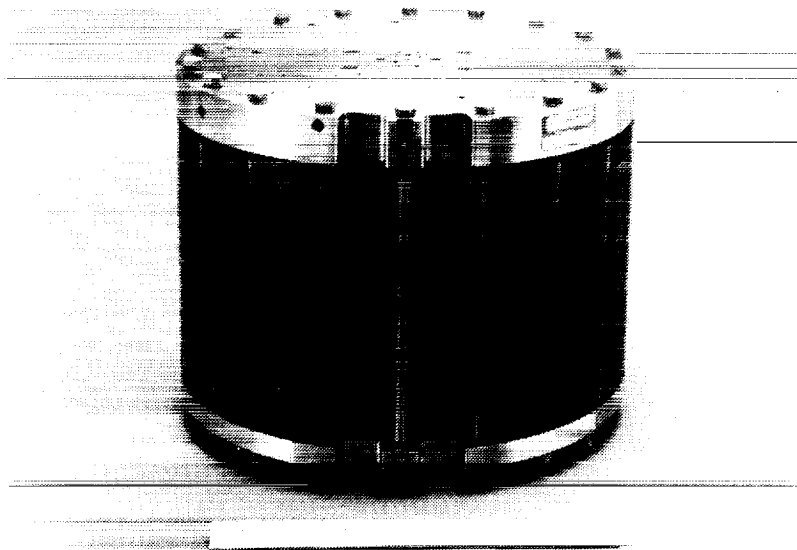


Fig. 10. Preprototype SFE propulsion electrolysis module

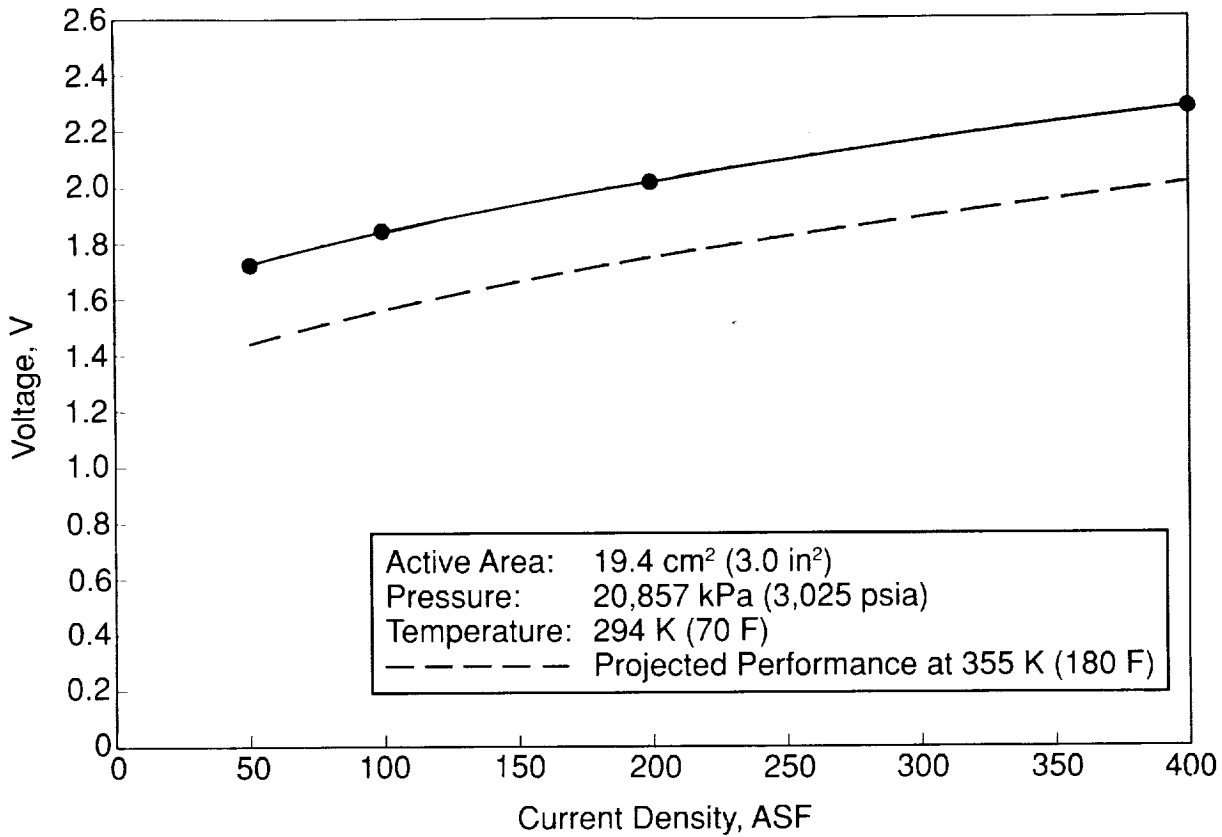


Fig. 11. Performance of 3,000 psia circular SFE cell

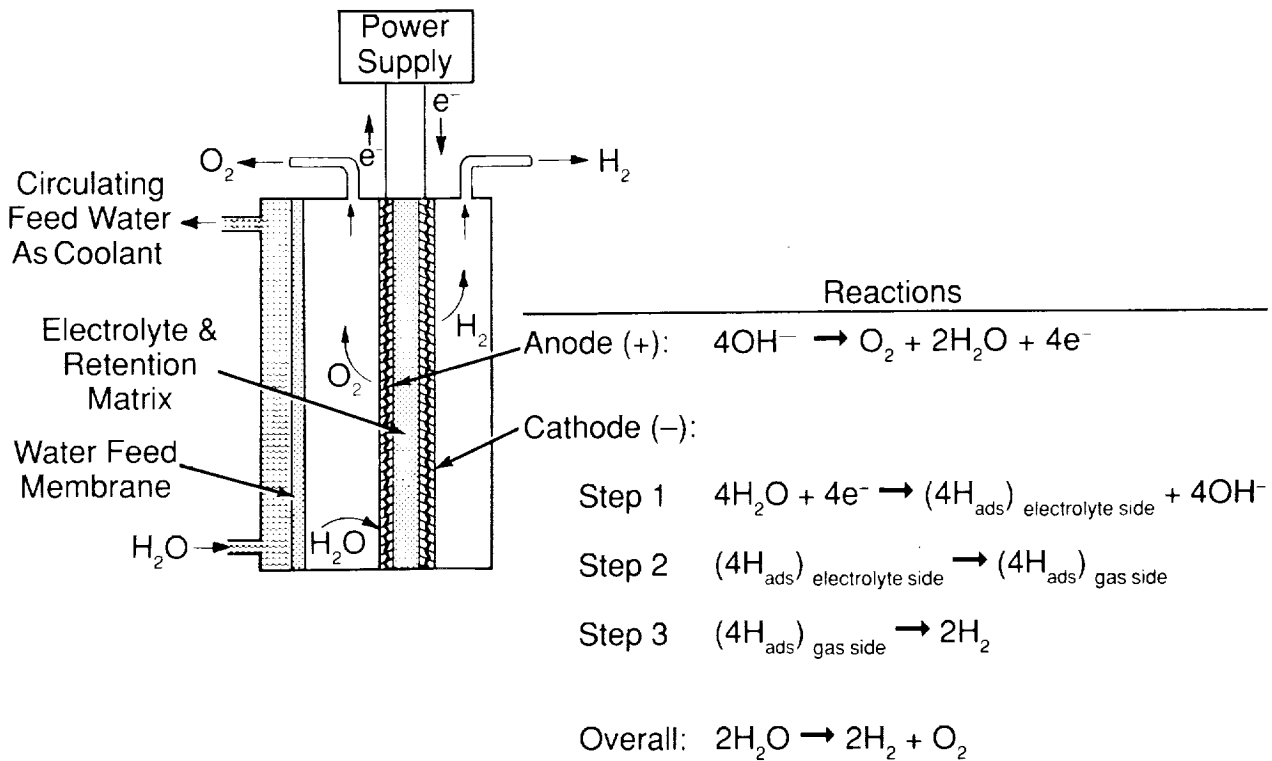


Fig. 12. Modified static feed electrolysis with a solid metal cathode

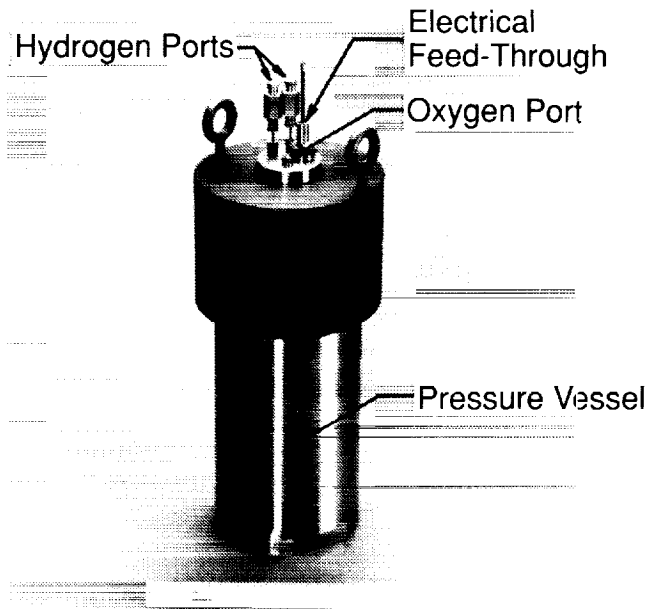


Fig. 13. High-pressure solid metal cathode electrolysis test vessel

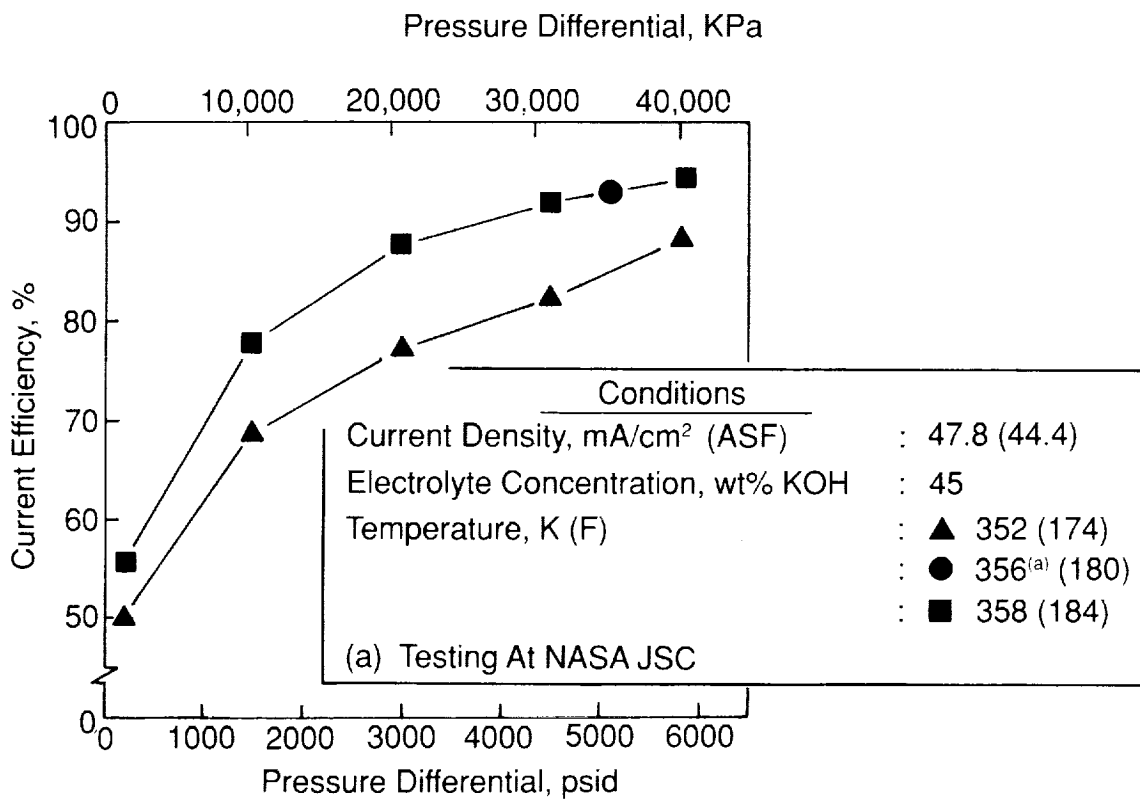


Fig. 14. Current efficiency versus pressure differential for a high-pressure SMC cell

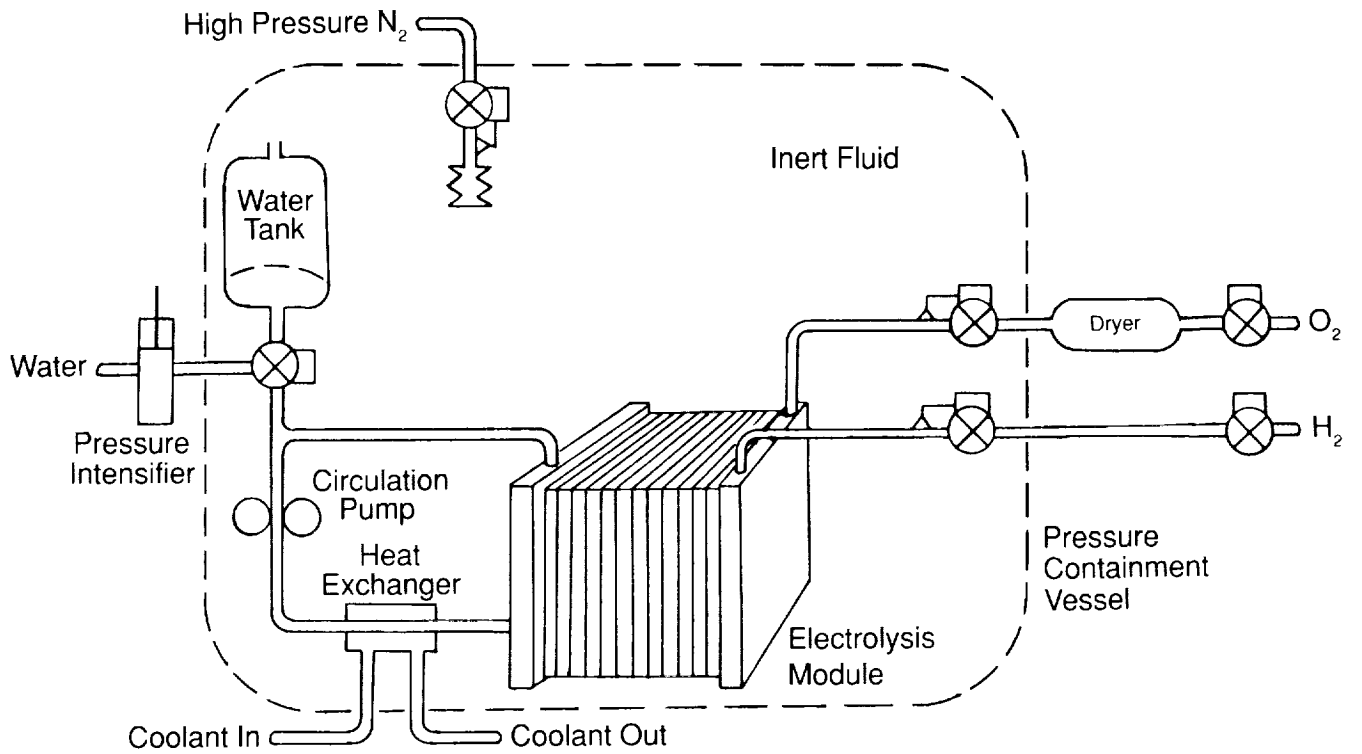


Fig. 15. SFE process schematic for the EVA application

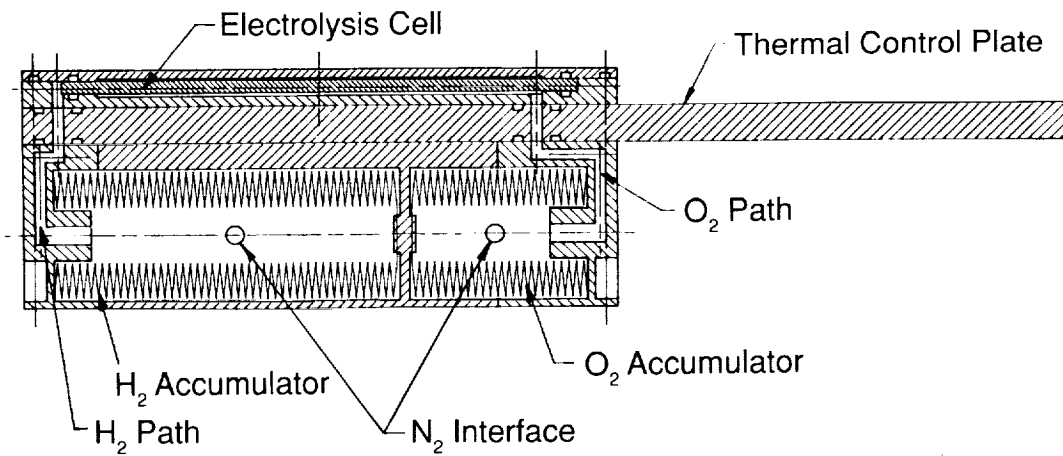


Fig. 16. Cross-section of integrated electrolysis unit

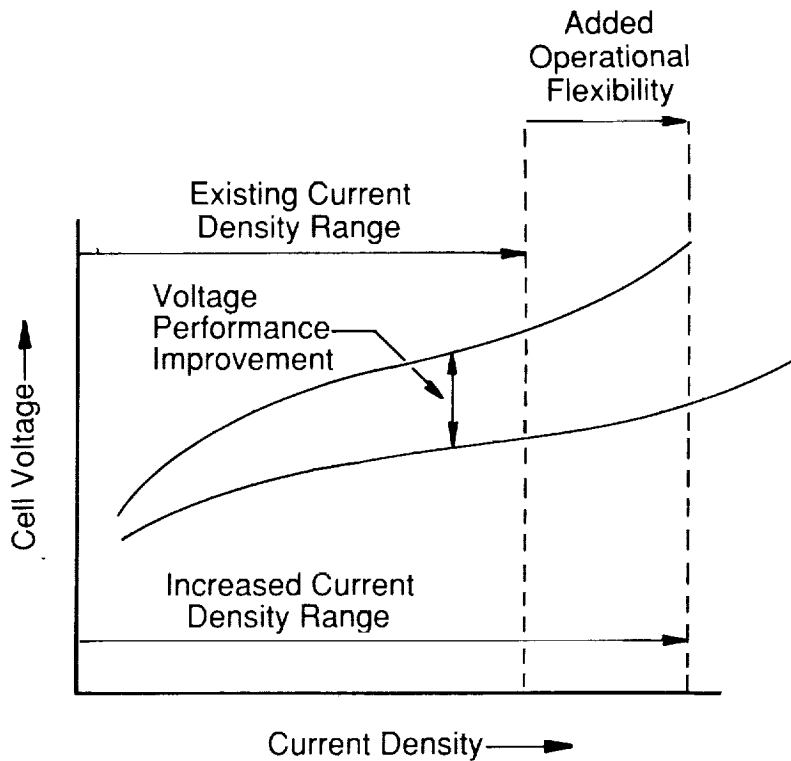


Fig. 17. Projected SFE performance improvements in 0-G environment

ORIGINAL PAGE
BLACK AND WHITE PHOTOGRAPH

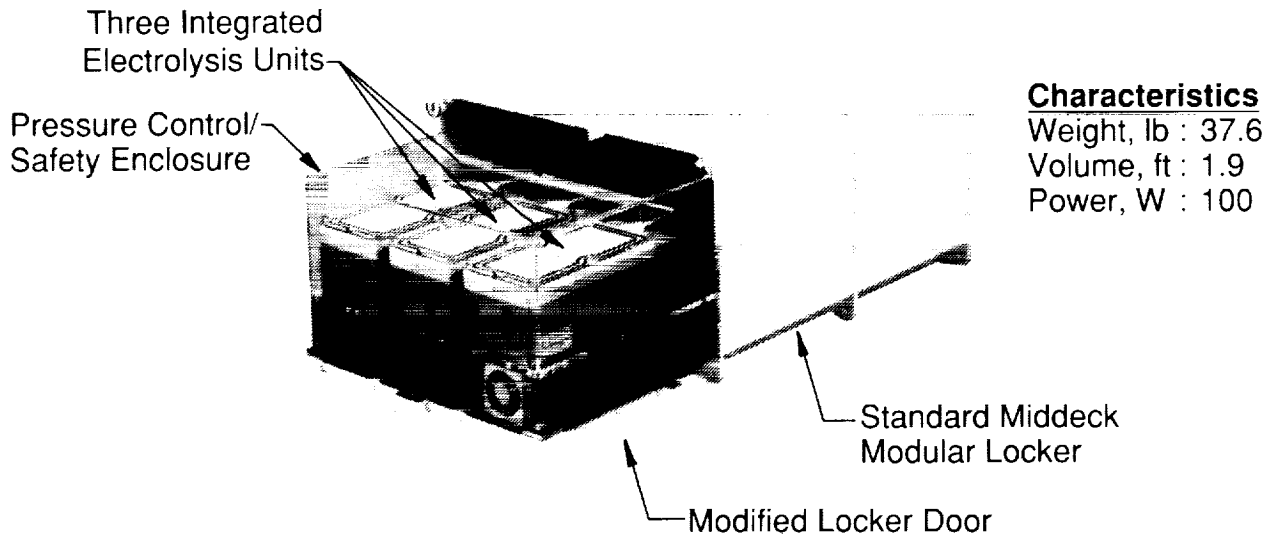


Fig. 18. EPICS experiment packaging concept

THE EFFECTS OF PLATINUM ON NICKEL ELECTRODES
IN THE NICKEL HYDROGEN CELL

Albert H. Zimmerman
The Aerospace Corp.
El Segundo, California 90245

Introduction

The performance of the nickel electrode used in nickel hydrogen cells has been subject to considerable variation by the incorporation of various additives, dopants, and other variations in the solid-state structure of the active material in the electrodes. Examples include the use of cobalt additives to the nickel hydroxide active material, the incorporation of potassium or lithium (Ref. 1) into the gamma-NiOOH charged material, and the interaction of hydrogen gas itself with the nickel electrode (Refs. 2, 3). Depending on conditions of cell potential and state of charge, numerous such reactions are possible that can result in changes to the active material. This study addresses the possible interactions of platinum and platinum compounds with the nickel electrode that are possible in the nickel hydrogen cell, where both the nickel electrode and a platinum catalyst hydrogen electrode are in intimate contact with the alkaline electrolyte.

Normal operation of the nickel hydrogen cell maintains the nickel electrode at highly oxidizing potentials, and the hydrogen electrode at quite reducing potentials. Under these conditions, the only possible path for platinum to interact with the nickel electrode is by physical transfer of platinum catalyst particles from the hydrogen electrode, through the separator, to the nickel electrode. Such transfer, which may occur by "popping" (Ref. 4), can leave platinum catalyst particles in contact with the nickel electrode. Such particles of platinum are then oxidized at the nickel electrode to platinum oxide PtO_2 , by electrochemical reaction (Ref. 5). Platinum oxide however, has some solubility in alkaline solutions (Ref. 6), resulting in the formation of the platinum complex ion $Pt(OH)_6^-$. While the platinum is likely to eventually be re-plated back onto the platinum catalyst hydrogen electrode by electrochemical reduction of the dissolved platinum species, until the slow transfer of platinum back to the hydrogen electrode occurs, both the PtO_2 and $Pt(OH)_6^-$ species can be present in the nickel electrode for possible interactions with the active material.

Another condition that the nickel hydrogen cell may be in for considerable periods of time is storage, typically discharged and either open circuit or short circuited. With a hydrogen precharge in the cell, both the nickel and hydrogen electrodes develop a quite reducing potential during storage, conditions under which platinum metal is stable at both electrodes. No reactions are likely in this situation for interaction of platinum with active nickel electrode material.

With a nickel precharge in a stored nickel hydrogen cell, the hydrogen electrode rises to the highly oxidizing potential of the nickel electrode as the hydrogen gas becomes depleted in the cell. Since the partially charged nickel electrode will maintain a slight oxygen pressure in the cell, the

platinum catalyst electrode becomes an oxygen electrode at about the same potential as the nickel electrode. At the oxidizing potential maintained by the nickel electrode the platinum metal in the catalyst electrode is not thermodynamically stable, and can undergo slow oxidation to PtO_2 . Furthermore, in alkaline solutions the PtO_2 will not be effective for passivating the platinum metal because the oxide is slightly soluble, again giving the $\text{Pt}(\text{OH})_6^=$ species. This ionic species can then diffuse through the cell electrolyte, thus making itself available for interactions with the active material in the nickel electrode.

Thus, there is certainly opportunity for both platinum oxides and soluble platinum complex ions to interact with the nickel electrode under a variety of conditions. The question remains, however, as to whether such interactions are either energetically or kinetically feasible under any of these conditions. Addressing this issue will be the primary purpose of this study.

Platinum Interactions with Nickel Electrodes -- Data from NiH_2 Cells

Data have been obtained from a variety of nickel hydrogen cells supporting the formation of a material not previously seen in nickel electrodes. This compound can be identified in tests on electrodes removed from nickel hydrogen cells by its unique electrochemical signature during the reduction of residual capacity in the nickel electrode, as indicated in Fig. 1. Since the cells from which these electrodes were removed were totally discharged, the existence of residual nickel electrode capacity indicates that this new material (compound x) is only formed in nickel hydrogen cells having a nickel precharge. The amount of compound x typically formed is in direct proportion to the amount of nickel precharge in the cell, as determined by the amount of residual charge in the nickel electrodes.

As indicated in Fig. 1, compound x may be recognized by its characteristic reduction at a potential of about 0.15 volts vs. Hg/HgO in 31% KOH electrolyte. If the electrode potential is increased immediately after reduction, it is possible to apparently re-oxidize at least some of the compound x at a potential of about 0.30 volts vs. Hg/HgO as indicated in Fig. 2. However, it is clear that in the reduced form compound x is not stable. After 24 hr at 0.0 volts, no compound x remains that can be either oxidized or reduced upon cycling the nickel electrode. This material has apparently decomposed when left in the reduced state. In contrast, the stability of compound x in the oxidized state appears to be quite high. Repetitive cycling of the nickel electrode does not alter compound x, as long as the electrode voltage is kept high enough so that compound x will not be reduced, i.e. above about 0.2 volts vs. Hg/HgO . Compound x seems to form in the nickel hydrogen cell in material that is never discharged during cell operation. Thus it is a more stable phase of active material that never undergoes discharge, and the increase in the amount of compound x tends to consume whatever nickel precharge that exists in the cell. It should be pointed out that the presence of compound x in NiH_2 cells is not necessarily a problem, in fact the cells containing the largest quantities of compound x were some of the best performing cells of a given design that have been made.

In nickel hydrogen cells containing approximately 20% nickel precharge, about 10% of the total capacity of the nickel electrode (about 5 mAh/cm^2) was found to be present in the oxidized form of compound x. Because this seemed

to be a quite large amount of modified active material, x-ray diffraction measurements were done on isolated active material (Ref. 7) in an attempt to identify the structure of the modified active material. The x-ray diffraction patterns, however, indicated no significant differences between active material from new nickel electrodes and that from the nickel electrodes containing compound x. Spectrographic chemical analysis of the bulk active material indicated that the only unexpected contaminant present in significant quantities was platinum, which comprised about 0.5% of the total active material weight.

A more precise chemical analysis of the modified active material was done by leaching the normal active material from the electrodes containing compound x, and analyzing the residue left behind. The normal active material was dissolved in 10% acetic acid at 70 deg C. The residue left after this dissolution process was filtered, washed, and dried. Analysis of the residue was done using EDAX, x-ray diffraction, and spectrographic analysis. The x-ray diffraction results were of little use, since no well defined diffraction peaks could be seen except those from small fragments of the zircar separator used in the nickel hydrogen cell. This result indicated that the compounds making up this residue were essentially amorphous rather than crystalline. EDAX analysis of the residue revealed that its major constituents were Ni, Co, Pt, and oxygen. The platinum was not present in the metallic state as catalyst particles, but was uniformly dispersed throughout the residue, most likely in the form of an oxide. Every part of the residue analyzed by EDAX had essentially identical proportions of Ni, Co, Pt, and oxygen.

The composition of the residue was quantified using semiquantitative spectrographic analysis. The weight percentages of each element found in the residue are indicated in Table 1. Consistent with the EDAX results, the primary constituents were Ni, O, Pt, and oxygen, with smaller amounts of zirconium oxide (from the cell separator), silicates, and iron.

Table 1. Elemental Composition of Nickel Electrode Residue

| <u>Element</u> | <u>Weight percent</u> | <u>Atom percent</u> |
|----------------|-----------------------|---------------------|
| Ni | 25.2 | 19.1 |
| Co | 27.2 | 20.6 |
| Pt | 25.5 | 5.8 |
| O | 18.8 | 52.4 |
| Zr | 2.5 | 1.2 |
| Si | 0.3 | 0.5 |
| Fe | 0.5 | 0.4 |

It is assumed that this residue bears some relationship to the composition of compound x, suggesting that this compound is some oxide of Ni, Co, or Pt. Since the amount of charge associated with compound x (from electrochemical measurements) was about 5% of the total electrode capacity, the amount of Pt found in the active material would have to undergo transfer of about 10 electrons per platinum atom if a platinum oxide were to be responsible for compound x. Clearly this is impossible, indicating that if Pt is involved in compound x at all, it is as a binary or ternary oxide with cobalt or nickel.

The redox potentials observed for compound x provide a signature that is characteristic of the specific compound undergoing redox reactions, and thus can be used to help identify compound x, assuming it is not a heretofore unknown material. Detailed review of redox potentials for oxides of Ni, Co, and Pt, as well as binary or ternary combinations of these elements, gave only one compound having redox potentials consistent with those observed for compound x (Ref. 8). This compound has a nominal formulation of $\text{NiCoO}_2(\text{OH})_2$, based on the preparation of this compound in Ref. 8 by co-precipitation and oxidation of mixed nickel and cobalt hydroxides. This material is also quite consistent with the residue analysis results of Table 1, where Ni and Co are present in about a 1:1 ratio. The platinum is likely to be present as a highly dispersed oxide mixed with the $\text{NiCoO}_2(\text{OH})_2$.

While the identification of compound x as $\text{NiCoO}_2(\text{OH})_2$ appears to be fully consistent with the available chemical and electrochemical data from modified nickel electrodes, the detailed mechanism by which this compound forms and the role, if any, of Pt in this mechanism is not clear. In addition, a number of details related to the electrochemical performance of the modified nickel electrodes are not fully consistent with this simple picture of an isolated $\text{NiCoO}_2(\text{OH})_2$ phase somehow being separated from otherwise stable active material. First of all, if 10% of the electrode capacity is present as $\text{NiCoO}_2(\text{OH})_2$, as was observed in extreme cases for electrodes containing 5% Co additive, then essentially all the cobalt has separated from the normal active material and has been incorporated into this modified phase. The loss of all cobalt from the remaining 90% of the active material should result in both significant increases in redox potentials (Ref. 8) and significant decreases in electrochemical utilization. Neither of these effects is seen. As indicated in Fig. 3, very little shift in potential for the 90% "normal" active material is seen, and if anything the utilization of this material is significantly increased relative to that in an unmodified electrode. The only significant modified characteristic for the normal charge/discharge processes is that the modified active material seems to be much more readily charged into the gamma-NiOOH phase, which discharges at potentials about 30 mv lower than the beta-NiOOH phase (see Fig. 3). The primary goal of the remainder of this study is to resolve these apparent inconsistencies, and to understand the mechanism and impact of $\text{NiCoO}_2(\text{OH})_2$ formation in nickel hydrogen cells.

Mechanism of Nickel-Cobalt Oxyhydroxide Formation in NiH_2 Cells

Before detailed studies related to the mechanism by which nickel electrode active material is modified to form $\text{NiCoO}_2(\text{OH})_2$ in nickel precharged nickel hydrogen cells could begin, it was necessary to identify laboratory conditions under which this compound could be produced from normal active material. Because platinum oxides were always found in modified active material, it was assumed that platinum species played some role in the reactions that occurred.

Initial tests simply involved placing a nickel electrode in 38% KOH with a Ni sheet counter electrode, and adding powdered platinum hydroxide or platinum oxide to the electrolyte. The nickel electrode was then continuously charged for 2 weeks at 0.2 ma/cm^2 . After the two weeks the nickel electrode was removed from this cell, placed in a test cell with 31% KOH and a reference electrode, and reduced as in Figs. 1 and 2. With either platinum hydroxide or

platinum oxide in the electrolyte, no evidence for nickel electrode active material modification was found. The only significant results were that after 2 weeks with these platinum compounds present in the electrolyte, the nickel counter electrode was coated with a uniform layer of platinum metal. This confirms that these platinum compounds dissolve slightly in KOH electrolyte, and that the $\text{Pt}(\text{OH})_6^-$ solution species is readily reduced to Pt metal by electrochemical processes.

The nickel electrode environment during storage of nickel precharged nickel hydrogen cells was then better simulated by placing a nickel electrode in a partially charged state in contact with a zircar separator and a platinum black catalyst electrode. The atmosphere over this simple cell was set to contain the ambient 0.2 atm of oxygen gas. All simulated cells were then wetted with KOH electrolyte and sealed in plastic containers while the reactions were allowed to occur. Initial simulations used nickel electrodes charged to 30, 60, 80, and 100% states of charge in 38% KOH in these test cells. After 30 days of stand time in a test cell, each nickel electrode was reduced as in Figs. 1 and 2. No evidence for modification of the active material was found for any of these nickel electrodes.

A truly accurate simulation of the storage condition of a nickel precharged nickel hydrogen cell must simulate the solid-state phase structure of the active material that is present in the oxidized and reduced materials that exist when the cell goes into storage. The state of the precharged active material consists of whatever active material remains undischarged following numerous charge/discharge cycles. As such, this material is the most stable, or lowest potential active material phase present in the nickel electrode. To simulate this situation, a nickel electrode was cycled 100 times in 38% KOH electrolyte. Each cycle involved discharge of 70% of the 20 mA \cdot h/cm² rated capacity at 10 ma/cm², followed by recharge at 2 ma/cm² to a charge return of 125% of the capacity discharged. After 100 cycles the 70% discharged electrode was put into a sealed storage condition with a platinum catalyst electrode wetted with 38% KOH electrolyte. After 60 days of storage, the nickel electrode was removed and reduced in 31% KOH as in Figs. 1 and 2 to determine whether any modification had occurred to the active material. The results are indicated in Fig. 4, and clearly show some modified active material had formed, as recognized by the peak at about 0.15 volts during electrode reduction.

A repeat of the above test involved cycling a nickel electrode in 31% KOH electrolyte 100 times, instead of in 38% electrolyte. In this case after 4 weeks of storage with a Pt electrode, the somewhat different reduction behavior indicated in Figure 4 was obtained. In this case a reduction peak is seen at about 0.22 volts vs. Hg/HgO, suggesting that either the active material structure that can undergo modification is quite sensitive to KOH concentration, or that 4 weeks was insufficient time to fully modify the active material.

Based on these exploratory studies a parametric matrix of 32 nickel electrodes was prepared as above, by cycling 100 times in 38% KOH, then being placed in a sealed storage cell in contact with platinum black electrodes. For control purposes, 2 electrodes were also stored without a platinum electrode. The variables that were included in this parametric study included: (1) storage time, 39 to 157 days; (2) storage temperature, 0, 20, and 40 deg C; (3) cobalt concentration in the active material, 0, 5, and 10%; and

(4) electrolyte concentration during storage, 31, 38, and 45% KOH. After various storage times, electrodes were removed from the stored cells and reduced using the same method indicated in Figs. 1 and 2. Modified active material was detected, when present, by the observation of a reduction peak near 0.15 volts in 31% KOH. The quantity of $\text{NiCoO}_2(\text{OH})_2$ that was present in each electrode was evaluated from the number of coulombs of charge required to fully reduce the $\text{NiCoO}_2(\text{OH})_2$ material. To evaluate the effect of KOH concentration on the redox potential for $\text{NiCoO}_2(\text{OH})_2$ reduction, some electrodes were reduced in test cells containing either 26 or 38% KOH electrolyte.

It was expected that there would be some variation in the amount of $\text{NiCoO}_2(\text{OH})_2$ formed as a function of storage time. However, as indicated in Fig. 5, there was no clear correlation with storage time from 39 to 157 days. The amount of this modified phase found in 5% Co containing electrodes varied from quite small amounts up to quite high levels, irrespective of the storage time allowed. It appears that the amount of this material formed depends on the amount of active material formed in a phase structure that can be readily converted to $\text{NiCoO}_2(\text{OH})_2$, an amount that seemed to vary quite widely for different electrode samples.

Figs. 6 and 7 indicate the relationships between the amount of $\text{NiCoO}_2(\text{OH})_2$ formed in nickel electrodes and the KOH concentration and temperature during storage. Within the variability in the data, there is no clear dependence on either of these two variables. Fig. 8 indicates the dependence of $\text{NiCoO}_2(\text{OH})_2$ formation on the amount of cobalt additive in the active material. As would be expected, this compound is not formed at all when there is no cobalt present in the active material. The amount of material that is formed increases sharply as the cobalt level in the active material goes from 5% to 10%.

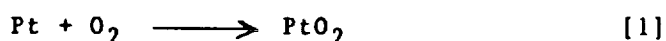
The dependence of the reduction potential of $\text{NiCoO}_2(\text{OH})_2$ on concentration is indicated in Fig. 9, where at each concentration the average reduction potential for several electrodes was used. The observed dependence of reduction potential in Fig. 9 on KOH concentration clearly indicates that hydroxide ions are involved in the rate limiting step of the reduction process. These observations as well as the observation that no $\text{NiCoO}_2(\text{OH})_2$ was formed in the control electrodes after up to 75 days of storage, allow a hypothesis concerning the mechanism for the formation of $\text{NiCoO}_2(\text{OH})_2$ in nickel electrodes to be developed.

Postulated Reaction Mechanism

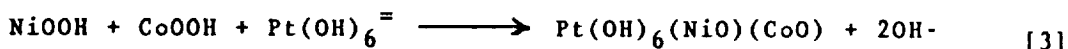
The fact that $\text{NiCoO}_2(\text{OH})_2$ is not found to form in the nickel electrode except when the electrode shares electrolytic contact with oxidized platinum metal surfaces, indicates that platinum species are clearly involved in the reaction mechanism. Because the reaction only requires contact with electrolyte that is also in contact with platinum metal at oxidizing potentials, it is concluded that the $\text{Pt}(\text{OH})_6^-$ ionic species catalyzes the formation of $\text{NiCoO}_2(\text{OH})_2$ from the oxidized nickel and cobalt oxyhydroxides in the solid-state lattice. This solid-state catalytic process results in the $\text{NiCoO}_2(\text{OH})_2$ compound because this is a more energetically stable structure. However, for this catalytic process to occur at a significant rate, it is necessary that adjacent Ni and Co centers in the

oxidized lattice have the proper physical proximity. This is why it is key that the proper phase structure be formed in the active material before $\text{NiCoO}_2(\text{OH})_2$ can form. The proper phase structure is clearly related to the γ - NiOOH structure, although it is not clear that any γ - NiOOH structure will engage in this reaction.

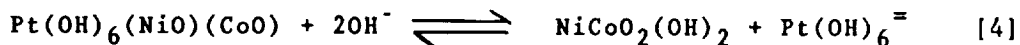
A sequence of reactions may be postulated to give $\text{NiCoO}_2(\text{OH})_2$ in the nickel electrode. First, platinum dissolution in an oxidizing environment produces $\text{Pt}(\text{OH})_6^-$.



The ionic platinum species can then diffuse to the nickel electrode, where they can react with adjacent Ni and Co centers in the solid-state lattice. This reaction is facilitated by the adjacent Ni and Co centers having the necessary geometry to form a complex with the octahedral platinum ions, according to reaction [3].



This platinum complex is in equilibrium with the ionic platinum species in solution. Therefore if the platinum is plated back onto the hydrogen electrode when a nickel hydrogen cell is brought from storage back into normal operation (or for these test cells, when the nickel electrode is put into a platinum free solution), the platinum complex formed in reaction [3] will fall apart, leaving the adjacent Ni and Co species associated in a new and more stable compound, $\text{NiCoO}_2(\text{OH})_2$.



These compounds are structurally illustrated in Fig. 10.

Electrochemical reduction of $\text{NiCoO}_2(\text{OH})_2$ must at least convert the nickel center to a divalent oxidation state. It is not fully clear whether the cobalt remains in a trivalent oxidation state. However, in any case it is clear that when these metal species are converted into a divalent oxidation state, the hydroxide structure becomes the most stable and they gradually revert back to a configuration much like their original structure in the solid-state lattice. Thus there is no irreversible degradation in the active material lattice as a result of these reactions, although the resultant structure does appear to make the lattice more easily oxidized to a γ -phase active material. The improvement in electrode capacity associated with these reactions is likely to arise from the increased formation of γ -phase charged material (which has a higher oxidation state) as well as from the high electrical conductivity of the $\text{NiCoO}_2(\text{OH})_2$ that is dispersed throughout the active material.

Conclusions

This study suggests that platinum complex ions that can form in nickel precharged nickel hydrogen cells under some conditions, can migrate to the nickel electrode, where they are capable of interacting with adjacent nickel and cobalt lattice sites that have an appropriate structural configuration. The appropriate lattice configuration appears to require that the active material be in a gamma-phase structure, and may also require a sufficiently large interlayer spacing for platinum ions to penetrate into the active material structure. The appropriate lattice configuration may also involve unique interlayer cobalt sites that have been suggested in recent EXAFS studies (Ref. 9). The platinum complex ions appear to make it energetically possible for adjacent nickel and cobalt centers in the lattice to reconfigure, thus catalyzing the formation of the compound $\text{NiCoO}_2(\text{OH})_2$ within the lattice. This compound has well defined redox voltage signatures that allow it to be readily identified in nickel electrodes.

The effects of these reactions on nickel hydrogen cell performance appear to be beneficial, based on all data presently available. Capacity is improved by making the gamma-phase active material more easily formed during cell recharge, and utilization is improved by the added conductivity imparted by the electrochemically active and highly dispersed $\text{NiCoO}_2(\text{OH})_2$. While the effects of these changes on ultimate cell cycle life are not yet fully established, limited life testing of nickel precharged cells that have also experienced some storage have generally given good performance. More intensive life testing in the future will address this issue more fully, as well as the issue of what state these unique compounds eventually end up in late in cell life, when corrosion processes have destroyed the initial nickel precharge in the cell.

References

1. R. Barnard, C. F. Randell, and F. L. Tye, *J. Applied Electrochem.* 10 (1980) 109; *J. Appl. Electrochem.* 11 (1981) 517.
2. A. H. Zimmerman, Nickel Hydroxide Electrodes, D.A. Corrigan and A.H. Zimmerman, eds., The Electrochemical Society, Inc., Proceedings Vol. 90-4, 1990, p. 311.
3. A. H. Zimmerman and R. Seaver, *J. Electrochem. Soc.* 137 (1990) 2662.
4. "Popping" is explosive reaction between bubbles of oxygen gas and hydrogen gas at the platinum catalyst surface of the hydrogen electrode, and can occur when a nickel hydrogen cell is in overcharge if there is sufficient electrolyte in the separator to enable oxygen to gather into bubbles.
5. M. S. Antelman, The Encyclopedia of Chemical Electrode Potentials, Plenum Press, New York, 1982.
6. M. Pourbaix, Atlas of Electrochemical Equilibria in Aqueous Solutions, National Assoc. Corr. Engineers, Houston, Texas, 1974, p. 379.
7. Active material was isolated from the sinter by grinding it into a fine slurry in DI water, then magnetically separating the nickel metal particles

from the active material in water solution. The active material was then filtered from the solution, dried, and used for further chemical analysis.

8. A. H. Zimmerman, Extended Abstracts of the Fall Meeting of the Electrochemical Society, 142 1987) 206.

9. D. A. Corrigan, T. W. Capehart, K. I. Pandya, and R. W. Hoffman, The Nickel Hydroxide Electrode, D. A. Corrigan and A. H. Zimmerman eds., The Electrochemical Society, Inc., Proceedings Vol. 90-4, 1990, p. 97.

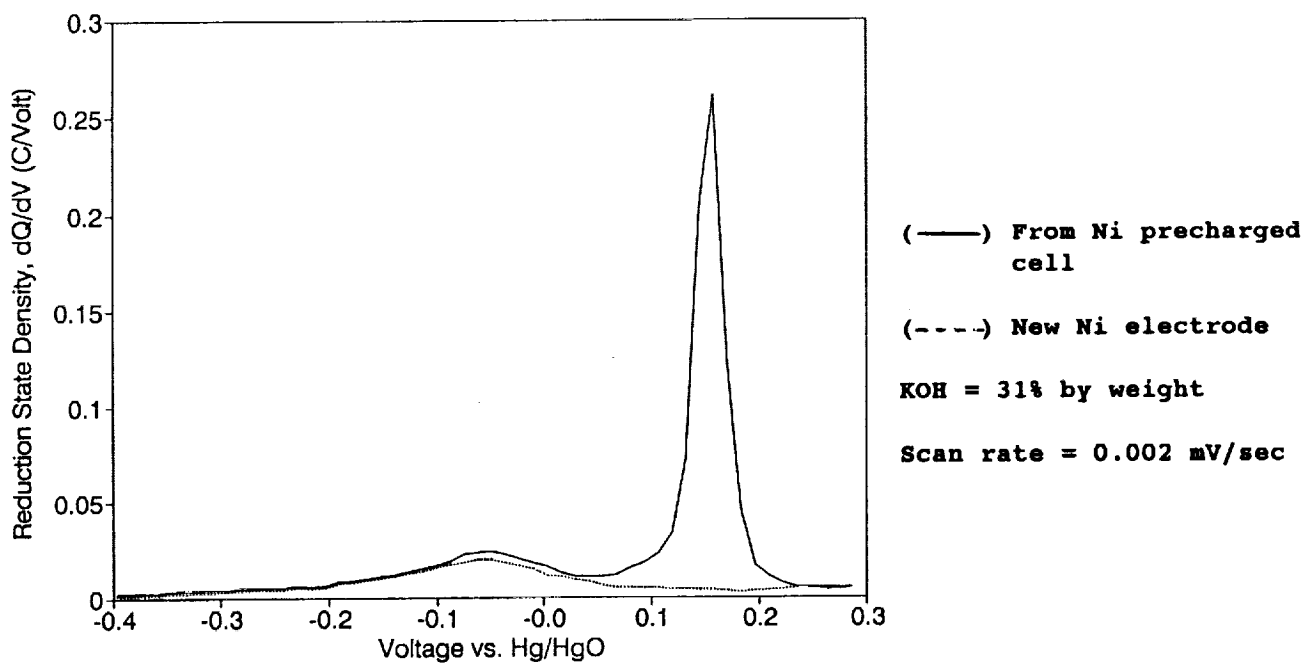


Figure 1. Electrochemically reducible state density vs. potential for nickel electrodes. Total charge in the peak near 0.15 volts is about 5 mAh/cm².

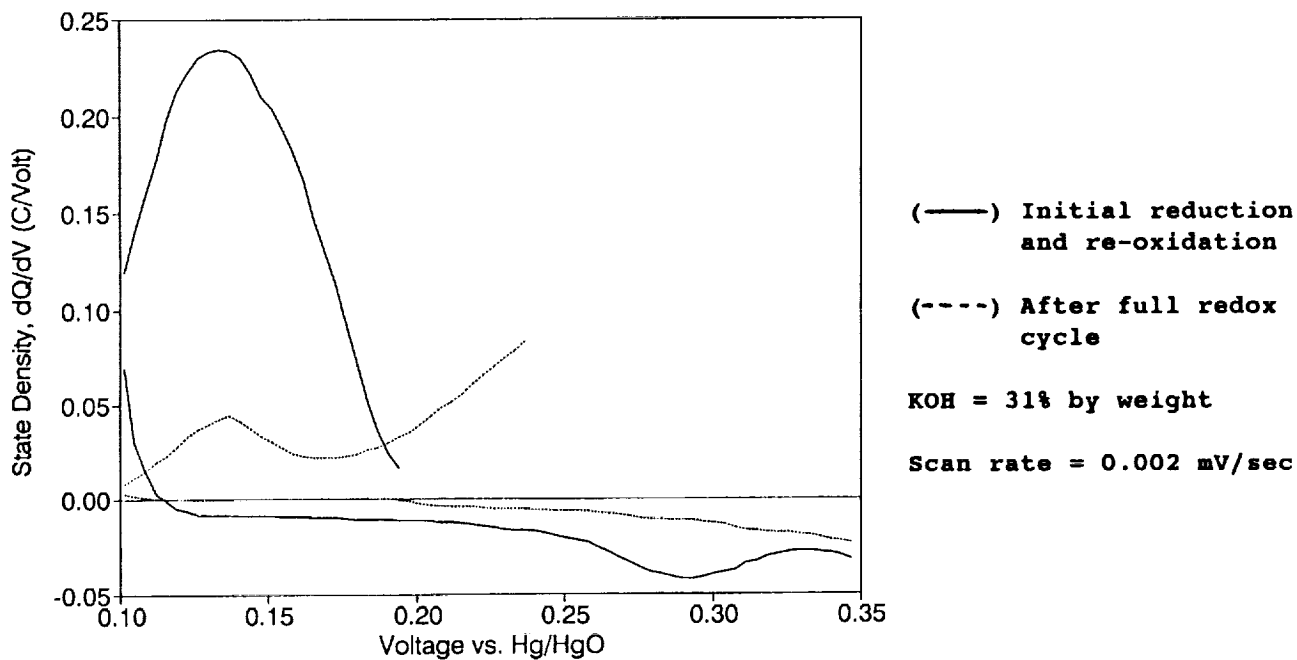


Figure 2. Electrochemically active state density vs. potential for electrodes from a Ni precharged NiH₂ cell, before and after reduction and re-oxidation

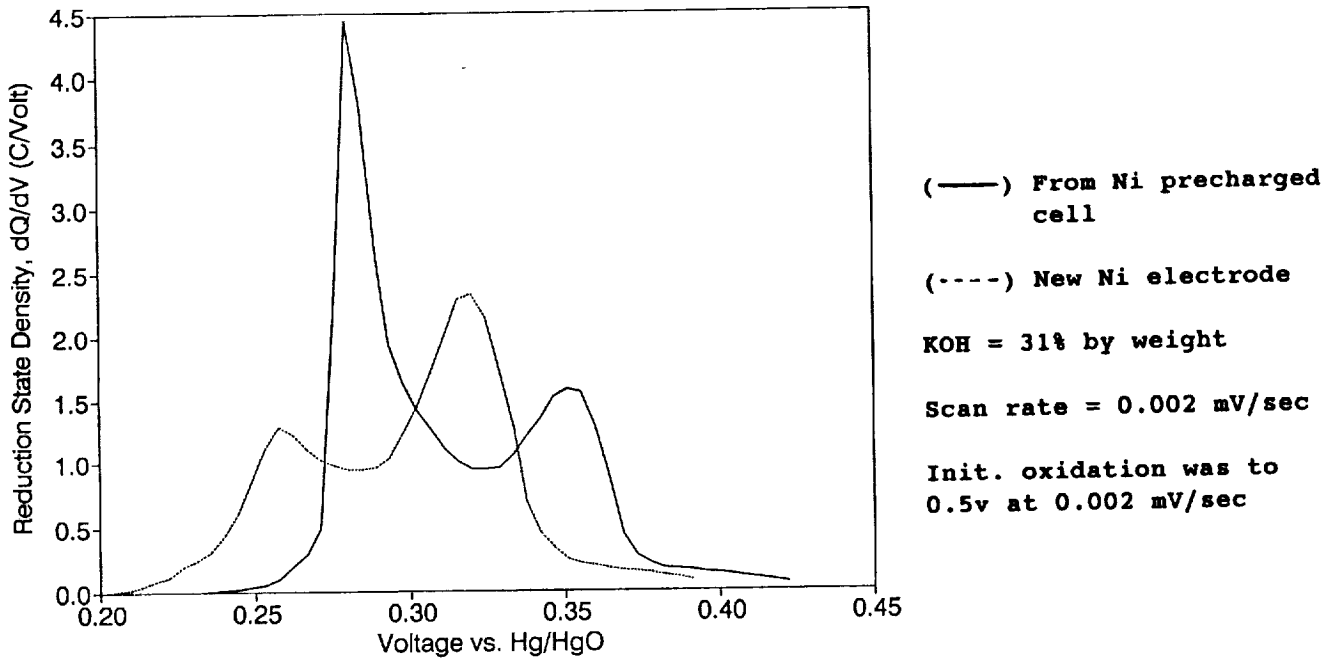


Figure 3. Density of reducible states for normal discharge of the capacity in a new nickel electrode and an electrode from a Ni precharged NiH_2 cell.

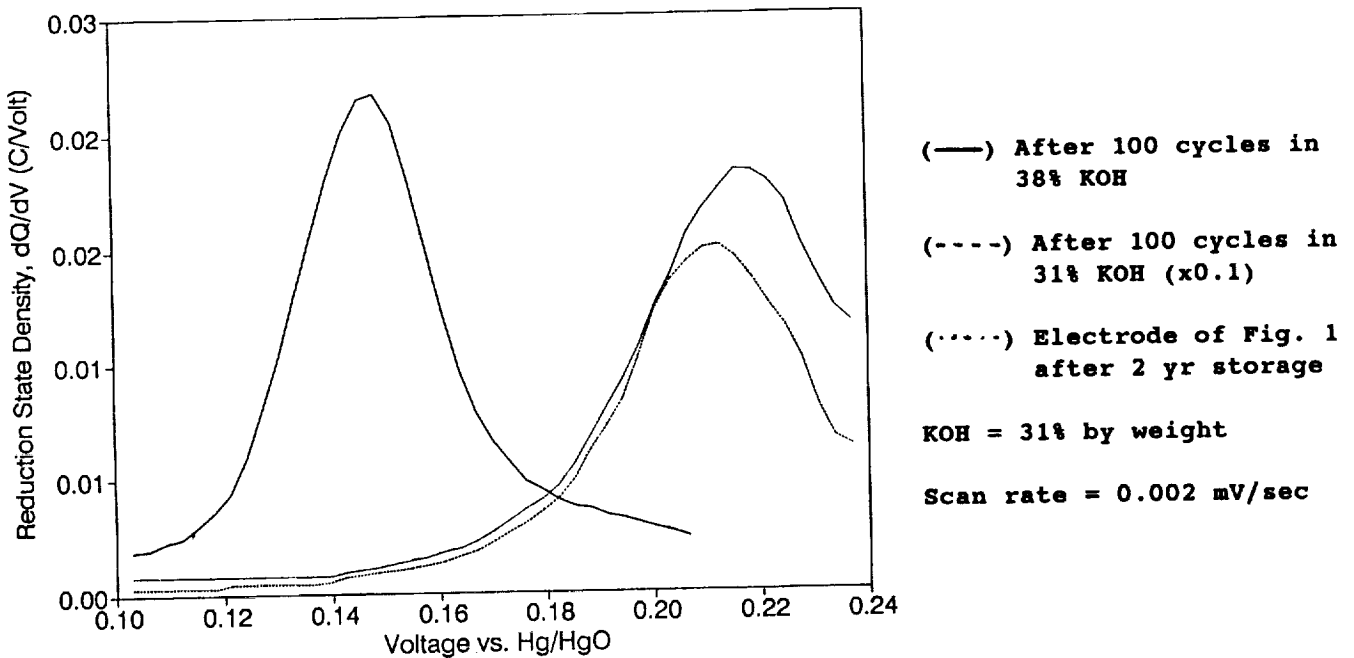


Figure 4. Density of reducible states for storage of nickel electrodes with Pt electrodes after several different electrode preparation methods.

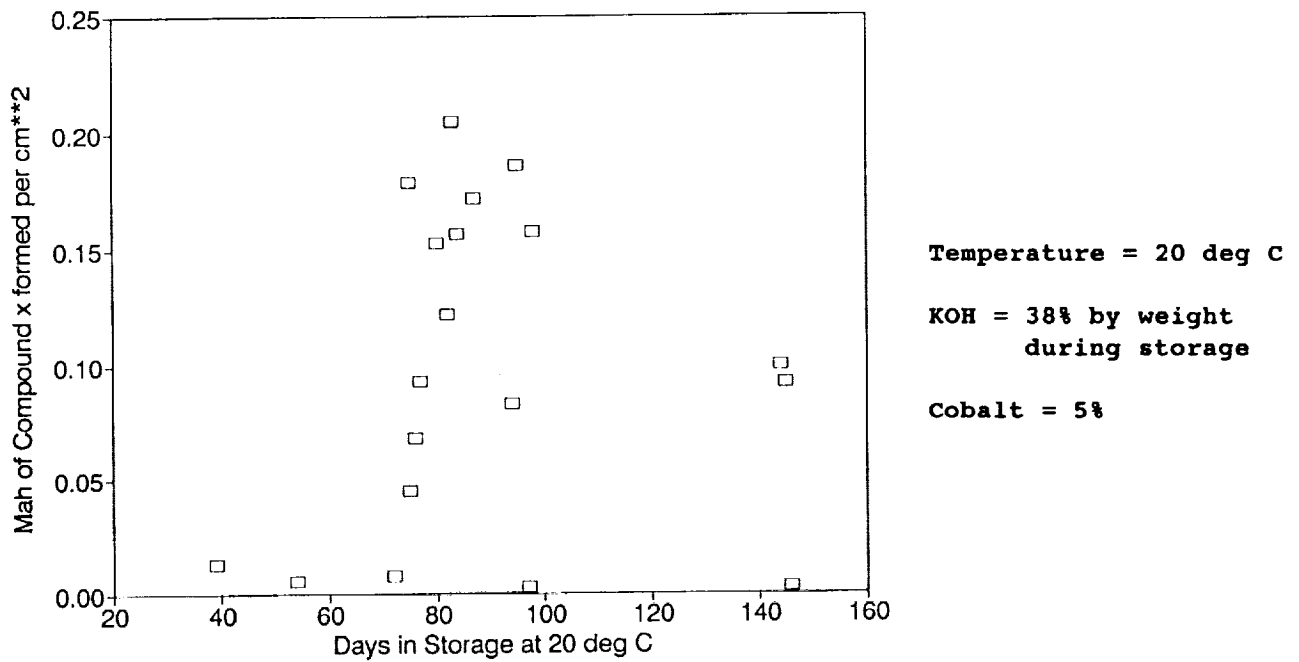


Figure 5. Amount of modified active material formed in nickel electrodes from simulated cell storage as a function of storage time.

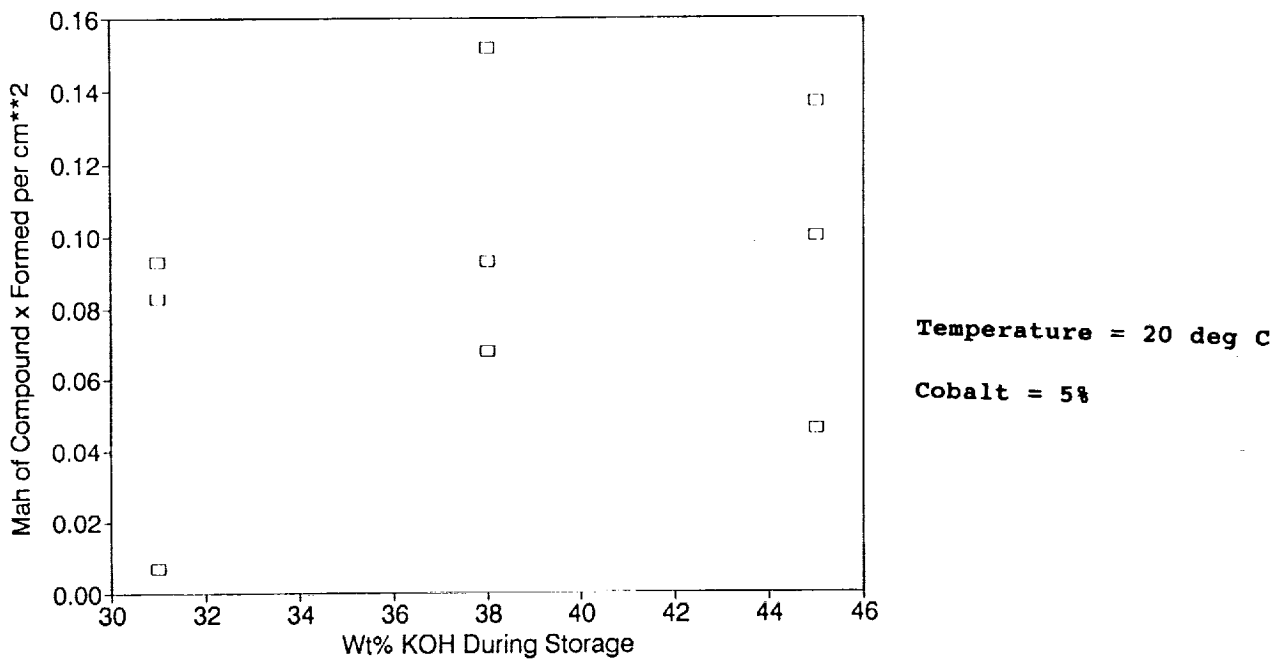


Figure 6. Amount of modified active material formed in nickel electrodes from simulated cell storage as a function of KOH concentration during storage.

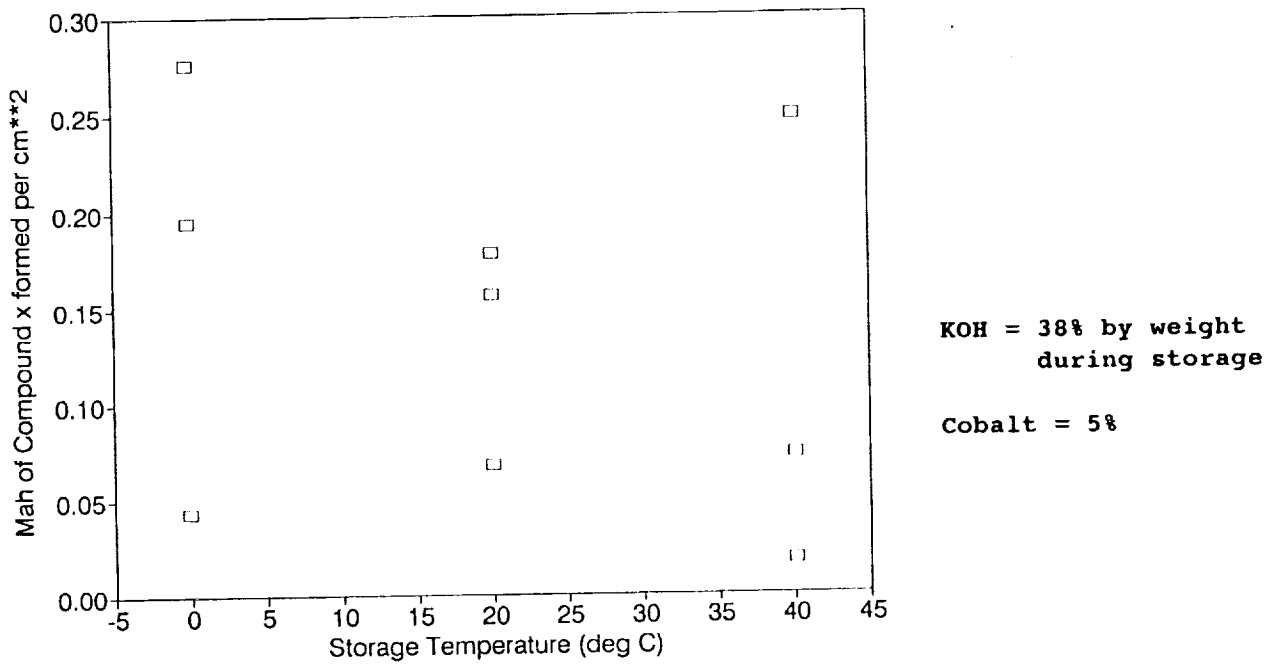


Figure 7. Amount of modified active material formed in nickel electrodes from simulated cell storage as a function of storage temperature.

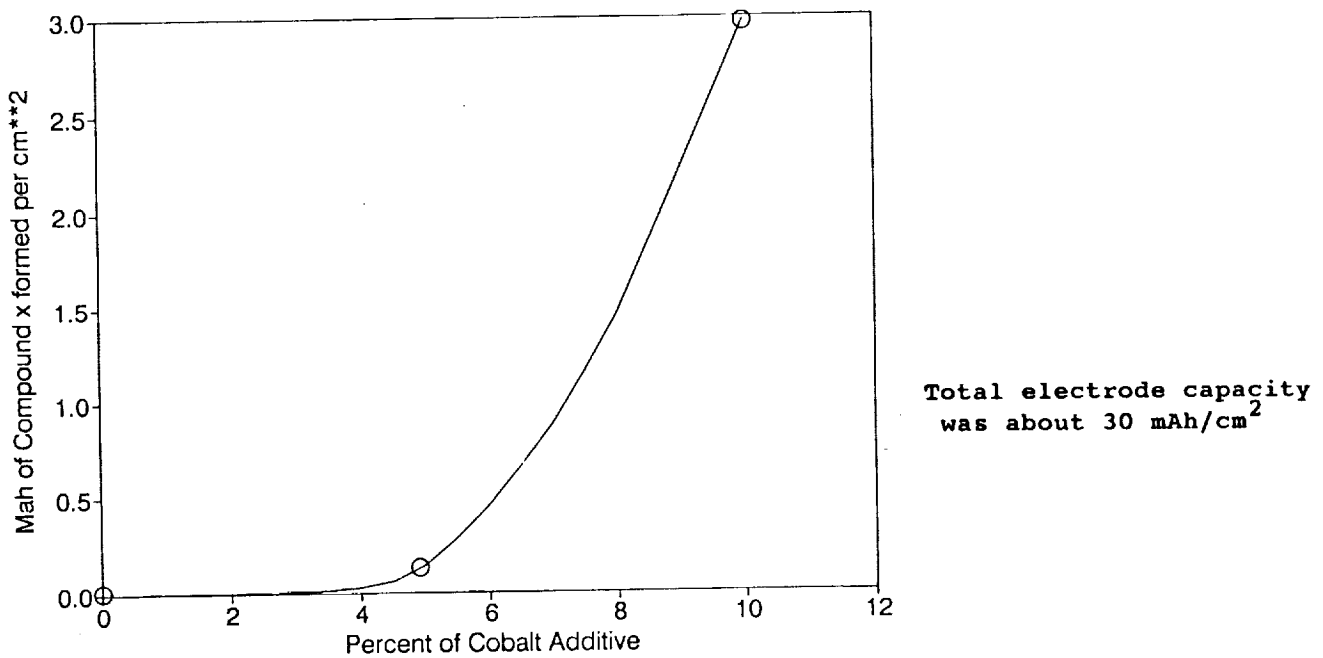


Figure 8. Average amount of modified active material formed in nickel electrodes during cell storage as a function of amount of cobalt additive.

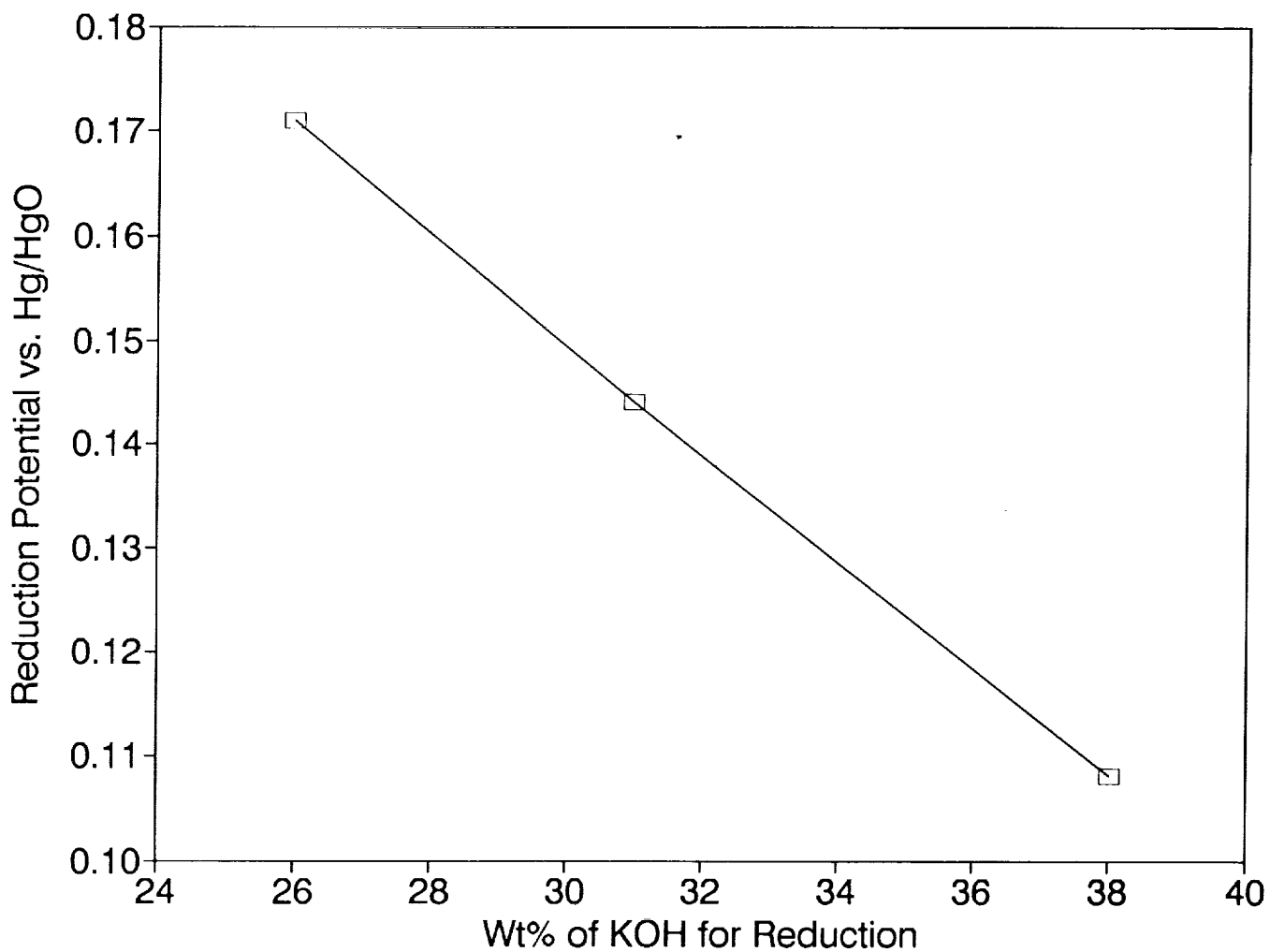
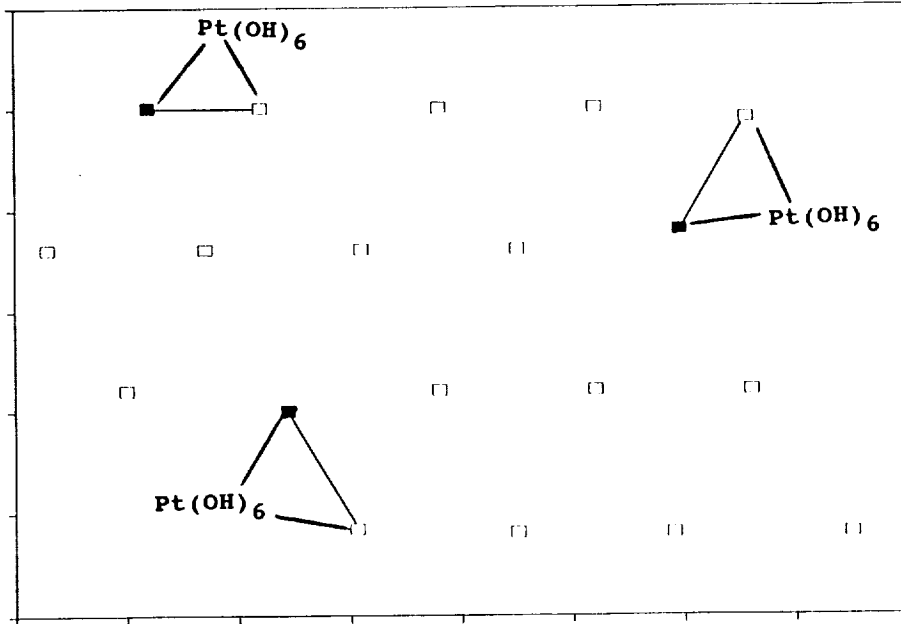


Figure 9. Reduction potential at 20 deg C for the modified active material phase formed during cell storage as a function of KOH concentration. These measurements were made in a cell flooded with KOH electrolyte, with the same electrolyte concentration in the reference electrode compartment as in the cell. The voltage was scanned at 0.002 mV/sec, which was slow enough that the peak reduction potential was independent of scan rate.

Pt(OH)₆(CoO)(NiO) Complex



NiCoO₂(OH)₂ Compound (■—□)

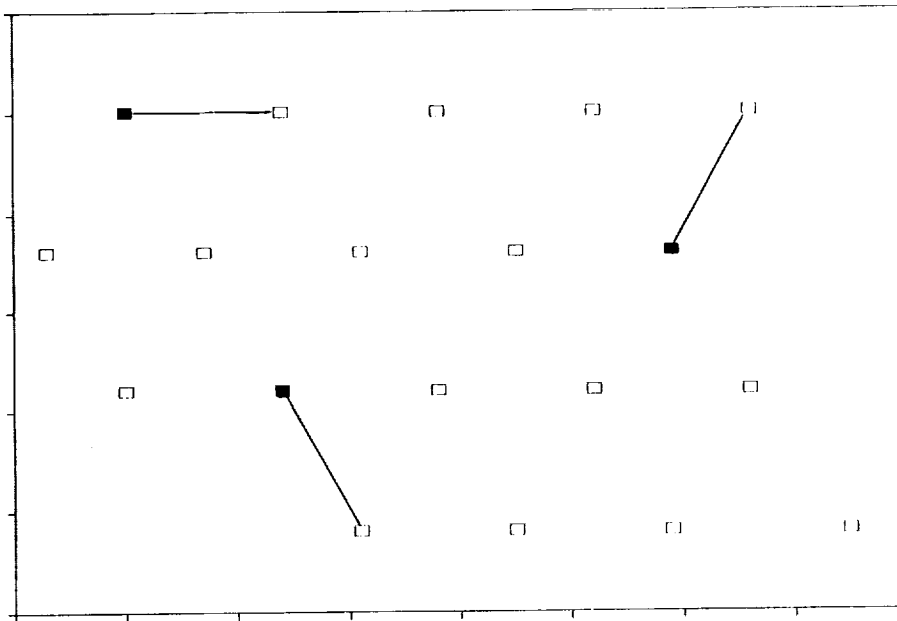


Figure 10. Illustrations of likely configurations for platinum-nickel-cobalt oxyhydroxide and nickel-cobalt oxyhydroxide materials in relation to the active material lattice.

Ni sites = □
Co sites = ■



PHYSICAL AND CHEMICAL ANALYSIS OF A Ni/H₂ CELL*

H. Vaidyanathan,** M.W. Earl, and T.D. Kirkendall
 Comsat Laboratories
 Clarksburg, Maryland 20871-9475

Abstract

A cycled aerospace nickel-hydrogen (Ni/H₂) cell was subjected to destructive physical analysis to determine the reason for a capacity loss after 5,967 cycles at 60-percent depth of discharge. The positive plates in the cell were analyzed in terms of chemical composition, active material utilization, charge efficiency, and thickness increase. The microstructure of a cross section of the positive plate was determined by backscattered electron image analysis. The results suggest that the capacity loss in the cell is caused by low charge acceptance and low active material utilization at the positive plate. The oxidized nickel species content of the positive plate increased due to corrosion of the nickel sintered skeleton. This appears to circumvent the orderly reaction of the active material. Microstructural analysis has indicated that a new phase of active material is formed with cycling.

INTRODUCTION

Tear-down analysis of an aerospace rechargeable cell is normally carried out for purposes such as preflight evaluation of design and manufacturing techniques, tracking the degradation of components in a life test experiment, and determining the reason for failure. The major elements of such an analysis include physical measurements at the cell level, as well as chemical, microstructural, and specialized examination of cell components. Some of the procedures used to analyze the cell are an extension of those used for aerospace nickel-cadmium (Ni/Cd) cells and are documented in the literature [1],[2].

Since nickel-hydrogen (Ni/H₂) cells last longer and cycle longer than any other battery, there is tremendous interest in understanding their gradual degradation with cycling and their failure mechanisms. Premature failure of Ni/H₂ cells in a cycling experiment has been reported, and in one instance the failure was attributed to the rapid reaction of oxygen with hydrogen [3]. In the study described here, a flight-model Ni/H₂ cell which was cycled in a simulated low earth orbit (LEO) regime at 4-percent overcharge and 60-percent depth of discharge (DOD) for 5,967 cycles was analyzed to determine the reason for capacity decline.

ELECTROCHEMICAL PERFORMANCE

The subject cell is a COMSAT/INTELSAT design which has asbestos separators in a back-to-back stack configuration. The cell was withdrawn from a LEO cycling test when its end-of-discharge voltage decreased below 1.0 V. Details and pertinent observations made during the LEO test are given in Ref. 4. As a first step, cell capacity was determined using a charge rate of C/10 and a discharge rate of C/2 at 10°C. Fig. 1 compares the voltage profile of the cell at the beginning of the cycling and after 5,967 cycles. As a result of cycling, the cell exhibited markedly lower discharge capacity, lower discharge voltages, and higher charge voltages. It is apparent from the capacity decay curve presented in Fig. 2 that cell capacity declined gradually after about 3,000 cycles. The cell was subjected to open-circuit stand in the fully charged condition at 10°C. More than 79 percent of the cell capacity was retained after 72 hr of stand, which is comparable to the value exhibited at the beginning of cycling. Thus, the capacity decay in the cell cannot be attributed to soft shorts.

CELL DISSECTION

The cell was dissected, and the stack was transferred to a Soxhlet extractor. After extraction of the electrolyte, the stack was dried and disassembled. Examination of cell mechanical components such as the seals, end plates, center rod, inside can wall, weld ring, and bus bars did not reveal any damage due to cycling. Evaluation of the anodes, cathodes, and separator from the cell revealed the following:

*This paper is based on work performed at COMSAT Laboratories under the sponsorship of the World Systems Division of the Communications Satellite Corporation.

**Please address any correspondence to Dr. Vaidyanathan at COMSAT Laboratories, 22300 Comsat Drive, Clarksburg, MD 20871-9475.

- Sticking of the separator to the positive and negative plates; however, no fluidization of asbestos or diffusion of asbestos particles through either electrode was observed.
- Melted areas comprising 30 percent of the polypropylene gas distribution screen.
- Burn holes in the negative plates, and several cracks and delamination in the Gore-Tex™ backing.
- A high degree of extrusion of active material in the positive plates.

The sticking of the separator probably occurred as a result of compression in the stack. The burn holes and melted areas indicate abnormal heat generation. Delamination of the Gore-Tex™ probably occurred as a result of a rapid oxygen and hydrogen reaction.

ANALYSIS OF POSITIVE PLATES

The positive plates were based on slurry plaque impregnated with Ni(OH)₂ and Co(OH)₂ using an aqueous electrochemical technique. They were analyzed to determine changes in their physical, chemical, and microstructural properties, as described below.

Swelling

The thickness of the plates was measured and compared against values obtained for similar uncycled plates. Swelling was calculated to be 10.5 percent. One important effect of swelling is compression in the stack, which leads to squeezing of the separator, thereby reducing the amount of electrolyte at the interface.

Electrolyte Absorbency

The amount of 30-percent KOH absorbed by a plate was determined using an immersion technique. A value of 0.20 gm of KOH per gram of plate was obtained, which was 23-percent higher than the absorbency of an uncycled plate. It was concluded that swelling of the positive plate leads to an increased number of voids in the positive plates, which capture electrolyte from the separator. In other words, the electrolyte in the stack components is redistributed in the cell.

Chemical Composition and Active Material

The positive plate was quantitatively analyzed, first by extracting the active material with acetic acid, and later by dissolving in HNO₃. The percentage of nickel and cobalt were then determined using atomic absorption spectroscopy. The amount of oxidized nickel species such as active Ni(OH)₂ was 22 percent higher in the cycled plate than in an uncycled positive plate, while the metallic nickel content due to the plaque structure had decreased by approximately a stoichiometrically equivalent amount. This was direct evidence of corrosion of the sintered plaque skeleton.

The porous sintered plaque void volume was calculated based on analytical data and thickness, yielding a value 25 percent higher than the void volume of the sintered plaque that was used prior to electrochemical impregnation. This value is in agreement with the increased plate electrolyte absorption discussed earlier. The loading of the active material [Co(OH)₂ and Ni(OH)₂] was 1.57 gm/cm³ of void—a value close to that for the uncycled plate. Therefore, the increase in void volume due to corrosion and swelling was offset by the increased amount of oxidized nickel species resident in the pores.

ELECTROCHEMICAL PROPERTIES

The capacity of the plate in 30-percent KOH was determined at 10°C to be 1.30 Ah, which is 15-percent less than the minimum capacity obtained for plates of similar design. When this value is factored into Faraday's law, a value of 81.6 percent is obtained for oxidized nickel species utilization, which is lower than the 115 percent obtained for an uncycled plate. The reported utilization in excess of 100 percent is due to the difference between the assumed valency change of 1 and the actual valency change, which is between 1 and 2. Even though the mass of the oxidized nickel species has increased by 22 percent, it is clear that this material is not available electrochemically. On the contrary, it appears that the presence of this corrosion product and the loss of conductive metallic nickel hinders the charge transfer reaction of the original active material. The charge efficiency of the plate was determined by charging at C/10 to a 50-percent state of charge, and capacity was determined by discharging at C/2. The charge efficiency was 81 percent, as compared to 100 percent for an uncycled plate.

MICROSTRUCTURAL ANALYSIS

An image analysis technique based on computer analysis of digitized backscattered electron (BSE) images generated in a scanning electron microscope was employed to study the cross section of the positive plate [5]. Samples were prepared for analysis by encapsulating positive plate sections in epoxy and then cross-sectioning them using metallographic polishing techniques. In the BSE micrograph of a positive plate cross section (Fig. 3), the gray level is directly related to the local composition of the plate. White areas indicate nickel sinter, gray areas indicate active material, and black areas indicate voids (which were filled with epoxy in the sample preparation step). The most remarkable features of this micrograph are the segregation of active material near the surface, the presence of voids, an increase in thickness, and a blistered region close to the surface.

The active material component can be separated from the sinter and voids and displayed separately by computer selection of the gray level in the digitized BSE image. Fig. 4 is a histogram of the gray levels of the 65,536 pixels displayed in the BSE image of Fig. 3. The three peaks correspond to voids, active material, and sinter particles. By dividing the broad central peak obtained for the active material into separate bins of varying gray level, digitized images of the active material distribution can be obtained. When this selectivity was applied, it was discovered that the active material comprises a range of gray levels in the BSE signal.

Figs. 5 and 6 were reconstructed from the BSE image of Fig. 3, using the above selection technique. The distribution of the lighter-appearing active material associated with bin 1 of Fig. 4 is shown in Fig. 5, and the darker active material corresponding to bin 2 is shown Fig. 6. The lighter active material is fairly evenly distributed across the plate, except for the blistered region near the edge. This region contains primarily dark active material. Because the scale in the BSE image is a nearly monotonic function of the average atomic number of the local material composition, this variation in the gray level of the active material is interpreted to mean that the blistered region contains active material of a different structure. The difference between this structure and the generally observed active material may be due to the H₂O and KOH content of Ni(OH)₂. This chemical change and redistribution of active material has not been observed in uncycled or low-cycled plates.

CYCLIC VOLTAMETRY

The voltage profile of a miniature (1-cm²) positive plate was obtained using cyclic voltametry. The voltage of the test electrode was scanned from -0.5 to +0.7 V (vs a Hg/HgO reference electrode) at a rate of 0.1 mV/s in 30-percent KOH. Fig. 7 shows two voltage profiles. Curve A corresponds to an uncycled positive plate, and curve B to a plate from the cycled cell. The uncycled plates exhibited the following features: an anodic peak at +0.557 V corresponding to Ni(OH)₂ oxidation, another anodic peak at +0.70 V corresponding to oxygen evolution, and a cathodic peak at +0.183 V corresponding to the reduction of the oxidized active material. The voltage profile of the cycled plate also contains a second cathodic peak which is very broad at -0.120 V. The peaks associated with active material oxidation and reduction are polarized by 19 and 36 mV (respectively) for the cycled plate, compared to the uncycled plate. The second cathodic peak could be due to the reduction of a new phase of charged active material which reacts at a much lower cathodic potential. This may be the phase of active material identified in the BSE image analysis.

The results of the positive plate analysis are summarized in Table 1.

ANALYSIS OF ELECTROLYTE

The electrolyte obtained from the Soxhlet extraction was analyzed for KOH and carbonate. The alkali content (OH, HCO₃, and CO₃²⁻) was 41.31 percent, of which 3 percent was carbonate. The electrolyte content translates into 2.92 cm³/Ah. There were no abnormalities in the carbonate content or in the normalized volume per ampere-hour of theoretical capacity.

DISCUSSION

The objective of this study was to explain the decline in capacity and average discharge voltage of a Ni/H₂ cell after 5,967 cycles. In addition to close examination of the electrode stack, a range of experiments were conducted to probe the positive plate. The results show that the sintered plaque has corroded, producing additional oxidized nickel species which do not contribute to usable capacity. Also, the plate has swelled, the active material is extruding, and electrolyte absorbency has increased. Digitized BSE analysis was used to obtain chemical information, based on the fact that the yield in number of electrons backscattered from a material increases with the average atomic number. BSE image analysis shows two types of

active material. This observation, in combination with the second cathodic peak obtained in the cyclic voltametry, suggests that a new phase of active material is produced with cycling which contains more water, hydroxyl, or potassium. The lower charge efficiency and lower active utilization can be attributed to a combination of factors, including the formation of a new phase, as well as slightly lower electrolyte content in the separator as a result of squeezing. The lower charge efficiency has resulted in the production of more oxygen, which is given off in streams and reacts with hydrogen, producing "pops" (microexplosions) that damage the negative electrode backing layer.

CONCLUSIONS

A systematic and regular analysis of a Ni/H₂ cell which exhibited gradual degradation in performance for 5,967 cycles has shown that the origin of the failure resides in the positive plates. The conspicuous signs of degradation, such as lower charge efficiency and lower active material utilization of the positive plate, are explained by hypothesizing the formation of a new structure which contains more hydroxyl and potassium. The oxidized nickel species have increased in the positive plate, and appear not only to be less active electrochemically, but also to impede the activity of otherwise good Ni(OH)₂.

ACKNOWLEDGMENTS

The authors wish to thank the following colleagues for their contributions: B. Shaw for BSE analysis, K. Burch for chemical analysis, and W. Nakhleh for cyclic voltametric experiments.

REFERENCES

1. J. D. Dunlop and M. Earl, "Evaluation of INTELSAT IV Ni/Cd Cells," 25th Power Sources Symposium, PSC Publications Committee, Red Bank, New Jersey, 1972, *Proc.*, pp. 40-42.
2. G. Halpert and V. Kunnigahalli, "Procedures for Analysis of Ni/Cd Cell Materials," NASA Publication X-711-74-279, NASA-Goddard Space Flight Center, Greenbelt, Maryland, 1980.
3. K. H. Fuhr, "Failure Analysis of 3.5 inch, 50 Ah Nickel-Hydrogen Cells Undergoing Low Earth Orbit Testing," 22nd Intersociety Energy Conversion Engineering Conference, Philadelphia, August 1987, *Proc.*, pp. 889-892. Available from AIAA, New York.
4. H. Vaidyanathan, "Effect of Design Variables on the Cycling Characteristics of Ni/H₂ Cells," 24th Intersociety Energy Conversion Engineering Conference, Washington, D.C., August 1989, *Proc.*, pp. 1405-1409. Available from IEEE, New York.
5. T. P. Rimmel and T. D. Kirkendall, "Quantitative Analysis of Positive Battery Plates by Means of BSE Image Analysis," *Microbeam Analysis*, A. D. Romig and J. I. Goldstein, eds., San Francisco Press, 1984, pp. 165-168.

Table 1. Changes in Positive Plate From the Cycled Cell

| Item | Uncycled Plate | Cycled Plate |
|------------------------------------|----------------------------|----------------------------------|
| Swelling | Initial thickness (stable) | 10.5% increase in thickness |
| Electrolyte Absorbency (gm KOH/gm) | 0.162 | 0.20 |
| Plaque Porosity (%) | 78 | 80.7 |
| Charge Efficiency (%) | 100 | 81 |
| Active Material Utilization (%) | 115 | 81.6 |
| BSE Image Analysis | Gray active material | Gray and dark active material |
| Cyclic Voltametry | No second cathodic peak | Second cathodic peak at -0.120 V |

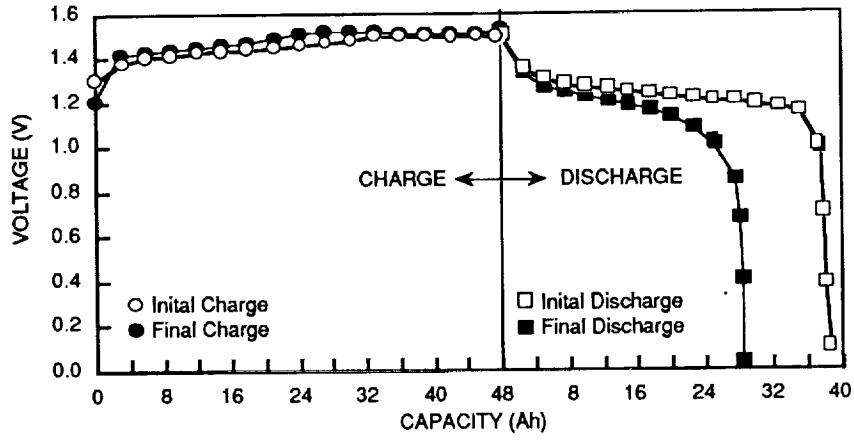


Fig. 1. Charge/discharge voltage profiles for the cell before and after cycling

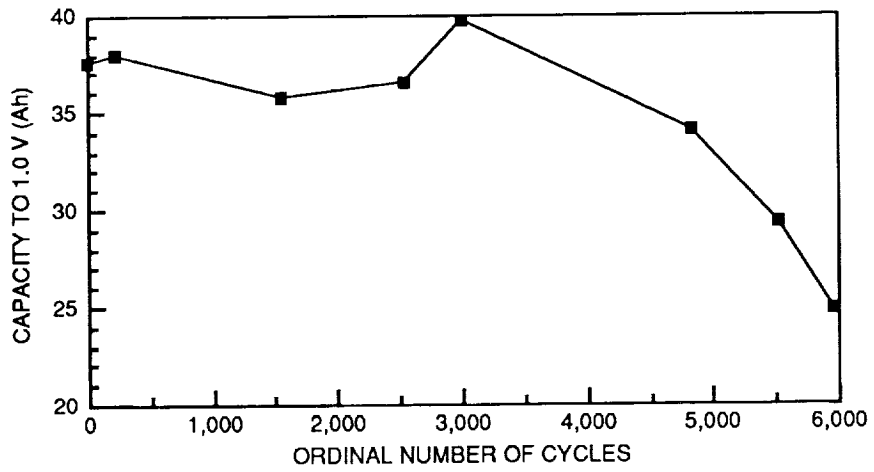


Fig. 2. Variation of capacity (1.0 V) with cycling (discharge rate C/2)

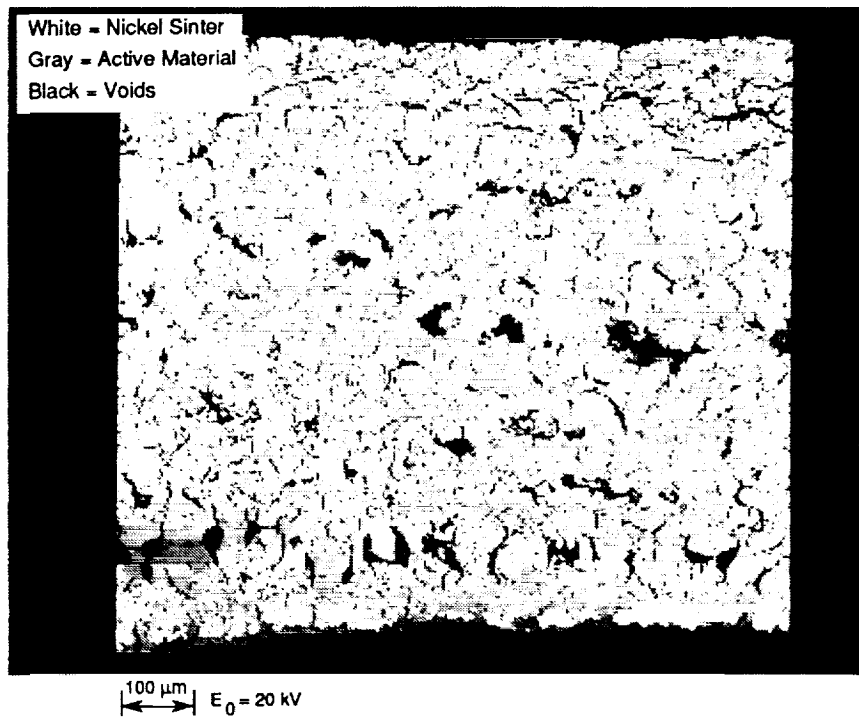


Fig. 3. Digitized BSE image of a cross-sectioned positive plate

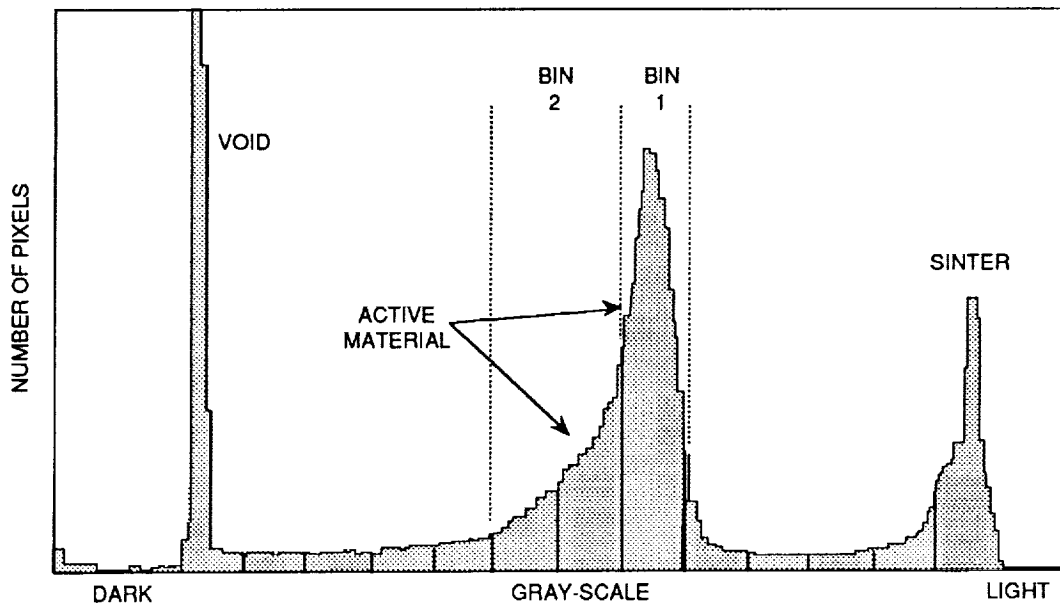
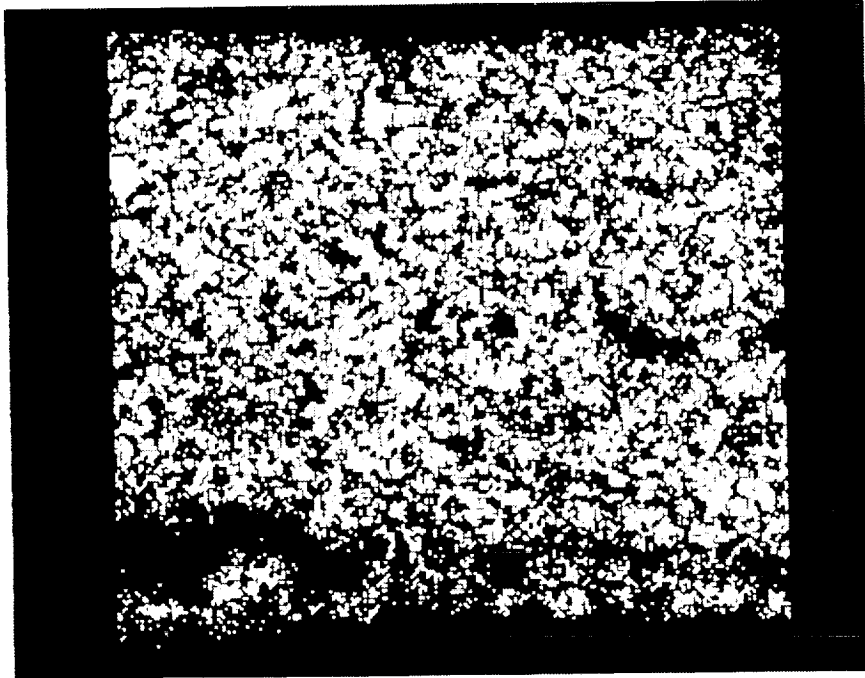
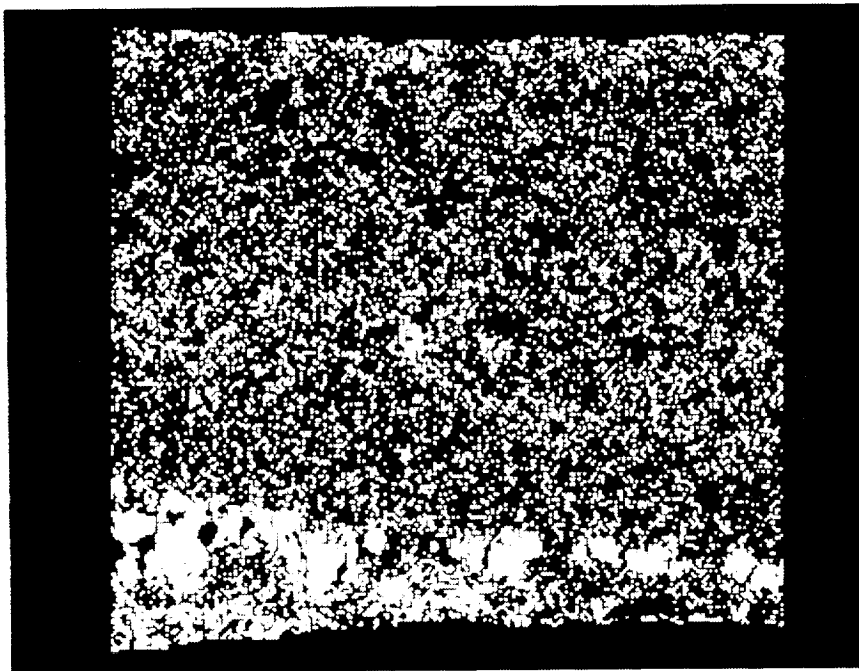


Fig. 4. Histogram of gray levels in the BSE image of the cross-sectioned positive plate shown in Fig. 3



100 μm

Fig. 5. Active material distribution from bin 1 of Fig. 4



100 μm

Fig. 6. Lower atomic number active material from bin 2 of Fig. 4

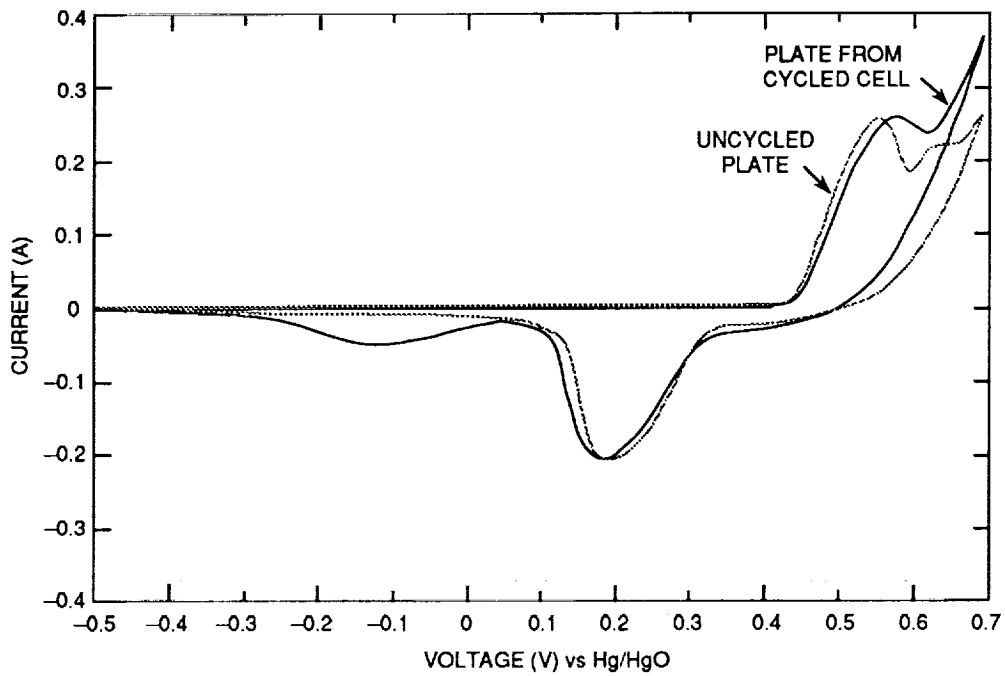


Fig. 7. Voltage profiles of cycled and uncycled positive plates (generated using cyclic voltametry)

RAMAN SPECTRAL OBSERVATION OF A "NEW PHASE" OBSERVED IN NICKEL
ELECTRODES CYCLED TO FAILURE

P.L. Loyselle,* X.Shan, and B.C. Cornilsen**
Michigan Technological University
Houghton, Michigan 49931

and

M.A. Reid
NASA Lewis Research Center
Cleveland, Ohio 44135

A "new phase" is reported in nickel electrodes from Ni/H₂ boilerplate cells which were cycled to failure in electrolyte of variable KOH concentration (21-36%). Raman spectra clearly show the presence of this phase, and these spectra have been used to estimate the amounts present on these electrodes. Ten of 12 electrodes examined contain this new phase. The cycle life at higher KOH concentrations (31 and 36%) was greatly reduced, and nickel electrodes from these cells exhibited extensive amounts of this new phase. The presence of this "new phase" correlates with cell failure defined by low end of discharge voltages. It is proposed that the lowered capacity and failure of these electrodes was caused by loss of active mass and formation of a phase with reduced electrochemical activity. These results indicate that formation of this new phase is accelerated at higher KOH concentrations.

INTRODUCTION

Ni/H₂ boilerplate cells containing 26% KOH displayed the longest cycle life in a recent study by Lim and Verzwylt [1]. Electrodes were cycled to failure in electrolyte of variable KOH concentration (21-36% KOH), at 80% depth of discharge in an accelerated cycle regime (6.24 Ah nominal capacity). The cycle life of the 26% KOH cells was nine times greater than the cycle life of the conventional 31% KOH cells.

The Raman spectra of electrodes from these cells have been studied to characterize the active mass structure, as well as any other phases that might be present. Observation of a second phase is important because such a phase can be detrimental, adversely influencing cycle life and contributing to failure. Raman spectra provide a signature which is characteristic of each solid phase (or compound) present [2]. Furthermore, each spectrum carries structural information about each phase.

* Current Address: NASA, Lewis Research Center, Cleveland.

** Author to whom correspondence should be addressed.

In previous work, it has been shown that Raman spectra can be used to characterize the NiO₂ layer stacking in nickel hydroxides and oxyhydroxides as close packed (ABAB...) or non-close packed (ABBCCA...) [2,3]. β -nickel hydroxides are close packed. Active mass, charged or discharged, is non-close packed. X-ray powder diffraction patterns and EXAFS spectra have been successfully interpreted using a non-close packed layer structure, supporting this structural conclusion [3,4]. Raman spectroscopy also allows structural differentiation of precursor materials and "formed" active mass [2]. The precursor structure with cobalt differs from the precursor structure without cobalt.

EXPERIMENTAL

Raman spectra discussed herein are ex situ scans of electrodes which were removed from the cells in the discharged state. Spectra have been collected for both the front (non-screen side) and the back (screen side) of sectors taken from these electrodes. Two electrodes were studied from each cell (positions 1, top, and 6, bottom of cell stack). The electrode ID numbers, KOH concentrations, and cycle lives are given in Table 1 [1]. The 26% KOH cell containing electrodes 21-05 and 03-02 was removed from cycling before failure. A low end of discharge voltage (EODV) accounted for failure of the 31 and 36% KOH cells. The remaining cells ($\leq 26\%$ KOH) failed by a soft short.

The Raman instrumentation and scan conditions have been previously described [2]. The compositions (weight percent "new phase") have been estimated from the relative peak intensities (I_{553} vs. I_{470} ratio), using a technique developed previously for quantitative analysis of coal dust - diesel particulate mixtures [5]. Material at or near the surface (in the volume illuminated and sampled by the laser beam) is measured. Material that is deeper within the electrode is not sampled. The compositions for the volumes sampled are believed to be representative, as an approximate measure of the amount of new phase.

RESULTS AND DISCUSSION

A Raman spectrum was scanned of each face of the 12 electrodes. Most spectra exhibit the expected doublet spectrum of discharged active mass (Fig. 1a) [2]. A four-peak spectral signature, which has not previously been documented, is observed in spectra scanned on 12 of 24 electrode faces (Table 1). This spectrum is characteristic of the presence of an additional phase, a phase not previously reported. A spectrum of an electrode displaying a predominant amount of this new phase is shown in Fig. 1b. This "new phase" shall be referred to hereafter as "phase-X."

Ten of the twelve electrodes studied contain phase-X (Table 1). Two of these show phase-X on both sides. In general, the front side exhibited the larger amount of phase-X. The front side faces the KOH and hydrogen electrode. The fact that the unused electrode (#08-09) showed no phase-X suggests that phase-X is produced during cycling in KOH electrolyte.

To facilitate electrode comparison, average compositions are given in Table 1, averaging over eight sides (for four electrodes) and over four sides (for two electrodes). The 31% and 36% KOH electrodes contain extensive amounts of phase-X on the average (56% average, over 8 electrode sides), and on both the front and back sides. By comparison, the 26% KOH electrodes display both a lower average (29%) and lower absolute percentages of phase-X.

First, the 26% KOH samples will be compared with the higher percent KOH samples (31% and 36% KOH). The high-KOH samples exhibited lower cycle life and more phase-X. The failure mode for these 4 high-KOH electrodes was a low end of discharge voltage (EODV) at low cycle life (<4000 cycles using either the 0.9 or 0.5 V EODV criterion) [1]. The observation that these electrodes display the most phase-X suggests that the phase-X may be instrumental in reducing cycle life, perhaps by inducing the low EODV. Also, a KOH concentration dependence is implied, with the 31% and 36% KOH concentrations favoring phase-X formation.

Phase-X is displayed on only one side, the front, of the lower KOH electrodes ($\leq 26\%$ KOH). These electrodes all cycled to greater than 28,000 cycles with the 0.5 EODV criterion [1]. Except for the cell removed before failure, they all failed due to a soft short. When phase-X is not formed on both sides of the electrode, it appears to have a less detrimental effect on cycle life, and a low EODV is not induced. This observation suggests phase-X is first formed on the front of the electrode. If formation begins on the front side and propagates through to the back side, observation on both sides indicates that much more phase-X is present, throughout the electrode. Therefore, observation of phase-X on both sides of the 31 and 36% KOH electrodes is indicative of a much more extensive formation of phase-X. This is consistent with the greatly reduced cycle lives.

A KOH concentration dependence is implied, with higher KOH concentrations favoring phase-X formation. The 26% KOH electrodes all have a lower amount of phase-X than the 31% and 36% KOH electrodes. The 21% KOH electrodes exhibit no phase-X on either side. The 23.5% KOH electrodes appear to break this trend. The 23.5% KOH electrodes display more phase-X on the front side than the 26% KOH electrodes. However, the semi-quantitative nature of these values suggests these numbers may not differ significantly. That is, the 46% phase-X value (average of 4) for the 23.5% KOH is not that much greater than the 33% phase-X value for the first 26% KOH cell (and is less than the 56% phase-X value (average of 8) for the 31 and 36% KOH cells). This is especially true in light of the fact that the phase-X is only observed on one side for the 23.5 and 26% KOH electrodes, and the amounts on the interior are not estimated. Therefore, the amount of phase-X increase can be taken in the order:

$$21\% < 23.5\% \approx 26\% < 31\% \approx 36\% \text{ KOH.}$$

We, therefore, propose that the higher KOH concentrations favor and accelerate phase-X formation.

Phase-X is not simply induced by extensive cycling, because it is clear that the phase-X content does not correlate with high cycle life. 31% and 36% KOH, with the most phase-X, show the lowest cycle life. The phase-X content is lower in the 26% KOH electrodes, which display the longest cycle life. The 21% KOH electrodes were cycled extensively, but display no phase-X.

Furthermore, since 21% and 23.5% KOH electrodes have drastically different amounts of phase-X, it appears that phase-X does not account for the secondary plateau formation reported below 26% KOH by Lim and Verzwylt [1].

The fact that the front of the electrode (which is closer to the counter electrode) has more phase-X than the back is consistent with greater utilization of the active mass on the side facing the hydrogen electrode and separator containing KOH. This front of the nickel electrode is directly exposed to KOH. This exposure as well as differences in current densities and voltage drops between the front and the back side of an electrode may be factors influencing phase-X formation.

CONCLUSION

The presence of phase-X is correlated with cell failure at high KOH concentration (31-36%) due to a low end of discharge voltage. That is, these electrodes display a reduced capacity at low cycle life. It is proposed that this lowered capacity is caused by a phase transformation from active mass to a phase which is less electrochemically active, thereby reducing electrode utilization. It is apparent that higher KOH concentrations favor formation of this new phase.

These results suggest that avoidance of the soft short failure mechanism, observed for <26% KOH electrodes, might allow even greater electrode cycle life for the KOH concentrations below 26% KOH. It becomes obvious that the apparent maximum performance at 26% KOH is controlled by multiple failure modes, not only phase-X formation.

It has often been proposed that a "less active phase" may be formed and may be detrimental to the electrochemical behavior of the nickel electrode. This is, to our knowledge, the first time that this phase has been directly observed in active mass. The structural identification of this phase is in progress.

Support by NASA, Lewis Research Center under Grant No. NAG3-519 is gratefully acknowledged.

REFERENCES

1. H. S. Lim and S. A. Verzwylt, *J. Power Sources*, 29 (1990) 503-519.
2. B. C. Cornilsen, X. Shan, and P. L. Loyselle, *J. Power Sources*, 29 (1990) 453-466.
3. B. C. Cornilsen, P. J. Karjala, and P. L. Loyselle, *J. Power Sources*, 22 (1988) 351-357.
4. B. C. Cornilsen, X. Shan, and P. L. Loyselle, in D. Corrigan and A. Zimmerman (eds.), *Nickel Hydroxide Electrodes*, Vol. 90-4, The Electrochemical Society, Pennington, NJ, 1990, pp. 82-96.
5. B. C. Cornilsen, J. H. Johnson, P. L. Loyselle, and D. H. Carlson, in R. E. Glenn (ed.), *Proceedings of the VIIth International Pneumoconioses Conference*, DHHS (NIOSH) Publication No. 90-108, Part 1, U.S. Dept. of Health and Human Services, NIOSH, Pittsburgh, PA, 1990, pp. 656-662.

TABLE 1

Quantitative Determination of "New-Phase" Content (%X) for Hughes Electrodes with Variable KOH Concentration, using Raman Spectral Analysis

| ID | %KOH | Position | No. of Cycles[1]* | Side | | Average (%X) | |
|-------|------|----------|-------------------|-------------------------|--------------------|--------------|------|
| | | | | Front (Non-screen) (%X) | Back (Screen) (%X) | of 4 | of 8 |
| 27-03 | 36 | 1 | 1,845/ 1,268 | 49 | 63 | 44 | 56 |
| 35-09 | 36 | 6 | | 62 | 0 | | |
| 25-09 | 31 | 1 | 3,275/ 2,979 | 71 | 0 | 68 | |
| 27-07 | 31 | 6 | | 100 | 100 | | |
| 20-01 | 26 | 1 | >39,573/39,230 | 52 | 0 | 33 | 29 |
| 19-06 | 26 | 6 | | 80 | 0 | | |
| 21-05 | 26 | 1 | >30,549/>30,549 | 27 | 0 | 24 | |
| 03-02 | 26 | 6 | | 69 | 0 | | |
| 04-03 | 23.5 | 1 | >28,495/ 4,803 | 100 | 0 | 46 | 23 |
| 16-09 | 23.5 | 6 | | 85 | 0 | | |
| 28-05 | 21 | 1 | >38,191/ 5,047 | 0 | 0 | 0 | |
| 2401 | 21 | 6 | | 0 | 0 | | |
| 08-09 | -- | - | | 0 | 0 | - | - |

* No. of cycles to 0.5 V EODV / No. of cycles to 0.9 V EODV.

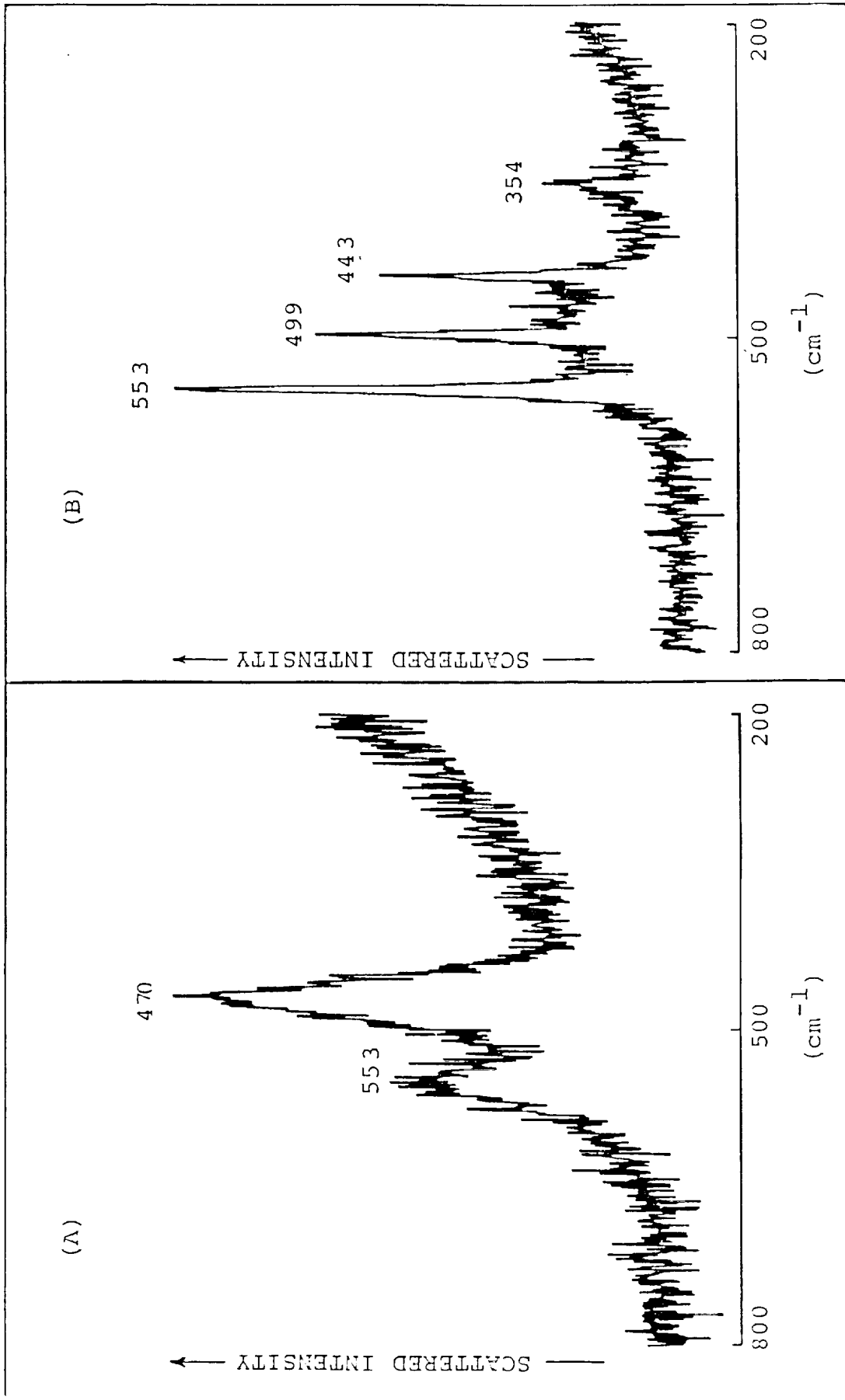


Figure 1. Raman spectra of A: discharged active mass (ID# 16-09)

and B: "Phase-x (ID# 04-03)".

IMPEDANCES OF NICKEL ELECTRODES CYCLED IN VARIOUS KOH
CONCENTRATIONS

Margaret A. Reid and Patricia L. Loyselle
NASA Lewis Research Center
Cleveland, Ohio 44135

ABSTRACT

Recent tests at Hughes have shown that Ni/H₂ cells cycled in 26% KOH have much longer lives than those cycled in other concentrations. As part of an ongoing program to try to correlate the impedances of nickel electrodes with their life and performance, impedances were measured of a number of electrodes from these tests that had been cycled in concentrations from 21% to 36% KOH. These had been cycled under double-time LEO conditions at 80% DOD to failure. Cell life ranged from about 1000 to 40,000 cycles. After cycling ten times to reduce possible changes due to storage, impedances were measured at five voltages corresponding to low states of charge. The results were analyzed using a standard circuit model including a Warburg impedance term. Lower kinetic resistances and Warburg slopes were found for several electrodes which had been cycled in 26% KOH even though they had been cycled for a much longer time than the others. Interpretation of the data is complicated by the fact that the cycle lives, storage times, and failure mechanisms varied. Several other circuit models have also been examined, but the best correlations with life were found with parameters obtained from the simple model.

INTRODUCTION

The effects of electrolyte concentration on the life of Ni/H₂ cells have recently been studied at Hughes Aircraft Corp. [1,2]. Cycle lives of up to 40,000 cycles were achieved with 21% KOH. Since no impedances have ever been measured on electrodes that had been cycled for such long times, these electrodes were investigated to determine the relationship of impedance to KOH concentration and cycle life. Impedances of nickel electrodes have been studied by many investigators [3-7]. It has been found that impedances increase by several orders of magnitude as the electrode goes from the fully charged to the fully discharged state. Results from different investigators are similar qualitatively but not quantitatively. Our earlier studies have shown this is not due to lack of reproducibility of the impedance measurements but is due to differences in the preparation and storage of the electrodes. Cells from a given lot from each manufacturer have been shown to have impedances that are very similar [7] provided that they have been cycled and stored in the same way, but cells from different manufacturers [8] and electrodes that have been stored for relatively long periods of time [3] have different impedance characteristics. Thus, impedance measurements provide a promising method for the study of nickel electrodes from different sources and under different operating conditions, especially since many other methods of study, i.e., X-rays, do not show clear distinctions between electrodes. However, considerable care must be taken in comparing electrodes and cells from different sources to insure that the cycling and storage conditions are the same. An additional advantage of impedance measurements is that they are electrical in nature; hence, they show the promise of providing information for constructing cell models to predict charge and discharge curves and other electrical characteristics. These models would ideally incorporate

differences due to cell manufacturer, KOH concentration, cycle regime, and numbers of cycles. Such models are not available as yet, but are needed by system designers to predict the behavior of cells and electrodes under various pulse and steady-state loads.

EXPERIMENTAL

The electrodes examined in this study were provided by Hughes Aircraft Corp. from their study on the effects on life of various KOH concentrations [1,2]. The cells were boilerplate cells with six electrodes each and were cycled in a double-time LEO regime at 80% DOD. All electrodes were from the same lot. Each cell had six electrodes, of which the top and bottom electrodes were used in this study. The results of the cycling experiments are summarized in Table 1. One uncycled electrode from the same lot was also studied.

Measurements were made using a Solartron 1250 Frequency Response Analyzer and a Solartron 1286 Electrochemical Interface from 1000 Hz to 0.001 Hz (six decades). At high frequencies a 1 mV RMS signal was used in order to keep the current within the limitations of the instruments. Some measurements at the lower frequencies where the impedances were much larger were made using a 5 mV signal to improve the sensitivity of the measurements. Data were taken using ZPLOT software (Scribner Associates, Charlottesville, VA).

A Hg/HgO reference electrode was used. For comparison with voltages in actual cells, Table 2 lists the voltages used along with the same voltages with respect to that of a H₂ electrode at the pressure that would be found in a sealed cell [3].

The electrodes studied here had been removed from the boilerplate cells after failure, rinsed and dried, and stored until the complete set of cells had failed. It is known that storage affects the impedance [3], but the magnitude of the effect and the effects of dry vs wet storage are unknown. In order to bring the electrodes as much as possible to a consistent state, they were cycled ten times, starting with four cycles at a C/10 charge rate for 18 hours and a C/4 discharge rate to a cut-off voltage of -0.50 V. The next five cycles were at a C/4 charge rate with 10% overcharge and a C/2 discharge rate to 80% DOD. They were then charged again at a C/4 rate with 10% overcharge before taking the impedance measurements, starting with the highest voltages. Before measurements were taken, the electrodes were equilibrated at the desired voltage, usually until the DC current fell below 10 mA. The electrode that had not been used in the cycling tests was conditioned in the same way.

The top and bottom electrodes from each cell were studied. In general the impedances from the top electrodes were somewhat higher. When the cells had been dismantled, it was noted that the top electrodes were drier [1]. The lesser amount of electrolyte during cycling is probably the cause of the higher impedance. The differences were generally much smaller than those between cells, so the parameters from the two electrodes were averaged for subsequent analysis.

The choice of potentials for the cell measurements was made based on the results of earlier measurements with electrodes from different manufacturers [8,9]. It has been found that at high states of charge the impedances are low, and differences between manufacturers are also small. However at low states of charge (in the voltage range from about 0.330 V to 0.170 V vs a Hg/HgO electrode or from 1.275 to 1.115 V in a cell) they increase by several orders of magnitude,

and there are significant differences between manufacturers. At voltages below 0.170 V the impedances are still higher, but there are smaller differences between electrodes from different manufacturers. There is also much more scatter, and a much longer time is required to reach equilibrium, so that the voltage range from 0.330 to 0.170 seems to be the best range for comparison.

RESULTS AND DISCUSSION

Bode plots and complex plane plots for one of these electrodes are shown in Figure 1. Figure 1c shows the overall complex plane curves, while Figure 1d shows the expanded portions at the higher frequency range. These figures are for an electrode cycled in 26% KOH for 30,549 cycles, at which point the cell was removed for further analysis. The same trends were observed for all the electrodes as the voltage was changed.

The simplest equivalent circuit that can be postulated for a battery electrode is shown in Figure 2a where Z_w represents a Warburg impedance due to slow diffusion processes. The complex plane plot for such a circuit is given in Figure 2b, where the ohmic resistance is the intercept of the curve with the x-axis, and the kinetic resistance is the diameter of the semicircle. Other parameters that can be obtained by further analysis are the Warburg slope and the capacitance. For a planar electrode the Warburg slope is proportional to $1/CD^{1/2}$ where C is the concentration of diffusing species and D is the diffusion coefficient. This model is satisfactory for simple reactions on planar electrodes but is not adequate for more complicated reactions and for porous or rough electrodes. Several models have been proposed for porous electrodes [10,11], and modeling studies are being carried out for electrodes such as the nickel oxide electrode where the metallic substrate is covered with relatively thick layers of oxides of mixed valences and conductivities [5,12]. Until the models for these electrodes are developed further, we will use some simple equivalent circuits as approximations, first looking at the circuit of Figure 2a.

The high frequency portion of the experimental curves in the complex plane representation often cannot be fit very satisfactorily by a semicircle, especially at higher voltages, as can be seen in Figure 1d. In such cases we have graphically fit the best semicircle to the initial part of the curve. The Warburg slope is interpreted here as an empirical parameter related qualitatively rather than quantitatively to the diffusion resistance, where a higher slope signifies a slower rate of diffusion and a low slope a more rapid rate of diffusion. The capacitance values were also obtained from the original ZPLOT figures by drawing the best semicircles. Plots of the kinetic resistances, Warburg slopes, and capacitances for the electrodes (given in Fig. 3) illustrate that, with the exception of the uncycled electrode, the impedances at the lower voltages are smallest for the electrodes cycled in 26%, which lasted for 30,549 cycles. It is believed that the high values for the other electrodes cycled in 26% KOH are due to their poor condition and that they probably failed by soft shorts. These figures also illustrate the large changes in impedance parameters with voltage. With few exceptions the parameters vary regularly as the voltage is changed.

All but three of the electrodes in this study had been cycled to failure (the electrodes from the cell which had been cycled over 30,000 cycles in 26% KOH before the cell was removed and the uncycled electrode). The fact that the

impedances are different indicates that the impedance parameters are probably not an indication of failure, otherwise they would all be similar.

Intuitively, one would expect that impedances would increase as the number of cycles increases and the cell approaches failure. However, this does not appear to be the case here. The effects of the KOH concentration seem to be more important than the numbers of cycles. We have very little other information about impedance as function of cycle history. Two Ni/Cd cells that have been cycled for 6,500 cycles showed decreases in impedance with cycling up to 1,500 cycles and then stayed fairly constant [13]. However, these cells had been stored for about five years before the measurements were taken, so the effects of storage cannot be separated from the effects of cycling. We have taken measurements on about 18 flightweight Ni/H₂ cells being tested for NASA missions after acceptance and after about 500-800 LEO cycles. It has not been possible to interrupt the cycle test and take further measurements to any extent since then; however, a few measurements indicate that the impedance is increasing somewhat after about 5,000 cycles.

Although some of the cells failed by soft shorts and others by loss of capacity (Table 1), this is not thought to be a major factor. The fact that a cell failed by a soft short does not mean that each electrode in the cell failed in this way, only that at least one electrode of the cell had a soft short. From observations of the physical condition of the electrodes that we tested, we believe that only the ones that had been cycled for 39,000 cycles had soft shorts, those indicated on Figure 3 as being in poor condition. We feel that if these electrodes and the uncycled electrode are excluded, the conclusion that lower impedance is related to longer life and to the KOH concentration is probably valid.

The capacitances obtained from this analysis are very large at the higher voltages and probably reflect not only the double layer capacitances but diffusion factors and any adsorption capacitances. They are obtained from plots of Y'/ω vs Y''/ω where Y' and Y'' are the real and imaginary parts of the complex admittance, i.e., the inverse of the complex impedance. (In a circuit with only one parallel RC circuit and no diffusion elements, the double layer capacitance is obtained unambiguously from this procedure.) If other circuit elements are present, one can consider the capacitance obtained by this method as an "effective capacitance" rather than a true double layer capacitance. As will be seen below, the use of other more detailed circuit models gives similar values for ohmic resistances and kinetic resistances, but the capacitances vary greatly depending on the model.

It is obvious from examination of the curves that a more complicated circuit is needed, particularly at higher voltages. Several circuits have been examined using commercially available programs which use a nonlinear least squares procedure to fit the data (ZFIT-CNRS from Schlumberger Instruments and EQUIVALENT CIRCUIT from Princeton Applied Research). Preliminary estimates of the parameters are required as inputs to these fitting programs, which were obtained in part from the graphical analysis of the data. In an attempt to reduce the subjectivity of the initial analysis of the simple circuit of Figure 2a, the EQUIVALENT CIRCUIT program was used to find the parameters rather than obtaining them from the graphs as before. The experimental and calculated curves are shown in Figure 4 for three voltages for the uncycled electrode. The calculated curves do not fit the experimental curves well, and the parameters derived from

the computer analysis do not show as consistent trends with voltage as did those obtained graphically.

Two other equivalent circuits have been extensively studied [14], and several others have been tried. The circuit in Fig. 5 incorporates two constant phase elements (CPE). These have been suggested for modeling fractal electrodes and for certain cases of diffusion, but the interpretation of this element is still not clearly understood. The calculated curves agree better with the experimental curves as shown in Fig. 6. Many of the parameters, as with the former analysis, do not show a regular trend with voltage. However, the capacitance associated with the CPE element which is in series with the kinetic resistance does increase regularly with voltage and may prove to be a suitable parameter for comparison.

Another equivalent circuit is suggested by examination of the curves in the Bode phase angle plot in Figure 1b. The plateau in the data at 255 mV suggests that a circuit with more than one RC circuit might be a better fit to the experimental curves. Figure 7 gives the circuit used. Again, we can fit the experimental curves more closely (Fig. 8), but the parameters still do not always vary regularly with voltage. Table 3 gives the results of this analysis for the uncycled electrode. Similar results were obtained for the other electrodes. The best parameters for comparison with cycle life so far seem to be the Warburg slopes at the lower voltages from the analysis of the simple circuit, since these can be determined accurately with a minimum of subjective judgement. The capacitance associated with the CPE element of the second circuit may also prove to be useful.

As mentioned above, the double layer capacitances obtained with these more detailed circuit models are much less than the "effective capacitances" obtained with the simplistic model, often by several orders of magnitude, whereas the kinetic resistances obtained by the different models do not vary by more than a factor of two. The double layer capacitance values obtained with the more detailed model of Figure 7 are of the same order of magnitude as those calculated using the BET surface area and are probably a good indication of the true double layer capacitance, since the adsorption and diffusion terms have been separated out. We feel that this latter model is a better physical approximation to the electrode, but because it consists of more elements, a least-squares computer fit requires extremely accurate data which are not always obtainable for these electrodes. One must remember that none of these equivalent circuit models can represent the true situation in the highly complex porous nickel oxide, but in the absence of an adequate theoretical model, a simple model is needed to obtain parameters for comparison of electrodes and cells.

The measurements here are intriguing, but obviously a much larger data base is needed to determine the effects of KOH concentration and cycle life on the impedance. We are planning to carry out experiments with individual electrodes to obtain a more complete set of impedance data as functions of manufacturer, KOH concentration, cycle life, and storage conditions.

SUMMARY

Impedances were measured of electrodes from boiler-plate cells that had been cycled in KOH concentrations from 21% to 36%. These cells had been cycled under double-time LEO conditions at 80% DOD to failure. Cell life ranged from about

1,000 to 40,000 cycles. Measurements were made at five voltages corresponding to low states of charge. The results were analyzed using a simple circuit model including a Warburg impedance term. With the exception of the uncycled electrode and the electrode that is believed to have failed by a soft short, the kinetic resistances and Warburg slopes were greater for those electrodes that had failed earlier after cycling in KOH concentrations other than 26% and were smallest for the electrode that had been cycled for over 30,000 cycles in 26% KOH. The impedances are not an indication of failure since the electrodes had different impedances although they had all been cycled to failure. The results are not conclusive, since in addition to the varying numbers of cycles that the electrodes had been subjected to, the cells had been stored after failure for varying lengths of time, which is known to affect the impedance. In order to minimize the effects of storage, the electrodes were cycled 10 times before the impedance measurements were taken.

Several more detailed circuit models were also tried. The data can be fit more satisfactorily with these, but the parameters obtained have greater scatter and do not correlate as well with the cycle lives as those obtained from the simple circuit. To improve the data base we are initiating a comprehensive study of the effects on the impedance of electrodes as functions of storage conditions, cycle life, KOH concentration, and manufacturer.

REFERENCES

- [1] H.S. Lim and S.Z. Verzwylf, *J. Power Sources*, 22 (1988) 213-220.
- [2] H.S. Lim and S.Z. Verzwylf, *J. Power Sources*, 29 (1990) 503-519.
- [3] M.A. Reid, *Nickel Hydroxide Electrodes* (D.A. Corrigan and A.H. Zimmerman, eds.), *Proceedings Vol. 90-4*, The Electrochemical Society, Pennington, NJ, 1990, pp. 296-310, and *Extended Abstracts of the 176th Electrochemical Society Meeting, Hollywood, FL, 1990*, pp. 117-118.
- [4] A.H. Zimmerman, M.R. Martinelli, M.C. Janecki, and C.C. Badcock, *J. Electrochem. Soc.*, 129 (1982) 289-293.
- [5] S.J. Lenhart, D.D. Macdonald, and B.G. Pound, *J. Electrochem. Soc.*, 135 (1985) 1063-1071.
- [6] R. Haak, C. Ogden, and D. Tench, *J. Power Sources*, 12 (1984) 289-303.
- [7] M.A. Reid, *Proceedings of the 25th Intersociety Energy Conversion Engineering Conference, Reno, NV, Aug. 1990*. Vol. 3, pp. 48-53.
- [8] M.A. Reid, *Impedances of Electrochemically Impregnated Nickel Electrodes as Functions of Potential, KOH Concentration, and Impregnation Method*, NASA TM 103283 (1990).
- [9] M.A. Reid, *Extended Abstracts of the 174th Electrochemical Society Meeting, Chicago, IL, Oct. 1988*, pp. 122-123.
- [10] R. de Levie, *Electrochim. Acta*, 10, 113 (1965).

- [11] H. Keiser, K.D. Beccu and M.A. Gutjahr, *Electrochim. Acta*, 21 (1976) 539-543.
- [12] S. Bhakta, D.D. Macdonald, B. Pound, and M. Urquidi-Macdonald, *Extended Abstracts of the 178th Meeting of The Electrochemical Society*, Seattle, WA, October 1990, p. 114.
- [13] M.A. Reid, *Proceedings of the 2nd SERT Conference*, NASA Lewis Research Center, NASA CP-3056, pp. 197-209; and *J. Power Sources*, 29 (1990) 467-476.
- [14] M.A. Reid and P.L. Loyselle, *Extended Abstracts of the 178th Meeting of The Electrochemical Society*, Seattle, WA, October 1990, pp. 117-118.

TABLE 1. LIFE TEST RESULTS OF Ni/H₂ CELLS AT 80% DEPTH-OF-DISCHARGE

| CELL NO. | [KOH] % | NO. CYCLE TO 0.9 V | NO. CYCLE TO 0.5 V | TOTAL NO. CYCLES | FAILURE MODE |
|----------|---------|--------------------|--------------------|------------------|--------------|
| BP1 | 21 | 5,047 | >38,191 | 38,191 | SOFT SHORT |
| BP2 | 26 | 39,230 | >39,573 | 39,573 | SOFT SHORT |
| BP3 | 26 | 4,329 | 9,241 | 9,241 | LOW EODV |
| BP4 | 31 | 2,979 | 3,275 | 3,286 | LOW EODV |
| BP5 | 31 | 3,620 | 4,230 | 4,230 | LOW EODV |
| BP6 | 36 | 1,268 | 1,845 | 1,845 | LOW EODV |
| BP7* | 21 | 1,037 | 6,508 | 9,402 | LOW EODV |
| BP8 | 26 | >30,549 | >30,549 | 30,549 | REMOVED |
| BP9 | 26 | 23,598 | >24,594 | 24,594 | SOFT SHORT |
| BP10 | 23.5 | 4,803 | 28,495 | 28,495 | SOFT SHORT |

* CYCLED AT 70% DEPTH-OF-DISCHARGE (DOD) FROM 1644 TO 4644 CYCLES AND AFTER 6508 CYCLES.

TABLE 2. VOLTAGES OF Ni/H₂ CELLS CORRESPONDING TO VARIOUS HALF-CELL VOLTAGES.

| Ni vs Hg/HgO | Comparable Ni/H ₂ |
|--------------|------------------------------|
| 0.170 | 1.115 |
| 0.200 | 1.145 |
| 0.255 | 1.200 |
| 0.290 | 1.235 |
| 0.330 | 1.275 |

TABLE 3. IMPEDANCE PARAMETERS AT SEVERAL VOLTAGES OBTAINED BY ANALYSIS WITH CNLS AND ZFIT

| V vs Hg/HgO | 0.330 | 0.290 | 0.255 | 0.200 | 0.170 |
|-------------------------|--------|---------|--------|-------|--------|
| R _{kin} /Ω | 0.0052 | 0.00073 | 0.057 | 0.048 | 0.118 |
| C _d / F | 1.19 | 3.65 | 0.48 | 0.43 | 0.5 |
| R _{adsorp} /Ω | 0.0066 | 0.00087 | 0.0078 | 0.011 | 0.0097 |
| C _{adsorp} / F | 41 | 75 | 123 | 3.7 | 350 |
| R _{difl} /Ω | 0.17 | 0.15 | 0.56 | 0.59 | 1.00 |
| T | 479 | 436 | 420 | 443 | 477 |
| Phi | 0.70 | 0.67 | 0.65 | 0.63 | 0.61 |

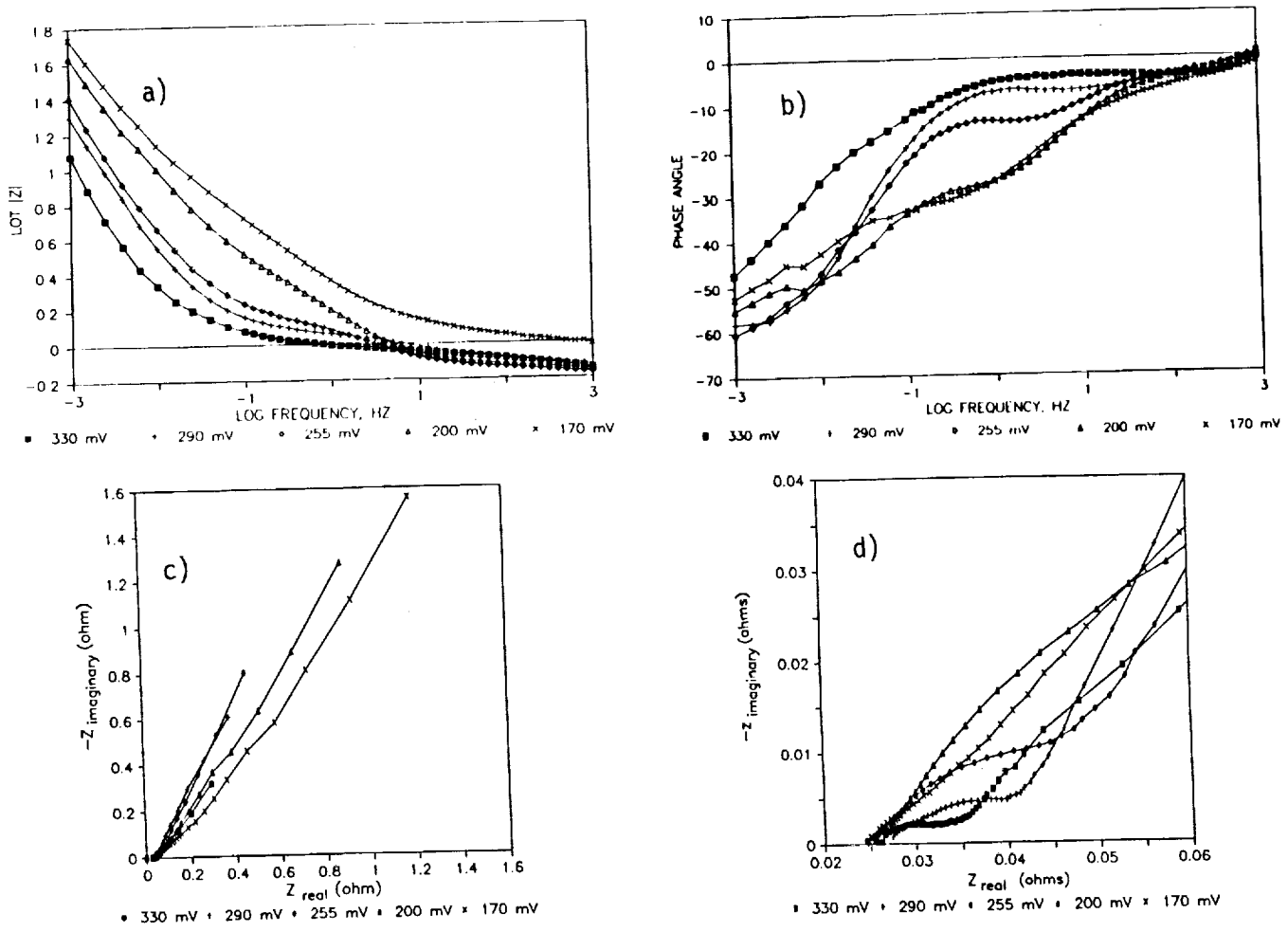


Fig. 1 Changes of Impedance with Voltage for Electrode Cycled 30,549 Cycles in 26% KOH. (a) Bode Magnitude Plot, Normalized Data. (b) Bode Theta Plot. (c) Complex Plane Plot. (d) Expanded High Frequency Portion of Complex Plane Plot. (c) and (d) are Nonnormalized Data. Electrode Area = 27.9 cm².

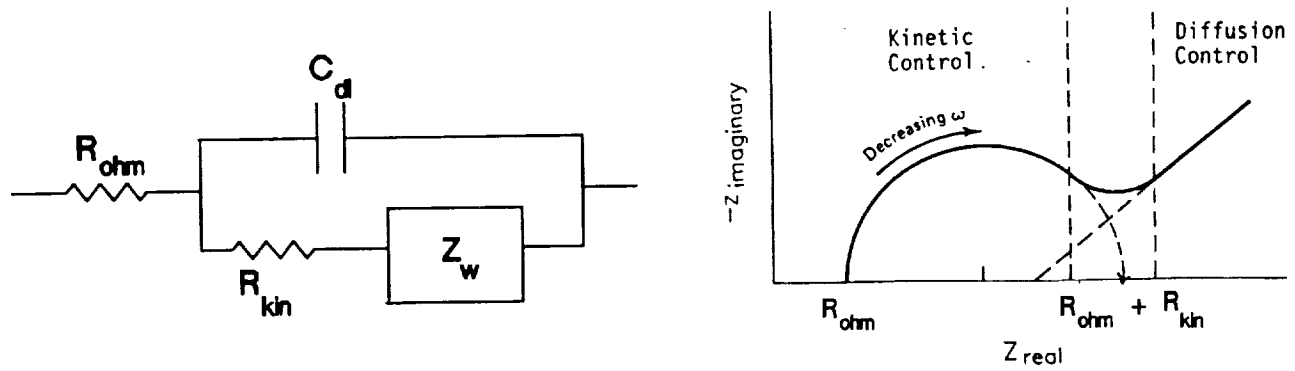


Fig. 2 (a) Simple Circuit Used for Initial Analysis of Impedance Data. (b) Complex Plane Plot for Typical Circuit of Figure 2a.

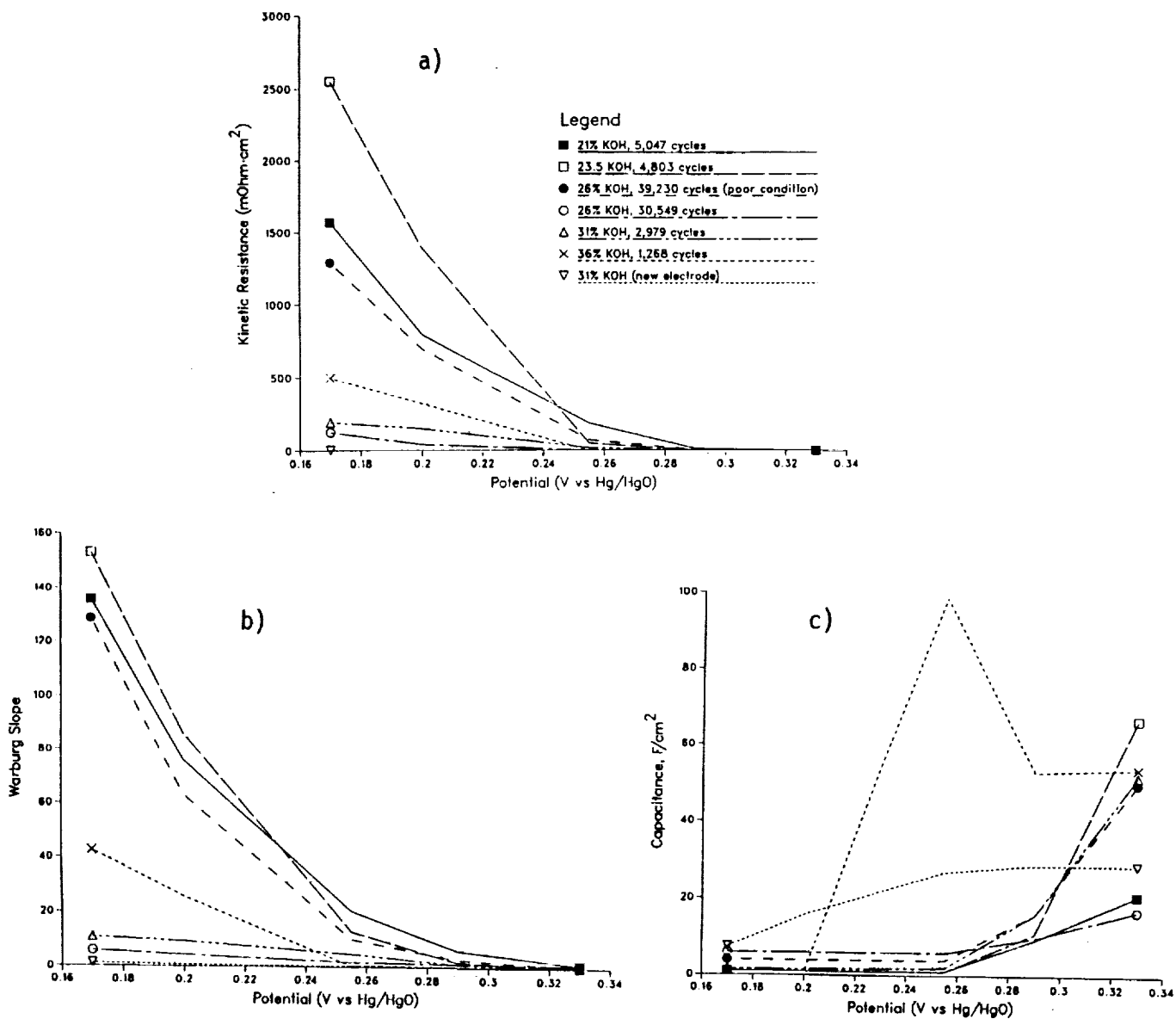


Fig. 3 Impedance Parameters for Various Electrodes Obtained from Graphical Analysis Using Circuit of Fig. 2. All Parameters are Normalized. (a) Kinetic Resistances, (b) Warburg Slopes, (c) Capacitances.

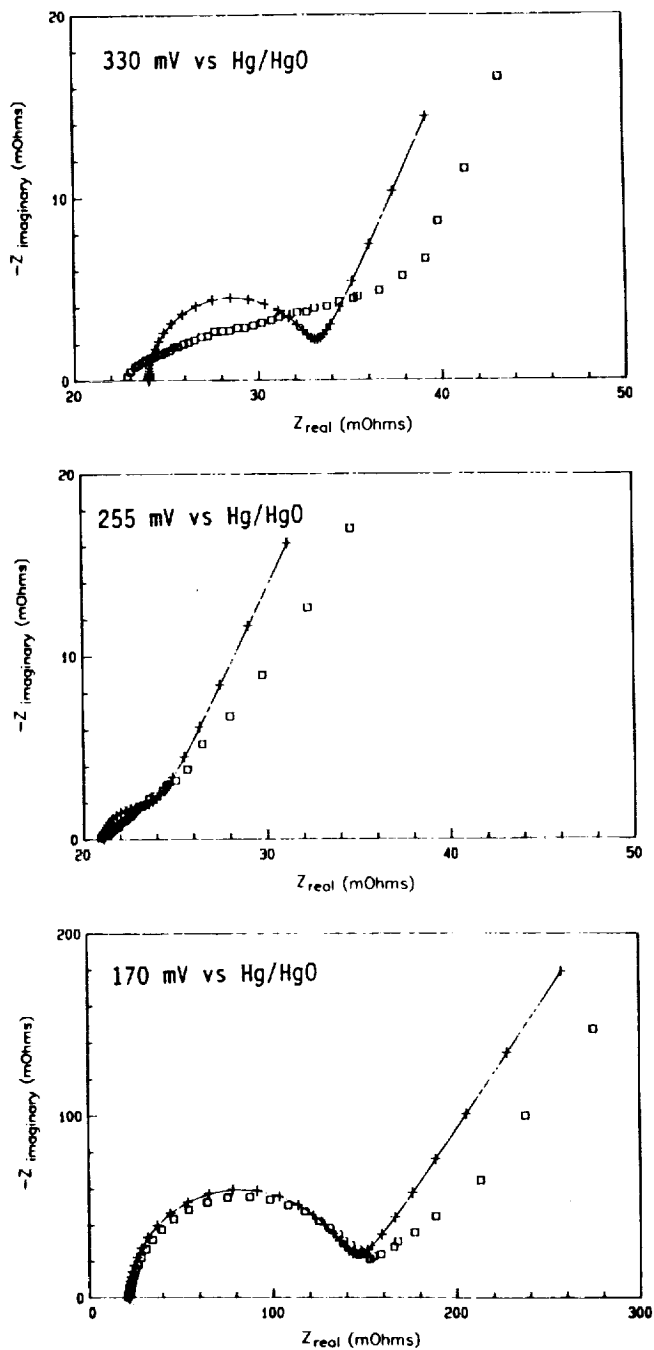


Fig. 4 Comparison of Some Experimental and Simulated Complex Plane Plots Using Best Parameters Obtained Using EQUIVALENT CIRCUIT Program and Circuit of Fig. 2(a). Uncycled Electrode. \square , Experimental; +, Simulated.

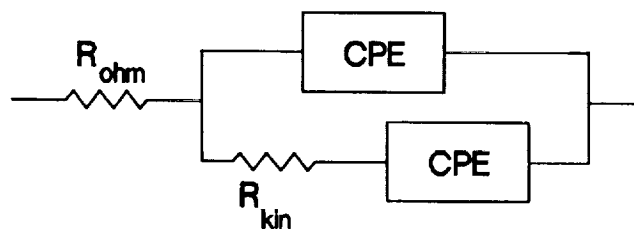


Fig. 5 (a) Circuit with Two Constant Phase Elements Used for Further Analysis of Data.

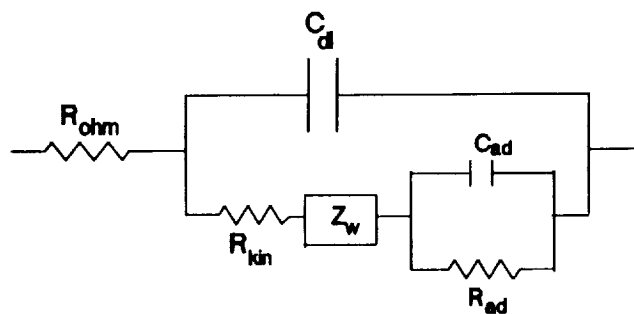


Fig. 5 (b) Circuit Incorporating Adsorption Capacitance and Resistance for Further Analysis of Data.

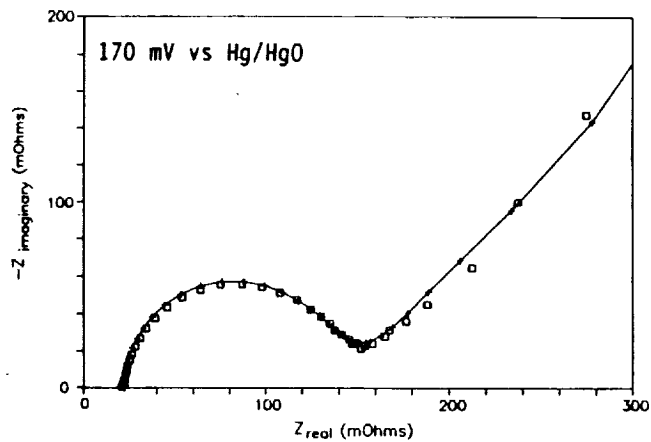
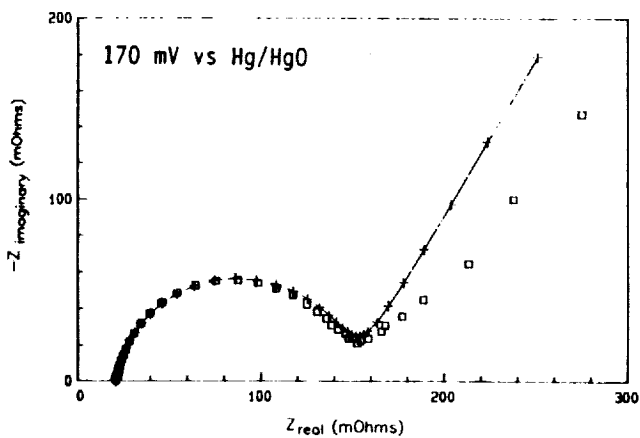
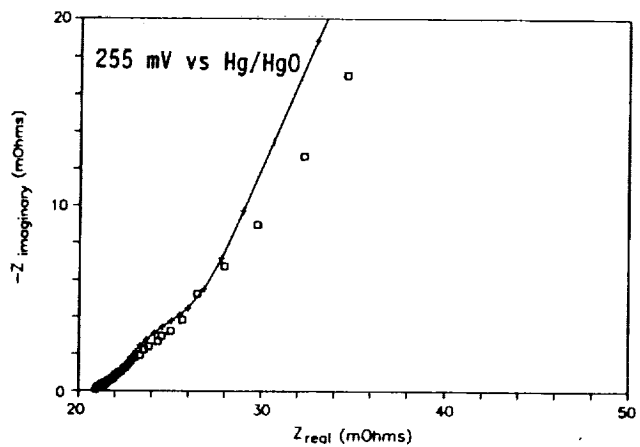
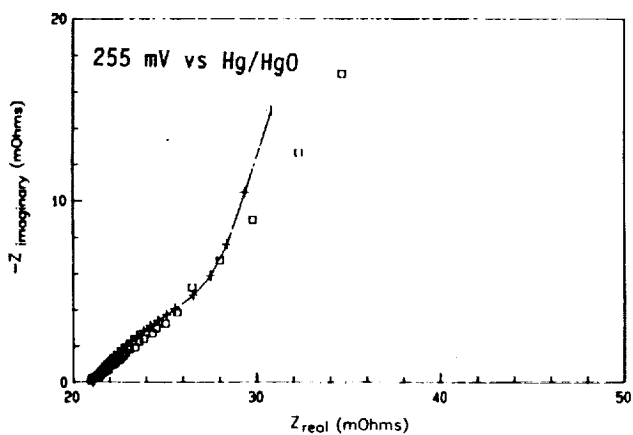
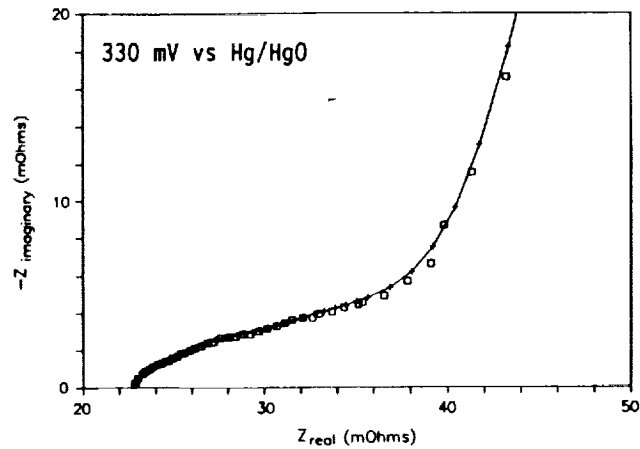
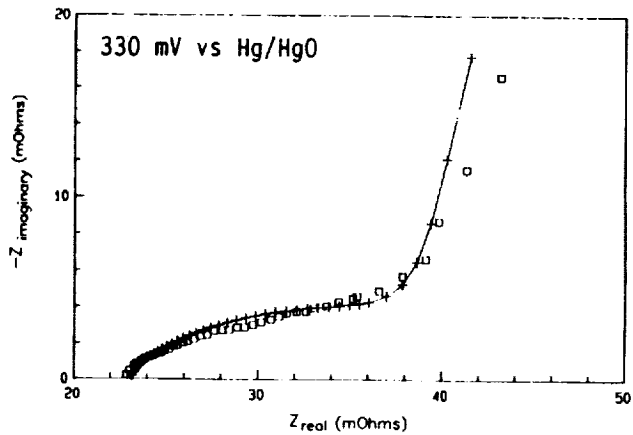


Fig. 6 Same as Fig. 4 Using Circuit of Fig. 5(a).

Fig. 7 Same as Fig. 4 but Using ZFIT-CNLS Program and Circuit of Fig. 5(b).

HIGH ENERGY EFFICIENCY AND HIGH POWER DENSITY PROTON EXCHANGE MEMBRANE FUEL CELLS — ELECTRODE KINETICS AND MASS TRANSPORT

Supramaniam Srinivasan, Omourtag A. Velev, Arvind Parthasarthy,
David J. Manko, and A. John Appleby
Center for Electrochemical Systems and Hydrogen Research
Texas Engineering Experiment Station
Texas A & M University System
College Station, Texas 77843-3402

The development of proton exchange membrane (PEM) fuel cell power plants with high energy efficiencies and high power densities is gaining momentum because of the vital need of such high levels of performance for extraterrestrial (space, underwater) and terrestrial (power source for electric vehicles) applications. Since 1987, considerable progress has been made in achieving energy efficiencies of about 60% at a current density of 200 mA/cm² and high power densities (> 1 W/cm²) in PEM fuel cells with high (4 mg/cm²) or low (0.4 mg/cm²) platinum loadings in electrodes. This article focuses on (1) methods to obtain these high levels of performance with low Pt loading electrodes - by proton conductor impregnation into electrodes, localization of Pt near front surface; (2) a novel microelectrode technique which yields electrode kinetic parameters for oxygen reduction and mass transport parameters; (3) demonstration of lack of water transport from anode to cathode; (4) modeling analysis of PEM fuel cell for comparison with experimental results and predicting further improvements in performance; and (5) recommendations of needed R&D for achieving the above goals.

1. HIGH ENERGY EFFICIENCY AND HIGH POWER DENSITY FUEL CELL SYSTEMS

1.1 Vital Needs, Essential Criteria, and Candidate Fuel Cells

High energy efficiency and high power density fuel cells are vitally needed for extra-terrestrial (space, underwater) and terrestrial (electric vehicles, stand-by or remote power, portable power source) applications to minimize fuel consumption, weight, volume, and capital cost of power plants. The relative importance of energy efficiency and of power density depends on the application. In some cases, as for example, for a hydrogen energy storage system to be coupled with photovoltaic power plants for NASA's long lunar and Mars missions (14 days of darkness, 14 days of light), the energy efficiency is more critical than the power density because the weight of the energy storage sub-systems exceeds that of the fuel cell power conversion system by more than a factor of five. For military applications, where pulsed power is required, the power density is the over-riding factor. For the terrestrial transportation application, both the energy efficiency and power density have to be as high as possible.

The essential criteria for the attainment of high energy efficiencies and high power densities in fuel cells are (i) low activation overpotentials which can be achieved by (a) using electrocatalysts with high exchange current densities for the oxygen reduction (ORR) reaction (the exchange current density for the hydrogen oxidation reaction is sufficiently high and thus activation overpotential losses due to this electrode reaction are minimal in all types of fuel cells); and (b) maximizing the electrochemically active surface areas; (ii) minimal mass transport overpotential, for example, by optimization of electrode structure to accelerate the transport of reactants to and products away from the active sites; and (iii) low ohmic overpotentials, for example, by minimization of the thickness of electrolyte layer and use of membranes with higher proton conductivities. All forms of overpotential can be reduced by operation at elevated temperatures and pressures. The fundamental limitation in fuel cells operating at low to intermediate temperatures (i.e., fuel cells with alkaline, phosphoric acid, proton exchange membrane electrolytes) is the

low exchange current density for the oxygen reduction reaction, while in the higher temperature systems (molten carbonate and solid oxide), mass transport and ohmic overpotentials impede the attainment of high energy efficiencies and high power densities. In order to achieve high power densities, it is vitally important to minimize mass transport and ohmic overpotentials [1,2].

The phosphoric acid fuel cell system, which is the most advanced fuel cell technology and close to commercialization for terrestrial applications, suffers from the problems of slow oxygen electrode kinetics, compared to that in alkaline and solid polymer electrolyte fuel cells. Thus, this system does not show promise for attainment of high energy efficiencies and high power densities. The molten carbonate and solid oxide fuel cells exhibit good oxygen electrode kinetics at the high operating temperatures of 650°C and 1000°C, respectively. However, the mass transport and ohmic problems are quite severe in these systems, thus making it difficult to attain both high energy efficiencies and high power densities. The only systems in which high energy efficiencies and high power densities have been simultaneously demonstrated are the alkaline and proton exchange membrane (PEM) fuel cells.

1.2 Demonstration of High Power Densities in Alkaline and Proton Exchange Membrane Fuel Cells

Significant progress has been made in achieving high energy efficiencies and high power densities in alkaline and proton exchange membrane fuel cells, particularly because (i) the ORR is considerably faster in these electrolytes than in any other electrolytes; (ii) the structures of the porous gas diffusion electrodes have been optimized to minimize mass transport overpotential; and (iii) very thin electrolyte layers are used to reduce ohmic overpotentials to negligible values. International Fuel Cells (IFC) has demonstrated that in advanced alkaline fuel cells the cell potential is as high as 1.0 V at 100 mA/cm² while it is 0.5 V at 8 A/cm² [2]. The high performances of the PEM fuel cells at Ballard Power Systems (BPS) may be represented by a cell potential of 0.9 V at 100 mA/cm² and 0.5 V at 6 A/cm² [3]. In the IFC and BPS fuel cells, the noble metal loading in the electrodes is quite high (≥ 4 mg/cm²). Relatively high energy efficiencies and high power densities in PEM fuel cells with low platinum loading (≈ 0.4 mg/cm²) electrodes (necessary for transportation applications) were demonstrated first at Los Alamos National Laboratory (LANL) and later at Texas A&M University (TAMU) by Srinivasan and coworkers [4,5]. The best performance, reported by these workers to date, is 0.88 V at 100 mA/cm² and 0.62 V at 2 A/cm². In all the above cases, the pristine gases H₂ and O₂ were used as reactants. When using H₂/Air as reactants in the fuel cells with low platinum loading electrodes, the cell potential at 100 mA/cm² was 40 mV (the theoretical value) lower and at 2 A/cm² was 250 mV lower than when H₂/O₂ were used as reactants - the deviation from the theoretically expected value of 40 mV starts to occur at about 1.5 A/cm².

1.3 Methods of Attainment of High Power Densities in Proton Exchange Membrane Fuel Cells with Low Platinum Loading Electrodes

1.3.1 Extension of Three-Dimensional Reaction Zone by Impregnation of Proton Conductor into Active Layer of Electrode and Hot-Pressing of Electrode to Proton Conduction Membrane

An ingenious method, which was developed by Raistrick [6] to extend the three-dimensional reaction zone, is the impregnation of a proton conductor (say, Nafion®) into the active layer of the electrode (say, Prototech electrode with a platinum loading of 0.4 mg/cm²). In this work, it was shown that such an electrode, mechanically pressed to a Nafion® membrane, exhibited a considerable improvement in oxygen reduction kinetics, as compared to that at an unimpregnated electrode/Nafion® interface. However, the first demonstration of high power densities in fuel cells with such impregnated electrodes was by Srinivasan, Ticianelli, Derouin, and Redondo [7], who found it necessary to hot-press the electrodes onto the proton conducting membrane at a slightly higher temperature than the glass-transition temperature of the membrane and at a pressure of about 15 atm. Fig. 1(a) and (b) illustrate the significant improvement in cell performance and the increase in electrochemically active surface area respectively by Nafion® impregnation of the electrode. These figures also demonstrate the comparable

performances and electrochemically active surface areas of single cells with high platinum loading and Nafion® impregnated low platinum loading electrodes.

1.3.2 Localization of Platinum Near Front Surface to Minimize Activation, Mass-Transport, and Ohmic Overpotentials

From the cyclic voltammetric results, shown in Fig. 1(b), as well as from Rutherford Back Scattering experiments on a cross-section of the electrodes, it was shown that the proton conductor penetrates only about 10 μm within the front surface. The active layer thickness in the state-of-the-art low platinum loading electrodes (say, from Prototech or ETEK) is about 100 μm . These electrodes contain 10% Pt on carbon supports. In order to minimize activation, mass transport and ohmic overpotentials, which is vital for the attainment of high energy efficiencies and high power densities, Srinivasan and coworkers utilized (i) custom-made fuel cell electrodes with 20% or 40% (instead of 10%) platinum on carbon, while maintaining the same platinum loading (0.4 mg/cm^2); and (ii) sputter-deposited a thin layer of platinum (0.05 mg/cm^2) on the front surface of these electrodes [4]. The results of these studies, which are presented in Fig. 2 and Table 1 signify that (i) the platinum utilization of the electrodes is improved; and (ii) current densities of 1 A/cm^2 at a cell potential of 0.6 V can be achieved. It has recently been shown [5] that electrodes with thin layers of platinum, deposited using chemical or electrochemical techniques, yield performances close to those of the sputter-deposited electrodes (Fig. 3).

1.3.3 Use of Thinner and Alternate Membranes

In most studies, which have been reported, DuPont's Nafion® 117 membranes (thickness of 175 μm) have been used. To minimize ohmic and mass transport overpotentials in the membrane of a PEM fuel cell, two approaches, which were taken at LANL and TAMU, are the use of (i) thinner Nafion® membranes; and (ii) Dow® membranes with lower equivalent weight. Typical results are presented in Fig. 4. The cell with the 50 μm thick Nafion® membrane exhibits the highest cell potential at 2 A/cm^2 . However, the open-circuit potential in this cell was 50-100 mV lower than in the cells with the other membranes because of cross-over of the hydrogen gas. The cross-over effect is also reflected by a lower potential in the cell with the 50 μm thick membrane than in the cell with a 175 or 100 μm thick membrane, at low current densities. The cell with the Dow® membrane, 125 μm thick, showed the next best result. Due to its lower equivalent weight than that of Nafion®, it has a better conductivity and water retention capability. It is also striking that the cells with the Nafion® membrane (thicknesses 100 and 175 μm) encounter mass transport limitations at higher current densities but the cell with the Dow® membrane does not.

2. OXYGEN ELECTRODE KINETICS AT PLATINUM/NAFION® INTERFACE

2.1 Tafel Parameters on Microelectrode from Slow Potential Sweep and Electrochemical Impedance Spectroscopic Experiments

The objectives of this work [8] were to determine the electrode kinetic parameters for the reduction of oxygen at the Pt/Nafion® interface under totally solid state conditions (i.e., no contacting liquid electrolyte phase). Thus, these investigations were carried out under the same conditions as in a practical fuel cell. The concentration and diffusion coefficient of oxygen in Nafion® were also determined. Earlier studies of the platinum/solid polymer electrolyte interface using platinum gauze electrodes indicated that kinetic information was masked by large contributions from ohmic and mass transport effects [9]. Such problems were addressed in this investigation by using a novel solid state cell, incorporating a platinum microelectrode (Fig. 5). Cyclic voltammetric and potentiostatic transient measurements were made at the Pt/Nafion® interface. From the high scan rate cyclic voltammetric experiments, the purity of Nafion® and of the electrode was ascertained and the roughness factor of the electrode was calculated. The slow sweep experiments yielded the Tafel parameters for oxygen reduction. From the two-section Tafel plot (Fig. 6),

the exchange current densities were calculated and found to be higher than those obtained at any other Pt/acid interface. The electrode kinetic parameters obtained therefrom are presented in Table 2.

These results were also substantiated by electrochemical impedance spectroscopic (EIS) investigations [10]. A typical impedance plot (Nyquist plot) at the open-circuit potential is shown in Fig. 7. From the charge transfer resistance R_{ct} at this potential, one can calculate the corrosion current density according to the Eq.

$$R_{ct} = \frac{RT}{n i_{corr} F} \quad (1)$$

The corrosion current density (i_{corr}) corresponds to the current density for oxygen reduction, as well as that for the platinum oxide formation, at the open-circuit potential. From EIS measurements over a range of potentials and a plot of $\log R_{ct}$ vs. current density, the Tafel slope which was obtained was found to agree with the results of the pseudo-steady state method (Table 2). From the values of i_{corr} and Tafel slope, the exchange current density for oxygen reduction on the platinum microelectrode was calculated; its value was consistent with that obtained by the pseudo-steady state method (Table 2).

2.2 Tafel Parameters on Fuel Cell Electrodes from Galvanostatic Measurements

Electrode kinetic studies of oxygen reduction in PEM fuel cells (single cells) have been conducted at LANL since 1986 and at TAMU since 1988. A systematic study of ORR in fuel cells, as a function of temperature and pressure was recently carried out at TAMU. The fuel cell electrodes contained either high (4-10 mg/cm²) or low (\approx 0.4 mg/cm²) platinum loadings. The plot of the potential of the oxygen electrode, with respect to the reversible hydrogen electrode potential, as well as that of the single cell versus the current density fits the Eq.

$$E = E_0 - b \log i - Ri \quad (2)$$

where $E_0 = E_r + b \log i_0$ (3)

and E_r is the reversible potential for the half or single cell; i_0 and b are the exchange current density and Tafel slope for the ORR and R represents the resistance (predominantly ohmic as well as the charge transfer resistance for the hydrogen electrode) which causes a linear variation of the potential with current density. The Tafel plots for ORR in single cells with high and low platinum loading electrode at 50°C are presented in Fig. 8. From such plots, the exchange current densities (based on geometric areas of electrodes) and Tafel slopes were determined. In these experiments, cyclic voltammograms were also recorded on the electrodes; from the coulombic charge required for hydrogen adsorption or desorption, the electrochemically active surface areas and hence of the roughness factors of the electrodes were calculated. Using these roughness factors, the exchange current densities, based on the real surface area of the electrode were obtained. Table 2 also illustrates a comparison of the electrode kinetic parameters for ORR on fuel cell electrodes at 50°C and on the microelectrodes at 25°C. The fuel cell electrodes exhibit only the low Tafel slope, 60 mV/decade, because even at the high current density of 2 A/cm² (based on geometric areas of the electrode) the half cell potential is still in the platinum oxide covered region, where the low Tafel slope is observed on smooth platinum microelectrode. The exchange current densities (based on the real surface area of the platinum) are nearly the same on the fuel cell electrode and on the microelectrode. More details of this work, including that of the effects of pressure and temperature will be published shortly [11].

3. MASS TRANSPORT AND OHMIC PHENOMENA

3.1 Oxygen Solubility and Diffusion Coefficient in Proton Exchange Membrane from Microelectrode Experiments

The microelectrode technique is a unique method for determining the electrode kinetic parameters (as described in Section 2.1) and mass transport parameters. It involves chronoamperometry - the potential of the microelectrode is stepped from a value where no oxygen reduction occurs (open-circuit potential) to that at which oxygen reduction occurs at the limiting current density. According to microelectrode theory [12], the dependence of the current density (i) on time (t) for such an experiment follows the Eq.

$$i = \frac{nF\pi^{1/2}D^{1/2}C r^2}{t^{1/2}} + \pi nFD Cr \quad (3)$$

where n is the number of electrons transferred in the overall reaction ($n = 4$ for ORR); D and C are the diffusion coefficient and solubility of oxygen in the PEM; and r is the radius of the microelectrode. Thus, a plot of the i vs. $t^{-1/2}$ is linear and from the values of the slope and of the intercept, the diffusion coefficients and solubilities can be easily calculated. It must be noted that this is not the case when transient methods (AC impedance, cyclic voltammetry) are used on macroelectrodes. In these cases, only the product $D^{1/2}C$ is obtained and unless some other method can be used to find D or C independently, the two values cannot be individually determined. A typical plot of i vs. $t^{-1/2}$ for ORR on Pt in Nafion® is shown in Fig. 9 [8]. The values of the diffusion coefficient and solubility, calculated from this plot are presented in Table 3. The difference between these values and those reported by other workers are probably due to different experimental conditions - water content of membrane, measurements with other acids in membrane, etc.

3.2 Dependence on Temperature and Pressure

Both the temperature and pressure of operation of the cell have a significant influence on its performance. The effect of temperature on performance is illustrated in Fig. 10 for four temperatures from 50°C to 95°C at a pressure of 5 atm. The slope of the linear region of the cell potential vs. current density plot decreases, which is indicative of a lowering of the internal resistance of the cell; this decrease is predominantly due to the decrease ohmic resistance of the electrolyte. Further, the plots show that mass transport losses are also significantly reduced at the higher temperature, as seen by the extension of the linear region with increase of temperature. The mass transport limitations are caused by the slow diffusion of the reactants through the PEM to the active platinum sites and the slow transport of protons from the anode to the cathode. At a temperature of 95°C and pressure of 5 atm, it has recently been shown in our laboratory that the linear region extends to over 3 A/cm², indicating that the mass transport limitations are minimal up to this current density.

3.3 Dependence on Cathodic Reactant - Oxygen vs. Air

By necessity, the source of oxygen for terrestrial applications is air and it is the pure gas (cryogenic or compressed gas) for extraterrestrial (space, underwater) applications. Experiments using both these gases in single cells, operating in the temperature range of 25°C to 95°C and at pressures from 1 to 5 atm, show the striking influences of mass transport phenomena in the cell and half cell potential vs. current density plots (Fig. 11 and 12). Fig. 11 demonstrates the effect of pressure at 50°C, while Fig. 12 represents the effect of temperature, at a pressure of 5 atm on the cell potential vs. current density plot using H₂/O₂ and H₂/Air as reactants. Two effects are apparent on passing over from oxygen to air as the cathodic reactant: (i) the slope of the linear region of the E- i plot is 50% higher; and (ii) deviations from

the linear region are visible at lower current densities. In the higher temperature fuel cells (phosphoric, molten carbonate, solid oxide) the oxygen gain in potential is constant at all current densities in the linear region and thus the slopes of the E-i plot are the same with H₂/O₂ and H₂/Air as reactants. The dependence of the slope of the E-i line on the oxygen partial pressure is indicative of mass transport limitations, which also cause a linear variation of E with i at lower current densities. It is very probable that there is a "nitrogen barrier layer effect" which causes this mass transport limitations. In a previous study, it was also shown that the dependence of the cell potential (E_P) on pressure (P) at a constant current density may be expressed by the Eq.:

$$E_P = E_1 + b \log P \quad (4)$$

where E₁ is the cell potential at 1 atm and b is the Tafel slope for the reaction. The derivation of this equation is based on a reaction order of unity for the ORR. This equation is valid over the entire region of P, investigated with oxygen but at pressures between 1 and 1.5 atm there is a more rapid increase of E with P, when using air.

The second effect, i.e., deviations from the linear region of the E vs. i plot at lower current densities with air than with oxygen is clearly due to the effect of partial pressure of oxygen. The "nitrogen barrier layer effect" could still play a role. A challenge is to be capable of operating a cell at least at 2 A/cm² and a cell potential above 0.5 using steam-reformed hydrogen and air as reactants. Optimization of the structure of the electrode to minimize mass transport limitations is essential.

3.4 Dependence on Thickness and Conductivity of Membrane

The spade work on proton exchange membrane fuel cells has been carried out using DuPont's Nafion® 1100 as the electrolyte layer. Nafion® membranes, with different thicknesses (50, 100 and 175 μm) have been incorporated as the proton exchange membrane in single cells and their performances determined (see Section 1.3.3). As one may expect, the thinner the membrane, the lower is the slope of the linear region of the cell potential vs. current density plot (Fig. 4). However, another significant effect is that mass transport limitations are greatly reduced or even eliminated by using thinner membranes. The mass transport effects are clearly due to phenomena within the membrane - water and/or proton transport.

The emerging proton exchange membrane for fuel cells is the one with a lower equivalent weight, manufactured by Dow Chemical Company than that of Nafion® 1100. The chemical structures of the DuPont and Dow membranes are illustrated in Fig. 13. The presence of more sulfonic acid groups per CF₂ in the Dow membrane than in Nafion® enhances the electrolyte conductivity and water retention capability. A well humidified membrane in PEM fuel cells is vital as otherwise (i.e., drying out) problems of increase in electrolyte resistance and consequent loss in performance are encountered. Fig. 4 also shows that the cell with the Dow membrane (thickness 125 μm) shows a lower slope in the linear region of the E-i plot than that in the cell with the Nafion® membrane (thickness 100 μm). Further, mass transport limitations are visible at high current densities in the latter but not in the former cell. The higher conductivity and the better mass transport (proton and water) capabilities of the Dow membranes are reflected in Fig. 4.

3.5 Evidence for Lack of Net Water Transport from Anode to Cathode

It has been reported that in the PEM fuel cell, a proton crossing the membrane carries with it four to six water molecules. In the present study, the amount of water transported across the membrane during the cell operation was measured in order to evaluate more accurately the mass balance conditions in the cell [13]. A PEM fuel cell with a 50 cm² electrode geometric area was used in the experiments with two different types of proton conducting membranes - Nafion® from DuPont and Dow experimental type. The electrodes used in this study were supplied from Prototech, Inc., and contained 20% Pt on carbon (0.4 mg/cm²) on a carbon cloth substrate. Details of the experimental set up are published elsewhere [5].

In these experiments, the oxygen gas entering the cell was dry. The hydrogen gas was saturated with water vapor. The gas exiting the cell from the cathode chamber was passed through a condenser consisting of a copper spiral immersed in iced-water. The water exiting the condenser was collected and its rate calculated. The results of experiments with a Dow experimental type membrane (125 μm thick) are presented in Fig. 14. The solid line presents the rate of water production corresponding to Faraday's law. The points represent the experimentally measured collection rates. At low current densities, the measurements are not very accurate because of the long period of time needed to collect measurable amounts of water. As can be seen from Fig. 14, the amount of water produced at atmospheric pressure and 50°C corresponds to Faraday's law. There are two possible explanations for this effect. The first is that there is no water transport across the membrane and that the proton transport is by a hopping mechanism (Grothus conduction). The second one is that due to the concentration gradient of water, which will be set up during current flow, the back-diffusion of water compensates for the water molecules dragged with the protons. The first explanation is the most likely one. Experiments are underway to determine if there is water transport across the membrane at higher operating temperatures and pressures (3-5 atm), which are necessary to attain the high power densities required of fuel cells for transportation, space and defense applications.

4. PROGNOSIS OF ATTAINABLE ENERGY EFFICIENCY AND POWER DENSITIES

4.1 Best Performances Obtained With High and Low Platinum Loading Electrodes

The cell potential vs. current density plot up to the end of its linear region fits equation (2). In Table 4 are presented the values of E_0 , b and R , evaluated by nonlinear least squares fits to the experimental points, for the cells exhibiting high levels of performance: cells with (i) high platinum loading (10 mg/cm^2), electrodes and 125 μm thick Dow membranes (Fig. 15); (ii) low platinum loading electrodes and 125 μm thick Dow membranes (Fig. 4); and (iii) low platinum loading electrodes and Nafion® membranes with thicknesses of 100 or 175 μm (Fig. 4). Also in Table 4 are presented the current densities at a cell potential of 0.9 V. All these cells were operated at 85°C and 5 atm pressure. Table 4 illustrates that E_0 is generally approximately equal to 1.0 V, b is between 0.05 and 0.06 V/decade and R is between 0.1 and 0.2 ohm cm^2 . The electrochemically active surface area is about 10 times higher for the high platinum loading than for the low platinum loading electrode, even though the platinum content in the former case is 20 times higher than in the latter. The effective utilization of the platinum is about 5% for the cell with the high platinum loading electrodes and about 10% for the ones with low platinum loading electrodes. It is also worthwhile noting that the current density in the predominantly activation-controlled region, based on the electrochemically active surface area of the electrodes, is approximately the same for the cells with the high and low platinum loading electrodes. In order to attain high power densities, the value of R has to be as low as possible, as in the case 125 μm thick Dow membrane.

4.2 Prediction of Performance Improvements - Modeling Analysis

Since Eq. 2 is quite representative of the cell potential vs. current density plot up to the end of the linear region, a simplified modeling analysis was carried out to determine the effects of the parameters E_0 , b and R . The results of this analysis are presented in Fig. 16(a) to 16(c). Figure 16(a) shows that increase of the value of E_0 (for constant b and R values) causes a parallel shift of the cell potential vs. current density plot and thus for a 50 mV increase, the energy efficiency is increased by about 4%. This figure also shows that the power density can be significantly improved by higher values of E_0 . However, the power density is also influenced by the value of R . For $R = 0.1 \text{ ohm cm}^2$, which value was used for the plots in Fig. 16(a), the current density at a cell potential of 0.8 V increases by a factor of only two for E_0 increasing from 1.0 V to 1.05, whereas it will be close to two orders of magnitude higher if R were equal to zero (i.e., when fuel cell is only activation-controlled). It must be noted that E_0 is expressed by Eq. 2 and hence the basic parameter which determines E_0 is the exchange current density for the ORR (based on the geometric area of the electrode). Two possible approaches to increasing i_0 are (i) finding

better electrocatalysts; and (ii) increasing the effective utilization of platinum. E_0 can also be increased by increasing value of E_r the thermodynamic reversible potential. Operation at higher pressures is the only way of obtaining a higher E_r . The Nernst Eq. shows that for a ten fold increase of pressure, E_r increases for the hydrogen/oxygen fuel cell by 45 mV.

According to Eq. 2 if the current density is expressed in mA/cm², E_0 is the value of E at 1 mA/cm² (geometric). At this current density the contribution of ohmic overpotential to the cell potential is negligible. The current density, based on the electrochemically active surface area of the electrode is about fifty times lower for the cell with the low platinum loading electrodes and 500 times lower for the one with high platinum loading electrodes. At these low values of current densities, the value of E_0 will be very close to the open circuit potential. The open circuit potential is a mixed potential involving oxygen reduction (and to a small extent platinum dissolution) as the cathodic reaction and the platinum oxide formation as the anodic reaction. When using carbon in the active layer of the electrode, as with supported electrocatalysts, the electrochemical oxidation of the carbon also influences the open circuit potential. This is one of the main reasons for the E_0 values being lower for electrodes with supported than with unsupported electrocatalysts. A problem, which may thus arise by attaining higher E_0 values, is that the rates of the above mentioned anodic reactions will increase and cause degradation of structure of electrode and hence of performance.

Fig. 16(b) shows the effect of variation of Tafel slope for the ORR on the cell potential vs. current density plot. The values of the Tafel slope chosen are in the range of those experimentally observed. The lower the Tafel slope, the better is the performance and it is more significant at higher current densities because the slope of the cell potential vs. current density plot increases with increase of Tafel slope. The Tafel slope of 60 mV/decade is representative of oxygen reduction on the oxide covered platinum in acid medium [14], including the PEM [8]. Tafel slopes, lower than the assumed values, have rarely been observed for oxygen reduction. One can expect lower Tafel slopes if an intermediate step, further down the reaction sequence, say after 2 of the 4 electrons have been transferred to the oxygen molecule, is the rate-determining step [15]. An alternative mechanism which could yield low Tafel slopes is via redox catalysis which may be possible by use of alloys such as PtCr, PtCo, PtNi, etc., where the electrochemical reaction is the reduction of the transition metal ion from a higher valence state to a lower one and oxygen chemically oxidizes the lower valent metal ion to the higher one.

The most difficult challenge in achieving higher power densities is exemplified in Fig. 16(c), i.e., the marked effect of R, which represents the effective resistance causing a linear variation of overpotential (predominantly ohmic) with current density. As stated in Section 3.4, the best performance has been achieved in the single cell with the Dow membrane and hence in Fig. 16(c), the highest R value used is that for the best performing cell (Fig. 4). The other extreme is for the case when $R = 0$, which is a hypothetical case, where the overpotential loss is only due to activation control of the ORR. The intermediate value chosen is $R = 0.08$ ohm cm². The corresponding values of the cell potential at a current density of 2 A/cm² are 0.80, 0.60 and 0.64 V, respectively. The assumption that $R = 0$ is invalid because R includes at least the contributions of the ohmic resistance of the electrolyte layer and of the charge transfer resistance of the hydrogen oxidation reaction. Further, it will be extremely difficult to completely eliminate resistances of contacts, fixtures, including bipolar plates in multi-cell stacks. Assuming that (i) these resistances are negligible; (ii) the electrolyte resistance is 0.05 ohm cm² (using a specific resistance of 5 ohm cm and thickness of the 100 μm for the electrolyte); and (iii) the charge transfer resistance for hydrogen oxidation is 0.025 ohm cm² (which is the best value obtained in our laboratory, the total value of R is 0.075 ohm cm² (i.e., very close to the assumed intermediate value of 0.08 ohm cm²). This brief analysis gives a realistic estimate of a cell potential of 0.64 V at a current density of 2 A/cm², corresponding to an energy efficiency of 43% and a power density of 1.28 W/cm² (assuming $E_0 = 1.0$ V and $b = 0.055$ V/decade). The maximum power density for this cell will be about 3 W/cm². If, however, E_0 is 1.10 V instead of 1.0 V, the cell potential will increase to 0.74 V at 2 A/cm² and thus the energy efficiency and power density at this current density will be 50% and 1.48 W/cm².

Fig. 16(d) shows the validity of the present treatment for the best performances achieved in single cells with high and low platinum loading electrodes. There is close agreement between the results of the numerical simulation and experimental results.

4.3 Needed Research and Development to Attain Projected Performance Levels

4.3.1 Increase of Platinum Utilization and Use of Alloy Electrocatalysts

One of the main contributions to the loss in efficiency and power density in PEM fuel cells is the activation overpotential at the cathode, which is highly visible from the cell and half cell performance in Fig. 15 (single cell with electrodes having a Pt loading of 0.45 mg/cm^2). This figure also shows that, over the entire current density range, the potentials in a cell with the high platinum loading electrodes are about 50 mV higher at all current densities than those in a cell with low platinum loading electrodes. However, because of the vital importance to develop fuel cells with low platinum loading electrodes, a two pronged attack should be followed: (i) increase the effective utilization of platinum, at least by a factor of 2 over the present value ($\approx 10\%$); and (ii) use alloy electrocatalysts with higher exchange current densities. Possible approaches for the former are use of (i) still thinner active layers with a higher percent platinum on carbon (say, 40% Pt/C); and (ii) vacuum impregnation or incorporation of the proton conductor (during fabrication) into the electrode to further extend the three-dimensional reaction zone. In the case of the latter, alloys of platinum with Co, Cr, or Ni, which have been successfully used to enhance oxygen reduction kinetics in phosphoric acid fuel cells, need be evaluated [16].

4.3.2 Optimization of Structure of Electrode and of Membrane and Electrode Assembly to Minimize Mass Transport and Ohmic Overpotentials with Air as Reactant

One of the challenges in PEM fuel cells is to minimize mass transport and ohmic overpotentials. As seen from Fig. 11 and 12, when using hydrogen/air rather than hydrogen/oxygen as reactants, the slopes of the linear region in the cell potential vs. current density plots are about 50% higher. Further, these figures show that at higher current densities mass transport limitations are encountered with H_2/air as reactant, but not with H_2/O_2 . To minimize these rate-controlling processes, optimizations of the structure of the electrode and of the membrane and electrode assembly are essential. Possible solutions are (i) altering the Teflon content of the electrode; (ii) use of electrodes with thinner diffusion and active layers; and (iii) incorporation of a proton conductor during the fabrication of electrodes.

4.3.3 CO-Tolerant Electrocatalysts for Hydrogen Oxidation and Methanol Oxidation Electrocatalysts

In the above sections, hardly any mention has been made about necessary improvements in the hydrogen electrode, because most of the experimental results quoted are when pristine hydrogen is used as the anodic reactant and oxygen or air is the cathodic reactant. Pure hydrogen and oxygen are, invariably, the reactants for extraterrestrial applications. However, for transportation and other terrestrial applications where PEM fuel cells will be used, methanol is presently the fuel of choice. Because of the low activity of the best electrocatalysts for methanol oxidation, the indirect route (reformer - fuel cell) is most promising for the near to intermediate term time-frame (say, up to the year 2010). The CO content of the reformed fuel is 1%, which cannot be tolerated by the anode. Ballard Power Systems made excellent progress in reducing this value to about 100 ppm by selective oxidation - passing the reformed gas with 1% to 2% oxygen over a platinum/alumina catalyst at 160°C . Even 100 ppm of CO poisons the platinum anode, but platinum/ruthenium alloy electrocatalysts are tolerant to this level of CO. It is essential that investigations be made on alloy electrocatalysts and/or oxide supports, which enhance CO oxidation and reduce the poisoning problem.

Finding CO tolerant electrocatalysts and/or oxide supports may also solve the "Fuel Cell Researcher's Dream" - the direct oxidation of methanol in fuel cells. FTIR studies reveal that the intermediate, which is formed during methanol oxidation and causes a poisoning problem, appears to be the same as the poisoning species adsorbed from carbon monoxide [17]. Potential electrocatalysts for methanol oxidation, which are of the redox type (i.e., electrochemical oxidation of the metallic species to a higher valence state, which chemically oxidizes the methanol) are Pt-Ru, Pt-Sn, Pt-Mo alloys.

5. CONCLUDING REMARKS

The conclusions, which may be drawn from this article may be summarized as follows:

- (i) PEM and alkaline fuel cells are the strongest candidates for achieving high energy efficiencies and high power densities, vitally needed for extraterrestrial and terrestrial applications. The PEM fuel cell has the advantage over the alkaline fuel cell because of CO₂ tolerance and longer lifetimes.
- (ii) Significant progress has been made in the attainment of high energy efficiencies and high power densities in PEM fuel cells with high (4.0 mg/cm²) and low (0.4 mg/cm²) platinum loading electrodes.
- (iii) Novel approaches have been used in PEM fuel cells with low Pt loading electrodes to attain the same levels of performance as those with high Pt loading - (a) proton conductor impregnation into the electrode; (b) optimized conditions for the hot-pressing of electrodes to PEM's and of pressure and temperature; (c) localization of platinum near the front surface; and (d) use of thin membranes with better conductivity and water retention capability.
- (iv) Electrode kinetic and mass transport parameters for ORR at a Pt/PEM interface were determined using a Pt microelectrode and pseudo-steady state, transient and impedance spectroscopic techniques. Values of the electrode kinetic parameters are comparable on the smooth microelectrodes and high surface area fuel cell electrodes.
- (v) The absence of net water transport from anode to cathode was demonstrated.
- (vi) A modeling analysis was carried out to demonstrate that the performance levels obtained in PEM fuel cells are approaching those projected, which are based on realistic values for the electrode kinetic and ohmic parameters.
- (vii) In order to achieve the projected performance levels, it is necessary to (a) improve the effective utilization of platinum from 10% to about 50% and/or use Pt alloy electrocatalysts for the ORR; (b) find membranes with better conductivity; and (c) discover CO tolerant electrocatalysts for hydrogen oxidation and electrocatalysts with a high activity for the direct oxidation of methanol - the latter is the "Fuel Cell Researcher's Dream". Both these areas are vitally important for the transportation application.

ACKNOWLEDGEMENTS

The authors wish to express their sincere appreciation to Dr. Edson Ticianelli of the University of Sao Paulo at Sao Carlos, Mr. Charles R. Derouin of Los Alamos National Laboratory and Dr. Mohammad A. Enayetullah of Johnson Matthey, Inc., who made significant contributions to the work carried out at LANL and/or TAMU. The research work at LANL was sponsored by the U.S. Department of Energy and at TAMU by the Defense Advanced Research Project Agency, Energy Research in Application Program - Texas Higher Education Coordinating Board, Electrochem, Inc., Center for Space Power - TAMU and

NASA Johnson Space Center. The authors are also grateful to the Dow Chemical Company (Drs. Jeffrey A. Gunsher, Glenn A. Eisman and Alan Cisar) and DuPont Chemical Company for providing the proton exchange membranes for this work.

REFERENCES

1. A.J. Appleby and F.R. Foulkes, "Fuel Cell Handbook", Van Nostrand Reinhold, New York (1989).
2. S. Srinivasan, *J. Electrochem. Soc.*, **136** (1989), 41C.
3. K. Prater, "Fuel Cells - Grove Anniversary Symposium: 1989", D.G. Lovering, Ed., Elsevier Applied Science Division, London, New York (1990), 239.
4. E.A. Ticianelli, C.R. Derouin and S. Srinivasan, *J. Electroanal. Chem.*, **251** (1988), 275.
5. S. Srinivasan, D.J. Manko, H. Koch, M.A. Enayetullah and A.J. Appleby, *J. Power Sources*, **29** (1990), 367.
6. I.D. Raistrick, U.S.P. 4,876,115 (10/24/1989).
7. S. Srinivasan, E.A. Ticianelli, C.R. Derouin and A. Redondo, *J. Power Sources*, **22** (1988), 359.
8. A. Parthasarathy, C.R. Martin and S. Srinivasan, *J. Electrochem. Soc.*, In press.
9. W. Paik, T.E. Springer and S. Srinivasan, *J. Electrochem. Soc.*, **136** (1989), 644.
10. A. Parthasarathy, B. Dave, S. Srinivasan, A.J. Appleby and C.R. Martin, Paper to be submitted to *J. Electroanal. Chem.*
11. A. Parthasarathy, S. Srinivasan, A.J. Appleby and C.R. Martin, Paper in course of preparation.
12. C.P. Winlove, K.H. Parker and R.K.C. Oxenham, *J. Electroanal. Chem.*, **170** (1984), 293.
13. H. Koch, A. Nandi, N.K. Anand, O. Velev, D.H. Swan, S. Srinivasan and A.J. Appleby, Extd. Abstracts of the 178th Meeting of the Electrochemical Society, Seattle, Washington, October 14-19, 1990, Abst. # 115.
14. A. Damjanovic and V. Brusic, *Electrochim. Acta*, **12** (1967), 615.
15. J.O'M. Bockris and S. Srinivasan, "Fuel Cells: Their Electrochemistry", McGraw Hill Publishing Company, New York (1969).
16. D.A. Landsman and F.J. Luczak, U.S.P. 4,316,944 (2/23/1982); U.S.P. 4,373,014 (2/8/1983).
17. K. Kunitatsu, *Ber Bunsenges Phys. Chem.*, **94** (1990), 1025.

TABLE 1
Effects of Localization of Platinum Near Front Surface of Electrode
on Hydrogen Adsorption Charge and Roughness Factor as Determined
by Cyclic Voltammetry and on Percentage of Platinum Utilization

| Method of Pt Localization | $Q_H/mC\text{ cm}^{-2}$ | Roughness ^a Factor | Utilization of Pt ^b /% |
|---------------------------|-------------------------|-------------------------------|-----------------------------------|
| 10% Pt/C | 4.4 | 20 | 4 |
| 10% Pt/C+50 nm Pt film | 9.6 | 44 | 9 |
| 20% Pt/C | 11.4 | 53 | 11 |
| 20% Pt/C+50 nm Pt film | 15.3 | 70 | 14 |
| 40% Pt/C | 17.0 | 77 | 15 |
| 40% Pt/C+50 nm Pt film | 19.2 | 87 | 17 |

^a Calculated assuming $220\ \mu\text{C}/\text{cm}^2$ for Q_H on smooth Pt.

^b Estimated assuming a 2.0 nm particle size for the Pt on C catalyst, as was shown by electron microscopy of the materials. % of Pt utilization = (roughness factor/total Pt surface area x 100).

TABLE 2
Electrode Kinetic Parameters for Oxygen Reduction at the Pt/Nafion interface
using Fuel Cell Electrodes and Microelectrodes.

| Electrode/Membrane Interface @ 50°C, 1 atm pressure | Tafel slope b (mV/dec) | Exchange current density, i_o (A/cm ²) * |
|---|---------------------------|---|
| Unsupported Pt black (10mg/cm ² on carbon cloth (ElectroChem Inc.)/125- μm Dow membrane | -58 | 3.09×10^{-7} r.f. 773 |
| Platinum supported on carbon (20%Pt/C), Pt loading 0.4 mg/cm ² ; Nafion impregnated-4 mg/cm ² (Etek, Inc)/ 125- μm Dow membrane | -64 | 1.09×10^{-7} r.f. 52 |
| 100- μm Pt microelectrode/175- μm Nafion @ 25°C, 1 atm pressure. Pseudo-steady state voltammetry | -63 | 2.05×10^{-9} |
| | -118 | 7.8×10^{-7} |
| 100- μm Pt microelectrode/175- μm Nafion @ 25 C, 1 atm pressure. Electrochemical Impedance Spectroscopy | -65 | 4.09×10^{-8} |
| | -133 | 5.9×10^{-7} |

r.f. : roughness factor

* - Normalized for electrochemically active surface area

TABLE 3
 Transport Parameters for Oxygen in Nafion from
 Measurements at Pt/Microelectrode Interface

| | |
|--|----------------------|
| Diffusion coefficient, D (cm ² /s) | 7.4×10^{-7} |
| Solubility, C(mM) | 26 |

TABLE 4
 Electrode Kinetic Parameters for PEM H₂/O₂ Fuel Cells, As Evaluated by Non-Linear
 Least Squares Fit of Experimental Results. Also Included are
 Current Densities at Cell Potential of 0.9 V, Temperature 85°C, Pressure 5 atm.

| Electrode, Platinum Loading, Membrane | E ₀ V | b V/decade | R ohm cm ² | i _{0.9} A/cm ² |
|--|---------------------|---------------|--------------------------|---------------------------------------|
| Electrochem, Inc., 10 mg/cm ² Dow Membrane, 125 μm | 1.065 | 0.055 | 0.110 | 300 |
| Prototech, 0.4 mg/cm ² Nafion®, 175 μm | 1.007 | 0.046 | 0.298 | 70 |
| ibid, 100 μm | 1.008 | 0.045 | 0.201 | 61 |
| ibid, Dow Membrane 125 μm | 1.002 | 0.053 | 0.111 | 62 |

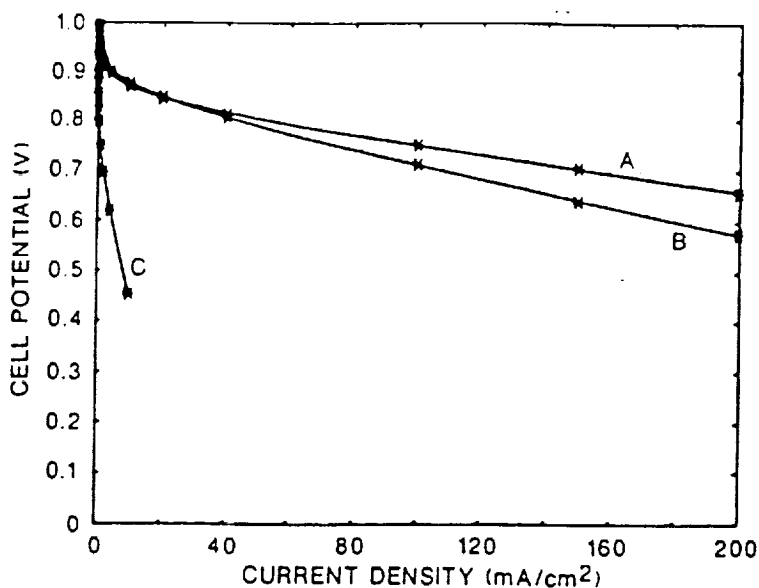


Fig. 1a. Cell potential/current density plots for H_2/O_2 fuel cells at $50\text{ }^\circ\text{C}$ and 1 atm pressure (electrodes 5 cm^2): A and C, Nafion-impregnated and as-received Prototech electrodes ($0 - 35\text{ mg cm}^{-2}\text{ Pt}$) hot-pressed to Nafion membranes; B, GE/HS-UTC membrane and electrode ($4\text{ mg cm}^{-2}\text{ Pt}$). Solid lines, computer generated plots; \star , experimental points.

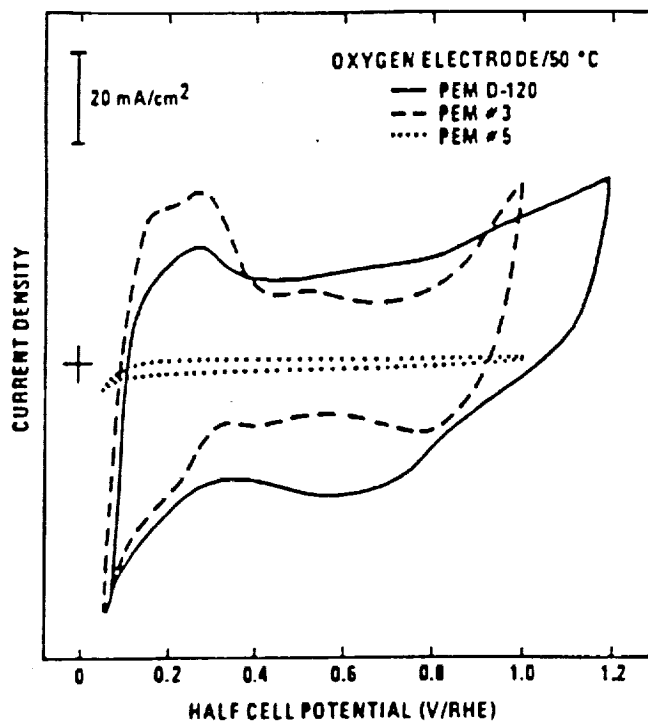


Fig. 1b. Cyclic voltammograms on oxygen electrodes in fuel cells (electrodes 5 cm^2). PEM D-120-cell with Nafion-impregnated Prototech electrodes ($0.35\text{ mg cm}^{-2}\text{ Pt}$) hot-pressed to Dow membrane; PEM #3-cell with GE/HS-UTC membrane and electrode assembly ($4\text{ mg cm}^{-2}\text{ Pt}$); and PEM #5-cell with as-received Prototech electrodes ($0.35\text{ mg cm}^{-2}\text{ Pt}$) hot-pressed to Nafion membrane.

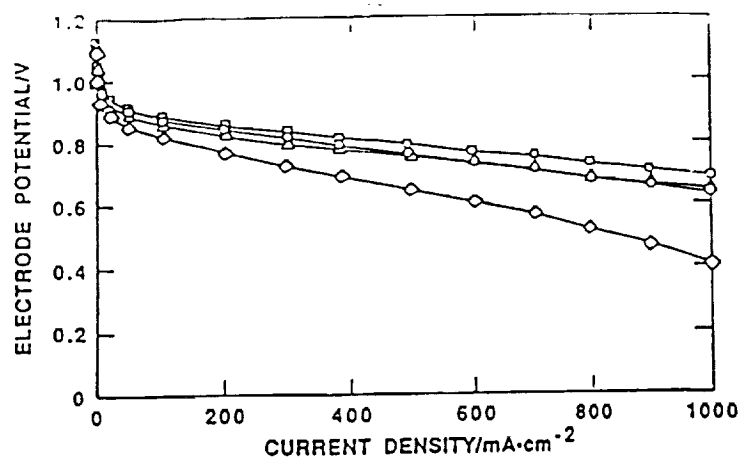


Fig. 2. Effect of localization of Pt near front surface of Prototech electrodes on performance of oxygen electrode in H_2/O_2 single cell at $80^\circ C$ and at $3/5$ atm. 40 wt% Pt/C plus 50 nm sputtered film of Pt (o); 20 wt% Pt/C plus sputtered film of Pt (\square); 20 wt% Pt/C (Δ); and 10 wt% Pt/C (\diamond). The H_2 counter electrode in each case was the same as the working electrodes (4).

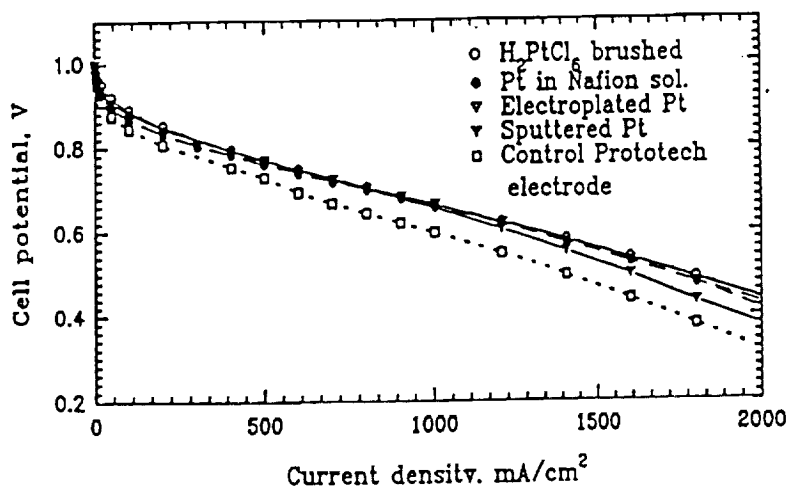


Fig. 3. Cell potential vs. current density plots for single cells with electrodes having localized Pt layer deposited by different methods, all operating at $95^\circ C$ and with H_2/O_2 at $4/5$ atm.

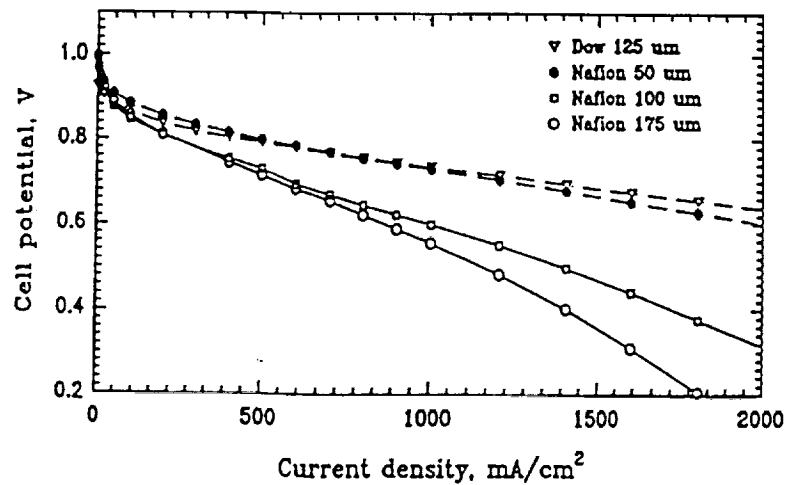


Fig. 4. Cell potential vs. current density plots for single cells with different membrane materials, operating at 95°C with H₂/O₂ at 4/5 atm. Pt loading on each electrode: 0.45 mg/cm² (5).

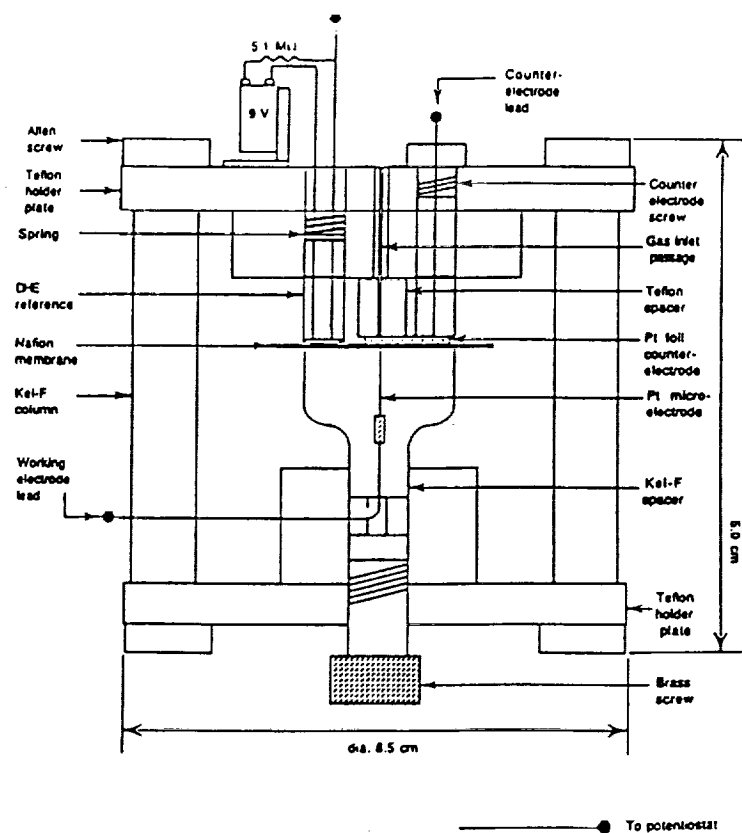


Fig. 5: Schematic of the solid state cell incorporating a platinum microelectrode (8).

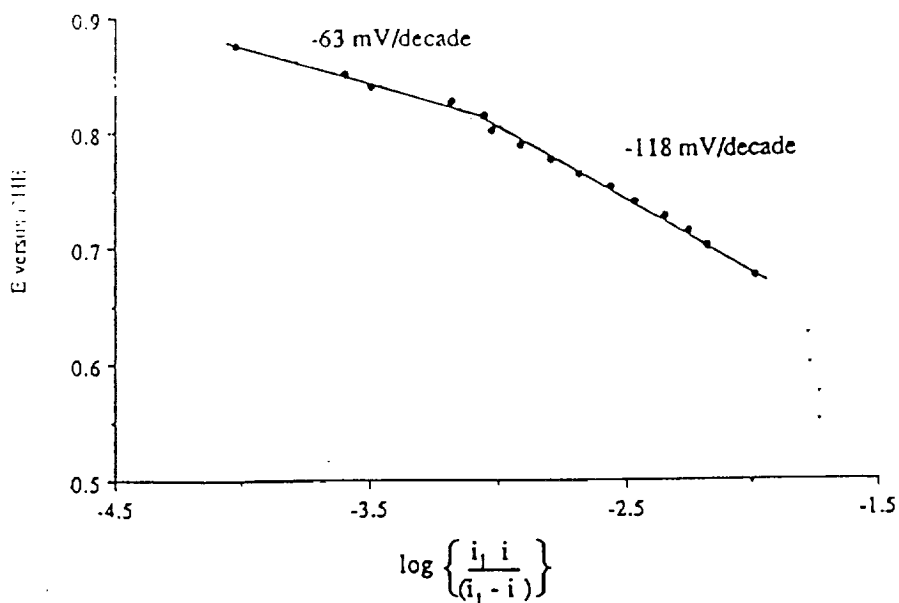


Fig. 6: Mass transfer corrected Tafel plot for oxygen reduction at the platinum microelectrode/Nafion interface, at 25 °C (8).

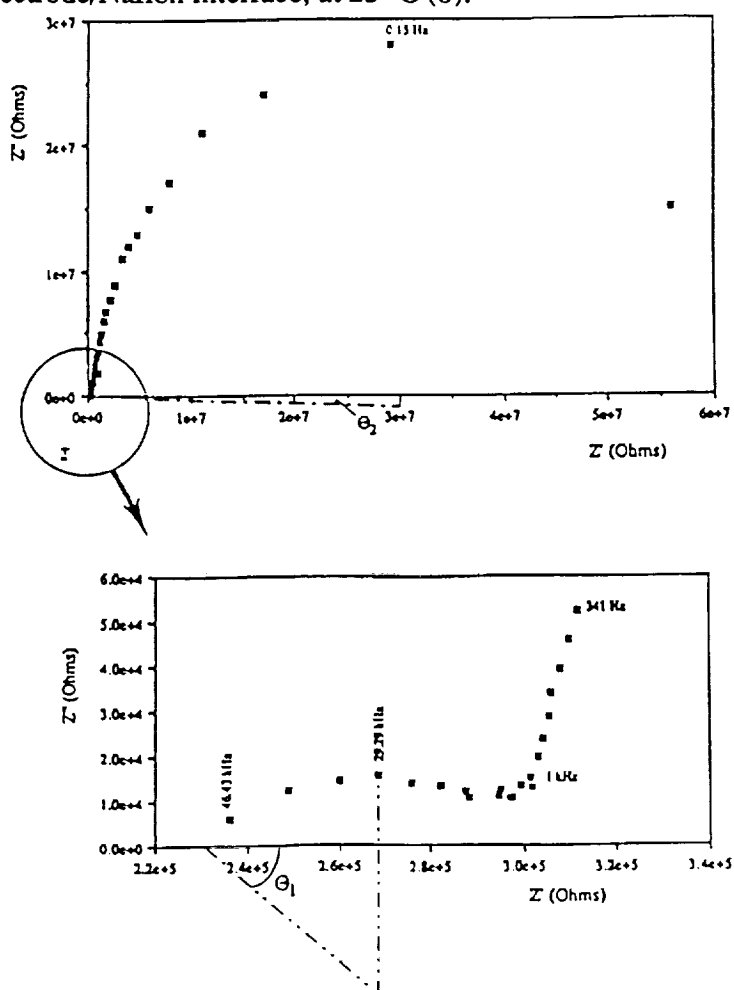


Fig. 7: Nyquist plot obtained at open circuit at the platinum/Nafion interface showing charge transfer relaxation; inset shows high frequency membrane relaxation process (10).

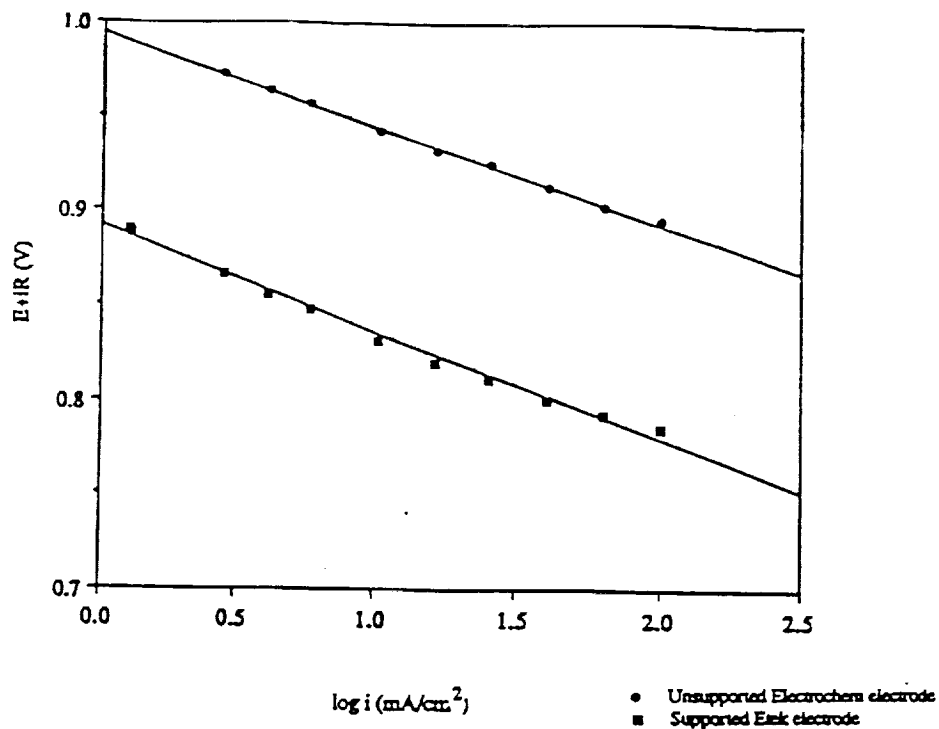


Fig. 8: iR corrected Tafel plots for oxygen reduction at membrane electrode assemblies using unsupported and supported platinum gas diffusion electrodes (11).

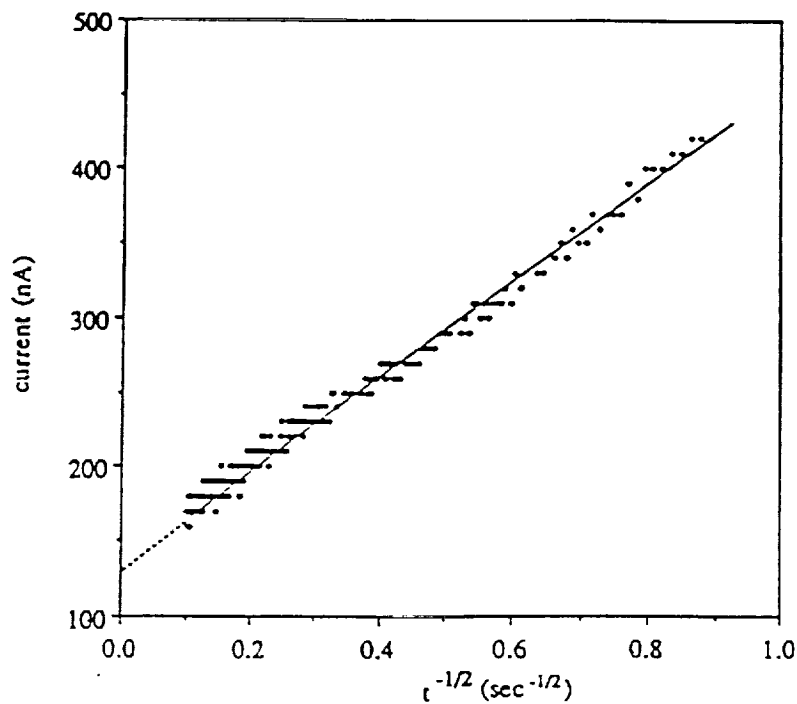


Fig. 9: Current versus $\tau^{-1/2}$ plot at the platinum/Nafion interface to determine mass transport parameters of oxygen in Nafion (8).

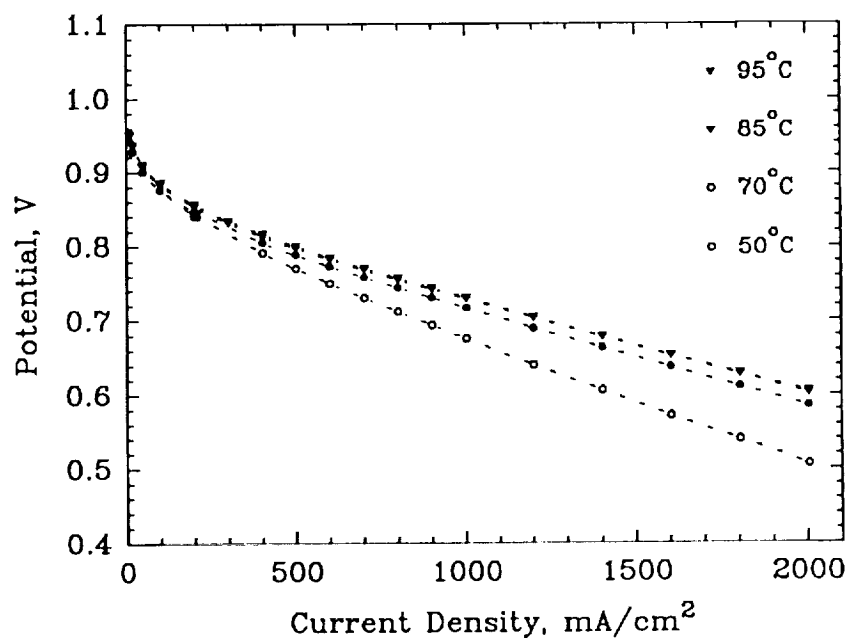


Fig.10 Effect of temperature on the performance of a PEM H₂/O₂ fuel cell, Pt loading of electrodes 0.45mg/cm², Dow membrane, 5 atm.

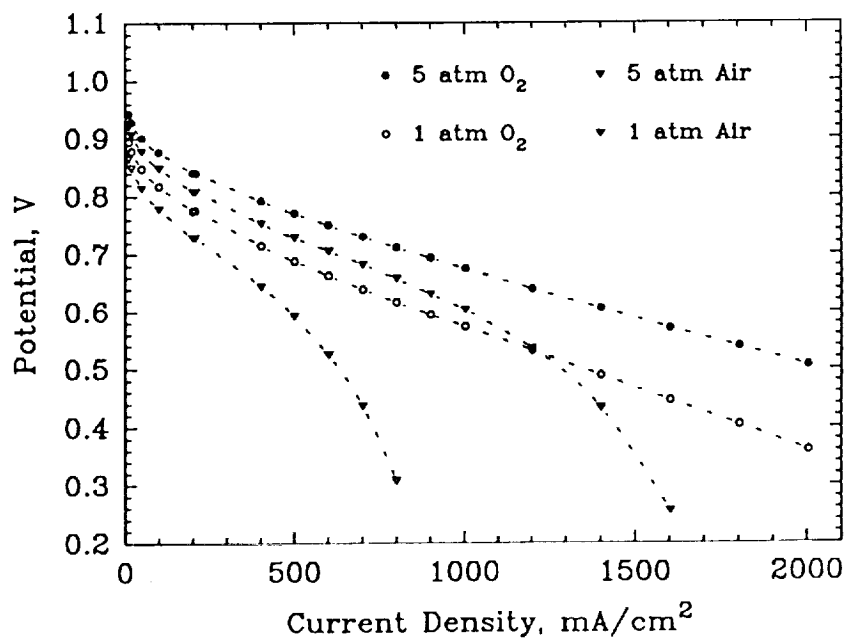


Fig.11 Effect of pressure and reactant gas on the performance of a PEM fuel cell, Pt loading of electrodes 0.45mg/cm², Dow membrane, 50°C.

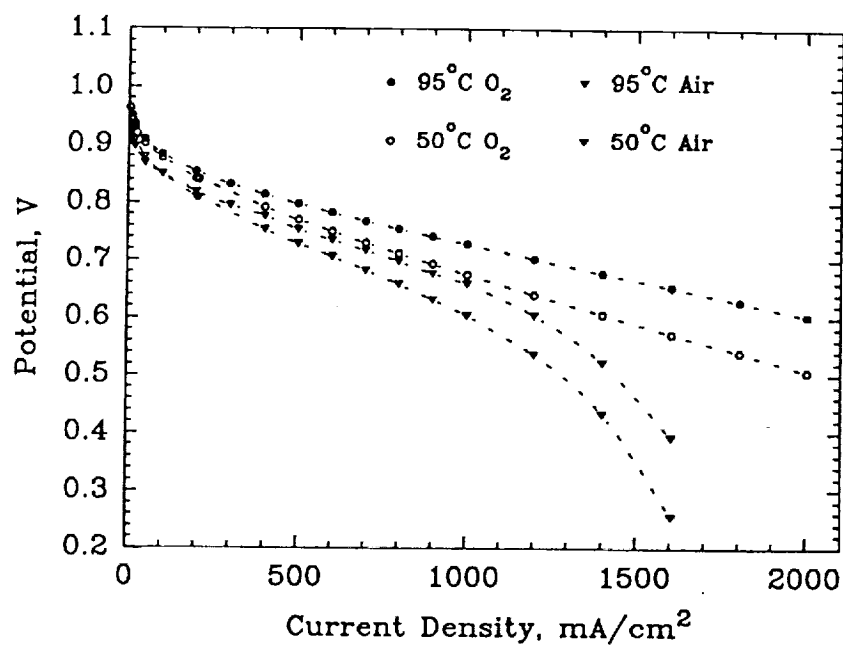
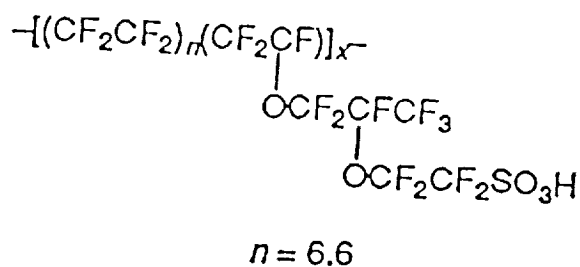
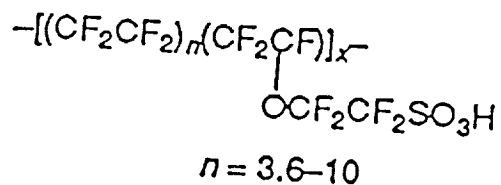


Fig.12 Effect of temperature and reactant gas on the performance of a PEM fuel cell, Pt loading of electrodes 0.45 mg/cm², Dow membrane, 5 atm.



DuPont's Nafion®



Dow Perfluorosulfonate Ionomers

Fig.13 The skeleton structure of DuPont's Nafion® and Dow's perfluorosulfonate membrane

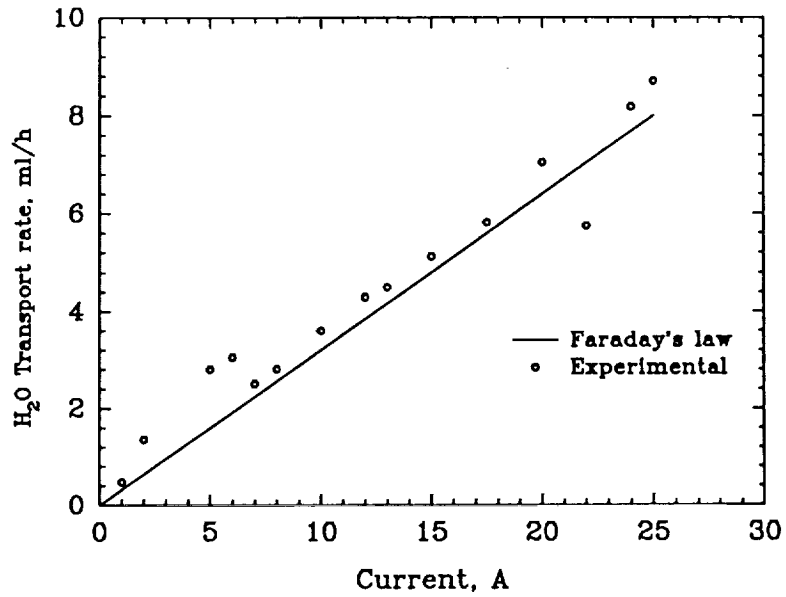


Fig. 14 Water production rate in a 50 cm² area PEM H₂/O₂ fuel cell with Dow membrane, 50°C, 1atm.

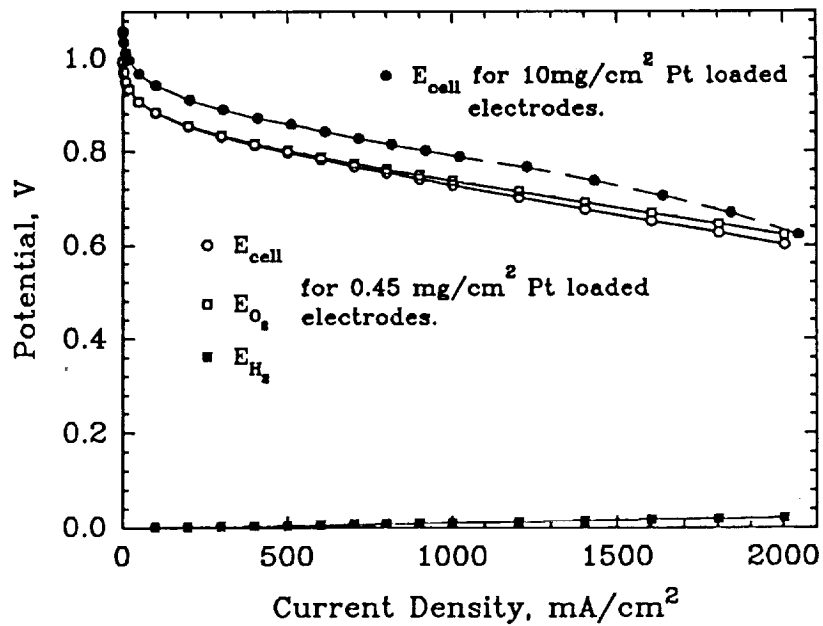


Fig.15 Half cell and single cell performance in PEM H₂/O₂ fuel cell, 95°C, Dow membrane, 5 atm.

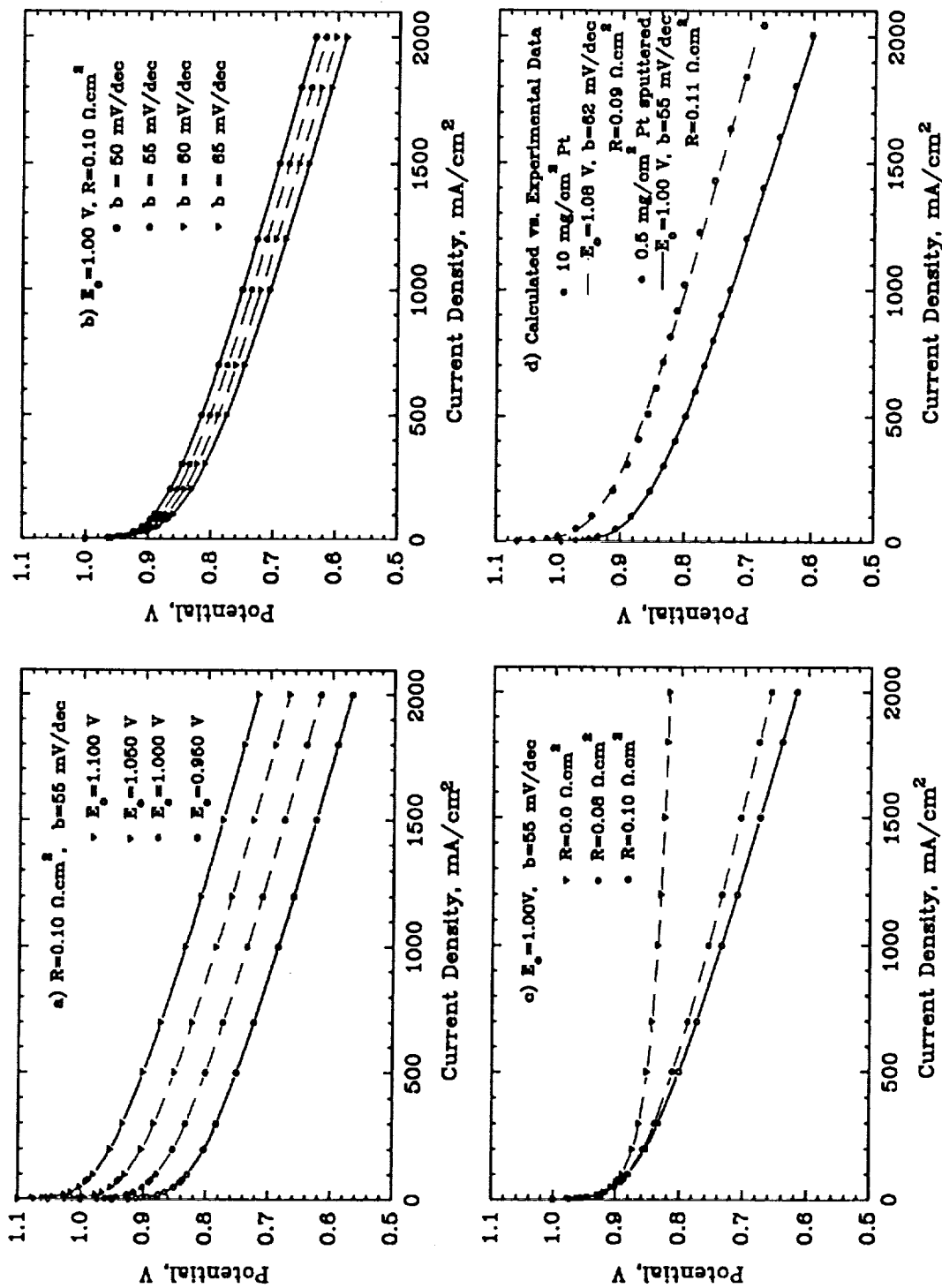


Fig.16 Cell Potential -Current Density plots: (a) to (c) modelling analysis; (d) Least square fit of experimental results in PEM H₂/O₂ fuel cell, 95°C, 5 atm.

I-BIEM CALCULATIONS OF THE FREQUENCY DISPERSION AND AC CURRENT DISTRIBUTION AT DISK AND RING - DISK ELECTRODES

Boris D. Cahan
Case Center for Electrochemical Sciences and
The Department of Chemistry
Case Western Reserve University
Cleveland, Ohio 44106

ABSTRACT

The Iterative Boundary Integral Equation Method (I-BIEM) has been applied to the problem of frequency dispersion at a disk electrode in a finite geometry. The I-BIEM permits the direct evaluation of the AC potential (a complex variable) using complex boundary conditions. The point spacing was made highly non-uniform, to give extremely high resolution in those regions where the variables change most rapidly, i.e. in the vicinity of the edge of the disk. Results are analyzed with respect to "IR correction", equipotential surfaces and reference electrode placement. The current distribution is also examined for a ring-disk configuration, with the ring and the disk at the same AC potential. It is shown that the apparent impedance of the disk is inductive at higher frequencies. The results are compared to analytic calculations from the literature, and usually agree to better than 0.001%.

INTRODUCTION

One of the more useful electrode configurations for use in electrochemical studies is the Rotating Disk Electrode (RDE) and the Rotating Ring-Disk Electrode (RRDE). As such, they are often available in many laboratories and are used as general purpose electrodes, even without rotation, and often for applications for which the geometry is not well suited. Although a number of papers have appeared in the literature which treat the frequency dispersion problem of such electrodes, most have been analytic^{1,2,3} solutions with restrictive boundary conditions, and/or restrictive boundary geometries. The choice of geometry and boundary conditions used in finding analytic solutions is often governed as much by the feasibility of formulating the proper relationships so as to yield a solution as by their relevance to the problem at hand. Real cells are usually of finite dimension, and rarely do electrochemical interfaces have the linear responses invoked in heat transfer problems.

Some of the problems that still need attention are the questions of:

1. The local distribution of current, and the partition of current between ring and disk,
2. The placement of the reference electrode, and the meaning of AC equipotentials,
3. The influence of the insulating gap,
4. The interaction of the ring and disk when they are driven by different potential regimes,
5. The effect of real non-linear kinetics both in terms of overall reactions, and in pseudo-capacitive substeps.

This paper will deal primarily with items 1 and 2. The last three will be the subject of a later paper.

The I-BIEM⁴ has proven to be a powerful algorithm for solving problems of this type with difficult boundary conditions and geometries. It has been applied here to the analysis of the impedance of the RDE and the RRDE. A number of changes have been made to the original algorithm which place the method on a more rigorous footing⁵ and eliminate some of the initial approximations. These are discussed briefly

below. Details will be given in a separate publication⁶.

MODIFICATIONS TO I-BIEM

We are seeking the solution to Laplace's equation for a domain Ω with a boundary Γ

$$\nabla^2\phi = 0 \quad (1)$$

where ϕ is the dependent variable (e.g. potential, temperature, concentration *etc*) with general boundary conditions

$$f(\phi, D|\phi|, \mathbf{x}) = 0 \quad (2)$$

where D is a differential operator, and \mathbf{x} is the space variable (x, y, z). On a Dirichlet (e.g. conducting) boundary, $f = f(\phi, \mathbf{x})$ while on a Neuman (e.g. insulating) segment $f = f(D|\phi|, \mathbf{x})$ at most. Choosing a function G to be a free space Green's function, $G(\mathbf{x}, \mathbf{x}')$, where \mathbf{x} and \mathbf{x}' are coordinates at two points, such that $\nabla^2 G(\mathbf{x}, \mathbf{x}') = \delta(\mathbf{x}, \mathbf{x}')$, we can show from the divergence theorem that

$$\alpha\phi(\mathbf{x}) = \int_{\Omega} \nabla^2\phi(\mathbf{x}')G(\mathbf{x}, \mathbf{x}')d\Omega + \int_{\Gamma} [\phi(\mathbf{x}')G^*(\mathbf{x}, \mathbf{x}') - \phi^*(\mathbf{x}')G(\mathbf{x}, \mathbf{x}')]d\Gamma \quad (3)$$

where α is the Cauchy principal value of the integration of the Green's function singularity. [For example, in two dimensions, $\alpha = 0$ for points outside Γ , $\alpha = 2\pi$ inside, and $\alpha = \pi$ on a straight boundary.] Here ϕ^* and G^* are derivative functions of ϕ and G respectively. In cases where $\nabla^2\phi = 0$, the first integral in (3) vanishes and

$$\alpha\phi(\mathbf{x}) = \int_{\Gamma} [\phi(\mathbf{x}')G^*(\mathbf{x}, \mathbf{x}') - \phi^*(\mathbf{x}')G(\mathbf{x}, \mathbf{x}')]d\Gamma \quad (4)$$

For the function ϕ on Γ , we write

$$\phi(\mathbf{x}) = \sum_i N_i(\mathbf{x})\phi_i, \quad \phi^*(\mathbf{x}) = \sum_i N_i^*(\mathbf{x})\phi_i^* \quad (5)$$

where ϕ_i and ϕ_i^* are the values at discrete points on the boundary and N_i are shape functions. If we integrate piecewise over Γ , using a finite number of points \mathbf{x}_j , eqn. (5) becomes

$$\sum_{j=1}^m a_{ij}\phi_j = \sum_{j=1}^m b_{ij}\phi_j^* + c_i \quad i=1,2,\dots,m \quad (6)$$

where

$$a_{ij} = \int_{\Gamma_j} N_i^*(\mathbf{x})G(\mathbf{x}, \mathbf{x}')d\Gamma$$

$$b_{ij} = \int_{\Gamma_j} N_i(\mathbf{x}')G^*(\mathbf{x}, \mathbf{x}')d\Gamma$$

$$c_i = \sum_k F(\mathbf{x}_k)G(\mathbf{x}, \mathbf{x}_k)$$

In a conventional BIEM, the boundary conditions are introduced into the system of equations (6) and then assembled into the form

$$\sum_{j=1}^m d_{ij}u_j = e_i \quad i = 1,2,\dots,m \quad (7)$$

where the u_j represent the unknown ϕ or ϕ^* at the m nodes. Equation (7) is then

inverted to obtain these unknown quantities. For problems with non-linear boundary conditions equation (7) becomes a non-linear system of equations, and the assembling process may even have to be repeated a number of times to use linear matrix inversion techniques. In a system where the point spacing is highly non-uniform, the inversion of the matrices can introduce near-singularities.

The approach of the I-BIEM is different since the assembly and inversion symbolized by equation (7) is never performed. Rather, equation (6) is utilized directly. To solve for the unknown ϕ and ϕ^* at the nodes, we start by guessing values ϕ_e and ϕ_e^* for these quantities. The actual values chosen are rather unimportant. For Dirichlet (known ϕ_e) or Neuman (known ϕ_e^*) boundaries the values can be used once and for all and absorbed into the c_i of eqn. (6). For non-linear mixed boundary conditions, the iterative process described below readily accepts any root finding process in the solution. When the guesses are used in the equation for the i th node as origin of integration, the result is an error:

$$\epsilon_i = \sum_{j=1}^m a_{ij}\phi_{e_j} - \sum_{j=1}^m b_{ij}\phi_{e_j}^* + c_i \quad (8)$$

Since the largest contribution to ϵ_i comes from the $j = i$ terms, the $j \neq i$ terms of equation (8) can be used to get an expression for updating the unknowns at the i th node. Thus:

$$\text{Neuman Boundary} \quad \phi_i = \phi_{e_i} - \lambda \frac{\epsilon}{a_{ii}} \quad (9a)$$

$$\text{Dirichlet Boundary} \quad \phi_i^* = \phi_{e_i}^* - \lambda \frac{\epsilon}{b_{ii}} \quad (9b)$$

$$\text{Mixed Linear Boundary} \quad a_{ii} (\phi_i - \phi_{e_i}) - b_{ii} (\phi_i^* - \phi_{e_i}^*) = -\lambda \epsilon_i \quad (9c)$$

$$\text{Non-linear Boundary} \quad \frac{a_{ii}}{b_{ii}} (\phi_i - \phi_{e_i}) - (B(\phi_i) - \phi_{e_i}^*) = -\frac{\lambda \epsilon_i}{b_{ii}} \quad (9d)$$

where the $B(\phi_i)$ represent the functional relationship between the ϕ and ϕ^* from the boundary conditions and λ is an over-relaxation factor which can be shown⁵ to be $\approx 0.6 - 0.75$.

The updating process is continued for all points in sequential fashion for k passes, until a suitable convergence criterion, $\epsilon_k = \sum \epsilon_j < \zeta$ ($j = 1$ to N) is satisfied, where ζ is an arbitrarily small number, as desired. [The smaller the value of ζ , the more accurate the solution, but the longer the iteration time.]

For two dimensional problems the $G(\mathbf{x}, \mathbf{x}')$ function is

$$G(\mathbf{x} - \mathbf{x}') = \ln r \quad (10)$$

where r is the distance between \mathbf{x} and \mathbf{x}' ,

$$G^* = \frac{\partial}{\partial n}(\ln r) = \frac{1}{r} \frac{\partial r}{\partial n} = \frac{1}{r} (\nabla r \cdot \mathbf{n}) = -\frac{1}{r} \quad (11)$$

and equation (4) becomes (see equation (3) of ref [4])

$$\alpha \phi(\mathbf{x}) = \int_{\Gamma} [\phi(\mathbf{x}') \frac{1}{r} \frac{\partial r}{\partial n} - \phi^*(\mathbf{x}') \ln r] d\Gamma \quad (12)$$

Similarly, in three dimensions $G(\mathbf{x} - \mathbf{x}') = 1/R$ and

$$-\alpha \phi(\mathbf{x}) = \int_{\Gamma} [\phi(\mathbf{x}') \frac{\partial}{\partial n} \left[\frac{1}{R} \right] - \phi^*(\mathbf{x}') \frac{1}{R}] d\Gamma \quad (13)$$

Also,
$$\frac{\partial G}{\partial n} = \frac{\partial G}{\partial r} n_r + \frac{\partial G}{\partial z} n_z$$

$$= \frac{2 n_r}{\sqrt{a+b}} [E(m) - K(m)] - 4 \frac{[n_r(r-r_i) + n_z z]}{(a-b)\sqrt{a+b}} E(m) \quad (18)$$

where (n_r, n_z) are direction cosines, $K(m)$ and $E(m)$ are complete elliptic integrals of the first and second kind. When these are substituted into eqn. (15), the expression can no longer be integrated analytically, but can be approximated adequately using e.g. Gaussian⁸ or adaptive quadrature. The elliptic integral can be approximated by suitable polynomial expansions⁸ or from Lamdens' transformation⁹. [Note that the constants for the expressions used for Gaussian quadrature and for the elliptic integrals in ref. (7) contain several typographic errors, and should be obtained directly from ref. (8) or some other suitable source.] Although these integrals are much more complicated than those for the two dimensional case, their values can also be stored in a dense linear array, and evaluated once for the entire process.

In the direct BIEM there are several classes of singularities which must often be treated carefully. [In a recent conference on Boundary Element Technology¹⁰ seven papers dealt with aspects of this problem.] For example:

1. Discontinuities or multiple valued points.

In the integration of each segment, Γ_i , there is, in effect, a term in $\Delta \mathbf{x}$ in the denominator. If $\Delta \mathbf{x} \rightarrow 0$, The matrix becomes singular on inversion. If the spacing is very small, the matrix becomes near-singular and imprecise on inversion.

2. Acute or re-entrant corners.

At any corner where the two adjacent sides are not orthogonal or straight, the normal derivative has multiple (two or more, depending on the geometry) values, but only one independent equation.

3. Integrable singularities at intersections with different boundary conditions.

At an edge between two different boundaries, such as the one treated in this paper, the value of the current density can go to an integrable infinity. Such is the case for *primary* current distributions. This is evidently not possible with the finite number set of computer calculations. It also does not conform well to a linear basis function.

In the I-BIEM, many of these simply do not occur, or can be safely ignored.

1. Multiply defined values.

Since the matrix (7) is never inverted, multiple values cause no problems. Each element is simply integrated and summed. A multiply defined value is integrated using the value appropriate to its element, and the "missing" element of zero size is ignored.

2. Non-orthogonal intersections.

Consider any one corner where such a condition occurs. If the value at that one point were known, and all of the other values known, then from eqn. (14) a *value* can be determined which uniquely satisfies the equation, such that all sub-integrals containing that point are defined. This situation actually occurs at any curved boundary which is represented by a set of linear elements. In the process of iteration, as long as e.g. the normals are interpreted consistently and the process is convergent, *all* values will be the "best fit" to the problem in the sense of a "least error".

3. Integrable singularities.

Similar reasoning can be used to show that the integral(s) over any element(s) with the singular point as an end point must be *exactly* equal to the true integral over the integrable singularity, even though the numerical value at that point is finite.

In all such cases, the element containing the "problem" may be made as small as desired, without difficulty.

It may be noted here that the α 's are sometimes difficult to evaluate, especially when the boundaries are highly structured. However they may be evaluated simply from the same equation (14 or 15) by the simple expedient of setting all of the ϕ terms to unity, and all of the ϕ^* terms to zero.

NEAR-BOUNDARY ERRORS

One of the problems associated with solutions found with the BIEM (or BEM) is that values computed for points just inside the boundary after solution suffer from reduced accuracy. It is stated in ref. [7] pages 31-32, "...there exists a 'boundary layer' where the numerical accuracy suffers...As a rule of thumb, a degeneration of accuracy may occur at distances less than one element length from a boundary." This problem does not appear to exist in 2-D problems (where the exact integral⁴ can be used) with the I-BIEM, or at least is much less severe. For the axi-symmetric 3-D case the problem does exist, although to a very small degree, and only on some boundaries. We have not yet been able to establish a fundamental reason for this discrepancy.

It has been found that precision of the math used is very significant. With single precision, the results with the axi-symmetric case are much less accurate, dropping to 0.1-1.0% agreement for some cases. We also use 16 point Gaussian quadrature for the integration, to preserve precision as much as possible.

A related question deals with the value of ϕ on the boundary, but between points. On a straight orthogonal segment, the problem is solved using linear interpolation between the end-point values of each element. When such a value is computed for ϕ , it does not yield a value on the straight line. This is especially noticeable on boundaries with a high curvature of the potential, or a low number of points on a segment. Rather, the curve generated by computing values at closely spaced intervals along the curve after convergence for a coarser grid is very smooth.

Some problems have been experienced on curved non-orthogonal boundaries. This is clearly related to the problem of deciding whether a point is on, inside or outside of a line with finite precision math. Even with a high precision, a point which is mathematically on a line does not in general coincide *exactly*¹¹ with computer floating point numbers.

APPLICATION TO THE RDE AND RRDE IMPEDANCE PROBLEM

1. Choice of Geometry

In order to verify the technique and at the same time to perform a useful calculation, it was decided to make a comparison to an existing solution of the RDE problem, constructing the geometry so as to approach that used for the analytic solution of Newman¹. However, his solutions were generated with the counter electrode "at infinity". With any numerical technique it is difficult to know where to terminate the calculations with such a boundary. A real cell is never infinite, however, and it is desirable to be able to incorporate "real" cell geometries into the solution. The equipotential surfaces for *primary* current distribution (including the "infinite frequency" behavior of an RDE) with the counter electrode at infinity, in cylindrical coordinates

$$z = a\xi\eta$$

$$r = a\sqrt{(1+\xi^2)(1-\eta^2)} \quad (20)$$

where r is the distance from the axis of symmetry, z is the normal distance from the disk, a is the radius of the disk, and ξ and η are rotational elliptic coordinates, were shown¹² to be

$$\phi/\phi_0 = 1 - (2/\pi) \tan^{-1}\xi \quad (21)$$

where ϕ is the potential at some ξ , and ϕ_0 is the potential difference between

infinity (counter electrode) and the disk. Rearranging (21) for the conditions (19),

$$\xi = \tan \left[\frac{(\pi/2)(\phi/\phi_{ce})}{\phi_{ce}} \right] \quad (22)$$
where $\phi_{ce} = 1 - \phi/\phi_0$. Many of the calculations were done using the location of these equipotentials as the location of the counter electrode. For the *primary* current case or for "infinite" frequencies the solutions are identical to Newman's results, differing only by a scale factor. [It will be shown later that at finite frequencies, this is no longer true. Indeed, the concept of an equipotential *surface* of the complex variable ϕ has no meaning except in very special cases.] The scale factor actually used in the calculations was determined by the desirability (for plotting purposes) of maintaining the vertical dimension, z , as unity. Then, after the choice of ϕ/ϕ_{ce} and the determination of ξ from eqn. (22), a , the disk radius can be found from eqn. (20), when $\eta=1$ (i.e. on the vertical axis) as $a=1/\xi$. The radius of the equipotential at the plane of the disk is thus $r = a\sqrt{(1+\xi^2)} = \sqrt{(1+\xi^2)}/\xi$.

Figure 1a shows the usual geometry used. Other geometries (Fig. 1b) were also used, because they were more amenable to the rectangular coordinates used for some of the more difficult graphics routines. These represent finite cylindrical cells with the counter electrode as a large disk parallel to the RDE, with a cylindrical electrode coaxial with the RDE, or both.

In all calculations, the current in the outer portion of the disk was integrated separately to model the RRDE used as a segmented electrode with both segments driven at the same potential. In some calculations a small insulating segment was interposed between the ring and the disk.

2. Choice of Boundary Conditions

The impedance of the RDE or RRDE is a problem of a complex variable $\phi = \phi_R + j\phi_I$ where $\phi_R (= \Re\phi)$ and $\phi_I (= \Im\phi)$ are two independent variables in the domain Ω . In this paper, only a purely capacitive boundary at the disk is treated. The real and imaginary components are related only on the capacitive boundary, Γ_{cap} , by the relations

$$\phi_R = \frac{1}{\omega C} \frac{\partial \phi_I}{\partial n} \quad \phi_I = -\frac{1}{\omega C} \frac{\partial \phi_R}{\partial n} \quad \text{on } \Gamma_{cap} \quad (19a)$$

The potential *inside* the electrode is taken to be zero.

The counter electrode is taken to be a Dirichlet boundary. This is equivalent to the statement that the counter electrode is perfectly reversible or unpolarized, or that the counter electrode is at "infinity" and that this boundary, Γ_{ce} is at the position of an equipotential surface. Insulating boundaries Γ_{ins} (and symmetry planes) are taken to be Neuman boundaries. Thus:

$$\{\phi_R = V, \phi_I = 0\} \text{ on } \Gamma_{ce}; \{\phi_R^* = \phi_I^* = 0\} \text{ on } \Gamma_{ins} \quad (19b)$$

3. Choice of point location and density.

The I-BIEM allows an economy of spacing not readily obtainable with other techniques. A uniform point spacing in the r direction along the $z = 0$ surface is undesirable, since the area of the annuli corresponding to this spacing increases quadratically with the radius. A more desirable spacing is one where the Δr decreases with the square of r . This is equivalent, for e.g. 64 points per segment to a linear resolution of 4096 points at the disk near the edge. At the higher frequencies covered in this work, the local structure of the potential near the edge (singular for primary current distributions) varies so strongly that a finer resolution is required. In some, a quartic spacing was used. This is equivalent to a resolution at the edge of better than $1:10^{-8}$ with 64 points. Such fine spacing in a conventional BIEM (or BEM) could create severe stability problems as a result of the near-singularity induced by the inversion of the matrix. Similar spacings were used for the calculation of the potential at the insulator in the region of the edge.

Spacing and resolution at the counter electrode is not as critical, as the region of interest is primarily near or at the disk. Indeed, numerous sets of calculations with various sets of spacings showed negligible effects on the overall solution. For those calculations using a primary current equipotential as the counter electrode, points were chosen to have equal η values. For those cases with cylindrical counter electrodes, equally spaced intervals were usually chosen.

In the axi-symmetric case, point spacing on the axis is irrelevant, since these values are not used in the integration, and need be calculated only for display of the values.

With quadratic spacing, "satisfactory" (see below) results can often be obtained with surprising accuracy even with a limited number of points, especially at low frequencies, where current distribution is more uniform. At the highest frequencies, where the structure of the potential profile has significant detail within one point spacing, the algorithm loses accuracy, as expected with low point density.

Specific values were used for the calculation, in contrast to the dimensionless variables used in [11], but the results can be scaled as desired. The conductivity, κ , of the electrolyte was taken as unity, while the capacitance of the electrode was taken as $100 \mu\text{Fd}/\text{cm}^2$ (actual area for 3-D calculations and capacitance/cm per linear cm for 2-D). Frequencies solved ranged from three decades above the corner frequency (where $\theta \approx 45^\circ$, and the resistive component is approximately equal to the capacitive impedance) to three decades below. In most cases, this resulted in a frequency range of 10^2 to 10^8 Hz, and up to 10^{10} Hz for quartic spacing. It should be remembered that all frequencies can be scaled to actual conditions. Thus, for example, a decrease in conductivity of a factor of 100 lowers all frequencies by two decades.

CRITERIA FOR ACCURACY AND VALIDITY OF SOLUTIONS

In the case of the solutions using primary current equipotentials, the analytic solutions of Newman¹ were used to check the results where applicable. This was not considered to be sufficient, since it is conceivable that overall numerical values could be correct, yet errors could exist in the local values of the variables. Even in this case, the choice of a finite counter electrode *vs.* one at infinity produces differences at finite frequencies. Other criteria must therefore be utilized for all cases.

1. Continued minimization of residual errors.

The sum of the *absolute values* of the residual error $\Sigma \epsilon_j$ ($j=1 \rightarrow N$) over the contour Γ must continue to decrease without limit with increasing number of iterations. Oscillatory convergence is allowed, but not a finite asymptotic value (until the residuals are determined by the truncation error of the precision of the real number set chosen). Thus the final solution will satisfy Laplace's equation and the boundary conditions as closely as desired at all points.

2. Equality of anodic and cathodic currents.

A necessary consequence of the validity of the solution is that Gauss' law be obeyed. That is, even though all points on the boundary are computed independently, the integrals of both the real and imaginary currents into and out of the domains must be separately equal. This is a less stringent requirement than the first, since local variations could integrate to the same overall value. In practice, *when the problem is set up correctly*, these currents agree within the specified convergence tolerance. [This is typically less than 0.01% and often better than 0.001%] In *all* cases where equality was not observed, some error in bookkeeping was "discovered".

3. Other criteria.

a. Interior right-angled corners between conductors— In Fig. 1b, when the top (BC) and right (CD) side segments are both equipotentials, the derivative in the x and y directions must both be zero, and the computed current density in

the corner should be zero. In practice, remembering that the value at a point is only valid in terms of the integral over the line segments containing it, the typical value computed without any imposed constraints is always less than 1 part in 10^5 of the average current density on the remainder of the electrode.

b. It is often possible to derive other special and/or limiting relationships for particular parts of the problem which can be tested separately. It will be shown later that this can be done for the complex current density at the edge of the disk.

RESULTS OF COMPUTATION AND DISCUSSION

Although the analytic solution given by Newman¹ could not be duplicated completely because of the finite number limitations of a numerical solution, a number of points of similarity could be replicated. As pointed out above, at "infinite" frequency the choice of a counter electrode at the location of an equipotential surface as determined from eqn. (22) should have a series solution resistance equal to $R_{\infty} \cdot \phi_{ce}/\phi_0$ ($= 1/4\kappa a \cdot \phi_{ce}/\phi_0$). A series of calculations were done at several resolutions at values for ϕ/ϕ_0 of 0.5, 0.7, 0.9, 0.95 and 0.98 with resolutions of 8, 16, 32 and 64 quadratically spaced points on the disk. Frequencies from 10^3 to 10^8 Hz (with 4 to 16 points per decade) were used for most of the calculations, although some sets were checked with frequencies as low as 10 and as high as 10^{10} Hz [It should be pointed out that a ϕ_{ce}/ϕ_0 value of 0.95 with 64 point resolution with quartic spacing is a severe test of the robustness of the algorithm, since dimensional ratios of the order of 3×10^{-9} to 1 are involved.] Direct comparison can be made between the calculated values at high frequency and R_{∞} from the analytic solution. The ratio of low frequency to high frequency resistance can also be compared. Some results are summarized in Table 1.

It can be seen that at high frequencies the series R_{eff} approaches very closely to the theoretical value. As $\phi_{ce}/\phi_0 \rightarrow 1$ (and $r \rightarrow 0$), the corner frequency increases and a frequency of 10^8 Hz is not sufficient to achieve "infinite frequency behavior" for these large cell/electrode aspect ratios. On the other hand, the use of a small aspect ratio causes significant departure from the anticipated behavior at low frequencies.

Because the solution generates large amounts of data in the form of complex variables, representation in a 2-D plot can be difficult. Referring to Fig. 1, the rotational symmetry of the system means that all points can be represented in terms of the highlighted area. Using this cross section as the X-Y plane in an orthographic projection, the real and imaginary components can be plotted as vectors up and down in the +Z and -Z direction, respectively. The left hand side is the axis of rotation.

After solution of the boundary values, the values of the variable internal to the boundary can be calculated using the same algorithm (14a) or (15a) and plotted as two independent surfaces. [These surfaces appear similar to those produced by a Finite Difference calculation, but are the exact solutions for the linear basis function boundaries.] Any desired resolution can be obtained by the simple expedient of choosing the points. At high resolution, the initial integration time can be 10 to 20 minutes on a VAX 2000 microcomputer, but the coefficients are saved in an array for use at all frequencies. [Because of complexities of programming the plotting of the surface near the curved contour of the counter electrode, these points in the immediate vicinity of the counter electrode are omitted in the figure, but are calculated.]

Figure 2 shows the complex potential profiles for a disk electrode, and the corresponding surfaces for a 20 x 20 array with an "equipotential" counter electrode at $\phi_{ce}/\phi_0 = 0.7$ for a set of six frequencies (3×10^3 , 10^4 , 3×10^4 , 10^5 , 3×10^5 , and 10^6) selected to show the development of the complex potentials at the boundaries as the

frequency is decreased. These curves can be compared to Fig. 3 of ref. 1 remembering that the $\bar{\eta}$ of that paper is in stretched coordinates. [$\bar{\eta} = \eta\sqrt{\Omega}$ where $\Omega = \omega C\tau_0/\kappa$ and $\eta = \sqrt{1-(r/a)^2}$] Thus the apparent reverse curvature of \bar{U}_{or} and \bar{U}_{oi} as $r \rightarrow 0$ there can be misleading and is not present in linear coordinates. From the boundary conditions (19a) it can be seen that the real current density is proportional to the imaginary potential and *vice versa*. The maximum of the real current density is thus *not at the edge* for any finite frequency! Indeed at *all* frequencies lower than 10^4 Hz the highest real current is at the center of the disk!

Of even more interest is the observation that \bar{U}_{or} is *negative* on the interior of the disk at frequencies above 10^5 Hz. [This can be seen from Newman's figure on close examination and on ours before reduction for publication, but is not immediately evident. When we first obtained negative values in our calculations we spent many fruitless hours looking for the "bug".] This means that the imaginary current on the inner part of the disk is negative, and that portion of the electrode appears *inductive*.

Once the values at a regular array inside the domain were determined, standard routines (DEC LGP software) were used to generate equipotential plots of the real and imaginary parts of the variable. In these routines, a uniform grid and linear interpolation is used and thus the resultant curves have no higher resolution than the chosen set of data points. They can be used only as a guide, and do not represent the true contours close to the region of the edge. They are, however, useful in giving an overall picture of the complex potential distribution, and can be generated at any resolution desired (see below). Figures 3a-f show such contours for cases equivalent to those of Fig. 2, but for frequencies of 10^4 to 10^8 Hz. The real contours are plotted with light lines, and the imaginary contours are drawn heavier. The position of the counter electrode and of the disk are marked with an even heavier line.

Figure 4 shows a surface calculated at 10^5 Hz for a much finer grid in the vicinity of the edge. These were also calculated for a 20×20 grid, but only plotted as a 10×10 grid, for clarity in publication after reduction. Figures 5a-f show contour plots of these restricted areas at higher resolution.

Several important points can be observed from these contour plots.

1. It is only at the highest frequencies, that the *real* contours *approach* the equipotentials (ellipsoids of revolution) predicted for primary distribution. At these frequencies, the imaginary contours are more like tightly spaced and skewed hemitoroids centered over the edge.
2. At very low frequencies, the real and imaginary contours approach the same shape, but are never identical, since at these frequencies the real current is highest at the center and the imaginary current is highest at the edge. A significant fraction intersect the surface of the disk, and the solution immediately outside the disk is no longer an equipotential.
3. At all intermediate frequencies, the contours move and change shape from frequency to frequency, and are no longer ellipsoids.
4. At frequencies above the corner, where the disk becomes "inductive", the imaginary contours intersect the surface at an acute angle. Since the current streamlines are normal to the contours, this means that a portion of the imaginary part of the current actually flows *out* of the central part of the disk and *into* the edge region!

Even for the low frequency limit, there is no such thing as an equipotential surface for this system, since any surface where the real part is constant will have significantly different imaginary parts over this surface. Likewise, the concept of an "*IR*" drop is meaningless. At intermediate frequencies, each annular segment has its own resistive element which is different than all others, and is a function of the

frequency, and is different from the IR drop at infinite frequencies.

Without defined equipotential surfaces, the question of where to place the reference electrode takes on new meaning. In a system without frequency dispersion, a reference electrode anywhere along an equipotential will give values equivalent to those at any other point on the same surface. In this case, only the axially symmetric lines (points in cross section) are degenerate. In general, no two asymmetric points will yield the same complex potential values at all frequencies.

While these calculations have been done in the frequency domain, similar considerations apply in the time domain, and will be discussed in a future publication.

The impedance, $Z (= E/I)$, or the admittance, $Y (= 1/Z = I/E)$, of the entire electrode or any portion of it can be determined by simple integration of the real and imaginary components of the current over the desired fraction of the electrode, using linear interpolation between points as needed. The admittance is proportional to this value and the impedance is its complex reciprocal (since the applied voltage is $1 + 0j$), and it can be expressed in terms of an effective series admittance, $G_{\text{eff}} (= \Re Y)$, and capacitance, $C_{\text{eff}} (= \omega \Im Y)$. Both Bode and complex plane admittance plots were generated from the calculations. In most cases, a cubic spline interpolation was used to smooth the data between points for presentation. This procedure was checked by comparison with curves generated with more data points (up to 10 per decade) and no difference was detected.

Fig 6a,b show a Bode plot of the impedance of the disk between 10^4 and 10^6 Hz. The solid line is the calculated curve and the dotted line is the theoretical curve for a series $R (= R_x)$ and $C (= C_0)$. It is clear that there are significant deviations from the "ideal", as expected.

Fig. 7 shows data similar to that of Fig 6 but over the range 10^3 to 10^8 Hz and plotted in the complex admittance plane. These plots show:

A. The admittance of a simple RC network with the value of $R = R_{\text{inf}}$ and $C = C_0$.

B. The admittance of the entire disk and electrolyte.

Also shown are:

C. The admittance of the outer 50% of the area as a ring and its share of the electrolyte resistance.

D. The corresponding admittance of the inner 50% as a disk.

The top dotted curve (a) is the ideal semi-circle for the series $R_x C_0$, while the solid line (b) is for the actual electrode. Curves (c) and (d) are the impedances of the ring and disk (outer and inner 50% of the area) as if they were measured independently with two potentiostats driven at the same potential. The ring impedance shows a significantly "flattened" semi-circle, while the disk shows a clear pseudo-inductive loop at higher frequencies, as indicated above. At the low frequency end of the curve, all four curves intercept the X-axis perpendicularly, while at high frequencies, the ring and the whole disk intercept at a finite angle.

The effect of resolution (number of points per segment) can be seen in Fig. 8a where C/C_{eff} is plotted *vs.* $\log \omega$ for resolutions of 64, 32, 16 and 8 points. Comparing this curve to Fig. 4 of ref. 1, $\partial(C/C_{\text{eff}})/\partial \log \omega$ has the expected limiting value of $2.303/4 = 0.576$ at high frequencies up to $\approx 10^8$ Hz for 64 points, $\approx 2 \cdot 10^7$ for 32, $\approx 5 \cdot 10^6$ for 16, $\approx 1.5 \cdot 10^6$ for 8 points. Clearly, if the point spacing for the points near the edge is not less than that required for $\bar{\eta} = 1$, which is the approximate location of the maximum in \bar{U}_{oi} , a discrete model cannot adequately represent the situation. [This is similar to the Nyquist criterion for harmonic content of digitized signals which states that the sampling rate must be at least twice the frequency of

the highest harmonic]. Using eqns. [9], [16], and [29] of ref. 1, we can obtain

$$\omega_{\max} = \frac{\Omega}{Cr_0} = \frac{\bar{\eta}^2}{\eta^2 Cr_0} = \frac{\bar{\eta}^2}{(1-(r/r_0)^2)Cr_0} \quad (23)$$

With the geometry used to obtain Fig. 8a, $C = 81.56 \mu\text{Fd}/\text{cm}^2$, $r_0 = 0.509525$ cm, and for the first point inside the disk is $r_{63} = 0.50940$. Thus the maximum frequency for which satisfactory results can be expected (for $\bar{\eta} = 1$) is $\sim 4.9 \times 10^7$ Hz. For 32 points $r_{31} = 0.50903$, yielding 1.24×10^7 Hz, for 16 points $r_{15} = 0.50754$ and $\omega_{\max} \approx 3.1 \times 10^6$ Hz and for 8 points $\omega_{\max} \approx 7.8 \times 10^5$ Hz, in excellent agreement with the observed values. In Fig. 8a, vertical dotted lines are drawn at these frequencies, showing that the computed curve deviates observably at about twice this number. The algorithm gives accurate solutions up to frequencies where fine structure of the actual boundary values is smaller than the resolution utilized. Doubling the resolution near the edge increases the frequency range of validity by a factor of four. [It should be noted that even above ω_{\max} the solution still converges, i.e. is stable, but the values are not correct.] A similar curve for a 64 point 2-D calculation with the same geometry is also shown in Fig. 8a. The C/C_{eff} curve is also straight, but with an obviously different slope. This is in contradiction to the implication in ref. [1] that the high frequency limit should be valid for any flat electrode in a plane with an edge. Fig. 8b shows the C/C_{eff} curves for a 2-D geometry like that of fig. 1b. In this case, the segment AB is a plane of symmetry, and the counter electrodes BC and CD are vertical and horizontal planes. Impedances are calculated per cm of electrode length. The two curves represent the values when segments BC or CD were used for the counter electrode. The third curve is the 2-D curve from fig. 8a computed with the same shape "Equipotential" electrode as for the 3-D curves. Clearly the proximity of the counter electrode to the edge changes this slope by more than 55%. This illustrates the desirability of using a geometry as close as possible to reality when modeling.

Table 2 shows the local current density at selected points from the edge to the center for a ϕ_{ce}/ϕ_0 ratio of 0.7 at three different resolutions at 10^6 Hz. It can be seen that agreement is very good where changes are slow, and where changes are more rapid (such as at $r = 0.5075$) the low resolution value is higher to give an overall integrated current value equivalent to that at higher resolution. Note the cross-over from capacitive currents to inductive currents between 0.4916 and 0.4777, marked with a "†". A "‡" marks the maximum in the real current density.

That the I-BIEM converges to the best integral fit for straight line elements can be seen from Table 3 which shows the agreement between several integrated quantities for the same geometry at 10^6 Hz as a function of resolution. It can be seen that even with only 8 points on a segment, which has an ω_{\max} below 10^6 , this agreement is typically better than 0.5%.

In order to obtain a higher resolution near the edge for higher frequencies, a quartic spacing was used. Table 4 shows the local values of the variables for quadratic and quartic spacings for several frequencies, using 64 points per segment. [Note that for quadratic spacing, 10^8 Hz is at the limiting frequency, ω_{\max} . For quartic spacing, however, $\omega_{\max} \approx 10^{11}$ Hz, and the results should still be valid. Table 5 shows that this appears to be the case.

From Fig 3 of ref. 1 it can be seen that at the edge ($\bar{\eta} = 0$), the values of \bar{U}_{or} and \bar{U}_{oi} are equal in the high frequency limit. From the boundary conditions (19a), this also implies that $\partial \bar{U}_{or}/\partial n$ and $\partial \bar{U}_{oi}/\partial n$ are equal and opposite in sign, and their magnitudes should increase as $\sqrt{\omega}$. Examination of the values of the local current density at the edge from Tables 2 and 4 show that this is indeed the case. The limiting current density at the edge approaches $(1-j)\cdot\infty$, not infinity, with a

constant phase angle of -45° !

It may be instructive to consider the effect of *real* dimensions on the current density at the edge. A real electrode, polished with real abrasives on real polishing cloth is unlikely to have a mathematically sharp edge. Repeated metallographic examination of well polished electrodes in this laboratory has shown that the edge will round to a radius of the order of a micron or more. Even a disk made by e.g. evaporation through a mask is likely to have a thickness, and therefore an edge size of the order of 0.1μ . This would put the system in the range of the first column of Table 2, and the current density at the edge would likely be no more than 10-30 times that at the center at the highest frequencies attainable in the laboratory. There is still a substantial problem with frequency dispersion, but the conceptual problem of "infinite" current density disappears, as does the problem of the "singularity" there.

Once the value of R_∞ has been found, it is interesting to do an "IR correction" of the data. If one had a "perfect" potentiostat, with IR correction (*not* compensation) capabilities, one could, in principle, subtract the "IR drop" and examine the behavior of the residual impedance of the double layer, and the rest of the included uncompensated solution resistance. Fig. 9 shows the Bode plot of the results of such a calculation. At low frequencies, there is a small series resistance, $R_\omega - R_\infty$ left uncorrected. However, this is small compared to the expected impedance of the capacitor (with $\partial \ln|Z|/\partial \ln\omega \approx -1$) below the "corner frequency" at $\omega \approx 10^4 - 10^5$ Hz, where this residual resistance is beginning to drop off, as shown in Fig. 10. Instead, above this frequency, the residual impedance curve has a smaller slope and the corresponding phase angle drops to a phase angle of $\approx -77^\circ$ to -85° . It can be shown simply that this behavior is compatible with the Kramers-Kronig relations using the algorithm in the Appendix.

With four points per decade, and integrating from the values of the residual impedance curve of Fig. 9, using values of -1 for the slopes below and above the minimum and maximum calculated frequencies, it can be seen from Figure 11 that excellent agreement is obtained up to about 10^7 Hz. The deviation above that frequency is caused by the assumed slope of -1 , and by small residual errors in the infinite frequency subtraction.

DISCUSSION

The finiteness of the geometry of the rotating disk and its associated cell configuration has been shown to have a significant effect on its high frequency behavior. While the analytic solution of this problem is useful in determining trends in behavior, the idealizations and approximations required for these solutions can lead to conclusions that are not necessarily realistic for real systems. A real cell does not have infinite extent, nor does it have ideally sharp corners or smooth surfaces, nor are frequencies much above 1MHz readily produced in the typical electrochemical potentiostatic setup.

With these restrictions in mind, the often referred to problem of the current at the edge going to infinity is far from the real situation. This is not to imply that the RDE is a good configuration for AC or for transient measurements. The current distribution is distorted as a result of the general configuration and not just because of the edge. The pseudo-inductive behavior of the central part of the disk will complicate any attempt at analysis of non-steady state behavior.

ACKNOWLEDGMENTS

The author would like to acknowledge the support of NASA Lewis Research Center and the Ohio Aerospace Institute for part of this work.

APPENDIX

From Bode¹³,
$$\theta_c = \frac{1}{\pi} \int_{-\infty}^{\infty} \frac{\partial \ln|Z|}{\partial u} \ln \operatorname{ctnh} \frac{|u|}{2} du \quad (24)$$

where $u = \ln(\omega/\omega_c)$. If $\partial \ln|Z|/\partial u$ is constant, it can be taken out of the integral. Since the definite integral has the value $\pi^2/2$, eqn. (24) then becomes

$$\theta_c = \frac{1}{\pi} \frac{\partial \ln|Z|}{\partial u} \int_{-\infty}^{\infty} \ln \operatorname{ctnh} \frac{|u|}{2} du = \frac{1}{\pi} \frac{\partial \ln|Z|}{\partial u} \frac{\pi^2}{2} = \frac{\partial \ln|Z|}{\partial u} \frac{\pi}{2} \quad (25)$$

For an ideal capacitor with a slope of -1 , the phase angle is -90° , and for a slope slightly less, the phase angle will decrease correspondingly. Similarly, for an ideal resistor, the slope is zero and the phase angle is zero.

In this case, the expected phase angle at a frequency ω_c can be calculated from eqn. (24) by splitting it into three parts. Thus

$$\theta_c = \frac{1}{\pi} \left[\frac{\Delta \ln|Z|}{\Delta u} \Big|_0 \int_{-\infty}^{u_1} \ln \operatorname{ctnh} \frac{|u|}{2} du + \sum_{n=1}^{N-1} \frac{\Delta \ln|Z|}{\Delta u} \Big|_n \int_{u_n}^{u_{n+1}} \ln \operatorname{ctnh} \frac{|u|}{2} du + \frac{\Delta \ln|Z|}{\Delta u} \Big|_N \int_{u_N}^{\infty} \ln \operatorname{ctnh} \frac{|u|}{2} du \right] \quad (26)$$

where $u_n = \ln(\omega_n/\omega_c)$, ω_n is a parameter of integration, and $\Delta \ln|Z|/\Delta u|_n$ is the average slope over the n^{th} interval. If, as in this problem, we have chosen equally spaced frequencies over a logarithmic scale, the evaluation in this form is simple in a computer. Remembering that the function $F(u) = \ln \operatorname{ctnh}(|u|/2)$ is symmetric around $u_c = \ln(\omega_c/\omega_c) = 0$, and has a logarithmic singularity at that point, we can evaluate the sub-integrals of the second (summation) term for each n from 1 to some appropriate number, M , with adaptive (or other) quadrature, and stored in an array, KK . [In practice, three to four decades is completely adequate, since the value of the integral is less than 10^{-9} beyond that point.] Choosing values for $\Delta \ln|Z|/\Delta u|_0$ and $\Delta \ln|Z|/\Delta u|_N$ as logical extensions of the low and high frequency limits or by

evaluation of some analytic extension, the following pseudo-algorithm can be used to find the expected values of θ_c , the I^{th} term.

1. Zero INT[I] and Zero KK[J] (J = 0 to M + N)
2. (Values of sub-integral)/ π \Rightarrow KK[J] (J = 0 to M \approx 30)
3. $\Delta \ln|Z|/\Delta u|_n$ \Rightarrow DZ[I] (I = 1 to N-1)
4. $\Delta \ln|Z|/\Delta u|_0$ \Rightarrow DZ[0]
5. $\Delta \ln|Z|/\Delta u|_N$ \Rightarrow DZ[N]
6. $m = I - M - 1$
6. For $k = -M$ to 0 do {left side of integral}
 - 7a. if $m < 1$ then INT[I] := INT[I] + DZ[0]*KK[ABS(k)]
 - 7b. else if $m \geq N$ then INT[I] := INT[I] + DZ[N]*KK[ABS(k)]
 - 7c. else INT[I] := INT[I] + DZ[m]*KK[ABS(k)]
 - 7d. $m = m + 1$
8. For $k = 0$ to M do steps 7. {right side}
9. Return INT[I]/ π

Table 1. Effective resistance as a function of domain size (quadratic spacing)

| ϕ_{ce}/ϕ_0 | Radius | $R_c(10^8\text{Hz})$ | $R_\infty(\text{anal.})$ | R_c/R_∞ | $R(10^3)/R(10^8)$ |
|-----------------------------|----------|----------------------|--------------------------|----------------|-------------------|
| 0.5 | 1.00000 | 0.12500 | 0.125 | 1.00000 | 1.15776 |
| 0.7 | 0.509525 | 0.34349 | 0.343454 | 1.00011 | 1.11511 |
| 0.9 | 0.158384 | 1.42110 | 1.42060 | 1.00035 | 1.08970 |
| 0.95 | 0.078702 | 3.01975 | 3.01771 | 1.00068 | 1.08536 |
| Analytic (R_0/R_∞) | | | | | 1.08076 |

Table 2. Local current density along disk at 10^6 Hz

| Point radius _n | $i_n(64 \text{ pt.})$ | $i_n(32 \text{ pt.})$ | $i_n(16 \text{ pt.})$ |
|---------------------------|-----------------------|-----------------------|-----------------------|
| 0.5095 | 11.025-j11.455 | 11.049-j11.434 | 11.135-j11.349 |
| 0.5094 | 11.219-j11.131 | | |
| 0.5090 | 11.537-j10.401 | 11.561-j10.380 | |
| 0.5084 | 11.818-j9.414 | | |
| 0.5075 | 11.981-j8.268 | †12.009-j8.245 | †12.107-j8.150 |
| 0.5064 | †11.986-j7.045 | | |
| 0.5050 | 11.817-j5.817 | 11.846-j5.789 | |
| 0.5034 | 11.483-j4.645 | | |
| 0.5016 | 11.008-j3.573 | 11.033-j3.537 | 11.123-j3.398 |
| 0.4916 | 8.388-j0.695 | 8.391-j0.652 | 8.399-j0.489 |
| 0.4777 | †6.011+j0.226 | †5.994+j0.253 | †5.926+j0.359 |
| 0.4598 | 4.521+j0.297 | 4.504+j0.304 | 4.434+j0.337 |
| 0.4379 | 3.663+j0.206 | 3.653+j0.207 | 3.614+j0.207 |
| 0.4120 | 3.127+j0.135 | 3.122+j0.135 | 3.103+j0.131 |
| : | : | : | : |
| 0.2229 | 2.002+j0.030 | 2.001+j0.030 | 1.999+j0.029 |
| 0.1783 | 1.912+j0.025 | 1.912+j0.024 | 1.909+j0.024 |
| 0.1194 | 1.848+j0.021 | 1.848+j0.021 | 1.846+j0.021 |
| 0.0617 | 1.809+j0.019 | 1.809+j0.019 | 1.807+j0.019 |
| Center | 1.795+j0.018 | 1.796+j0.018 | 1.793+j0.018 |

Table 3. Calculated values for macroscopic variables at 10^6 Hz
(64 pt.) (32 pt.) (16 pt.) (8 pt.)

| | (64 pt.) | (32 pt.) | (16 pt.) | (8 pt.) |
|------------------------------|------------------|-----------------|-----------------|-----------------|
| Integrated Current | | | | |
| I_{ce} | -2.86756+j0.1595 | -2.8682+j0.1596 | -2.8705+j0.1599 | -2.9264+j0.1613 |
| I_{we} | 2.86753-j0.1595 | 2.8680-j0.1596 | 2.8698-j0.1600 | 2.9242-j0.1615 |
| I_{ring} | 2.0057-j0.1751 | 2.0063-j0.1752 | 2.0089-j0.1755 | 2.0182-j0.1763 |
| I_{disk} | 0.8619+j0.0156 | 0.8619+j0.0156 | 0.8616+j0.0155 | 0.8528+j0.0150 |
| R_{eff} (ohms) | 0.34765 | 0.34758 | 0.34729 | 0.34616 |
| C_{eff} (μFd) | 51.71674 | 51.71975 | 51.68149 | 51.59226 |
| Phase shift | 3.1835° | 3.1839° | 3.1889° | 3.2048° |

Table 4. Local values for different spacings and frequencies

| Spacing ω (Hz) | Quadratic | Quartic | | |
|--------------------------|-----------------|-----------------|----------------------------|----------------------------|
| | 10^8 | 10^8 | 10^9 | 10^{10} |
| cm from edge | | | | |
| 0.0 | †118.48-j105.95 | 112.87-j112.49 | 357.08-j352.41 | 1147.75-j1104.8 |
| 6.0×10^{-8} | . | 112.95-j112.38 | 358.83-j349.57 | 1178.20-j1046.8 |
| 9.5×10^{-7} | . | 113.75-j111.06 | 371.77-j319.89 | †1197.26-j554.08 |
| 4.8×10^{-6} | . | 115.95-j106.56 | †385.72-j232.86 | †615.64+j118.47 |
| 1.5×10^{-5} | . | 119.16-j97.03 | 352.53-j102.99 | 333.33+j18.73 |
| 3.7×10^{-5} | . | †121.63-j81.36 | 254.93-j5.013 | 194.07+j4.65 |
| 7.7×10^{-5} | . | 120.39-j58.55 | †155.84+j15.96 | 140.33+j2.504 |
| 1.4×10^{-4} | . | 112.56-j36.95 | 107.11+j7.85 | 104.83+j1.721 |
| 2.4×10^{-4} | 99.76-j5.8. | 97.65-j15.84 | 80.68+j3.45 | 78.84+j1.067 |
| 3.9×10^{-4} | . | 78.66-j2.22 | 63.95+j1.84 | 63.10+j0.092 |
| 6.0×10^{-4} | . | †60.58+j3.49 | 51.70+j1.21 | 51.38+j0.148 |
| 8.7×10^{-4} | . | 46.82+j4.05 | 42.54+j0.74 | 42.43+j0.131 |
| 9.8×10^{-4} | †38.32+j6.47 | . | . | . |
| 1.2×10^{-3} | . | 37.65+j2.91 | 35.75+j0.32 | 35.67+j0.077 |
| 1.7×10^{-3} | . | 31.45+j1.90 | 30.51+j0.27 | 30.41+j0.037 |
| 2.2×10^{-3} | 26.47+j0.96 | . | . | . |
| 2.3×10^{-3} | . | 26.87+j1.28 | 26.32+j0.19 | 26.25+j0.020 |
| 3.0×10^{-3} | . | 23.28+j0.905 | 22.92+j0.16 | 22.89+j0.014 |
| 3.9×10^{-3} | 20.09+j0.58 | 20.39+j0.65 | 20.14+j0.12 | 20.14+j0.012 |
| ... | ... | ... | ... | ... |
| Center | 1.7844+j0.00048 | 1.7845+j0.00049 | 1.7845+j3x10 ⁻⁴ | 1.7844+j1x10 ⁻⁵ |

Table 5. Calculated values for macroscopic variables at several frequencies

| Spacing ω (Hz) | Quadratic | Quartic | | |
|--------------------------|-----------------|-----------------|------------------|----------------------------|
| | 10^8 | 10^8 | 10^9 | 10^{10} |
| Integrated Current | | | | |
| I_{ce} | -2.9114+j0.0028 | -2.9113+j0.0028 | -2.9117+j0.00034 | 2.9117+j4x10 ⁻⁵ |
| I_{we} | 2.9114-j0.0028 | 2.9113-j0.0028 | 2.9117-j0.00034 | 2.9117-j4x10 ⁻⁵ |
| I_{ring} | 2.0585-j0.0032 | 2.0583-j0.0032 | 2.0587-j0.00039 | 2.0589-j5x10 ⁻⁵ |
| I_{disk} | 0.8529+j0.0004 | 0.8530+j0.0004 | 0.8529+j0.00005 | 0.8528+j1x10 ⁻⁵ |
| R_{eff} (ohms) | 0.34348 | 0.34349 | 0.34345 | 0.34345 |
| C_{eff} (μ Fd) | 30.09175 | 30.24806 | 25.03443 | 21.49044 |
| Phase shift | 0.0554° | 0.0551° | 0.0067° | 0.0008° |

REFERENCES

- ¹ J. Newman, *J. Electrochem. Soc.*, **117**, 198 (1970).
- ² Glarum, *Calculation from variational calculus*.
- ³ Other refs here.
- ⁴ B. D. Cahan, D. Scherson, and M. A. Reid, *J. Electrochem. Soc.*, **135**, 285 (1988)
- ⁵ "On the Iterative Boundary Element Method", B. D. Cahan and O. Lafe, in "Computational Engineering with Boundary Elements", Vol. 2, 367-376, A. H-D. Cheng, C. A. Brebbia, and S. Grilli, eds., Proceedings of the 5th International Conference on Boundary Element Technology, July 1990.
- ⁶ B. D. Cahan, O. Lafe, in preparation.
- ⁷ J. A. Liggett and P. L-F. Liu, "The Boundary Integral Equation Method for Porous Media Flow", Chap. 6, Allen and Unwin, Boston (1983).
- ⁸ M. Abramowitz and I. A. Stegun, "Handbook of Mathematical Functions", New York, Dover, 1974.
- ⁹ R. Bullirsch, "Numerical Calculation of Elliptic Integrals and Elliptic Functions", Handbook Series Special Functions, Numerische Mathematik Vol. 7, 1965, pp.78-90.
- ¹⁰ "Computational Engineering with Boundary Elements", A. H-D. Cheng, C. A. Brebbia, and S. Grilli, eds., Proceedings of the 5th International Conference on Boundary Element Technology, July 1990.
- ¹¹ Scientific American...
- ¹² J. Newman, *J. Electrochem. Soc.*, **113**, 501 (1966).
- ¹³ H. W. Bode, *Network Analysis and Feedback Amplifier Design*, D. van Nostrand Co. (1945)

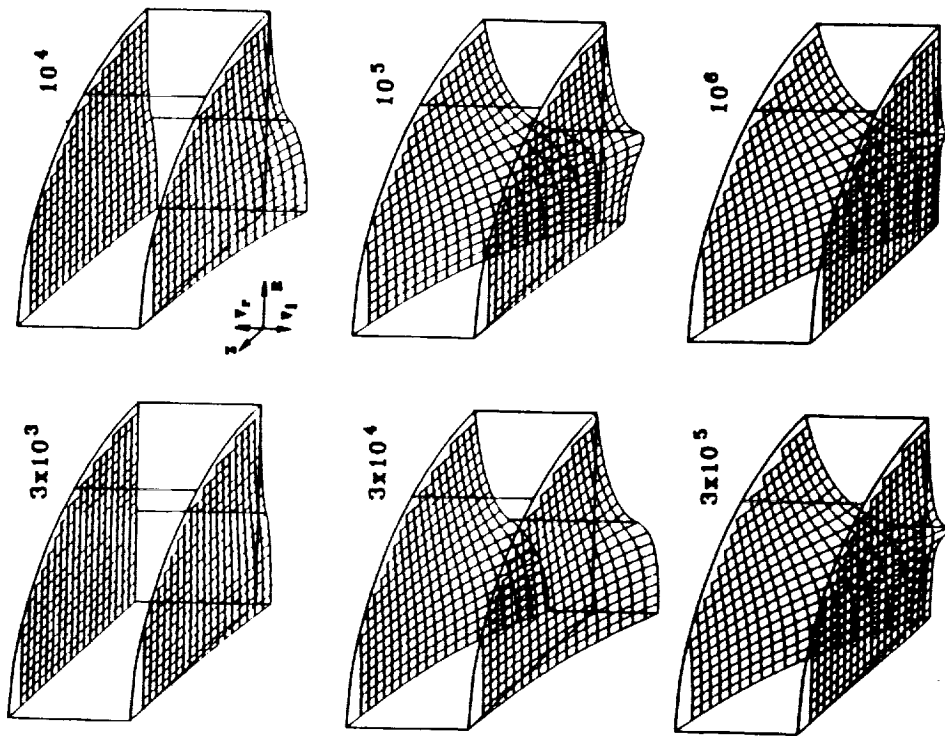


Fig. 2. Complex potential profiles for a cell of form 1A with $\xi = 0.7$. Dimensions: cell height: 1cm., cell radius: 1.122 cm, disk radius: 0.509 cm. a - f: Profiles and potential surfaces for frequencies of 3×10^3 , 10^4 , 3×10^4 , 10^5 , 3×10^5 and 10^6 Hz with 20×20 grid. Inset shows coordinate axes.

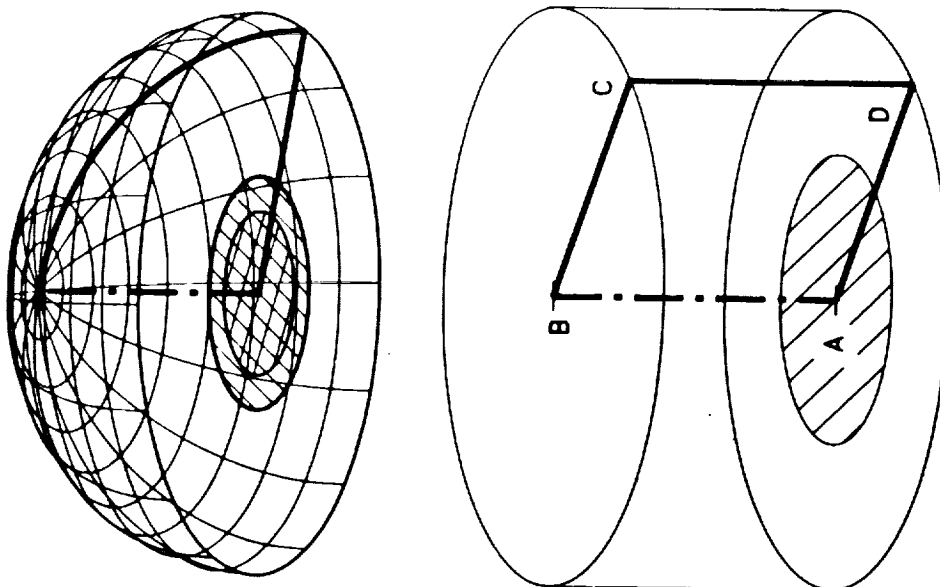


Fig. 1. Geometries of cells modeled by program. Disk (and/or ring-disk) shaded. Cross-section in bold outline, with dot dashed line as axis of symmetry: A. Top - Ellipsoidal counter electrode at a position equivalent to an equipotential of an electrode at "infinity", B. Bottom - Cylindrical counter electrode.

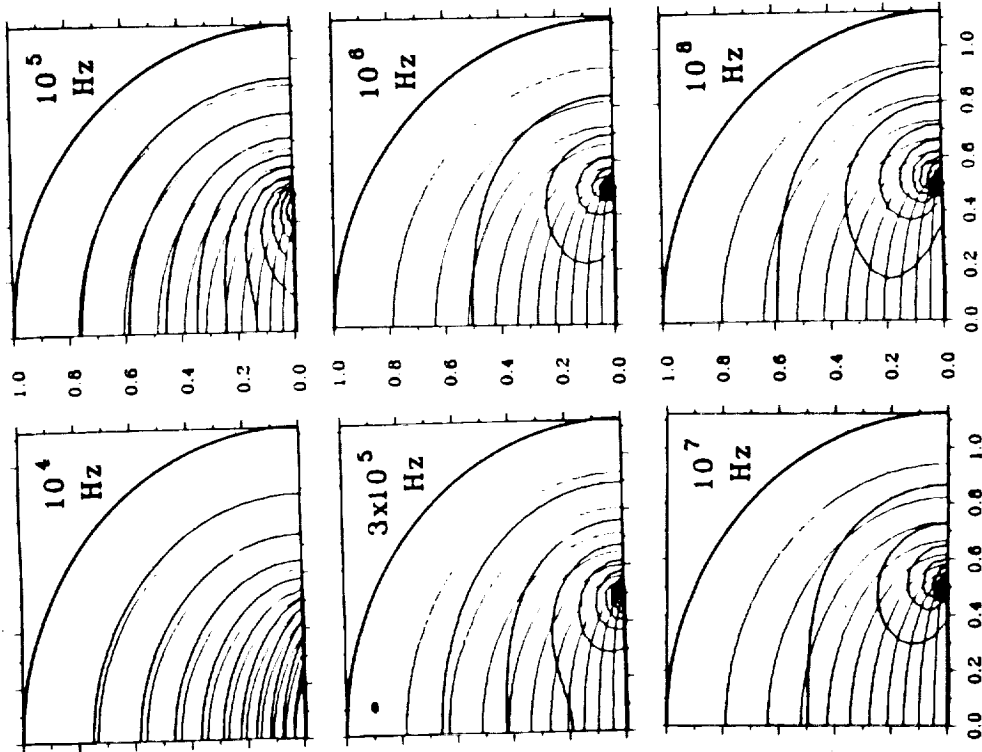


Fig. 3 Contour plots of surfaces similar to those generated for fig. 2. Frequencies are 10^4 , 10^6 , 3×10^5 , 10^6 , 10^7 and 10^8 Hz. Real equipotentials are light lines, imaginary values are bold.

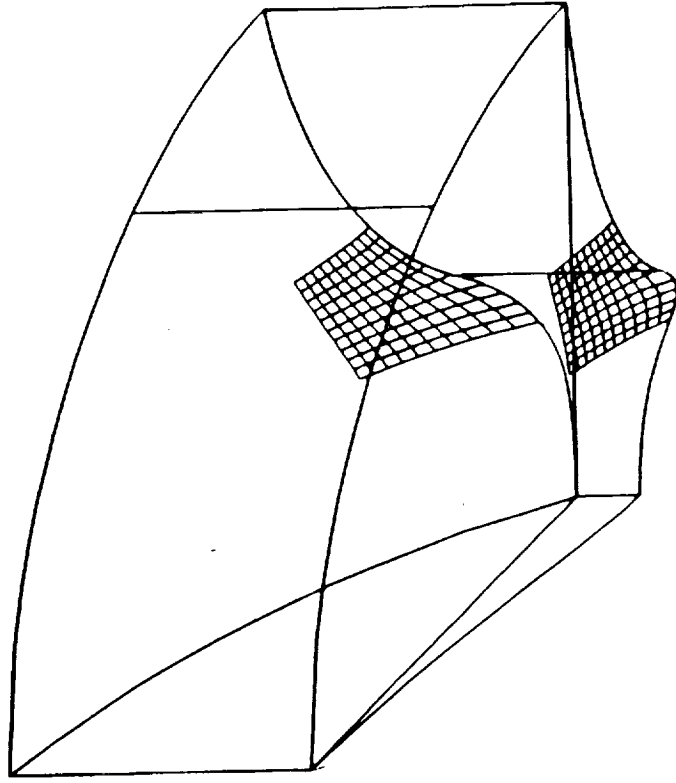


Fig. 4. Potential profile and surface for 10^9 Hz, showing small grid used for calculation of Fig. 5.

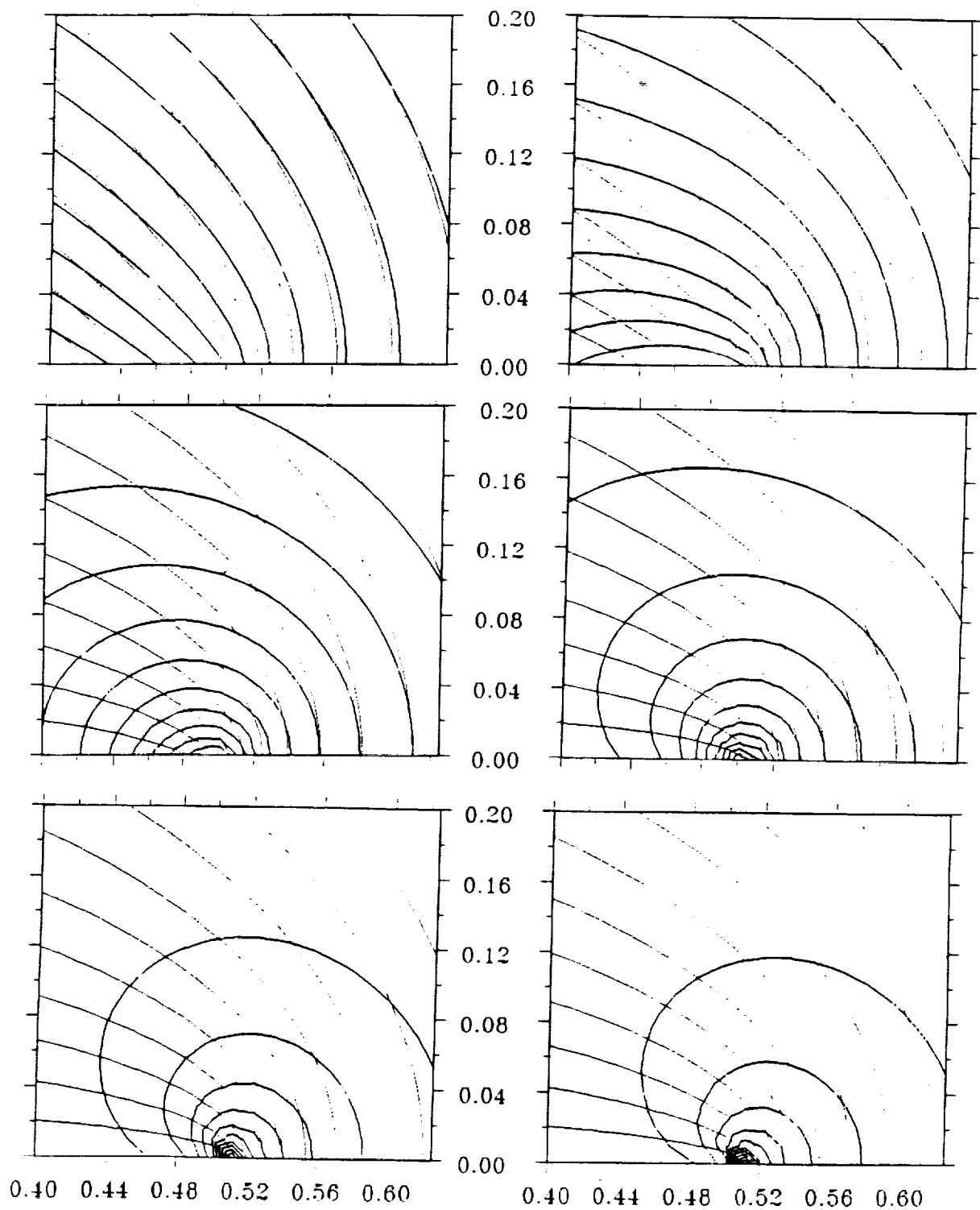


Fig. 5. Contour plots of surfaces similar to those of Fig. 4. Expanded in the region of the edge from Fig. 3. Frequencies are 10^4 , 10^5 , 3×10^5 , 10^6 , 10^7 and 10^8 Hz. Disk edge is at 0.509.

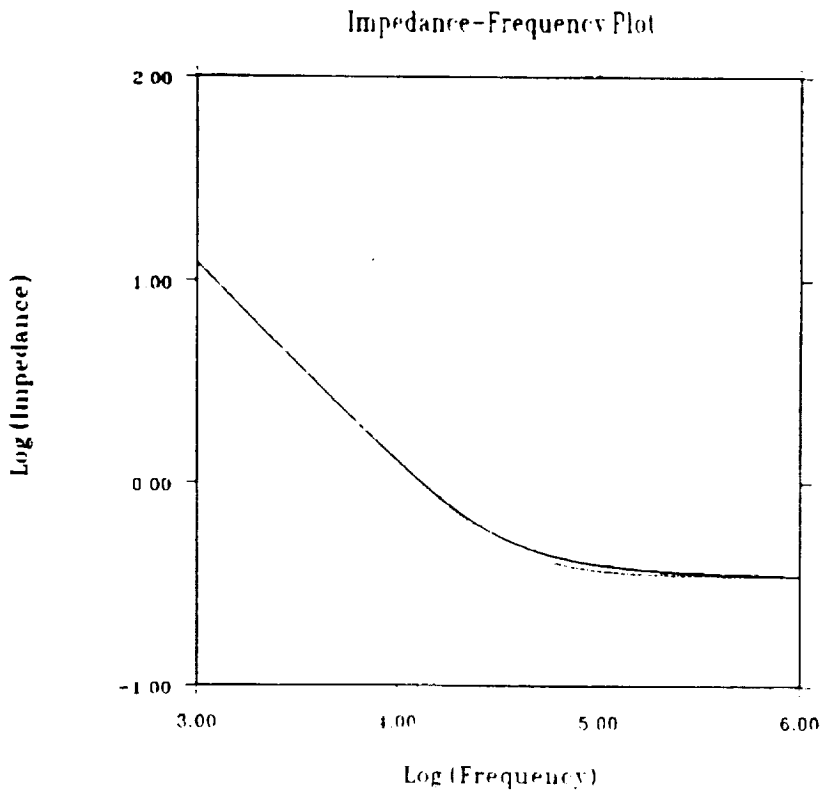
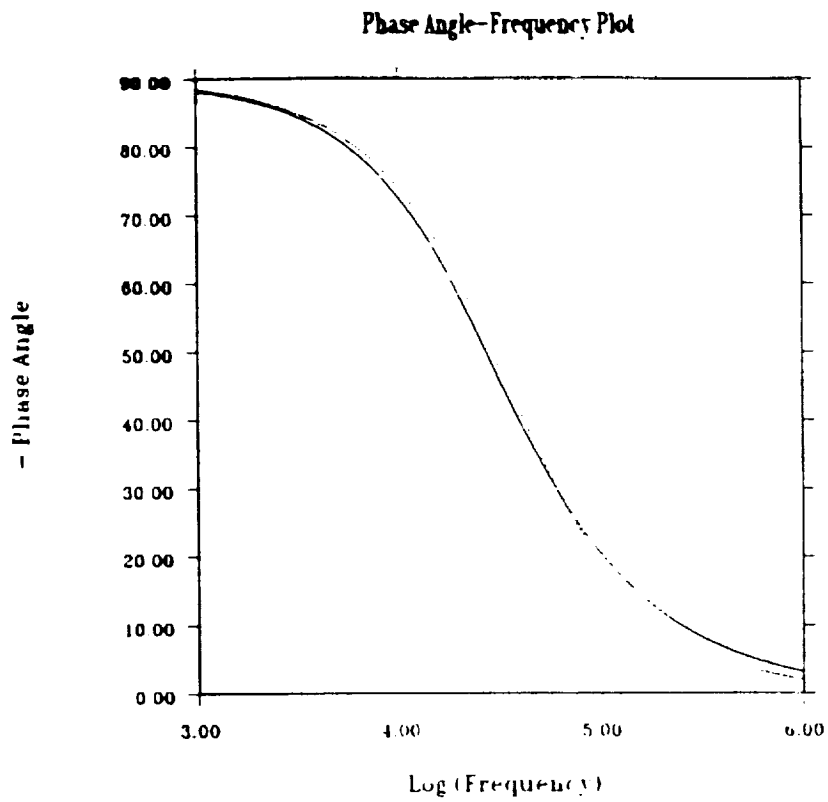


Fig. 6. Bode plots of the cell impedance over the frequency range of 10^3 to 10^6 Hz. Solid lines - total cell impedance, dotted line - impedance of a series equivalent circuit of R_1 and C_0 . a. Top:- Phase angle vs. $\log \omega$ b. Bottom:- $\log |Z|$ vs. $\log \omega$.

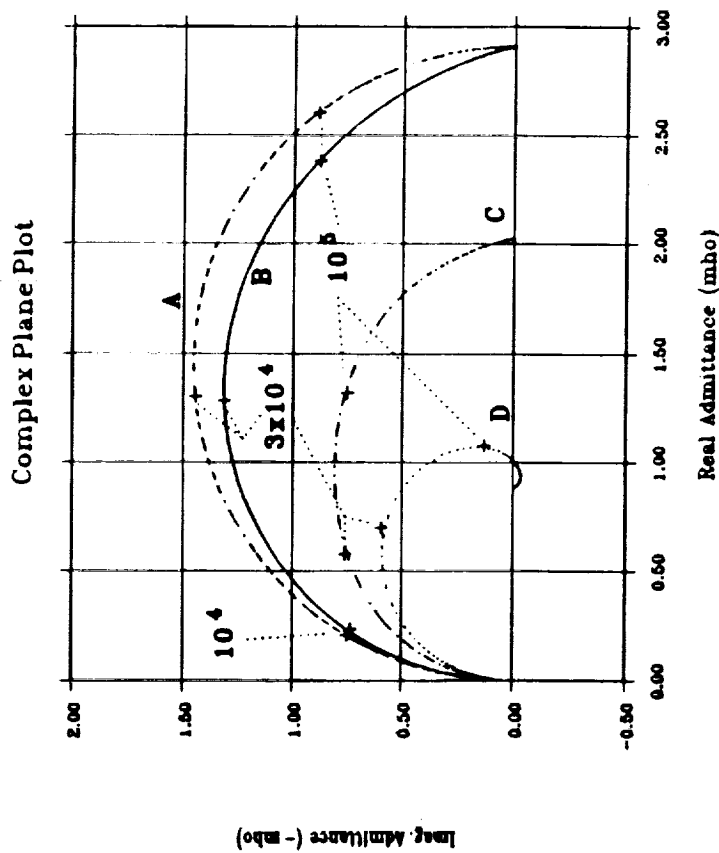


Fig. 7. Complex admittance plane plot of data of Fig. 6 with current integrated separately for ring and disk. Ring (or outer) radius - 0.509 cm, disk radius - 0.3603 cm. A - series equivalent circuit $R_e C_e$. B - Admittance of ring and disk combined. C - Admittance of ring only. D - Admittance of disk only. Note pseudo-inductive loop at high frequency end. Curve generated from 41 data points (8 per decade), but only a few frequencies labelled for orientation.

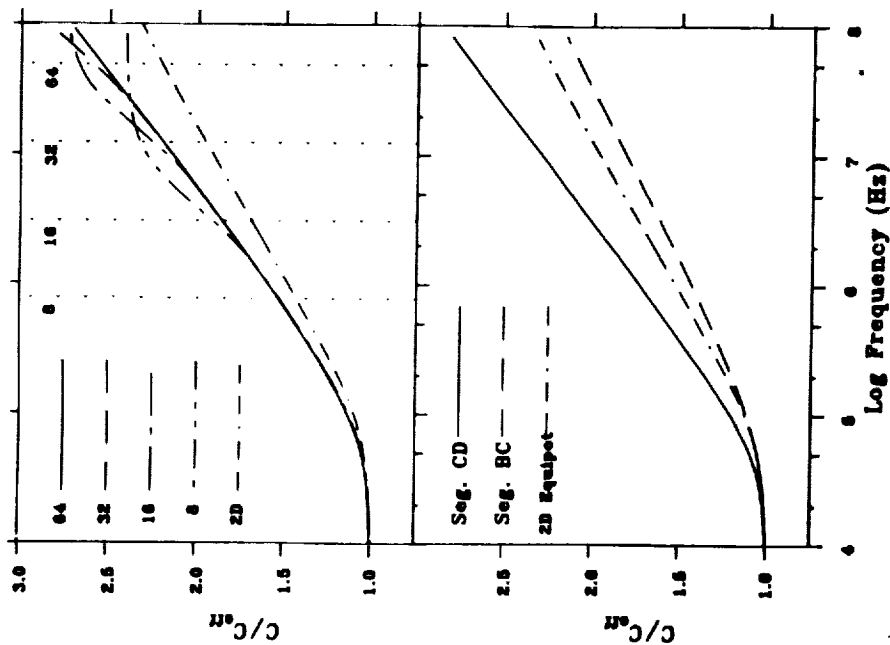


Fig. 8. A - top. C/C_{err} vs. $\log \omega$ as a function of resolution used in calculation. Labeled dotted lines indicate upper frequency for validity of solution. 64 pts. - - - 32 pts. - - - 16 pts. - - - 8 pts. - - - Also included is 2-D calculation using counter electrode at the same position. B - bottom. C/C_{err} vs. $\log \omega$ for 2-D geometry as a function of counter electrode position (see Fig. 1b). - - - Vertical planar electrode in position CD. - - - Horizontal counter electrode in position BC. Also included is 2-D curve from Fig. 8A.

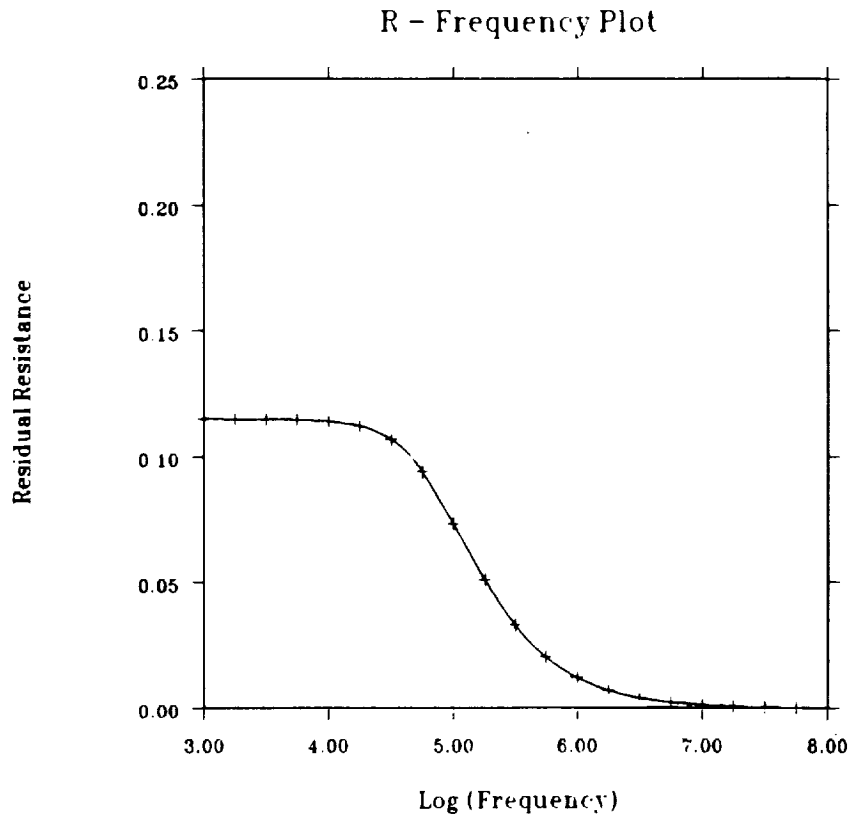


Fig.9. Residual resistance of fig. 4 (after subtraction of R_{ω}) vs. $\log \omega$.

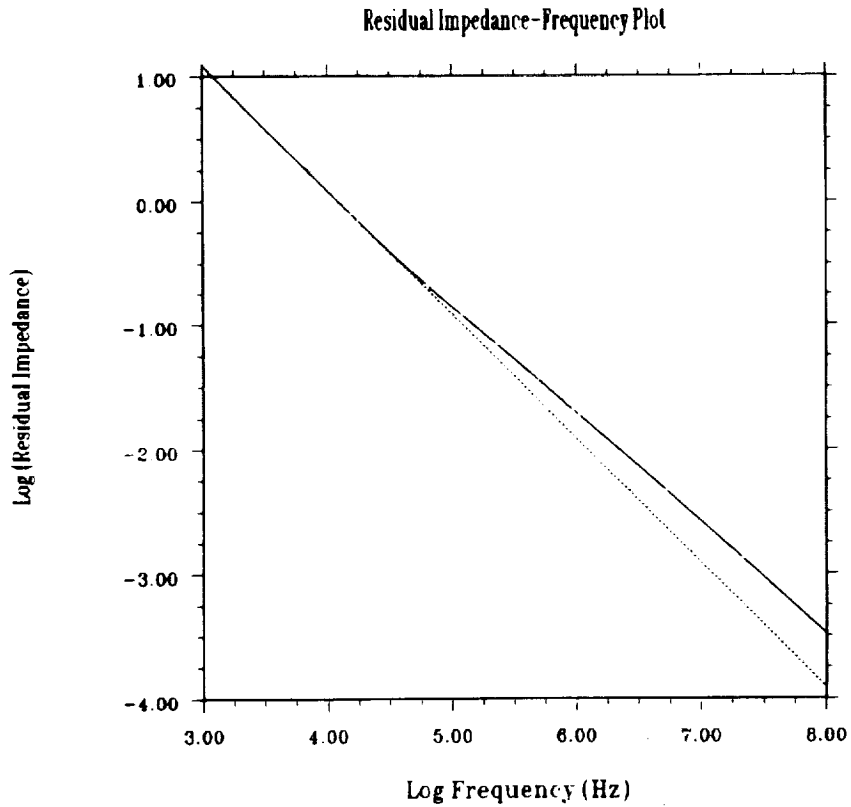


Fig.10. Solid line:- Bode plot of residual impedance from Fig. 4 after subtraction of R_{ω} . Dotted line:- Theoretical impedance of ideal capacitor with value equal to C_0 .

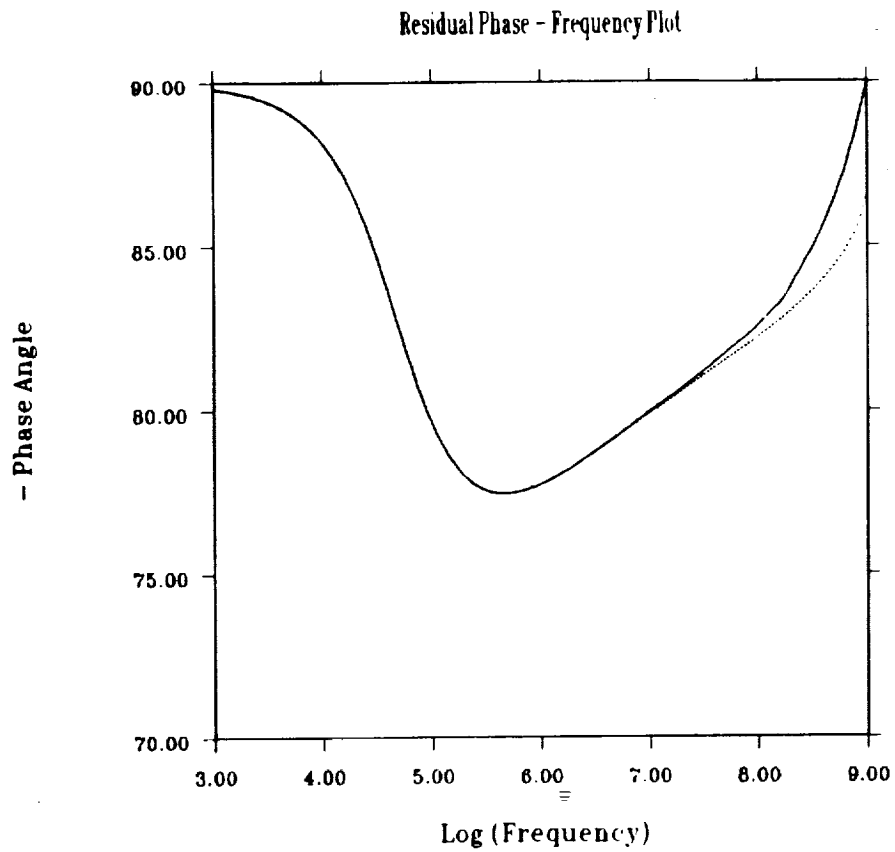


Fig.11. Result of K-K integration of data from Fig. 10. Solid line:- calculated values. Dotted line:- results of K-K integration.

**REGENERATIVE FUEL CELL ARCHITECTURES
FOR LUNAR SURFACE POWER**

D.W. Harris, S.P. Gill, T.M. Nguyen, and J.J. Vrolyk
Rocketdyne Division
Rockwell International
Canoga Park, California 91303

ABSTRACT

Power needs projected for the lunar and Mars exploration missions range from a few kilowatts for initial manned outposts and rovers to hundreds of kilowatts for permanent bases and in-situ resource utilization. The 354 hour lunar night presents a formidable challenge in energy storage systems for non-nuclear power systems. The Photovoltaic/Regenerative Fuel Cell (PV/RFC) power system is currently being considered as an option to meet the initial low power requirements.

For lunar applications, the RFC mass can be a critical driver in the overall PV/RFC system mass. For the long duration nighttime operation missions, the hydrogen/oxygen (H₂/O₂) reactants and storage are the dominant components from a mass standpoint. It is important, therefore, to examine options which may reduce the reactant and storage mass and, thereby, result in mass savings for the overall PV/RFC system.

Various RFC configurations for the stationary lunar missions has been examined using Rocketdyne's RFC computer model. For the stationary applications, a GaAs/Ge PV array with a 3000 psi gas storage proton exchange membrane (PEM) RFC providing 25 kWe during the day and 12.5 kWe at night was designed. PV/RFC systems utilizing super-critical H₂/O₂ storage and Cryogenic H₂/O₂ storage for the RFCs were then compared with the baseline high pressure gas storage RFC system. Preliminary results indicate that for long duration nighttime operation missions, the super-critical H₂/O₂ storage RFC systems offer over 20% mass advantage over the high pressure gas storage while the mass savings for the cryogenic H₂/O₂ storage RFC systems can be as high as 30%.

INTRODUCTION

To meet the challenge of president Bush's Space Exploration Initiative (SEI), NASA has conceptualized a set of different options that will facilitate the human exploration of the moon and Mars. Power needs projected under these options range from a few kilowatts for the initial manned outposts and mobile systems to hundreds of kilowatts for permanent bases and in-situ resource development. Figure 1 illustrates the range of power needs identified by NASA for their options 1, 5, and 5A. As shown, the maximum nighttime power requirements may be as high as 320 kWe. This presents a formidable challenge in energy storage system technologies for non nuclear power systems.

The objective of this work was to compare the mass of several methods of storing the reactants in a Regenerative Fuel Cell (RFC). The reactants were limited to a single set, namely water/hydrogen/oxygen. The storage conditions were further restricted to storing the water as liquid and the hydrogen and oxygen to one of the following three states: 1) as room temperature gas at high pressure (3000 psia and 60 F), 2) as cryogenic liquids at low pressure (315 psia, -419F(O₂), -292F(H₂)), and 3) as super-critical gas at cryogenic temperatures and at high pressure (-325F and 3000 psia).

Although initially, this study was for a Lunar mission environment, it was believed that the results would be applicable for use in preliminary studies for a Mars mission, since the percentage differences between storage methods should be comparable. In addition, this would reduce the Mars study cost since only relatively simple modifications would be required to adapt existing Lunar study calculations to the Mars conditions.

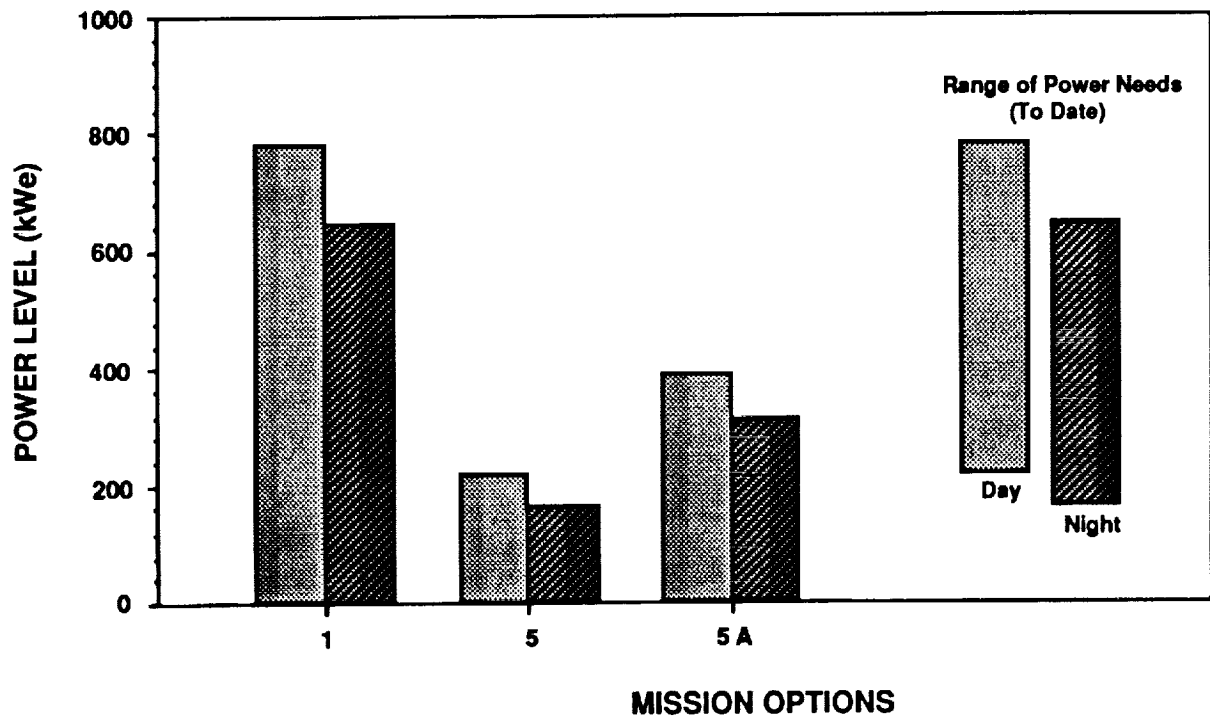


Figure 1: Lunar Surface Power Requirements

ANALYSIS

Modeling

Regenerative Fuel Cell energy storage has been examined extensively at Rocketdyne. Spreadsheet models were developed to characterize the performance of an RFC system. The cell stack description for this study was for PEM-type (acid) fuel and electrolyzer cells. However, the spreadsheet algorithms are intended to deal equally with both acid and alkaline type cells. Major participants in the cell business are Hamilton Standard, International Fuel Cells, and Life Systems. These organizations are our primary sources of information contained in this model. The fuel cell and electrolyzer cell models calculate the size of the cells and stacks based on the user defined load. From this load the model calculates the number and size of the cells stacks. From "standard" cell designs the mass of the cells and stack can be calculated. Added to this mass is the mass of other parts of the stack that are necessary to hold the units together (heads, tie rods, springs). The electrolyzer mass also includes mass for a containment vessel or dome. The size and mass of the dome is based on the electrolyzer stack size and pressure.

Because the mass of the reactant tanks can be the single greatest mass for the RFC (e.g., ~45%), the reactant tank mass calculations are carried out in considerable detail. The tanks are modeled as metal-lined,

high-strength, fiber-wound vessels; the shape is that of a cylinder with semi-elliptical heads, this shape being superior in reduced mass-to-volume ratio as compared to spheres (this is characteristic of fiber-wound structures). The approach taken for the tank model was to develop empirical equations which would fit design parameters for a number of preliminary tank designs prepared by Structural Composites Industries (SCI). The spreadsheet model for the tanks calculates fiber wrap mass is somewhat higher (~20-40%) than those from SCI. Even so, the spreadsheet predicts some excellent figures of merit (PbV/W) for the tanks. Because the spreadsheet model predicts heavier tanks masses, the model is considered to be conservative.

General Assumptions

The following assumptions and ground rules were made for all systems:

- 1) Conditions are assumed suitable for operation on the Lunar surface somewhere near the equator. The Lunar day is assumed to be 354.8 hrs long with the night 354.0 hrs long.
- 2) The nominal delivered electrical power to the user was assumed to be 25 kW during the day and 12.5 kW during the night.
- 3) The PV array and the PMAD masses are assumed to have the same specific mass in lb/kW output, all based on a value derived from Ref. 1. This was done to even out the relative influence of the PV and PMAD masses while comparing the storage system masses of the three system considered here.

System Specific Assumptions

Tank Sub-System Mass

Warm Gas Storage Tanks

All the data for the warm-gas storage option was taken directly from the spread sheet model.

Super Critical Storage Tanks

The super-critical tank mass was calculated from the same spread sheet model for the warm-gas system, except that a 4 in thick Multi-layer Insulation (MLI) layer was added to the hydrogen tank and a 3 in thick MLI layer was added to the oxygen tank. MLI mass was calculated by using the tank surface area and MLI thickness to determine MLI volume, and then the mass factor of 3.5 lb/cu.ft was applied. This resulted in an approximate 20 % increase in the tank mass. It should be noted that these tanks are "wrapped" tanks and have never been flown when filled with fluids at cryogenic temperatures. This is an obvious new technology area, although no problems are envisioned.

Cryogenic Storage Tanks

The Cryogenic System storage tank masses are based on linear scaling from the paper by L. Kohout.(Ref. 1)

Refrigeration Sub-System Mass

Warm Gas Refrigeration

Refrigeration is not required for the warm-gas storage sub-system.

Super-Critical Refrigeration

The amount of refrigeration needed to cool both the hydrogen and oxygen to their cold super-critical states at the high exit pressure of the electrolyzer was calculated from thermodynamic property tables. The

coolant, or working fluid in the cooling loop is liquid nitrogen and cold nitrogen gas. Because the storage temperatures are not extremely low, a nitrogen refrigeration system was selected. It is assumed that the liquid nitrogen enters the coldest super critical storage tank at the bottom and is evaporated there and the boiled off cold gas proceeds upward to cool the surrounding gas in the tank. It then exits the tank at the top and enters the first storage tank, to cool its contents. The nitrogen gas exiting at the tank top, which will have a temperature somewhat below the stored reactant gas which is entering (at the bottom) from the electrolyzer, is then returned to the nitrogen refrigeration system for re-liquefaction and re-use. Figure 2 shows this tank arrangement in the charge and discharge modes.

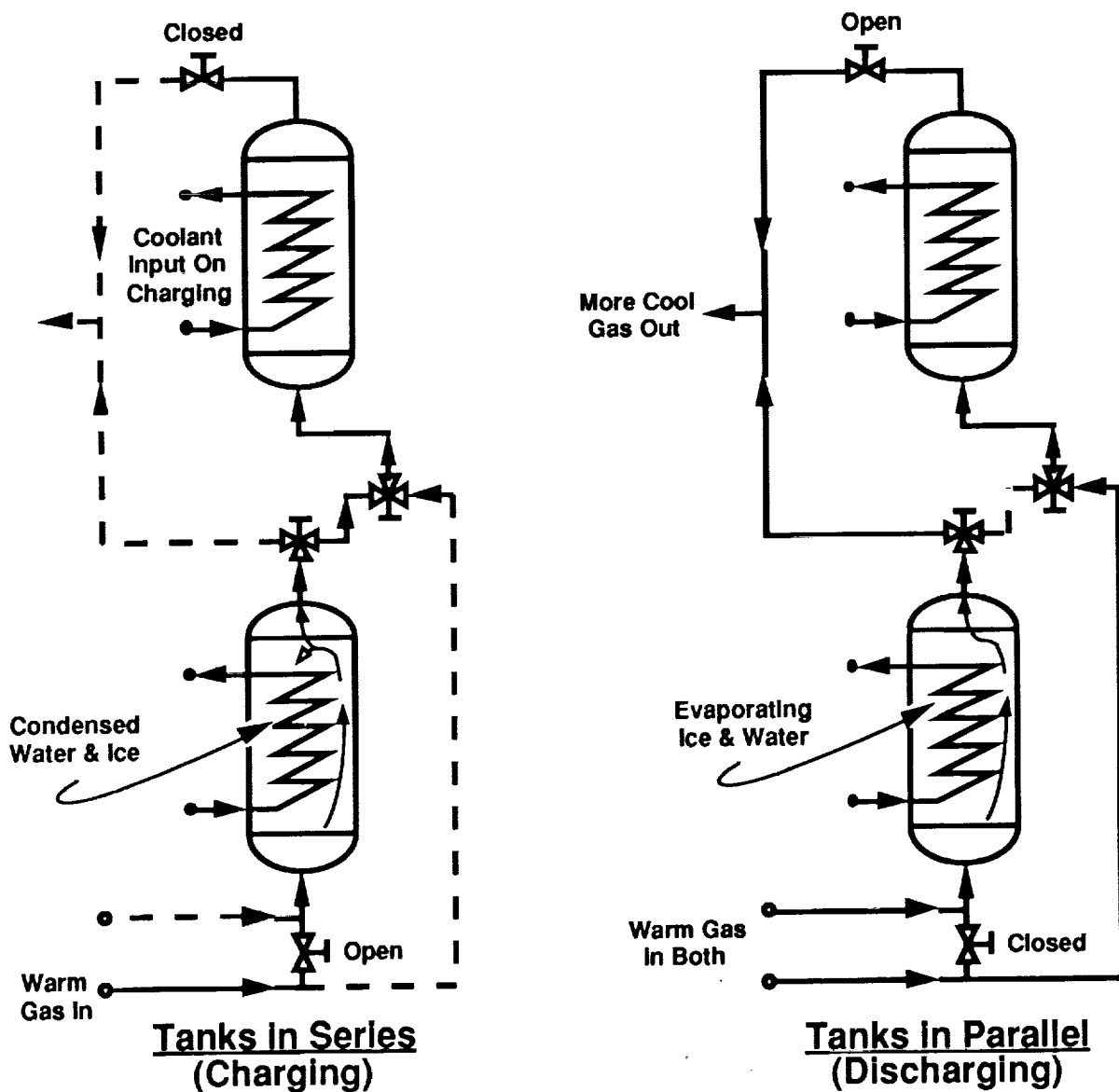


Figure 2: Super-critical Storage Tank Arrangement

The super-critical system refrigerator mass is based on combining a value of power required at the plant input per unit of nitrogen re-liquified (Ref.2) the reported data. First the power input requirements were calculated from the above data and the mass was then estimated from data in Ref.3, which contained the value of mass per unit power input for a very similar oxygen liquefaction facility. This is justified by the fact that the boiling points of oxygen and nitrogen are relatively close together and also because their molecular weights are also close together (only a 14% difference in molecular weight) and the physical properties of their gaseous and liquid states are also similar.

The power required to liquify one pound of nitrogen gas starting at room temperature was calculated from an existing plant described in Ref. 2. To obtain the estimated mass (since this was not given in Ref. 2) of such a plant, the mass per unit of input power was obtained for a similar plant designed for liquifying oxygen, (Ref. 3). The information from the above two references was then combined to obtain the mass of the refrigeration system. This mass was then doubled to allow for the mass of ancillary equipment. Even then the resulting mass required of the subject RFC refrigeration system was only 200 lb.

Cryogenic Refrigeration

Data from a paper by L. Kohout, Ref. 1, was linearly scaled based on user power requirements. Only the radiators associated with the reactant storage system are considered in the comparison.

PV Array and PMAD Sub-System Masses

The warm-gas system does not need any significant electrical power for its storage system. Therefore, no mass was allotted for the PV-PMAD required to obtain this power.

The super-critical system PV-PMAD mass was determined by first determining the power required by the storage system, and then a specific mass factor was utilized scaled from the values given in Ref. 1.

The mass of the PV-PMAD assignable to the cryogenic system was similarly treated based a scaling factor derived from data in Ref.1.

Radiator Sub-System Mass

Warm Gas Radiator Mass

The warm-gas sub-system does not require a radiator for the storage system, at least any cooling requirements are usually assigned to other sub-systems.

Super-Critical Radiator Mass

Waste heat loads were calculated and the mass was scaled linearly from data in Ref.1.

Cryogenic Radiator Mass

Mass was determined by linear scaling from data in Ref. 1.

RESULTS

The results of the analysis are shown in table 1. The PV/RFC mass includes all of the system mass except those parts related to H₂/O₂ storage. The super-critical storage shows a 16% savings in the over system mass while the Cryogenic system shows a 22% savings. If just the storage systems are compared then the savings increase to 40% and 55% for the super-critical and Cryogenic storage respectively.

Table 1. System Mass for Three Reactant Storage Options

| Component | Warm Gas System | Super Critical System | Cryogenic System |
|--|-----------------|-----------------------|------------------|
| Mass, lbs | | | |
| PV/RFC System (No Storage) | 9199.2 | 9199.2 | 9199.2 |
| Storage | | | |
| Tanks | 6112.3 | 1850.5 | 1214.6 |
| Refrigerator | | 400.0 | 295.6 |
| PV Array and PMAD | | 538.0 | 2944.0 |
| Radiator | | 867.0 | 500.5 |
| Total | 6112.3 | 3655.5 | 4954.7 |
| Total System Mass | 15311.5 | 12854.7 | 11981.2 |
| Savings (compared to warm gas system) | | 2456.8 | 3330.3 |
| Total Mass | | 16.0% | 21.8% |
| Storage Mass | | 40.2% | 54.5% |
| Volumes, cu. ft | | | |
| Reactant Tanks | 223.8 | 69.1 | 49.5 |
| Volume Savings (compared to warm gas system) | | 154.7 69.1% | 174.3 77.9% |

CONCLUSION

Storing fuel cell reactants at super-critical or cryogenic conditions can save system mass over a warm-gas storage. The mass savings can be translated into life cycle cost savings in terms of launch cost and delivery to the lunar surface. The advantages and disadvantages of each type of storage system are listed in table 2. Even though super-critical and Cryogenic storage have the mass advantage, warm-gas storage has the big advantage of system simplicity. The simpler the system the higher the reliability. If reliability becomes an issue it may become necessary to add a backup refrigeration system. Adding a second refrigeration system eliminates any mass advantage over the warm-gas system. For the cryogenic system an important advantage is in the area of Lunar Base architecture. Current plans for the Lunar base include cryogenic refrigeration systems for long term storage of Lunar Lander propellant. Cryogenic storage would allow for a commonality of equipment for the Lunar Base which could alleviate the back-up system problem. If water and it's elements (hydrogen and oxygen) become a "common" resource of Lunar and Mars surface system, many surface system will contain technology common to the PV/RFC power system. One issue not examined is technology readiness. Fuel cells and indirectly electrolyzer cells have space experience, but cryogenic refrigeration systems have little or no space experience.

Cryogenic and super-critical storage show major mass savings advantages over warm-gas storage, but in selecting the "best" system for Lunar/Mars missions, system reliability and the impact of the overall mission architecture must be evaluated.

Table 2. System Advantages/Disadvantages

| | Advantages | Disadvantages |
|------------------------|--|---|
| Warm Gas Storage | <ul style="list-style-type: none"> • Simple system No refrigeration system Higher reliability • Smallest PV array | <ul style="list-style-type: none"> • High Pressure Safety Issue • High storage volume Large storage tank mass • Highest mass system |
| Super Critical Storage | <ul style="list-style-type: none"> • Lighter mass compared to Warm Gas Storage • Smaller storage size compared to Warm Gas Storage • Safer <ul style="list-style-type: none"> Nitrogen working fluid provides shield between oxygen and hydrogen No Joule-Thompson type valves having small clearances (in oxygen and hydrogen Cases) which may plug up system. Nitrogen refrigerator contains hermetically sealed dry Nitrogen • No dryers required | <ul style="list-style-type: none"> • More complex - requires refrigerator which in turn: <ul style="list-style-type: none"> Requires electrical power - increases PV size and mass Requires cooling by radiation - increases radiator size and mass • High Pressure Safety Issue |
| Cryogenic Storage | <ul style="list-style-type: none"> • Lightest mass system • Smallest storage size • Safer Low system pressure • Compatible with propellant storage systems | <ul style="list-style-type: none"> • More complex - requires refrigerator which in turn: <ul style="list-style-type: none"> Requires electrical power - increases PV size and mass Requires cooling by radiation - increases radiator size and mass |

REFERENCES

- 1) Kohout, Lisa L., "Cryogenic Reactant Storage for Lunar Base Regenerative Fuel Cells", NASA Technical Memorandum 101980 June, 1989.
- 2) Mulholland, G.T., et al., "Design and Performance of a 90,000 Kilogram Per Day Nitrogen Reliquefier for the Fermilab Energy Saver", Advances in Cryogenic Engineering, Vol. 33d, 1987, pp. 827-836.

- 3) Brock, E.H., and J.G. Fisher, "In-Space Propellant Processing Using Water Delivered as Shuttle Contingency Payload", AIAA, 1978. (Authors were at General Dynamics when this was published.)
- 4) Robinson, J.W., et al., "Long Term Cryogenic Storage Study", report # AFRPL TR-83-082 prepared by Martin Marietta, Final report, Sept. 1983, p.78. (AD-B089-763).

OXYGEN ELECTRODES FOR RECHARGEABLE
ALKALINE FUEL CELLS — III

L. Swette*, N. Kackley, and S.A. McCatty
Giner, Inc.
Waltham, Massachusetts 02254-9147

ABSTRACT

The investigation and development of electrocatalysts and supports for the positive electrode of moderate-temperature single-unit rechargeable alkaline fuel cells is described with focus on chemical and electrochemical stability and O₂ reduction/evolution activity.

INTRODUCTION

The work presented here represents an update of the continuing investigation of candidate materials for moderate temperature single-unit rechargeable alkaline fuel cells, some of which have been described previously [1-3]. The focus is on new and previously studied materials which have undergone testing to either qualify them for further investigation and potential development or disqualify them for use in the rechargeable alkaline fuel cell application.

Viable candidate materials must meet the following requirements: 1) good electrical conductivity (a more demanding requirement for supports than electrocatalysts); 2) high resistance to chemical corrosion and electrochemical oxidation and/or reduction; 3) electrocatalysts, in addition, must exhibit high bifunctional electrocatalytic activity (O₂ evolution and reduction). Advanced development requires that the materials be prepared in high-surface-area forms, and may also entail integration of various candidate materials, e.g., one or two electrocatalysts unsupported or distributed on a stable conductive support.

Candidate support materials have been drawn from transition metal carbides, nitrides and oxides which have high electrical conductivity. Some candidate support materials exhibit catalytic activity for O₂ evolution and/or reduction. These materials, generally noble metal-containing oxides, are termed catalytic supports. Candidate catalyst materials have been selected largely from metal oxides of the form ABO_x (where A = Pb, Mn, Ti, Ni, Co, Zr, Na, and B = Pt, Ir, Rh, Ru). Some of these have been investigated and/or developed for one function only, either O₂ reduction or O₂ evolution. The electrical conductivity requirement for catalysts may be lower, especially if integrated with a higher conductivity support. For initial evaluation, materials have been purchased when available; subsequently, in-house preparations have been attempted, to affect surface area and composition, when necessary.

* Author to whom correspondence should be addressed

Candidate materials of acceptable conductivity are typically subjected to corrosion testing in three steps. Preliminary corrosion testing consists of exposure to 30% KOH at 80°C under oxygen for about 5 days. Materials that survive chemical testing are examined for electrochemical corrosion activity; the material is held at 1.4 V versus reversible hydrogen electrode (RHE) in 30% KOH at 80°C for 15 to 20 hours. An acceptable anodic current is on the order of a few microamps/mg of material. For more stringent corrosion testing, and for further evaluation of electrocatalysts (which generally show significant O₂ evolution at 1.4 V), samples are held at 1.6 V for about 100 hours and at 0.6 V for about 16 hours. The surviving materials are then physically and chemically analyzed for signs of degradation (visual examination, electron microscopy, X-ray diffraction).

To evaluate the bifunctional oxygen activity of candidate catalysts, Teflon-bonded electrodes are fabricated and tested in a floating electrode configuration [4]. Many of the experimental materials being studied have required development of a customized electrode fabrication procedure. For preliminary testing, catalysts of interest should show <500 mV polarization (from 1.2 V) in either mode at 200 mA/cm². In advanced development, the goal is to reduce the polarization to about 300-350 mV.

MATERIALS INVESTIGATED

Materials were originally assigned to the categories of support or electrocatalyst based on reported or anticipated performance. Some of the metal ratios shown are the targeted synthesis compositions only.

Candidate Supports:

LiNiO_x TiN ZrC ZrN

Candidate Catalytic Supports:

LaNiO₃ PbPdO₂ CoIrO₃ NiIrO₃ RhO₂ IrO₂

Candidate Electrocatalysts:

| | | | |
|--|-------------------------------------|------------------------------------|--------------------------------------|
| Na _x Pt ₃ O ₄ | IrMnO _x | PtTi _{1.5} O _x | RuTiO _x |
| Pb ₂ (Ir _{2-x} Pb _x)O _{7-y} | IrNiO _x | PtTi ₂ O _x | RuMn ₂ O _x |
| Rh black | IrNi ₃ O _x | PtZr ₂ O _x | RuMn ₃ O _x |
| Pt black | IrTi _{1.25} O _x | | (RuIr)Mn ₂ O _x |

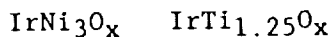
Reference Materials:

O₂ reduction
 10% Pt/Au (Johnson-Matthey, 11 m²/g)
 O₂ evolution
 Pt black (Englehard, 25 m²/g)

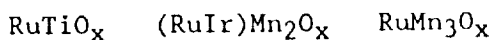
Several candidate materials have been eliminated from further consideration for various reasons, as shown below. Some of the noble-metal/transition-metal mixed oxide preparations resulted in two-phase materials consisting of a noble metal or noble metal oxide (e.g., Pt, RuO₂ or IrO₂) and a transition

metal oxide (e.g., TiO_2 , ZrO_2 , Mn_2O_3). These materials may show adequate conductivity and even some catalytic activity due to the noble metal or noble metal oxide component, but they were not investigated further.

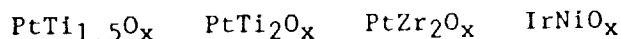
Inadequate Electrical Conductivity



Chemical Instability



Two-Phase Mixed Oxide



SOURCES OF CANDIDATE MATERIALS

Candidate materials for both catalysts and supports were purchased, if commercially available in powder form, as the most efficient approach for preliminary evaluation (electrical conductivity, chemical and electrochemical stability). Such materials offer the advantage of an economical purchase of a material of known purity in a quantity (5-25 g) sufficient for preliminary qualification, and particularly for disqualification. The disadvantage is that most of the commercially available materials have surface areas in the range from low ($<10 \text{ m}^2/\text{g}$) to very low ($<1 \text{ m}^2/\text{g}$). Consequently, most commercial materials that survive preliminary screening must be prepared in a higher surface area form, in-house or by a custom fabricator, for effective evaluation as potential catalysts and/or supports.

In many cases, especially for candidate catalysts, commercial materials were not available. Preparation methods described in the literature, either specific for the material or as a general model, were used when deemed appropriate to the material requirements in terms of yielding an electrically conductive, high-surface-area powder. IrO_2 and RhO_2 were prepared by the Adams method [5]. $Na_xPt_3O_4$ was prepared typically by firing Na_2CO_3 and PtO_2 at $>600^\circ\text{C}$ [1-3,6,7]. Synthesis of nickel-iridium oxide was attempted by the Adams method of fusion of the metal chlorides in sodium nitrate [5], but this yielded a two-phase product. As an alternative, $NiIrO_3$ and $CoIrO_3$ were prepared following the method of Chamberland and Silverman [8]; this consists of co-precipitation of the hydroxides and firing at 350°C . X-ray diffraction analysis has not been carried out because prior work [8] has indicated that, although the materials have the elemental compositions of ilmenites, they are not crystalline. Both materials had good surface area and conductivity, but the $CoIrO_3$ material showed higher values in both measurements. No chemical or electrochemical stability tests have been completed on these two materials to date.

CHARACTERIZATION OF CANDIDATE SUPPORT MATERIALS

Candidate material preparations are typically analyzed by X-ray diffraction (XRD) for chemical characterization. The objective of preparing fine powder materials, however, is generally in conflict with obtaining sharp XRD patterns (because of the line-broadening characteristic of high-surface-area powders); thus the quality of these results is sometimes compromised. Firing materials for a longer time or at a higher temperature usually increases the crystallinity and improves XRD results, but at the expense of decreased surface area and some uncertainty about the composition of the original higher surface area material. In some instances, materials of interest have been re-analyzed by XRD and/or scanning electron microscopy (SEM) after extended corrosion testing to check for changes in composition, reaction products and changes in morphology. SEM has also been used occasionally to observe the particle size range of powders.

A summary of the measured physical characteristics of candidate materials is presented in Table 1. The electrical conductivity of candidate materials is estimated by compressing a small volume (e.g., 0.5-1 cm³) of the powder at about 12,000 psi between metal pistons within an insulating cylinder. The resistance is determined by measuring the voltage drop across the powder under the flow of sufficient current to generate easily measured current and voltage signals. The more accurate 4-point method of measuring resistance has not been used because of the larger sample volume requirement. Surface areas of candidate materials are determined by the BET nitrogen adsorption method using a Micromeritics Flowsorb II 2300 instrument.

STABILITY TESTING

A preliminary assessment of the chemical stability of the candidate support materials is made by exposing the as-prepared powder to 30% KOH at 80°C under an oxygen atmosphere for about 5 days, as described in previous publications [1-3]. This test is useful for eliminating the more unstable candidate materials.

For an initial assessment of the electrochemical stability of candidate support materials and catalysts, a wettable electrode composition is prepared on gold mesh and the steady-state anodic current is measured in the range of 1.0 to 1.4 V versus RHE in 30% KOH at 80°C. If the anodic current observed, after initiation of potentiostatic control at 1.4 V, drops to the microamp range, the system is allowed to equilibrate overnight; the steady-state anodic current is then recorded. In a second stage of testing, candidate materials are subjected to higher potentials (1.6 V) representative of oxygen evolution conditions for about 100 hours, and lower potentials (0.6 V) representative of oxygen reduction conditions for about 16 hours. The latter is intended to place electrochemical stress on the materials used in the oxide form. The current values measured are combined with other observations such as weight loss or gain, color changes, changes in conductivity, microscopic examination (SEM, TEM) and analysis (EDAX, XRD, etc.) to assess the stability of the material.

Observations on chemical stability are summarized in Table 2. Electrochemical stability measurements are recorded in Tables 3 and 4.

LaNiO₃, LiNiO_x and ZrN are potentially promising support materials, as described previously [1-3], but have not been investigated further.

The following observations were made on candidate materials tested:

TiN: In previous work, the coarse commercial powder (<40 microns) and the low-surface-area Giner, Inc. preparation (1 micron, 2.3 m²/g) appeared to be quite stable at oxygen evolution potentials [2,3]. Post-test XRD analysis indicated a strong TiN pattern ($a = 4.240 \text{ \AA}$), no TiO₂, and a few lines possibly due to a silicate, phosphate or carbonate. The higher-surface-area material, TiN_x, (x = 0.72 to 0.86)* similarly appeared relatively stable in the chemical test and anodically up to 1.4 V. However, dissolution occurred when the electrode was held at 1.6 V. A gold-catalyzed TiN electrode was also found to be very reactive. After electrochemical testing, the surface of the electrode had degraded to a refractory non-conductive material. Post-test XRD analysis showed a strong second phase, possibly potassium titanate. Tracking of electrical conductivity through electrode processing in air revealed that the material increased in resistivity by about a factor of 1000 at 325°C, indicating oxidation. Sintering under 5% H₂/N₂ preserved the conductivity, but did not improve stability [2].

A stoichiometric form of TiN may prove to be suitable as a support for O₂ reduction catalysts, but it seems unlikely that it will be a viable candidate support for O₂ evolution catalysts.

ZrC: As described previously, a commercially available, coarse (<40 microns), low-surface-area powder with about 2% Hf impurity was evaluated [2,3]. Gas generation was noted during the initial period of the chemical stability test, but this was attributed to dissolution of the Hf impurity (weight change measurements were not successful). Very low anodic currents were measured at 1.4 V, although in testing at 1.6 V vs. RHE from 50 to 100 hours, there was a visible loss of material, as well as a measurable weight loss (e.g., ~40%). This may have been due to physical shedding during oxygen evolution, as there was no other evidence of reaction.

A "Hf-free" ZrC with similar conductivity, surface area and particle size, obtained from another vendor, was also investigated [2]. In chemical testing, no gassing or color changes were observed, but there was a weight loss of about 16% and a small amount of white flocculent precipitate. The electrical conductivity was higher after chemical stability testing (700 vs. 125 ohmcm⁻¹). In electrochemical stability testing, the anodic currents measured at 1.4 V were low, 0.5 to 1.0 microamp/mg. The electrode was tested at 1.6 V vs. RHE for approximately 81 hours. There was a visible thinning of the electrode and a weight loss of 36%, similar to that seen in tests of Hf-containing material. X-ray analysis of the post-test electrode showed broad lines for a ZrC phase, plus a strong secondary phase which could not be positively identified, but may be a Teflon or carbonaceous species.

* TiN_x prepared by Dr. J. Michaels, Dept. of Chem. Eng., Univ. of Calif. - Berkeley.

Preparation of high-surface-area ZrC by self-propagating high-temperature synthesis (SPHTS) was investigated. High-surface-area carbon and zirconium metal powder were combined and ignited with a resistance coil following the method of Mullins and Riley [9]. The SPHTS was partially successful, but X-ray diffraction analysis indicated that the product contained about 50% unreacted Zr. No further investigation of ZrC is planned.

PbPdO₂: A preparation of this compound by the Adams method, reported previously [2,3], had a very low surface area, but appeared to be quite stable in electrochemical testing. Attempts to prepare a higher-surface-area material have been unsuccessful to date.

Na_xPt₃O₄: Some initial preparations of this compound, described in previous publications [1-3], were determined by XRD to be single-phase Na_xPt₃O₄ with apparent x-values of 0.7-0.8. In a 17-day electrochemical stability test, this material showed no evidence of degradation. In a more demanding test, two Na_xPt₃O₄ electrodes were cycled between oxygen reduction and evolution for about 90 hours (45 one-hour cycles; see Fig. 2 and description in discussion of oxygen performance). At the conclusion of this test, both electrodes were subjected to XRD analysis (the final state of each electrode, reduction or evolution, was not recorded). Both catalysts exhibited the crystallographic pattern for Na_xPt₃O₄, but the value of x for the catalyst from one electrode may have been reduced slightly. X-ray diffraction peak broadening allows only very approximate determination of the unit cell parameter needed to establish x-values (± 0.2), thus we have not been able to establish a correlation between this parameter and physical characteristics and performance. For several more recent preparations, we have performed elemental analysis by inductively coupled plasma spectroscopy (ICP) to determine the sodium content. These measurements indicate a much lower value for x (~0.5) than estimated from XRD data. A preliminary conclusion is that the Na_xPt₃O₄ compositions with higher x-values are more conductive and may also be more catalytically active.

Pb₂(Ir_{2-x}Pb_x)O_{7-y}: In prior work [1], material prepared by a low-temperature precipitation method, based on a procedure described by Horowitz, et al. [10], was found to be unstable in 30% KOH at 80°C and showed substantial physical changes at 1.6 V. Refiring at 500°C improved crystallinity and decreased reactivity below 1.4 V. The test electrode survived 24 hours at 1.6 V, but delaminated from the current collector at 0.6 V [2,3]. Another method to prepare Pb₂(Ir_{2-x}Pb_x)O_{7-y}, by fusion of the respective salts in sodium nitrate [5], was investigated. The product had good surface area (95 m²/g) and conductivity (64 ohmcm⁻¹). The as-prepared material could not be analyzed due to lack of crystallinity. After heat treatment in oxygen at 750°C to increase particle size and crystallinity, X-ray diffraction analysis showed a 50/50 mixture of IrO₂ and the Pb-substituted pyrochlore. The effect of the heat treatment on the original composition is unknown. The lattice parameter of the pyrochlore was 10.316 Å, which leads to an approximate formula of Pb₂(Ir_{1.9}Pb_{0.1})O_{7-y}. In chemical stability tests, a 20% weight loss was measured. This material showed some catalytic activity, as described in the last section.

RhO₂: This material was also prepared by fusion of a Rh-salt in sodium nitrate [5]. The product showed excellent surface area (187 m²/g) and conductivity (14 ohmcm⁻¹). X-ray diffraction and thermogravimetric analyses showed the material to be RhO₂·(0.48)H₂O. In chemical stability tests, no weight loss was seen. Electrochemical stability testing also showed no significant weight loss, after 87 hours at 1.6 V and 18 hours at 0.6 V. The current densities measured were relatively high, at 1.3 to 1.6 V, due to the catalytic activity of the material. As described in the next section, RhO₂ shows potential as a catalyst and/or catalytic support material.

IrO₂: The sodium nitrate fusion method [5] was also used to prepare two different batches of high-surface-area IrO₂ (160 to 198 m²/g) with excellent conductivity (33 to 70 ohmcm⁻¹). X-ray analysis confirmed that the material (Batch #2) was single-phase IrO₂. Scanning electron microscopy showed a mix of thin platelets of several microns in width, as well as agglomerations of submicron-sized particles. In the chemical stability test, the Batch #1 material showed no visible change, but exhibited a 39% weight loss. This result is not consistent with the electrochemical test and may be a result of experimental error. In the electrochemical stability test, the IrO₂ electrode showed 1 to 8 microamps/mg at 1.0 to 1.3 V. There is significant oxygen evolution activity above 1.3 V. After a total test time of 83 hours at 1.6 V and 18 hours at 0.6 V in 30% KOH at 80°C, the electrode showed no significant deterioration and a weight loss of only 5%. This material shows significant promise, both as a catalyst and as a catalytic support and has been combined with Pt to form a bifunctional electrode as described in the next section.

IrMn₂O_x: This material had higher conductivity (12 ohmcm⁻¹) but slightly lower surface area than RuMn₂O_x. In preliminary chemical stability tests, it appeared more stable and did not cause a color change in the KOH solution. However, a yellow coloration was noted during the electrochemical stress test, along with a 17% weight loss from the test electrode. The IrMn₂O_x displayed considerable catalytic activity, as described below, and may merit further investigation. This material could not be analyzed in the as-prepared form because of its high surface area (small particle size) and possible lack of crystallinity. A heat-treated sample (900°C in O₂) showed a broad-line rutile phase in X-ray diffraction analysis. An approximate composition of Ir_{1-x}Mn_xO₂, where x was 0.05 to 0.10, was determined. However, the effect of the heat treatment on the chemical composition is unclear.

RuMn₂O_x: This material showed evidence of instability in chemical and electrochemical stability tests (weight loss and color change of the KOH). After leaching in KOH in order to remove any soluble component, the material still showed a 13% weight loss on exposure to 80°C KOH and produced coloration of the KOH solution. Another sample of the as-prepared RuMn₂O_x was heat treated at 650°C in oxygen. This treatment caused a large loss in surface area from 62 m²/g to 12 m²/g, and increased the conductivity slightly from 2.9 ohmcm⁻¹ to 5.6 ohmcm⁻¹. As before, the chemical stability was not improved (15% weight loss and coloration of the KOH solution were observed). The leached and heat-treated samples were not subjected to electrochemical stress testing.

OXYGEN ELECTRODE PERFORMANCE TESTING

Oxygen electrode performance testing was performed in a floating electrode cell [4] in 30% KOH at 80°C using a 1 cm x 1 cm electrode sample, as described in earlier publications [1-3]. The reference materials for O₂ reduction and O₂ evolution were 10% Pt/Au and Pt black, respectively. All candidate catalysts were compared to these reference materials as well as to each other.

The testing sequence is usually an oxygen reduction polarization test followed by an oxygen evolution polarization test, applying small potential steps sufficient to yield a few data points in each log-decade of current density from 1 to 1000 mA/cm². The potentials are controlled, and compensated for iR loss, with a Princeton Applied Research model 173 potentiostat. Collecting oxygen evolution data entails frequent interruptions to remove trapped gas bubbles. After an oxygen evolution test, electrodes that have not been optimized for bifunctional operation are sometimes too flooded to rerun an oxygen reduction test. Development of an electrode structure adequate for bifunctional operation with these candidate electrocatalysts is an independent research task. Some electrodes have been prepared using processing methods designed for optimization of bifunctional performance. Results on O₂ reduction and O₂ evolution tests on these electrodes are very promising, as described at the end of this section.

NiIrO₃ and CoIrO₃: Both of these candidate support materials showed some oxygen redox activity in preliminary testing, as shown in Fig. 1. The CoIrO₃ was poor in O₂ reduction, but is promising for O₂ evolution. After stability testing, further electrode development will be pursued if warranted.

IrMn₂O_x displayed excellent O₂ reduction and O₂ evolution performance, as shown in Fig. 1, but this level of performance proved difficult to reproduce on subsequent tests. As discussed above, this material shows signs of instability in anodic corrosion testing and requires further development, but it remains an interesting candidate for bifunctional oxygen catalysis.

IrO₂ was tested for comparison to the other iridium-based catalysts prepared. It can be seen that the oxygen evolution performance of IrMn₂O_x is similar to IrO₂, but the oxygen reduction performance of IrMn₂O_x is better. The latter effect may be due to electrode structural differences for the two materials.

Pb₂(Ir_{2-x}Pb_x)O_{7-y}: As shown in Fig. 1, this Adams fusion preparation (which turned out to contain two phases, Pb₂(Ir_{1-x}Pb_x)O_{7-y} and IrO₂) showed better O₂ reduction performance than IrO₂ alone, but was not as good as the IrMn₂O_x material. For O₂ evolution, it was slightly poorer than IrO₂ alone or IrMn₂O_x. At low current densities, this material showed performance similar to single-phase Pb₂(Ir_{1.33}Pb_{0.67})O_{7-y} prepared previously by the Horowitz method [10]. At higher current densities, it showed much improved performance (e.g., above about 50 mA/cm² in O₂-evolution mode and above about 200 mA/cm² in O₂-reduction mode). Some of these differences in performance may be due to differences in the electrode structure.

Na_xPt₃O₄: The Na_xPt₃O₄ catalyst [1-3,6,7] was evaluated in an O₂/O₂ cell under cyclic O₂ evolution/reduction conditions. Two Na_xPt₃O₄ electrodes were separated by a matrix material soaked in 30% KOH. The full cell was operated under a positive pressure oxygen atmosphere (50 psi) at 80°C. The cell voltage was measured at current densities of 50, 100 and 200 mA/cm².

One electrode underwent 30 minutes on O₂ reduction, 5 minutes on open circuit, then 30 minutes on O₂ evolution, while the other electrode was undergoing the opposite cycle. The measured voltage represents the difference between the electrode potentials, which may be positive or negative, depending on which electrode is at the O₂ evolution potential. Figure 2 shows the cell potential on progressive cycling at each current density. The cell polarization was 515 to 575 mV at 50 mA/cm²; 670 to 710 mV at 100 mA/cm²; and 900 to 995 mV at 200 mA/cm². The total cell potential increased slightly over time at 50 and 100 mA/cm². The cell potential increased more rapidly over time at 200 mA/cm². The difference between the absolute values of cell voltage on positive and negative portions of the cycle was near zero, indicating that the two electrodes were performing nearly identically, as expected.

This material is one of the best candidate bifunctional oxygen electrode catalysts developed to date in terms of both stability and oxygen reduction/evolution performance. The emphasis in the current development effort is on preparing larger quantities of single-phase material and correlating synthesis conditions, crystalline structure, sodium deficiency and performance. A number of our earlier attempts, for reasons we have not clearly established, contained a second phase of free Pt, probably from partial decomposition of the PtO₂ reactant. Generally this two-phase material exhibited lower conductivity and surface area and poorer performance than single-phase Na_xPt₃O₄. The Pt phase can be partially dissolved out with hot aqua regia, which improves conductivity, surface area and performance, but not significantly. Several recent preparations have yielded single-phase, conductive material, but the performance is lower than observed earlier. At the present time, we are trying to determine Na/Pt ratios by elemental analysis (ICP) for greater accuracy than that obtained from typical XRD back-reflection data. Some oxygen electrode performance data for recent preparations of Na_xPt₃O₄, compared to data presented in earlier publications, is shown in Fig. 3.

Rh-RhO₂, Pt-IrO₂, Pt-RhO₂: Three noble-metal/noble-metal-oxide electrodes were prepared; Rh-RhO₂, Pt-IrO₂ and Pt-RhO₂. The fabrication methods used to make these electrodes were chosen as our best estimate of a balanced mix of hydrophobic/hydrophilic character. Oxygen reduction performance often benefits from a more hydrophobic electrode character while a hydrophilic electrode may be better for oxygen evolution. Giner, Inc. has developed a unique proprietary process for controlling the hydrophilic/hydrophobic properties at the particle level and applied this technology for achieving superior bifunctional oxygen electrode performance.

The oxygen electrode performance of these three mixed-character electrodes was tested in evolution and reduction modes, as discussed below. In each case, earlier data on the performance of the individual component materials (Pt, Rh, RhO₂ and IrO₂) as oxygen electrodes is compared to the performance of the mixed electrode structure. (The single-catalyst electrodes

were also single-character structures, which usually compromises the performance in both modes.) In addition, the performance of the three mixed-character electrodes are compared directly.

In Fig. 4, the oxygen electrode performance of Rh black, RhO₂ and Rh/RhO₂ are compared versus the standard baseline materials: Pt for O₂ evolution and 10% Pt/Au for O₂ reduction. The Rh black, RhO₂ and Rh/RhO₂ electrodes all showed very similar O₂ evolution performance, achieving 200 mA/cm² at about 1.43 V vs. RHE. The Rh black and Rh/RhO₂ electrodes also showed very similar O₂ reduction performance, 200 mA/cm² at about 0.8 V; the RhO₂ alone did not perform as well. The level of improvement in O₂ reduction performance of the Rh/RhO₂ electrode over that of the RhO₂ electrode, was about 50 mV at 200 mA/cm². The mixed character of the Rh/RhO₂ electrode is believed to be the reason for the performance improvement.

The first mixed-character Pt/RhO₂ electrode (A) showed little improvement over the RhO₂ electrode, as shown in Fig. 5. The performance of the two electrodes in both evolution and reduction modes is very similar, 200 mA/cm² at about 0.77 to 0.78 V in O₂ reduction and at about 1.42 to 1.43 V in O₂ evolution. Post-test examination of the electrode suggested that the hydrophobic/hydrophilic character was not balanced in this trial (too wettable). Therefore, a second Pt/RhO₂ electrode was fabricated using a slightly different mixture ratio (B). As shown in Fig. 5, the resulting improvement in O₂ reduction performance was dramatic. The electrode was almost as good as the baseline 10% Pt/Au material. The O₂ evolution performance was basically unchanged.

In Fig. 6, pure Pt black and pure IrO₂ electrodes are compared to Pt/IrO₂ electrodes prepared by two different approaches. The catalyst for Electrode A was prepared in an Adams co-fusion of Pt and Ir chlorides and was fabricated as a single-character electrode. The mixed-character Pt/IrO₂ (B) electrode showed excellent O₂ reduction performance, greatly improved over that of pure IrO₂ or the co-fusion single-character Pt/IrO₂ electrode. This optimized electrode sustained 200 mA/cm² at about 0.87 V. This level of performance is close to that of the baseline catalyst, 10% Pt/Au, which held about 0.89 V at 200 mA/cm². In O₂ evolution, the mixed-character Pt/IrO₂ electrode also showed good performance, 200 mA/cm² at about 1.47 V. This level of performance was slightly lower than that for IrO₂, but was better than the co-fusion single-character Pt/IrO₂ electrode.

The performance of the three mixed-character electrodes is shown in Fig. 7. In O₂ reduction mode, the Pt/RhO₂ and Pt/IrO₂ electrodes are very similar in performance and very close to the 10% Pt/Au baseline electrode. In O₂ evolution mode, all three electrodes show similar superior performance; the Pt/RhO₂ and Rh/RhO₂ electrodes showed slightly better performance than the Pt/IrO₂ electrode.

CONCLUDING REMARKS

Two materials of lower catalytic activity that have been identified as potential bifunctional alkaline oxygen electrode supports are LiNiO_x and ZrN. Two other materials, TiN and ZrC, do not appear to be sufficiently stable at oxidation potentials, but ZrC may be suitable as a catalyst support for oxygen reduction. Of the more catalytic candidate supports, LaNiO₃ and PbPdO₂ appear

to be stable but need surface area development; CoIrO_3 and NiIrO_3 have been prepared in high-surface-area forms and show some oxygen evolution activity but need stability testing; RhO_2 and IrO_2 have been prepared in very high-surface-area forms, they appear to be stable and show high activity for oxygen evolution.

Recent work has focused on more complete development of the most promising bifunctional oxygen electrode catalyst, $\text{Na}_x\text{Pt}_3\text{O}_4$, and the application of wettability control at the catalyst/Teflon particle level to achieve superior bifunctional electrode operation. The latter approach has been successfully implemented with two catalysts integrated into "dual-character" electrodes, e.g., Pt/IrO_2 , Pt/RhO_2 or Rh/RhO_2 . The same approach can be applied to a single bifunctional catalyst also, e.g., a "dual-character" $\text{Na}_x\text{Pt}_3\text{O}_4$ electrode. Such electrodes show highly efficient bifunctional oxygen electrocatalysis.

ACKNOWLEDGMENTS

This work was supported by NASA Lewis Research Center under the direction of Dr. William Fielder and Dr. Richard Baldwin, Contract No. NAS3-24635.

We would like to acknowledge the assistance of Professor B.L. Chamberland of the University of Connecticut in the selection and identification of numerous materials tested in this program.

REFERENCES

1. L. Swette and J. Giner, "Oxygen Electrodes for Rechargeable Alkaline Fuel Cells," *J. of Power Sources*, 22 (1988) 399-408.
2. L. Swette and N. Kackley, "Rechargeable Alkaline Oxygen Electrode Development," Proceedings of American Institute of Chemical Engineers Annual Meeting, Nov. 5-10, 1989, San Francisco, CA.
3. L. Swette and N. Kackley, "Oxygen Electrodes for Rechargeable Alkaline Fuel Cells - II," *J. of Power Sources*, 29 (1990) 423-436.
4. J. Giner and S. Smith, "A Simple Method for Measuring the Polarization of Hydrophobic Gas Diffusion Electrodes," *Electrochem. Technol.*, 5 (1967) 59-61.
5. R. Adams and R.L. Shriner, "Platinum Oxide as a Catalyst in the Reduction of Organic Compounds. III. Preparation and Properties of the Oxide of Platinum Obtained by the Fusion of Chloroplatinic Acid with Sodium Nitrate," *J. Am. Chem. Soc.*, 45 (1923) 2171-2179.
6. K.B. Schwartz, C.T. Prewitt, R.D. Shannon, L.M. Corliss, J.M. Hastings and B.L. Chamberland, "Neutron Powder Diffraction Study of Two Sodium Oxides: $\text{Na}_{1.0}\text{Pt}_3\text{O}_4$ and $\text{Na}_{0.73}\text{Pt}_3\text{O}_4$," *Acta Cryst.*, 38 (1982) 363-368.
7. R.D. Shannon, T.E. Gier, P.F. Carcia, P.E. Bierstedt, R.B. Flippen and A.J. Vega, "Synthesis and Properties of Platinum Metal Oxides of the Type $\text{M}_x\text{Pt}_3\text{O}_4$," *Inorg. Chem.*, 21 (1982) 3372-3381.
8. B.L. Chamberland and S. Silverman, *J. Less Common Metals*, 65 (1979) 41-48.
9. M.E. Mullins and E. Riley, "The Effect of Carbon Morphology on the Combustion Synthesis of Titanium Carbide," *J. Mater. Res.*, 4 (1989) 408-411.
10. H.S. Horowitz, J.M. Longo and J.T. Lewandowski, "Lead Ruthenium Oxide, $\text{Pb}_2[\text{Ru}_{2-x}\text{Pb}_x^{4+}]\text{O}_{6.5}$," *Inorganic Synthesis*, Vol. 22, John-Wiley & Sons, New York, 1983, pp. 69-72.

TABLE 1

Physical characterization of candidate materials

| Material | Source [Reference] | Surface Area (m ² /g) | Elect. Conduct. (ohmcm ⁻¹) |
|--|--|------------------------------------|---|
| Pt | Engelhard | 25 | N/M |
| Rh | Johnson Matthey | 39 | N/M |
| Na _{0.8} Pt ₃ O ₄ | Giner, Inc. #1 [1-3,6,7] Giner, Inc. #2 [1-3,6,7] | 21 17 | 50 56 |
| Pb ₂ (Ir _{1.33} Pb _{0.67})O _{7-y} | Giner, Inc. #1 (400°C) [10] | 24 | 40 |
| Pb ₂ (Ir _{2-x} Pb _x)O _{7-y} | Giner, Inc. #3 [5] | 95 | 64 |
| RuMn ₂ Ox | Giner, Inc. #1 [5] | 62 | 2.9 |
| IrMn ₂ Ox | Giner, Inc. #1 [5] | 45 | 12 |
| IrOx | Giner, Inc. #1 [5] Giner, Inc. #2 [5] | 160 198 | 70 33 |
| RhO ₂ | Giner, Inc. #1 [5] | 187 | 14 |
| ZrC (2% Hf) | Aesar | 1 | 125 |
| ZrC (Hf free) | Alfa Prod. | 0.6 | 125 |
| ZrC + Zr (SPHTS) | Giner, Inc. [9] | 38 | 34 |
| TiN | Alfa Prod. Giner, Inc. Univ. of California #2 Univ. of California #3 Univ. of California #5 U. of C. #5 (950°C, 5% H ₂ /N ₂) | N/M 2.3 56 38 21 20 | 390 440 0.34 N/M 14 >700 |
| NiIrO ₃ | Giner, Inc. [8] | 47 | 16 |
| CoIrO ₃ | Giner, Inc. [8] | 57 | 47 |

TABLE 2

Results of stability tests of selected candidate materials

Codes: NVR - No Visible Reaction
 SR - Slight Reaction (C = Color, G = Gas)
 N/M - Not Measured

| Material | Source [Reference] | Weight Change (%) | Observations |
|--|---|-------------------|--------------|
| Na _{0.8} Pt ₃ O ₄ | Giner, Inc. #1 [1-3,6,7] | N/M | NVR |
| | Giner, Inc. #2 [1-3,6,7] | N/M | NVR |
| Pb ₂ (Ir _{1.33} Pb _{0.67})O _{7-y} | Giner, Inc. #1 (400°C) [10] | N/M | NVR |
| | Giner, Inc. #3 [5] | -20 | NVR |
| RuMn ₂ O _x | Giner, Inc. #1 [5] | -14 | SR-C |
| | Giner, Inc. #1 KOH leached | -13 | SR-C |
| | Giner, Inc. #1 650°C, O ₂ | -15 | SR-C |
| IrMn ₂ O _x | Giner, Inc. #1 [5] | -9 | NVR |
| IrO _x | Giner, Inc. #1 [5] | -39 | NVR |
| RhO ₂ | Giner, Inc. [5] | 0 | NVR |
| ZrC (2% Hf) | Aesar | N/M | SR-G |
| ZrC (Hf free) | Alfa Prod. | -16 | SR |
| TiN | Alfa | N/M | NVR |
| | Giner, Inc. | N/M | NVR |
| | Univ. of California #2 | N/M | SR-C |
| | U. of C. #5 (950°C, 5% H ₂ /N ₂) | -2 | NVR |

TABLE 3

Electrochemical stability measurements on selected candidate materials

| Material | Source [Reference] | Anodic Current (microamp/mg) at 1.0-1.4 V (vs. RHE) | | | |
|--|---|--|-----|-----|-----|
| | | 1.0 | 1.1 | 1.2 | 1.3 |
| Na _{0.8} Pt ₃ O ₄ | Giner, Inc. #1 [1-3,6,7] | 1.5 | 1.0 | 1.3 | 2.3 |
| Pb ₂ (Ir ₁₋₃₃ Pb _{0.67})O _{7-y} | Giner, Inc. #1 (400°C) [10] | 23 | --- | 32 | 50 |
| | Giner, Inc. #2 (500°C) [10] | --- | --- | 0.4 | 2.0 |
| | Giner, Inc. #3 [5] | 3.0 | 4.0 | 4.0 | 4.0 |
| Pb ₂ (Ir _{1-x} Pb _x)O _{7-y} | | | | | |
| IrMn ₂ O _x | Giner, Inc. #1 [5] | 1.0 | 1.0 | 2.0 | 5.0 |
| IrO _x | Giner, Inc. #1 [5] | 1.0 | 1.0 | 3.0 | 8.0 |
| RhO ₂ | Giner, Inc. [5] | 1.3 | 4.0 | 4.0 | 25 |
| ZrC (2% Hf) | Aesar | 0.5 | 1.1 | 1.2 | 0.7 |
| ZrC (Hf free) | Alfa | 0.5 | 0.9 | 0.9 | 0.7 |
| TiN | Alfa | 0.2 | 0.2 | 0.2 | 0.2 |
| | Giner, Inc. | 0.4 | 0.4 | 0.6 | 0.5 |
| | Univ. of California #2 | 1.0 | 2.0 | 2.0 | 1.0 |
| | Univ. of California #3 | 0.4 | 0.9 | 1.3 | 0.5 |
| | Univ. of California #5 | 1.3 | 1.3 | 1.2 | 0.5 |
| TiN (air-sintered elect.) | U. of C. #5 (950°C, 5% H ₂ /N ₂) | 0.3 | 1.4 | 1.2 | 0.7 |
| TiN (5% H ₂ /N ₂ sinter) | U. of C. #5 (950°C, 5% H ₂ /N ₂) | 5.0 | 4.0 | 2.0 | 0.7 |

TABLE 4

Electrochemical stress tests on selected candidate materials

| Material | Source [Reference] | Stress Test | | Observations (Wt. Change) |
|--|---|---------------------|-------|---|
| | | Hours at 1.6, 0.6 V | | |
| | | 1.6 V | 0.6 V | |
| Na _{0.8} Pt ₃ O ₄ | Giner, Inc. #1 [1-3,6,7] | 120 | 70 | No signif. deterior. |
| Pb ₂ (Ir _{1.33} Pb _{0.67})O _{7-y} | Giner, Inc. #1 (400°C) [10] | 24 | 112 | Cracking, shrinkage |
| | Giner, Inc. #2 (500°C) [10] | 108 | 72 | Delamin. at 0.6 V |
| | Giner, Inc. #3 [5] | 108 | 21 | Slight reaction, Gray particulate (-17%) |
| IrMn ₂ O _x | Giner, Inc. #1 [5] | 102 | 17 | Color in soln. (-17%) |
| IrO _x | Giner, Inc. #1 [5] | 83 | 18 | No signif. deterior. (-5%) |
| RhO ₂ | Giner, Inc. [5] | 87 | 18 | No signif. deterior. |
| ZrC (2% Hf) | Aesar Alfa | 48 | 17 | Mat. loss (-38%) |
| | | 81 | 18 | Mat. loss (-36%) |
| TiN | Giner, Inc. Univ. of California #3 Univ. of California #5 | 105 | | surf. color change (0%) |
| | | 46 | | Part. dissolved |
| | | 3 | | XRD analysis TiN + K ₂ TiO ₃ ? (+5%) |

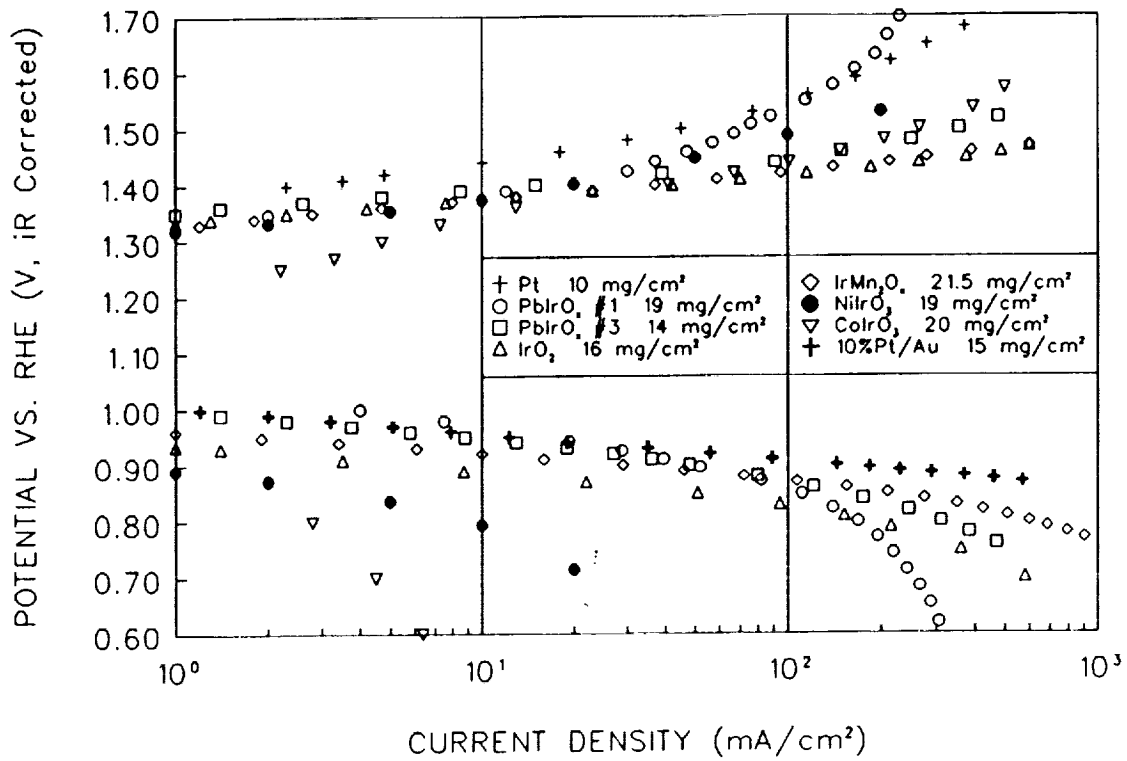


Fig. 1. O₂ reduction/evolution performance of Ir-containing electrodes, 30% KOH, 80°C.

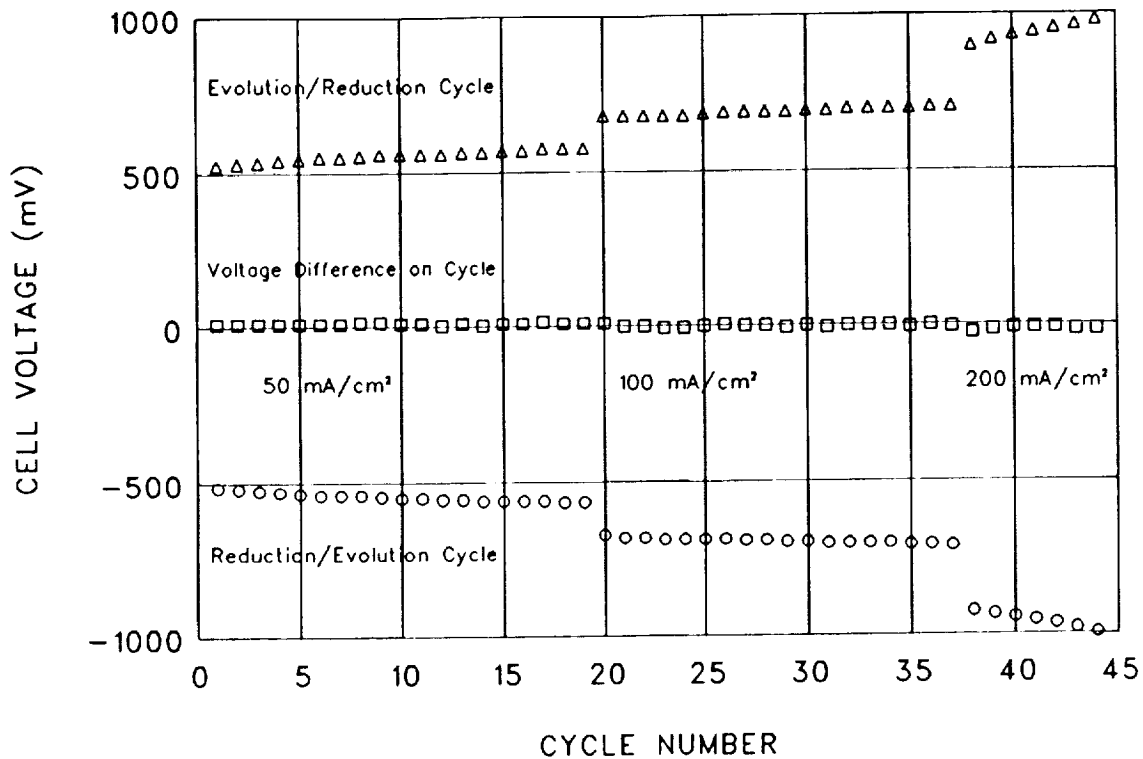


Fig. 2. O_2/O_2 cell cycling test of $Na_xPt_3O_4$: 30 min. O_2 red./evol., 5 min. open circ., 30 min. evol./red., 30% KOH, $80^\circ C$, 50 psi O_2 .

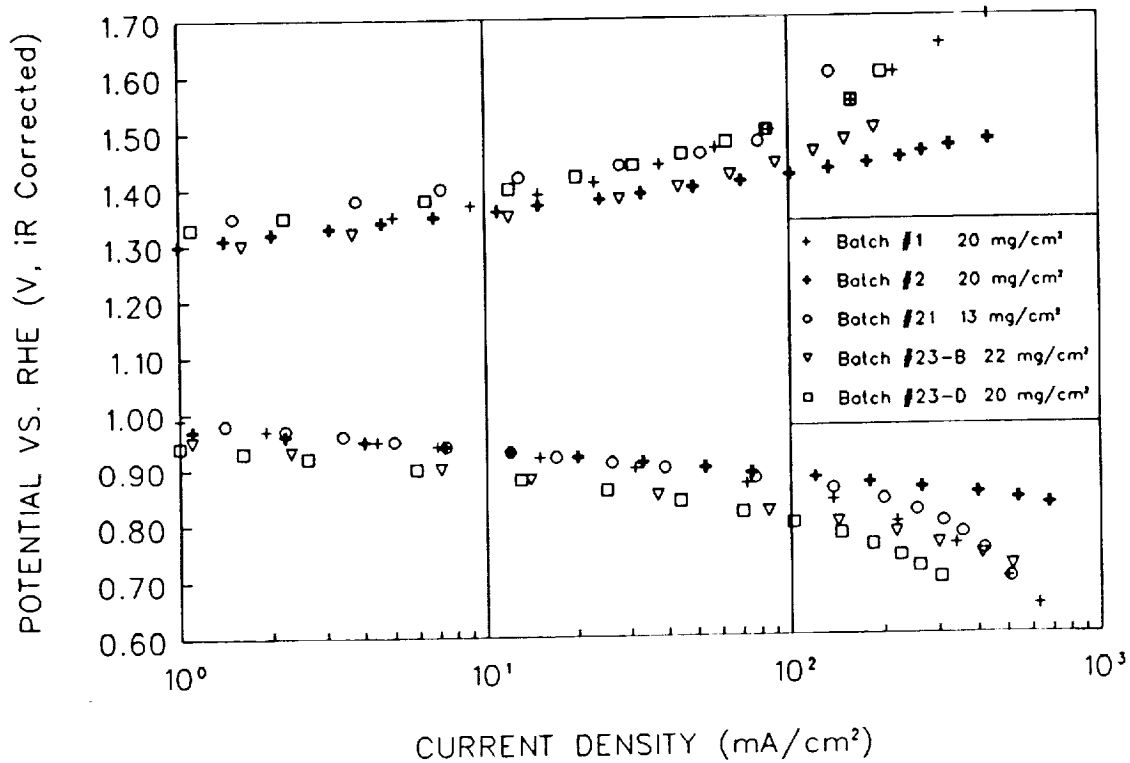


Fig. 3. O_2 reduction/evolution performance of $Na_xPt_3O_4$, 30% KOH, $80^\circ C$.

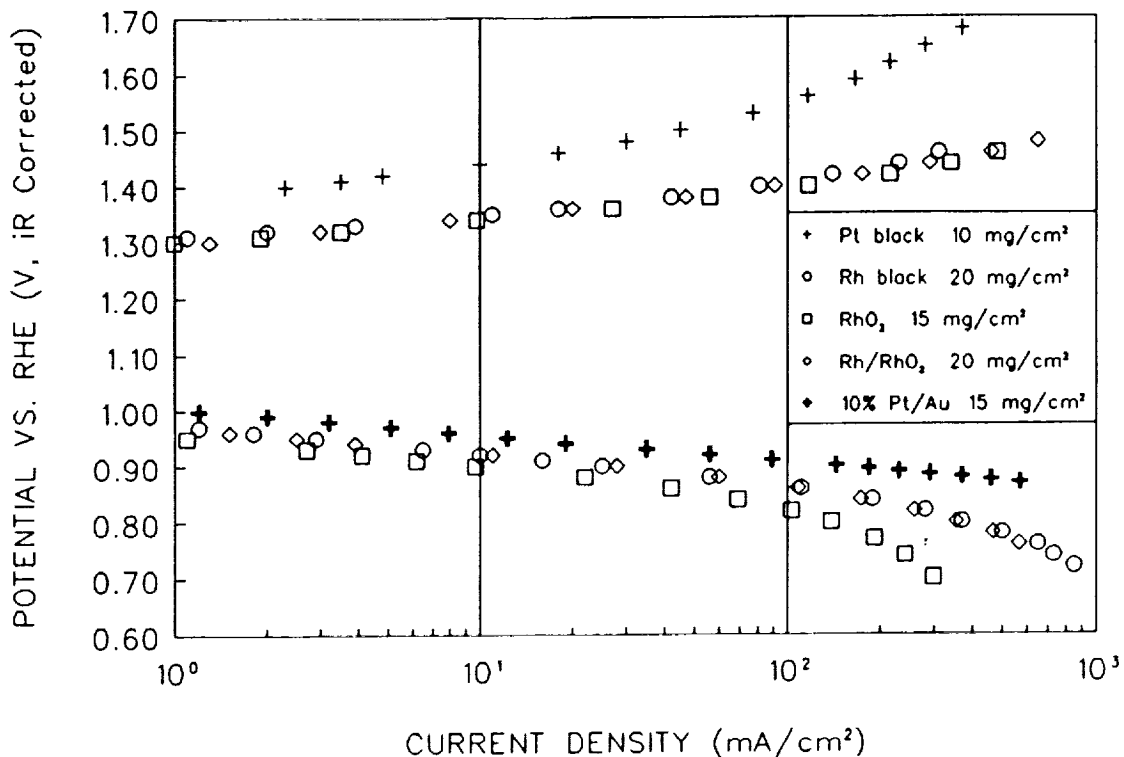


Fig. 4. O_2 reduction/evolution performance of Rh, RhO_2 and Rh/ RhO_2 electrodes, 30% KOH, 80°C.

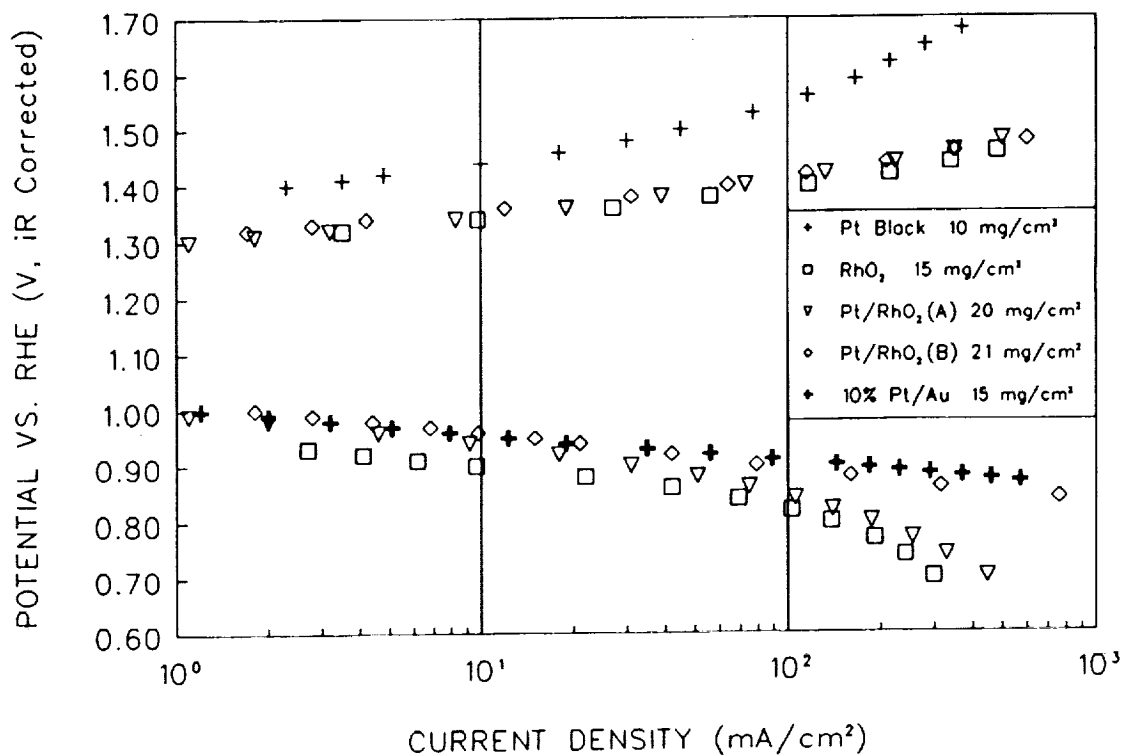


Fig. 5. O_2 reduction/evolution performance of RhO_2 and Pt/ RhO_2 electrodes, 30% KOH, 80°C.

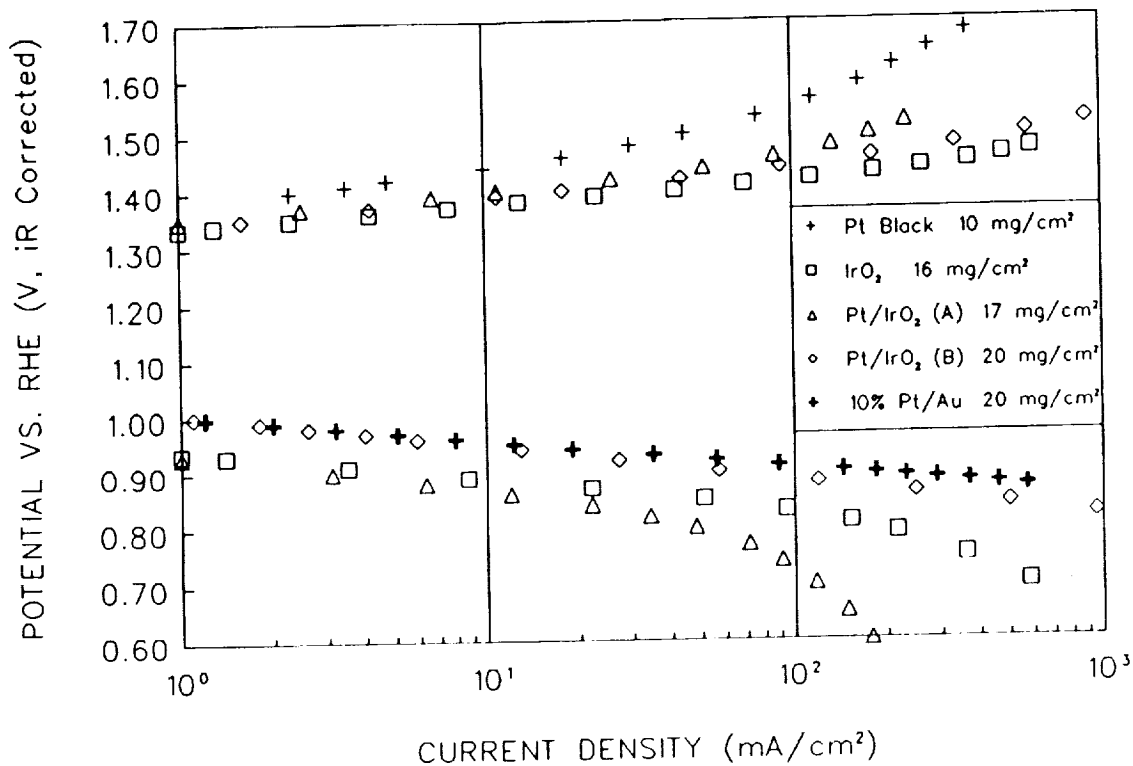


Fig. 6. O₂ reduction/evolution performance of IrO₂ and Pt/IrO₂ electrodes, 30% KOH, 80°C.

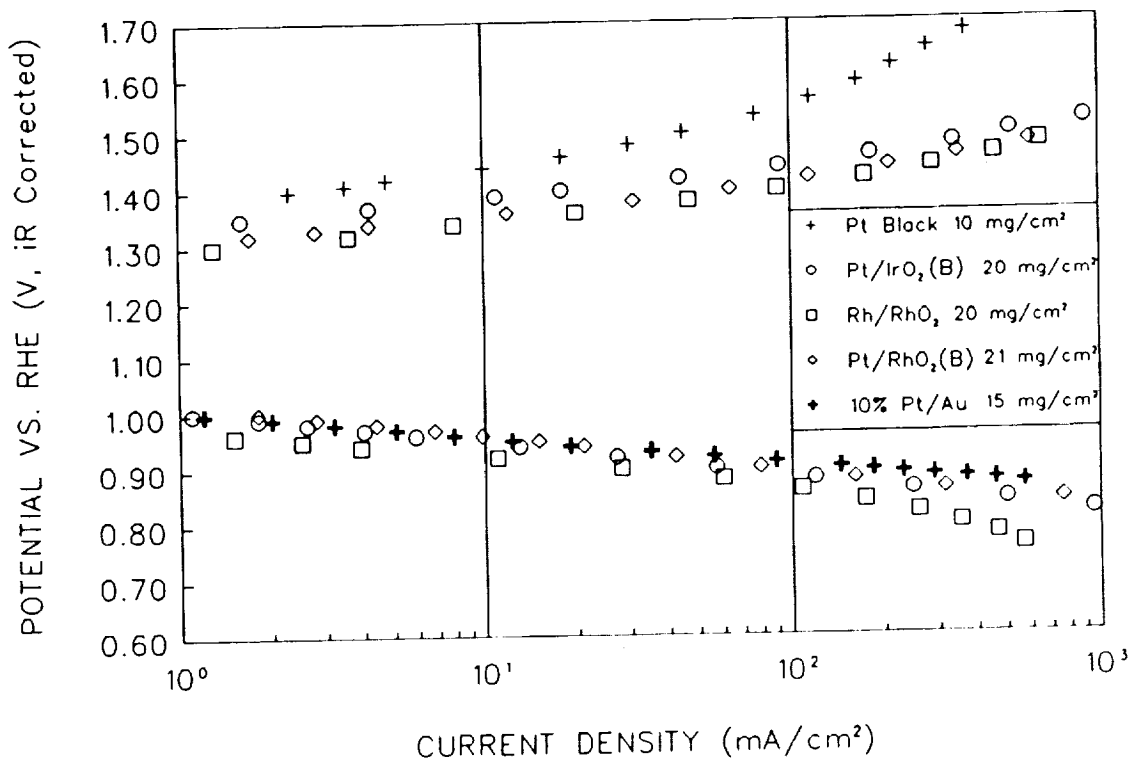


Fig. 7. O₂ reduction/evolution performance of "dual-character" bifunctional electrodes, 30% KOH, 80°C.

SOME RECENT STUDIES WITH THE SOLID-IONOMER
ELECTROCHEMICAL CAPACITOR

S. Sarangapani*, J. Forchione, A. Griffith, and A.B. LaConti
Giner, Inc.
Waltham, Massachusetts 02254-9147

and

R. Baldwin
NASA Lewis Research Center
Cleveland, Ohio 44135

ABSTRACT

Giner, Inc. has developed a high-energy-density, all-solid-ionomer electrochemical capacitor, completely free of liquid electrolyte. The novel features of this device include 1) a three-dimensional metal oxide-particulate-ionomer composite electrode structure, and 2) a unitized repeating cell element. The composite electrode structures are bonded to opposite sides of a thin sheet of a solid proton-conducting ionomer membrane and form an integrally bonded membrane and electrode assembly (MEA). Individual MEAs can be stacked in series as bipolar elements to form a multiple cell device. The discharge characteristics and energy storage properties of these devices are described. Typical capacitance measured for a unit cell is 1 F/cm². Life testing of a multicell capacitor on an intermittent basis has shown, that over a 10,000 hour period, the capacitance and resistance of the cell has remained invariant. There has been no maintenance required on the device since it was fabricated. Other multicell units of shorter life duration have exhibited similar reliable performance characteristics.

Recent work has focused on increasing the capacitance of the unitized structure and improving the low-temperature characteristics. The approaches and experimental results will be presented.

Some possible advanced NASA applications for these unique all-solid-ionomer devices will be discussed.

INTRODUCTION

Electrical pulse power generating systems include electrostatic (dielectric) and electrochemical capacitors. The former accumulate substantial energy only by developing a very high voltage difference across the dielectric gap. These very high potentials make them impractical for certain battery/capacitor high-energy-density pulse power applications. Electrochemical capacitors, on the other hand, can accumulate substantial charge (and deliver

* Author to whom correspondence should be addressed

it within the required times) at much lower voltages, compatible with the voltage of batteries. The classical "electrochemical supercapacitor" is a symmetric device in which the electrolyte is placed between two identical electrode systems (i.e., with the same electrode material under conditions causing the same process in each electrode but occurring in opposite direction). Pragmatically, the term "electrochemical capacitors" can be extended to asymmetric devices, i.e., devices with different electrode reactions at each electrode, although these latter devices may be closer to an ultra-high-power battery.

Symmetric electrochemical capacitors show respectable capacities from the double layer charging of their electrodes, which act as "perfectly polarizable electrodes" (i.e., electrodes, which can operate in an extended potential range without a faradaic reaction). Considerably higher capacities are obtained, however, with electrode systems having a substantial potential region over which a faradaic reaction takes place at a potential which depends more or less linearly, and reversibly (independent of the value of the current and without substantial hysteresis) on the charge that is transferred between the phases. The charge vs. potential slope represents the "pseudo capacity" of the system, which can be considerably higher than the capacity of the double layer (i.e., of a purely capacitative electrode interface). Since an electrochemical capacitor cell is made of two capacitors in series, each representing one electrode-electrolyte interface, the overall capacity of the cell is one-half the capacity of the individual electrode interface. But the stored energy is augmented by the cell voltage being twice that of the single electrode interface.

Symmetric electrochemical capacitors have electrical behavior similar to electrostatic capacitors. Of particular relevance to the proposed work is the question of energy (E) delivered by the capacitor, which is related to the integral capacity (C) and initial potential (V_i) and the final potential (V_f) of the capacitor by the expression:

$$E = 1/2C [V_i^2 - V_f^2] \quad [1]$$

or

$$E = 1/2CV_i^2 [1 - \alpha^2] \quad [2]$$

where α is the fraction of the initial voltage retained in the capacitor. If the internal resistance of the capacitor (R_i) is not negligible when compared with the external resistance (R_e), and both of these resistances are constant, the useful energy (E_u) is given by:

$$E_u = 1/2CV_i^2 [1 - \alpha^2] \frac{R_e}{R_e + R_i} \quad [3]$$

For the purpose of the following comparison of the energy of symmetric and asymmetric devices, the supercapacitor's energy can be expressed as a function of the charge, Q, which can be obtained by the complete discharge of the capacitor ($Q = CV_i$). Accordingly, Equation [2], for instance, can be converted to:

$$E = 1/2QV_i [1 - \alpha^2] \quad [4]$$

Symmetric electrochemical capacitor have a number of characteristics not exhibited by dielectric capacitors. As mentioned above, electrochemical capacitance is orders-of-magnitude higher than dielectric capacitance. On the

other hand, they have a relatively low limit to the voltage that they can tolerate before undesired reactions (e.g., H₂O electrolysis) occur.

Asymmetric devices have different reactions at each cell electrode. The reactions can be a) both capacitative in nature, b) one capacitative and the other battery-like or, c) both battery-like. The latter type represents an ultra-high power battery. The high-power characteristic can be obtained by the selection of materials with very reversible reactions (such as proton insertion in NiO to produce NiOOH, or in Raney nickel, or in palladium to give a hydride) and by the spreading the active materials over large electrode areas so that ohmic resistances within the electrodes, and the mass diffusion within the active material, are low.

The main advantage of the ultra-high-power battery is that it delivers the energy at a substantially invariant potential. Its energy is related to charge and voltage by:

$$E = QV_i \quad [5]$$

Comparison of Equations [4] and [5] shows that the energy obtained from the ultra-high-power battery operating at a voltage, V, is $2/(1 - \alpha^2)$ larger than that of the ultra-capacitor with the same initial voltage, V.

In principle, the potential electrochemical limitations of the super-capacitor discussed above apply to the ultra-high-power battery. In practice a specific system has to be selected with very high reversibility (e.g., a system involving only simple proton insertion reactions), with very low internal resistance, etc.

REVIEW OF PRIOR WORK

Carbon Capacitors

One of the first electrochemical capacitors developed had carbon paste electrodes and liquid sulfuric acid electrolyte, together with a microporous separator. Relatively thick (36 mil) electrodes were used to get 2 F/cm² capacitance from this system at low frequencies and/or low charge/discharge rates [1]. Later developments in electrode technology for the acid electrolyte electrochemical capacitor included lead counter electrodes [2] and polyoxometallate-deposited carbon paste electrodes, stabilized with an organic amine [3]. These modifications add either additional weight or manufacturing complexity to the capacitor system and resulted in poor stability during cycling.

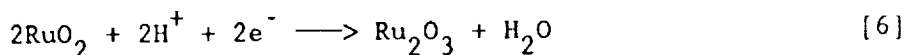
Several workers have attempted to improve the performance of carbon-based electrochemical capacitors [4,5,6,7]. John Currie investigated several carbons with different micropore volumes and compared the performance of H₂SO₄ and K₂SO₄ as electrolytes. An improvement in capacity with micropore surface area was noticed and the self-discharge rate was significantly reduced with K₂SO₄ electrolyte. A drawback of the later approach was the considerable increase in internal series resistance with the neutral electrolyte.

Researchers at Space Power Institute, Auburn University have been conducting research to minimize series resistance in carbon-based capacitor systems [5,6]. They point out that one of the main drawbacks of carbon black

as electrode material is its high resistivity arising out of poor particle-to-particle contact. The energy density (KJ/kg) is directly proportional to accessible surface area of electrode materials, and carbon black is the only known electrode material with surface areas in the range 1000-2000 m²/gm. They show that the series resistance can be decreased considerably by making a composite of nickel or stainless steel fiber (20 microns in diameter) and carbon black/fibers. More than an order-of-magnitude improvement in capacitance for unit weight is realized by this approach.

Noble Metal Capacitors

Oxides of noble metals, mostly RuO₂, have been investigated extensively as an electrode material. RuO₂ has a high capacity of about 150 microfarads/real cm² [8]. This is substantial due to pseudocapacity from surface reaction, which can be written approximately as:



This type of surface reaction, in combination with double-layer processes, has been shown to be capable of sustaining high current densities on the millisecond scale [9,10]. RuO₂ can be made into a high-surface-area coating [11] or as high-surface-area particulates [12]. Bonding of particulates to an ionomer membrane has been demonstrated for RuO₂ anodes for use in chlor-alkali cells [13] where membrane and electrode assemblies with active areas of up to 35 ft² have been prepared.

Craig [14] describes a supercapacitor based on ruthenium oxide and mixtures of Ru and Ta oxides, and reported capacitances as high as 2.8 F/cm².

Sierra Alcázar, et al. [15] have described an electrochemical capacitor cell using high-surface-area RuO₂ having a surface roughness (real area/geometric area) of greater than 10,000; this device used a liquid sulfuric acid electrolyte.

Other researchers have worked to increase the capacitance of electrode structures. A summary of some of the most applicable work is as follows:

The work of Craig, Pinnacle Research, and Giner, Inc. with RuO₂-based systems are attempts to improve the power output of capacitors while improving the charge storage capacity by one or two orders of magnitude. McHardy, et al. [16,17] at Hughes reported essentially on a similar system with IrO₂ as the electrode material, except that they paired it with a Pt/H system. This is fundamentally different from an electrochemical capacitor. The Pt-H electrode uses the fast electrode kinetics of the hydrogen reaction and the large pseudocapacitance associated with adsorbed hydrogen. The IrO₂ electrode is essentially the same as RuO₂ except that it has higher charge density and power capability, if properly prepared. McHardy, et al. report a typical capacity of 20 mC/cm² for their Pt-H/IrO₂ system for 5 mS pulses.

Rauh, et al. [18] have investigated IrO₂, and to a lesser degree RuO₂, as part of a program to screen several materials for pulse power applications. A sputtered IrO₂ film gave 11 mF/cm² for 0.1 micron thickness; a 5-micron film of thermally prepared IrO₂ gave 35 mF/cm².

Non-Noble Metal Oxide Capacitors

Rauh, et al. [19] investigated a nickel oxide film in combination with LaNi_5 as the hydrogen electrode. Sputtered, electrochemical, and chemical nickel oxides were examined -- only electrochemically formed oxide gave significant capacity. Several problems of scaling up these systems were noted which included current distribution, resistive/inductive losses, heat rejection, side reactions and limited cycle life for pulse power applications.

A recent investigation of the nickel oxide electrode was by the GM research labs [20]. A nickel-zinc battery designed for electric vehicles was tested for pulse power capabilities in this work. The power output was limited by the nickel oxide electrode, and depended on the state of charge of the battery. While sintered nickel oxide electrodes showed no degradation after 300-500 deep discharge cycles, pocket-type nickel oxide electrodes showed severe power capability degradation after only several cycles.

Rauh, et al. [18] also investigated WO_3 . This and other hydrous oxide films they claim, take advantage of both non-faradaic and faradaic processes. For example, a one-micron thick WO_3 film should give 22 mF/cm^2 in non-faradaic capacitance and 220 mF/cm^2 in faradaic capacitance. This translates into an energy density of 7.8 Whr/lb (258 kJ/l) and a power density of 434 kW/lb (1500 kW/l). Thicker films, unfortunately, do not appear to have linear scaling of capacity.

Craig, in his patent application [14] has also claimed supercapacitance behavior (in cyclic voltammetry studies) with metal oxides such as Mo, W, Co and Ni.

Several other battery systems such as Li/metal sulfide, Li/SO_2 , Pb/acid and several conducting polymer based systems have been investigated as pulse power sources. These suffer from either inadequate safety, poor cycle life, or low power capabilities.

Non-Aqueous Capacitors

Non-aqueous solutions, such as propylene carbonate with a dissolved salt have been used in capacitors. These electrolytes have been successfully used in the low-rate Dynacap capacitor [7] to achieve single-cell voltage of up to 2.8 V with a specific capacitance of 100 F/g . They are limited for pulse power applications because of their low conductivity. Also there is concern about the long-term stability of these materials.

Capacitors Based on Conducting Polymers

Conducting polymers are a class of materials that have interesting possibilities for capacitor applications. Polyaniline polymer films formed on Pt and nickel foils have been used as supercapacitor devices. Stability problems of these polymers appear to limit the cycle life at the present stage of development. In addition, they typically exhibit a much higher resistance.

Polyaniline is an electronic conductor only when immersed in acid electrolyte, between 0.2 and 0.8 V (vs. SCE) [21]. Gottesfeld, et al. [22] reported a capacitance of $800 \text{ Coulombs/cm}^3$ in aqueous acidic electrolyte for a

10-60 nm polyaniline film, cycling between 0 and 0.55 V (vs. Ag wire). In recent work, Bhakta, et al. [23] have described conductive polymers for use in super capacitors based on aniline copolymers. Polymer films were formed on Nafion coated platinum and nickel substrates using different aniline derivatives.

DEVICE CONCEPT AND DEVICE FABRICATION

The device concept and fabrication methods are fully explained in earlier publications [24,25]. The capacitor includes 1) a three-dimensional metal oxide-particulate-ionomer composite electrode structure, whereby the ionomer coats the individual particles and provides a mechanism for continuous proton transport throughout the composite structure and 2) a unitized repeating cell element that includes this three-dimensional composite electrode structure. The composite electrode structures are bonded to opposite sides of a thin sheet of a solid proton-conducting ionomer membrane such as the Dow XUS 13204.10 and form an integrally bonded membrane and electrode assembly (MEA). An exploded view of the cell components and assembly of a 35-cell stack are shown in Fig. 1. In this device, the membrane electrode assemblies (MEAs) are stacked in a bipolar arrangement. An electrically conductive pressure pad is used at one end to ensure isostatic conditions on all MEAs. The assembly is held in place using titanium bolts and nuts, torqued to the desired force. A photograph of this device is shown in Fig. 2.

EXPERIMENTAL/DISCUSSION

Capacitance test consisted of discharging the MEA across a 10-ohm load and measuring the RC time constant - the time to decay from 0.9 to 0.331 V (0.9/e). The MEA was charged to a potential of +1.000 V using a PAR 173 Potentiostat/Galvanostat in conjunction with a PAR 276 Interface. The cell was then disconnected and allowed to discharge across a 10-ohm load while the PAR 276 recorded the voltage decay curve. Internal resistance was determined by applying a square wave current pulse of ± 0.5 Amps, 100 Hz and measuring the instantaneous voltage decay at the break points.

Performance and Life Test Results of Multicell Stacks

Breadboard capacitor stacks containing 5, 10 and 35 cells were fabricated, as shown in Fig. 1, using Nafion-coated RuO_x particulate electrodes bonded to Dow XUS 13204.10 membranes. Individual (unit) cell area was 25 cm². Typical capacitance per unit cell ranged from 0.7 to 1 F/cm². The results of cycle testing (up to 1500 cycles) of the 5-cell unit on a 60-second charge/discharge cycle are shown in Fig. 3 together with the energy efficiency. The unit was charged at a constant current of 0.6 A to 5 V, then, after about an 8-second live hold, the unit was discharged into a 0.134 ohm load. This was repeated at 60-second intervals until 1574 cycles were completed. The energy efficiency for this very high load is ~35%. While part of the efficiency loss is due to iR dissipation, a significant portion of the energy loss can be attributed to slow discharge processes, which may be the charge/discharge of the inner core of the RuO_x particles. The efficiency improves to 82% for a 10-ohm load and about 89% for a 100-ohm load (Table 1). Charging rate does not seem to affect the energy efficiency appreciably at moderate rates (Table 2). The self-discharge behavior (or leakage current) is illustrated in

Table 3. Comparison of these data with that presented in Table 1 shows that approximately 15% of the energy is lost for a holding time of 5 minutes. The effect of temperature on capacitor efficiency is shown in Table 4. Efficiency decreases from approximately 66 to 61% as the temperature decreases from 46 to 10°C. At -4°C, the efficiency decreases dramatically to 29%. The approach to decreasing this efficiency loss at low temperatures is discussed in a subsequent section.

Figure 4 shows the capacitance and resistance of the 5- and 35-cell units as a function of time. Both the capacitance and resistance are steady over the duration of the test which is over a year for the 5-cell unit.

Figure 5 shows the gravimetric and volumetric power densities of our capacitors as a function of pulse width. For a 0.7 V cutoff, power densities as high as 2×10^3 watts/kg and 4×10^4 watts/L can be obtained for 5-msec pulses. This result can be improved further as the specific capacitance of these devices are increased as discussed below.

Approaches to Increasing Energy Density

The maximum capacitance that has been realized currently with the RuO_x^* 100 m^2/g Nafion-coated structures [24,25] is in the range of 75-80 F/g. Calculations based on 150 microfarads/ cm^2 show that a RuO_x particulate material of 100 m^2/g surface area should yield capacitances as high as 150 F/g. For a 20 mg/cm^2 RuO_x electrode structure this should give a calculated capacitance of 3 F/ cm^2 . The observed capacitance, however, is only ~ 1 F/ cm^2 . Through TEM studies in the above cited reference it has been observed that for the RuO_x particles the typical particle diameter is approximately 50,000 Å with a porous substructure which is only partially accessible to the solid ionomer. Thus there is a significant portion of the 100 m^2/g surface area that is not available for capacitive charging. If the particle size of RuO_x is reduced to 40 Å size, then assuming spherical particles, and using the equation below,

$$\text{Surface area} = \frac{6}{\rho D}, \quad \begin{array}{l} \rho = 7 \text{ g/cc for } \text{RuO}_x \\ D = 40 \text{ Å (particle diameter)} \end{array} \quad [7]$$

a surface area of 214 m^2/g is calculated. Of more importance is that essentially all of the surface area of the 40 Å particle should be accessible for coating with solid ionomer. For this surface area, capacitances of the order of 320 F/g are obtainable. Assuming a 20 mg/cm^2 RuO_x electrode structure (40 Å particles coated with solid ionomer) the calculated capacitance is 6.4 F/ cm^2 .

Table 5 shows our initial results on our attempts to increase the specific capacitance. Two approaches have been experimented in obtaining the data presented in Table 5. The first two entries in this table use $\text{RuO}_x\text{-IrO}_x$

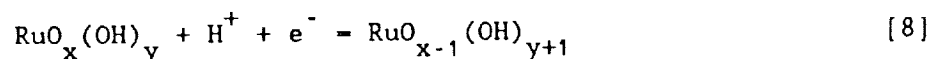
* Technically, RuO_x is a more correct expression of the chemical compound than RuO_2 since the x-value can range from 1.9 to above 2.0. In addition, the charging/discharging cycle of the capacitor may cause variations in the oxidation state of the compound.

alloy and IrO_x pure material to enhance capacitance. The addition of IrO_x to RuO_x increases the surface area and, perhaps, results in increased specific capacitance. The capacitance of a solid-ionomer cell fabricated with IrO_x was 1.4 F/cm², leading to a specific capacitance of 45 F/g. The second approach

is to disperse the RuO_x to 20-200 Å range particle size. To do this, we need to use a substrate on which the RuO_x can be deposited. Activated carbon was chosen as a support and RuO_x deposited onto it using various methods. The increase in specific capacitance is approximately one order of magnitude. One disadvantage in this approach is the loss of volume energy density. Approaches are being investigated to at least partially preserve the volume energy density while decreasing the RuO_x content.

Approaches to Increasing Low-Temperature Performance

The influence of temperature on the performance of a PEM all-solid ionomer capacitor is shown in Table 4. The capacitor contains only hydrated water which is part of the ionomer structure. The performance of these capacitors drops abruptly below the freezing point of water. Two factors appear to contribute to the performance decrease: the conductivity of the electrolyte and the rate of the proton transfer reaction



We attempted to improve the performance of these devices by lowering the freezing point of water through the addition of certain solutes.

Figure 6 shows the capacitance and ESR behavior as a function of temperature for MEAs treated in several ways. The capacitance of the baseline Nafion 117 MEA (contains only water) dropped drastically from 0.693 F/cm² at room temperature (25°C) to 0.048 F/cm² at -14°C, while internal resistance increased from 17 to 220 milliohms. The test results obtained after soaking the MEAs in phosphoric acid, glycol and N-methylformamide solution are summarized below.

DOW MEAs were tested after treating by soaking overnight in 43% H₃PO₄ (50% by volume solution of Fisher 85% Phosphoric Acid), 40%, 50% and 70% solutions of ethylene glycol (J.T. Baker #3-9300), and 50% N-methylformamide, then tested at various temperatures down to approximately -40°C to obtain performance curves. Treatments with all the solutions above were carried out at room temperature. Some testing was also conducted by soaking the MEAs in glycol solutions for 1 hour at 25°C. In one set of these experiments, a treatment solution containing 5% Nafion in glycol/water was used.

Phosphoric Acid Treatment of MEAs: The DOW MEA treated in 43% H₃PO₄ was clearly superior at retaining capacitance and internal resistance characteristics. From 25°C temperature, down to -38°C, capacitance dropped from 0.577 F/cm² to 0.543 F/cm² (94% retention) while internal resistance rose from 4.2 to 25 milliohms.

Ethylene Glycol Treatment of MEAs: The MEAs treated with 40% and 50% ethylene glycol in water for one hour at 25°C appear to show good low-temperature performance as shown in Fig. 7. Also included in these tests was a MEA treatment with a 5% Nafion ionomer in 50/50 glycol water. The 40% ethylene

glycol in water showed the best overall capacitance from 25°C down to a temperature of approximately -25°C. From 25°C, down to -20°C, capacitance dropped from 0.701 to 0.532 F/cm² (76% retention). However, at a temperature of -30°C, capacitance dropped to 0.164 F/cm². The effect of using 1) 50% ethylene glycol in water and 2) 5% Nafion ionomer in the 50/50 glycol/water is also shown in Fig. 7. The capacitance data for the MEA soaked in 50% glycol in water have been normalized for making a direct comparison of the data. It appears some improvement in -30°C low-temperature performance for the glycol systems is obtained when using 50% rather than 40% glycol in water. Addition of dissolved Nafion ionomer (5%) to the 50% glycol solution appears to improve the MEA performance compared to the 50% glycol alone. Further work is required to define the optimum water/glycol ratio and treatment conditions. A potential advantage of the water/glycol system versus the H₃PO₄ system for improving low-temperature capacitor performance is that the glycol is not a liquid electrolyte, thus minimizing the possibility of shunt currents, corrosion and leakage.

N-Methylformamide Treatment of MEAs: The performance of an MEA soaked in a 50% N-methylformamide solution is shown in Fig. 6. Generally, the overall performance of the cell as to capacitance and resistance was poor, compared to the H₃PO₄ and the 40%, 50% glycol solutions.

A summary of the low-temperature results is shown in Table 6. In the above experiments, we have used a new MEA for each low-temperature experiment in order to avoid contamination from one experiment to another. However, the capacitance of the several MEAs used in this test program varied somewhat. The best low-temperature results were obtained for phosphoric acid; the capacitance value at -30°C for the MEA soaked in phosphoric acid is approximately 95% of the 25°C value. Both 40 and 50% ethylene glycol treated samples retain 60-80% at -20°C of the 25°C capacitance; however at -30°C, 50% glycol shows better performance.

AEROSPACE APPLICATIONS

Although the projected energy densities for electrochemical capacitors are about two orders of magnitude lower than that of batteries, the high-power-density characteristics of these devices renders them as potentially viable candidates for meeting pulse or peak electrical power requirements for some anticipated aerospace mission scenarios, especially those with discharge times on the millisecond to second time scale. On a volumetric or gravimetric basis, the advantages of utilizing electrochemical capacitors rather than batteries for meeting the peak power demands associated with a specific mission scenario will largely depend upon the total and pulse durations of the power peaks.

Projected energy and power densities for electrochemical capacitors and batteries [25] can be used to make approximate volumetric comparisons between these two power sources for peaking applications. For example, for a defined peak power level and total duration, the total energy required for storage in an electrochemical capacitor can be calculated. If one assumes that the total charge will be stored in the cell structure of the capacitor, then the volume of the capacitor which satisfies both its energy and power density characteristics can be estimated. A similar calculation can be made to estimate the volume of the reserve portion of a battery power source, i.e., the additional

size to meet the peaking demands which exceed the steady-state power needs. Based on the data cited above, the estimated volumes of an electrochemical capacitor and a battery for supplying the peak power needs would be equal for a total peak power duration of 2.0 minutes. For a total duration of 30 seconds, the volume of a battery peaking power source would be four times larger than that of an electrochemical capacitor. If a mission scenario is such that there is sufficient time for recharging between transients, then the required capacitor volume could be reduced even further.

Besides the potential for volume and/or mass reductions, other inherent characteristics of electrochemical capacitors could be critical drivers for selection of this technology for specific missions. High reliability and safety have significant impact on technology selection, and solid-ionomer electrochemical capacitors contain no toxic or corrosive electrolyte nor are any appreciable reaction products formed. They have a very high cycle life, and thus, can be utilized as a rechargeable secondary power source, if this is a feasible option for a mission scenario. Assessments of power source technologies will also need to consider effects of the thermal environment which will be encountered upon the power source, as well as any operational constraints which may be imposed by incorporation of the power source in high-speed circuitry.

Specific applications for electrochemical capacitor technology may be envisioned within the advanced launch systems (ALS) development and Orbiter upgrade programs which are presently being pursued within NASA. With such goals as increasing safety, reducing turnaround time, lowering recurring costs, reducing vehicle weight, and increasing operational efficiency in mind, a major objective of these programs is to replace existing auxiliary power unit (APU)/hydraulic actuator systems with electromechanical actuator (EMA) systems.

An advanced EMA system, which is depicted in Fig. 8, will require a highly reliable power source to meet its unique electrical power requirements, which include high peak power pulses for short durations (<100 milliseconds). The advanced EMA system, which would be composed of independent power channels to meet failure-tolerant design requirements, would be developed to have high-power and high switching-speed capabilities. Multi-phase induction motors would be controlled via a high-frequency AC link using resonant power processing technology. For shuttle evolution programs, the proposed EMA system would power and control all the flight control surfaces, landing gear, and the Orbiter's thrust vector control (TVC) systems. These systems are powered just before launch, during ascent, and throughout re-entry and roll-out.

As part of a Shuttle EMA system study performed for the Johnson Space Center, several candidate electrical power system configurations were conceived to meet EMA power requirements and were compared to determine which would be the most suitable option [26]. The electrical power requirements per power channel which were used to synthesize the power systems included:

- 3.5 kW average power
- 5.5 kWh energy
- 120 kW peak power (400 ms total; 40-80 ms pulses)
- 270 VDC

The candidates for the conceptual study included several high-power-density battery systems, modified Orbiter fuel cells in both dedicated and integrated design approaches, and advanced (high power density) alkaline fuel cells.

In the above study, the modified Orbiter fuel cell design approaches were favored with respect to imposing the least impact upon the implementation schedule and initial cost of implementation. Both of the conceptual design approaches incorporated the solid-ionomer electrochemical capacitor for providing the 120-kW peak power pulses specified for the ascent and descent phases of EMA operation. The scaled-up 270-volt capacitor required per power channel, which was sized based upon existing data, would contain 300 cells, weigh approximately 60 pounds, and occupy a volume of approximately 0.5 ft³. A schematic of an integrated design approach is shown in Fig. 9.

As mentioned earlier, the replacement of hydraulic actuators with EMA systems is also a critical element in NASA's ALS program, which addresses TVC technology for solid rocket boosters, Atlas/Centaur launch vehicles, etc. Electrical power system trade studies have also been performed within this program, and candidate power sources have included high-rate primary and secondary batteries, fuel cells, turboalternator systems, and flywheel energy storage systems [27]. The recommended system for development based on these studies, which did not include electrochemical capacitor technology, was the bipolar lead-acid battery. The electrochemical capacitor could prove to be a viable competitor for meeting peak power demands, and an approach incorporating electrochemical capacitor technology needs to be evaluated with respect to satisfying overall mission requirements.

CONCLUDING REMARKS

Life testing of a multicell capacitor on an intermittent basis has shown, that over a 10,000-hour period, the capacitance and resistance of the cell has remained invariant. There has been no maintenance required on the device since it was fabricated. Other multicell units of shorter-life duration have exhibited similar reliable performance characteristics.

Test results obtained with multicell solid-ionomer electrochemical capacitors indicate gravimetric and volumetric power densities in the range of 2×10^3 W/g and 4×10^4 W/L, respectively, can be obtained for 5-msec pulses. Initial testing indicates that the specific capacitance of these devices can be further increased by 1) use of additives, or alloying of the RuO_x particles to result in a higher-surface-area particulate electrode structure and 2) dispersion of the RuO_x to the 20 to 200 Å range particle size by depositing the RuO_x on high-surface-area carbon. This should result in further increase in power and energy densities. Further work in this area is recommended.

Testing indicates there is loss in efficiency (joules out/joules in) when discharging the capacitor devices across a low-resistance load. The efficiency decreases from 83% for a 10-ohm load to 35% for a 0.134-ohm load. The formation of smaller RuO_x particles (20-200 Å) and improved ionomer coating should help access more of the RuO_x surface structure and improve efficiency.

Some initial testing of the self-discharge characteristics of the solid-ionomer capacitor indicate that approximately 15% of the energy is lost for a holding time of 5 minutes. This loss can likely be decreased by using improved quality procedures when fabricating the individual cells to minimize electrical shunt paths.

The performance of the solid-ionomer capacitor, containing only hydrated water, drops abruptly below the freezing point of water. Two factors appear to contribute to the performance decrease: the conductivity of the electrolyte and the proton transfer reaction. The performance of the capacitors was improved by lowering the freezing point of water through the addition of certain solutes. Addition of phosphoric acid to the MEAs extends the low-temperature limit of our capacitors to -30°C , without any significant loss in performance. Treatment of the MEAs with certain concentrations of glycol in water also improves the low-temperature performance significantly compared to the baseline MEA. The low-temperature performance of capacitors equilibrated with glycol appears to depend on the quantity of glycol in the membrane and treatment conditions. A range of 40 to 50% glycol in water and one-hour treatment at 25°C gave the best results in this study. The addition of dissolved Nafion ionomer (5%) to the 50% glycol solution appears to improve MEA performance compared to 50% glycol alone. A potential advantage of the water/glycol system versus the H_3PO_4 system for improving low-temperature capacitor performance, is that the glycol is not a liquid electrolyte, thus minimizing the possibility of shunt currents, corrosion and leakage. A systematic study of the proton mobility and ionic conductance at low temperatures in proton-exchange membranes equilibrated with different types and quantities of non-electrolyte solutes may lead to optimum low-temperature behavior of our capacitors and is recommended for future studies.

ACKNOWLEDGEMENTS

This work was supported in part by the following: DARPA/Office of Naval Research Contract N00014-88-C-0391, Sandia National Laboratories, and National Science Foundation Grant: ISI-9060142.

REFERENCES

1. D.L. Boos, U.S. Patent No. 3,536,963 (October 27, 1970).
2. J. Phillips and H. Takei, U.S. Patent No. 4,438,481 (March 20, 1984).
3. E.A. Cuellar and M.J. Desmond, U.S. Patent No. 4,630,176 (Dec. 16, 1986).
4. J.C. Currie, US Army Workshop on Capacitors and Batteries for Pulse Power Application, Asbury Park, NJ, 1987, p. 211.
5. M.F. Rose, M.F., S. Best, B. Tatarchuk, US Army Workshop on Capacitors and Batteries for Pulse Power Applications, Asbury Park, NJ, 1987, p.249.
6. F. Rose, D. Kohler and B. Tatarchuk, J. Electrochem. Soc., 137 (1990), 6.
7. K. Hiratsuka, T. Morimoto, Y. Sanada, and K. Kurihara, Seattle, Washington, Extended Abstracts, Electrochem. Soc., 1990, p. 129.
8. J.M. Kleijn and J. Lyklema, J. Colloid and Interf. Sci., 120, (1987) 511.
9. G.L. Holleck, B.H. Jackman, and R.D. Rauh, Abstract No. 18, The 173rd Electrochemical Society Meeting, Atlanta, GA, May 1988.
10. Ho-Lun Lee, G. Mason, and K. Kern, Final Report for ONR Contract No. N00014-87-C-0705, 1988.

11. S. Trasatti and G. Lodi, in *Electrodes of Conductive Metallic Oxides Part A*, S. Trasatti (Ed.), Elsevier, Amsterdam, 1980, Ch. 7.
12. E.N. Balko, C.R. Davidson, and A.B. LaConti, *J. Inorg. Nucl. Chem.*, 42 (1980) 1778.
13. T.G. Coker, R.M. Dempsey, A.B. LaConti, U.S. Patent No. 4,191,618 (1980).
14. D.R. Craig, Canadian Patent No. 1,196,683 (1985).
15. H.B. Sierra Alcázar, K.A. Kern, G.E. Mason, and R. Tong, in *Proceedings of the 33rd International Power Sources Symposium*, June 13-16, 1988, The Electrochemical Society, 1988, p. 607.
16. J. McHardy, US Army Workshop on Capacitors and Batteries for Pulse Power Applications, Asbury Park, NJ, 1987, p. 277.
17. J. McHardy J., F.A. Ludwig, L.R. Higley, A. Kindler, and C.W. Townsend, U.S. Patent No. 4,766,522 (1988).
18. R.D. Rauh, US Army Workshop on Capacitors and Batteries for Pulse Power Applications, Asbury Park, NJ, 1987a, p.408.
19. R.D. Rauh, Office of Naval Research, Final Report, Contract No. N00014-86-C-0803, 1987b.
20. D.A. Corrigan, *J. Power Sources*, 21, (1987) 33.
21. S. Glarum and J. Marshall, *J. Electrochem. Soc.*, 134, (1987) 2160.
22. S. Gottesfeld, A. Redondo, and S.W. Feldberg, *Electrochemical Society Extended Abstracts*, No. 507, San Diego, CA, 1986.
23. S.D. Bhakta, D.D. Macdonald, and S.C. Narang, *Extended Abstracts*, Vol. 90-2, The Electrochemical Society, 1990 (Seattle Mtg).
24. S. Sarangapani, P. Lessner, J. Forchione, A. Griffith, and A.B. LaConti, *J. Power Sources*, 29, (1990a) 355.
25. S. Sarangapani, P. Lessner, J. Forchione, A. Griffith, and A.B. LaConti, *Proceedings of the 25th Intersociety Energy Conversion Engineering Conference*, 3, 1990b, 137.
26. H. McBryar, private communication, 1991.
27. L. Burrows, private communication, 1991.

PEM ELECTROCHEMICAL CAPACITOR - 5-CELL UNIT

Charge at constant current to 5 V
 Held at constant terminal EMF (5 V)/OCV for specified time
 Discharged into selected load resistor

TABLE 1 - Effects of discharge resistor

| I_{chg} (mA) | R_L (Ohms) | Charge Time at Const. I (Sec.) | Hold Time at Const. V (Sec.) | Energy In Const. I (Joules) | Energy Out (Joules) | Efficiency (%) | Discharge Time to $V(0)/e$ (Sec.) |
|-------------------|-----------------|--------------------------------------|------------------------------------|-----------------------------------|---------------------------|-------------------|---|
| 500 | 10 | 39.7 | 0 | 55.8 | 46.1 | 83 | 41.1 |
| 500 | 1.0 | 40.1 | 0 | 56.8 | 37.9 | 67 | 4.0 |
| 500 | 0.14 ±0.01 | 39.5 | 1 | 55.4 | 17.8 | 32 | 0.20 |

TABLE 2 - Effects of constant current charge rate

| R_L (ohms) | I_{chg} (mA) | t_{chg} (Sec.) | t_{hold} (Sec.) | $(E_{in})_I$ (J) | $(E_{in})_V$ (J) | E_{out} (J) | Eff. (%) | Discharge Time to $V(0)/e$ (Sec.) |
|-----------------|-------------------|---------------------|----------------------|---------------------|---------------------|------------------|-------------|---|
| 1.0 | 300 | 69.1 | 1.1 | 59.4 | 0.8 | 38.3 | 64 | 4.0 |
| 1.0 | 500 | 39.3 | 6.0 | 55.3 | 5.0 | 37.9 | 63 | 4.2 |
| 1.0 | 1000 | 21.3 | 1.1 | 54.2 | 2.0 | 36.0 | 64 | 4.1 |
| 1.0 | 1000 | 18.7 | 1.4 | 52.8 | 3.4 | 37.3 | 66 | 3.9 |

TABLE 3 - Effects of open-circuit hold time

| (t_{chg}) (Sec.) | $(t_{hold})_{ocv}$ (Sec.) | $(E_{in})_I$ (J) | E_{out} (J) | Eff. (%) | Discharge Time to $V(0)/e$ (Sec.) |
|-----------------------|------------------------------|---------------------|------------------|-------------|---|
| 38.6 | 0 | 53.7 | 38.9 | 72 | 3.9 |
| 37.8 | 10.9 | 53.3 | 36.1 | 68 | 4.1 |
| 38.4 | 20.5 | 53.5 | 34.2 | 64 | 4.2 |
| 38.2 | 60.5 | 53.7 | 32.2 | 60 | 4.2 |
| 38.8 | 199.0 | 54.1 | 31.2 | 58 | 4.8 |
| 38.9 | 301.9 | 54.5 | 29.7 | 54 | 4.9 |

PEM ELECTROCHEMICAL CAPACITOR - 5-CELL UNIT

TABLE 4 - Effects of Temperature

| Temp. (°C) | t _{chg} (Sec.) | t _{hold} (Sec.) | (E _{in}) ¹ (J) | E _{out} (J) | Eff. (%) | Discharge Time to V(0)/e (Sec.) |
|------------|-------------------------|--------------------------|-------------------------------------|----------------------|----------|---------------------------------|
| -4 | 27.2 | 2.8 | 42.3 | 12.3 | 29 | 1.1 |
| 10 | 40.1 | 0 | 56.3 | 34.1 | 61 | 4.1 |
| 25 | 40.1 | 0 | 56.8 | 37.9 | 67 | 4.0 |
| 46 | 47.2 | 0 | 64.1 | 42.3 | 66 | 4.4 |

TABLE 5 - Approaches to increasing the specific capacitance of the all-solid ionomer capacitor

| Type | Loading (mg/cm ²) | Internal Resistance (ohm-cm ²) | Capacitance (F/cm ²) | Capacitance (F/gm metal) |
|--|-------------------------------|--|----------------------------------|--------------------------|
| RuO _x -IrO _x | 5 | 0.25 | 0.40 | 40 |
| IrO _x | 16 | 1.25 | 1.40 | 45 |
| 5% RuO _x on Carbon (I) | 10 | 0.21 | 0.48 | 480 |
| 5% RuO _x on Carbon (II) | 20 | 0.60 | 0.75 | 375 |
| 5% RuO _x on Carbon (III) | 20 | 0.48 | 0.68 | 340 |
| 50% RuO _x /IrO _x on Carbon | 13 | 0.38 | 0.63 | 63 |

TABLE 6 - Performance of treated capacitors

| SOLUTION | BEFORE TREATMENT | | AFTER TREATMENT | | | | | | | |
|--------------------------------|------------------|----------------------|-----------------------|---------------------|----------|--------------------|-----------|--------------------|-----------|--------------------|
| | CONC (%) | TEMP TIME (°C) (hrs) | 25°C ESR ¹ | 25°C C ² | 25°C ESR | 25°C C | -20°C ESR | -20°C C | -30°C ESR | -30°C C |
| H ₃ PO ₄ | 43 | 25 20 | 5 | 0.505 | 4.2 | 0.577 | 11 | 0.556 | 17 | 0.549 |
| ETHYLENE GLYCOL | 50 | 25 20 | 5 | 0.529 | 14 | 0.386 | 55 | 0.327 | 92 | 0.227 |
| ETHYLENE GLYCOL | 70 | 25 20 | 5 | 0.529 | -- | -- | 180 | 0.161 | 337 | 0.063 |
| N-METHYFORMAMIDE | 50 | 25 20 | 5 | 0.527 | 42 | 0.172 | 194 | 0.120 | 332 | 0.101 |
| ETHYLENE GLYCOL | 40 | 25 1 | 6 | 0.614 | 19 | 0.701 | 57 | 0.532 | 410 | 0.164 |
| ETHYL GLYC, 5% NAF | 50 | 25 1 | 6 | 0.586 ³ | 31 | 0.525 | 92 | 0.428 | 144 | 0.324 |
| ETHYLENE GLYCOL | 50 | 25 1 | 5.5 | 0.586 ³ | 46 | 0.450 ³ | 105 | 0.367 ³ | 152 | 0.331 ³ |

1. Milllicms, 2. Farads/cm², 3. Normalized

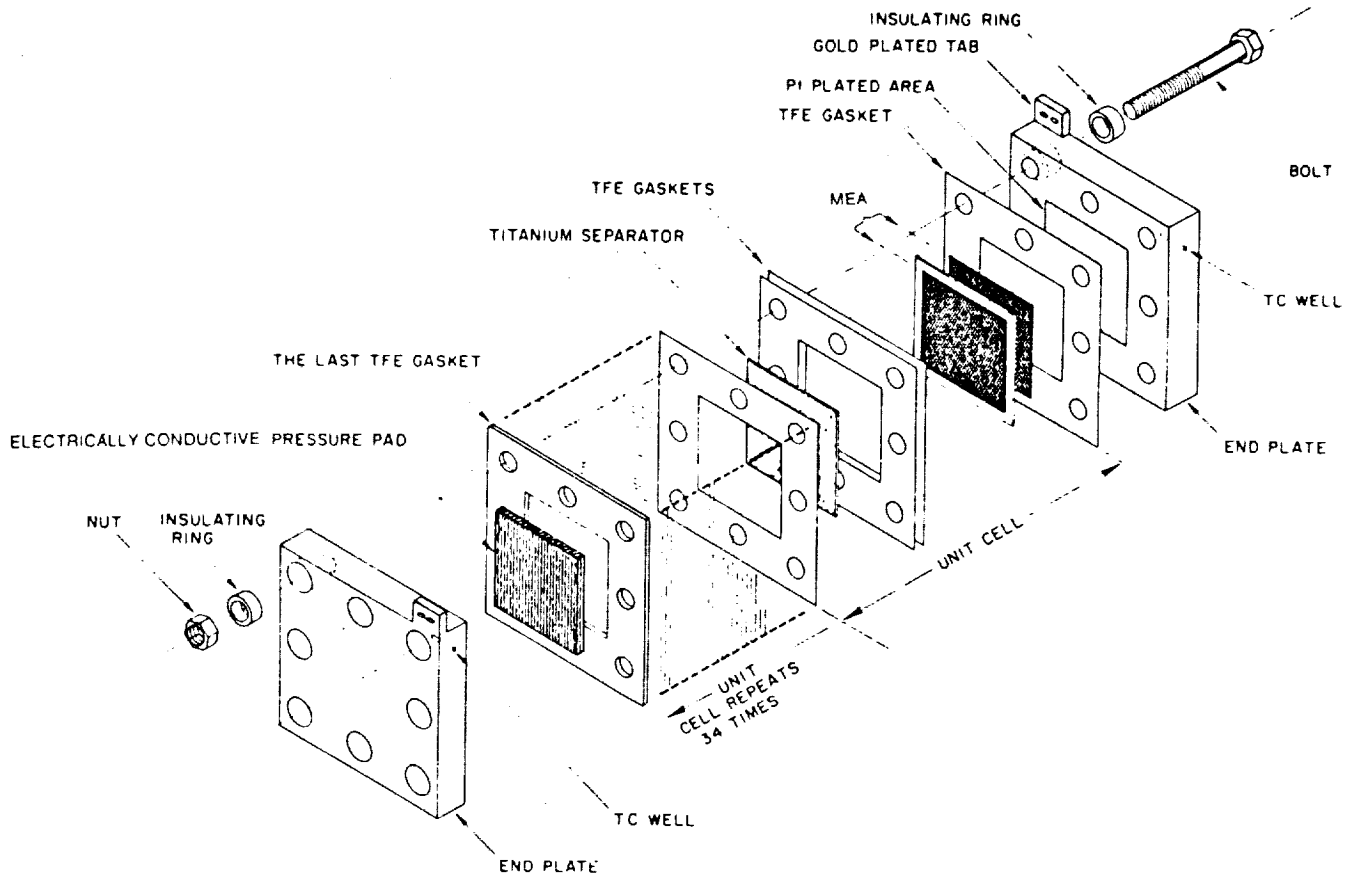


Fig. 1. Exploded schematic view of cell components.

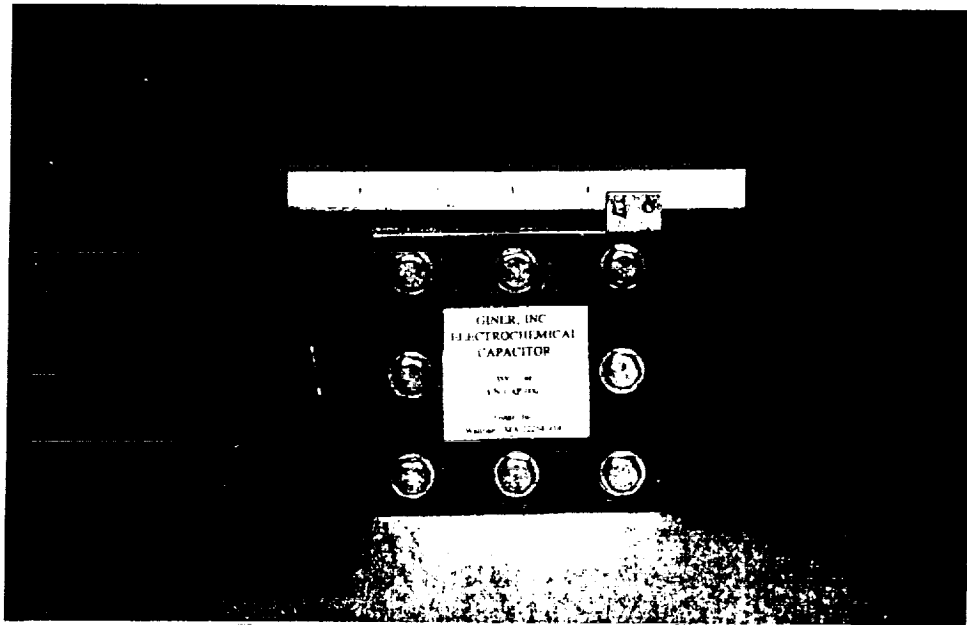


Fig. 2. Giner, Inc. 35-cell PEM electrochemical capacitor.

GINER CAPACITOR CYCLE TEST

The Giner 5-cell capacitor was tested for cycle performance. The unit was charged at a constant current of 0.6 amps to 5 volts. Then, after about an 8-second live hold, the unit was discharged into 0.14 ohms. This was repeated at 60-second intervals until 1574 cycles were completed. For 9 of the cycles, energy in and out was recorded. Result is summarized on the following charts:

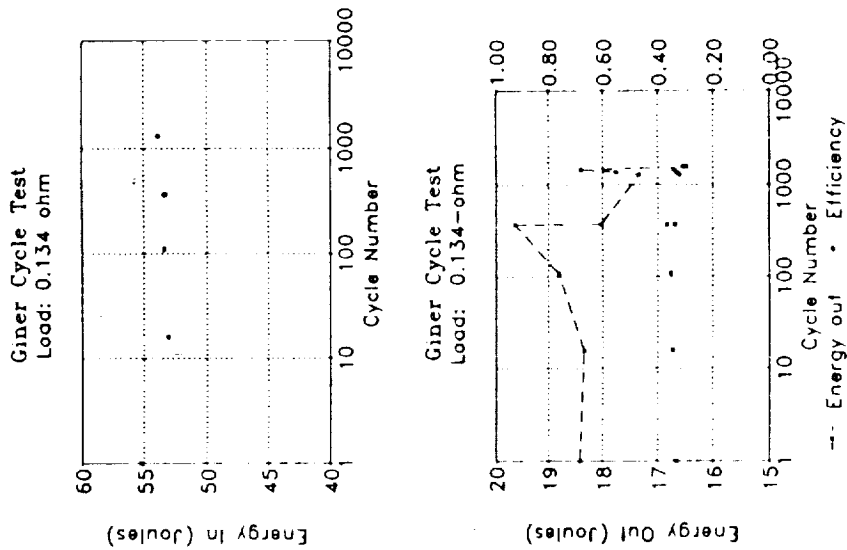


Fig. 3. Cycle testing of 5-cell unit on a 60-second charge/discharge cycle.

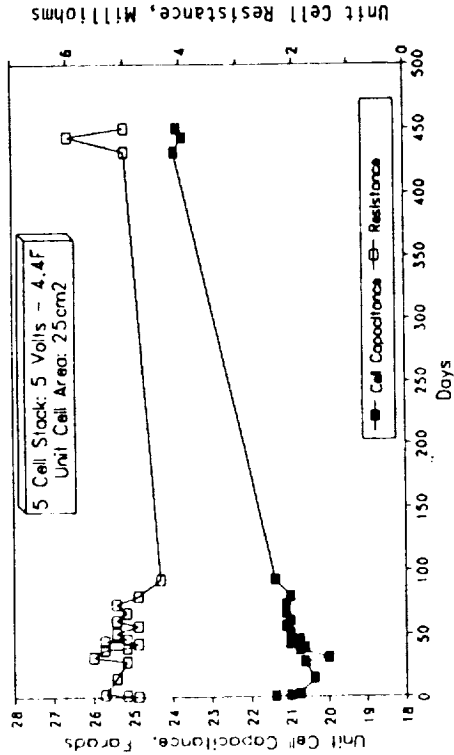


Fig. 4b. 5-cell stack; discharge across 10-ohm load.

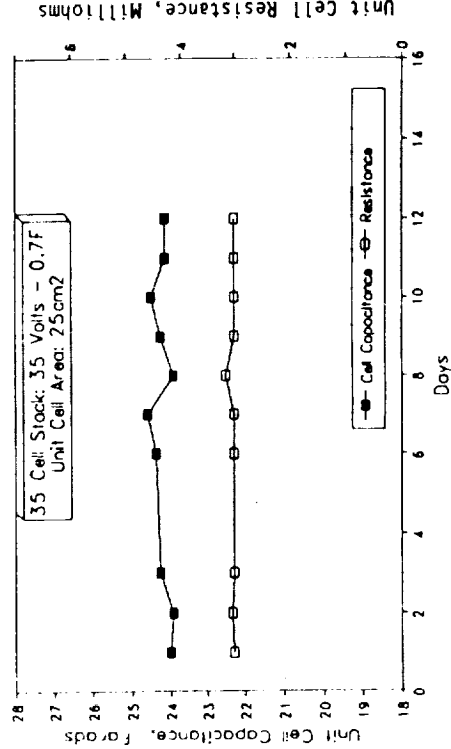
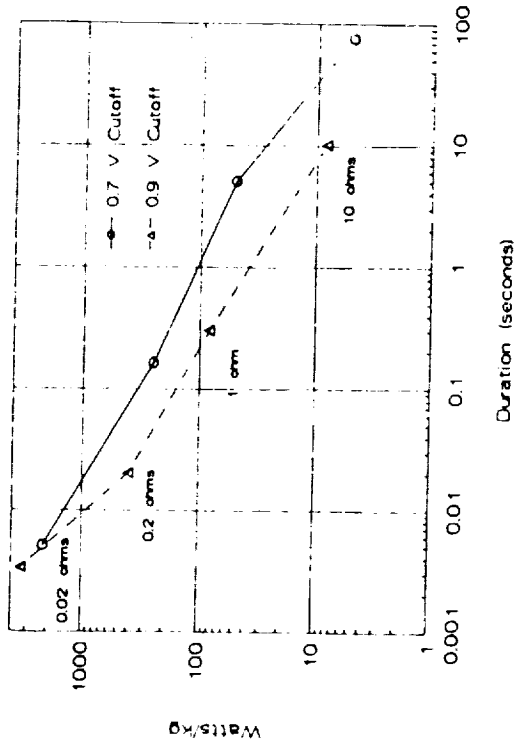


Fig. 4a. 35-cell stack; discharge across 35-ohm load.

Fig. 4. Cell capacitance and resistance of 5- and 35-cell stacks as a function of days of cell operation.

ORIGINAL PAGE IS
OF POOR QUALITY

Grav. Power Density vs. Pulse Duration
Giner, Inc. PEM Capacitor



Volum. Power Density vs. Pulse Duration
Giner, Inc. PEM Capacitor

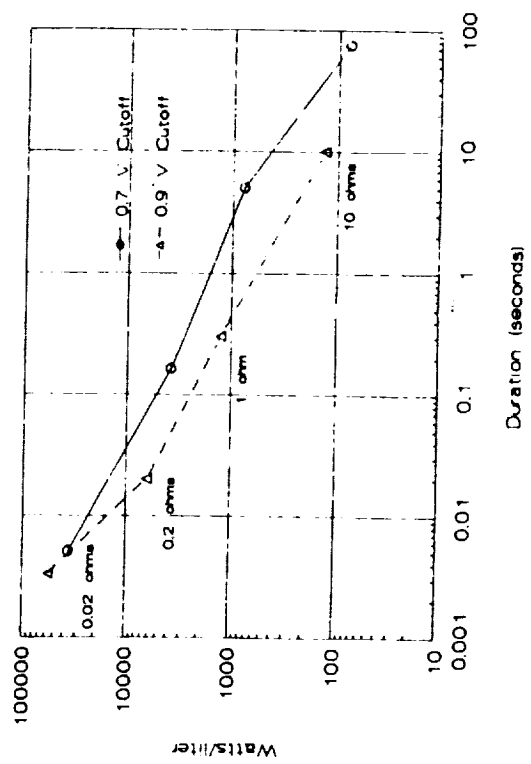


Fig. 5. Gravimetric and volumetric power density vs. pulse duration.

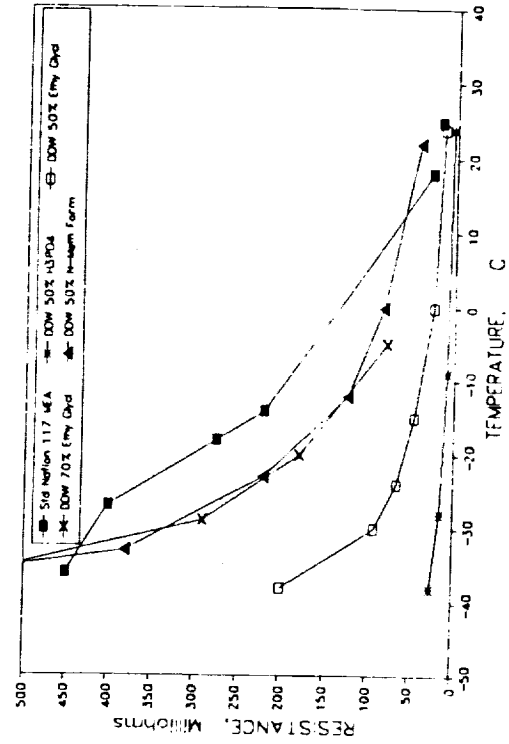
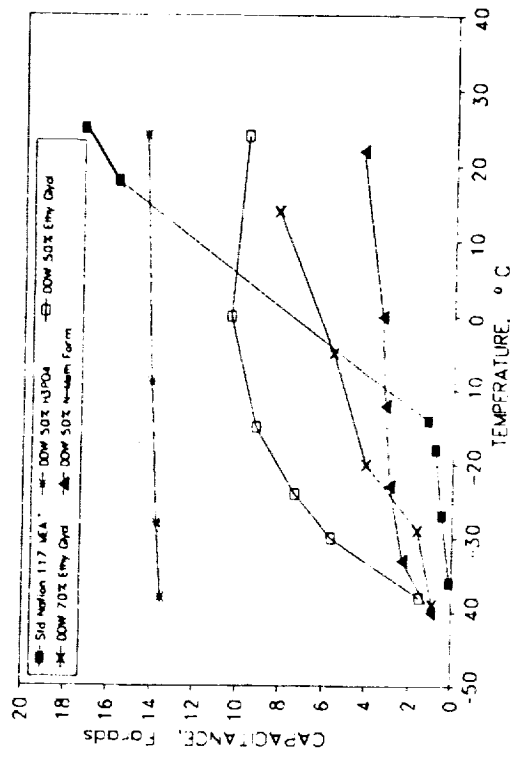


Fig. 6. Effect of variation in room-temperature treatment conditions on MEA capacitance and ESR behavior as a function of temperature of MEA operation, measured by discharge across 10 ohms (cell area = 25 cm²).

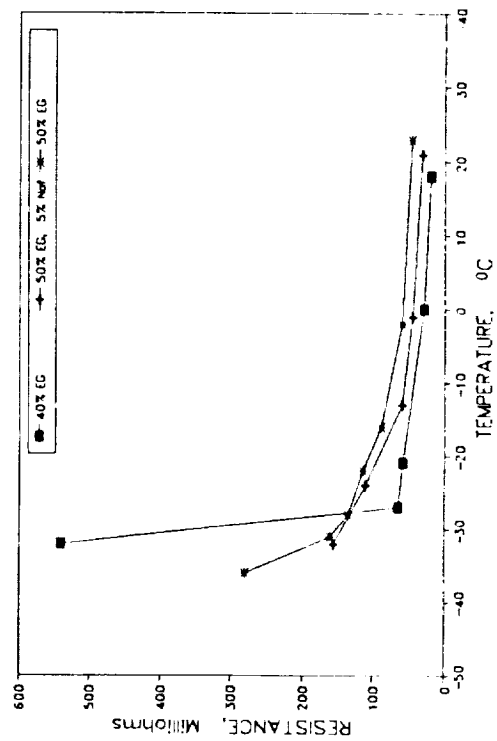
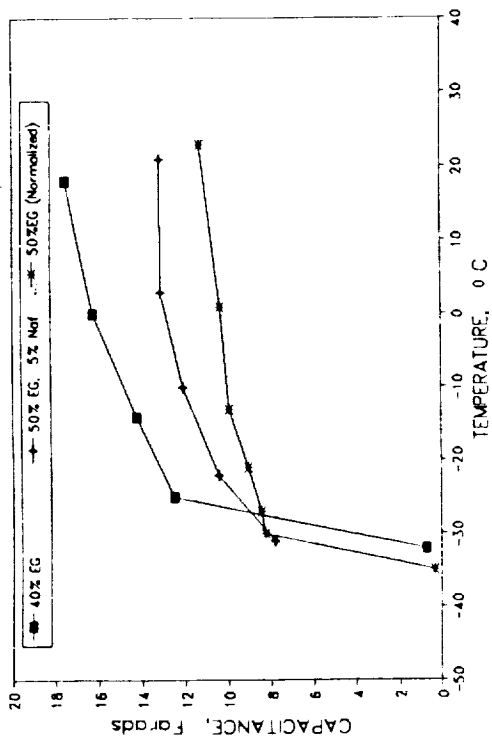


Fig. 7. Effect of short-term, room-temperature treatment in glycol-water mixtures (with and without Nafion) on MEA capacitance and resistance as a function of MEA operation, measured by discharge across 10 ohms (cell area = 25 cm²).

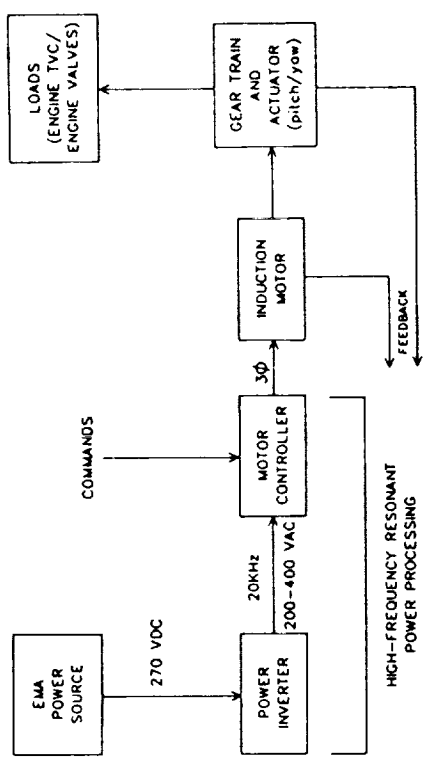


Fig. 8. Electromechanical actuator (EMA) system elements.

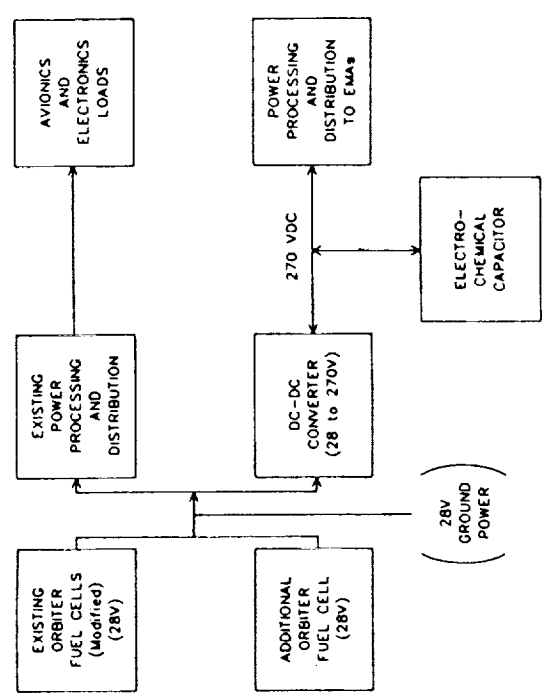


Fig. 9. Schematic of an integrated Orbiter fuel cell design approach for meeting EMA power requirements.

PERFORMANCE OF A DUAL ANODE NICKEL-HYDROGEN CELL

Randall F. Gahn
NASA Lewis Research Center
Cleveland, Ohio 44135

An experimental study was conducted to characterize the voltage performance of a nickel-hydrogen cell containing a hydrogen electrode on both sides of the nickel electrode. The dual anode cell was compared with a conventional single anode cell using the same nickel electrode. Higher discharge voltages and lower charge voltages were obtained with the dual anode cell during constant current discharges to 10C, pulse discharges to 8C, and polarization measurements at 50% state-of-charge.

INTRODUCTION

Nickel-hydrogen batteries are currently being used in numerous geosynchronous orbit (GEO) applications and also on the Hubble Space Telescope in low-Earth orbit (LEO) [1]. GEO applications require approximately 100 charge/discharge cycles per year whereas LEO applications require about 6000 cycles per year. Recent improvements in the cycle life indicate nickel-hydrogen batteries could meet the five-year life requirements for a LEO satellite (e.g., Space Station Freedom) and replace nickel-cadmium batteries for other LEO applications [2,3]. Reduction in battery weight to increase the specific energy is also being addressed through the development of lighter weight nickel electrodes [4].

This investigation focused on the improvement in the voltage performance of the nickel-hydrogen cell by reducing the polarization factors of the components. Voltage losses in a cell are a function of the ohmic resistance of the components and the electrochemical polarization parameters of the electrodes [5]. The ohmic resistance fraction of the total polarization is determined by the separator conductivity, the electrolyte concentration, the compression of the components, and the resistivity of the electrode current collectors. The electrochemical polarization portion of the total polarization is attributed to the kinetics of the reactions and mass transport of the ionic species. Reduction in the effect of any of these variables will improve the voltage performance of the cell.

In an attempt to reduce cell voltage losses, a second hydrogen electrode was introduced into the cell on the other side of the nickel electrode. (A second separator was also added between the second hydrogen electrode and the nickel electrode.) The addition of the second anode reduces the current density on the hydrogen electrode by one-half, and the additional separator provides electrolyte on the "backside" of the nickel electrodes and in effect shortens the electrolyte diffusion path into the nickel electrode by one-half. Thus, these modifications should reduce the overall polarization losses by about one-half.

The purpose of this investigation was to experimentally evaluate the voltage characteristics of a nickel-hydrogen cell containing a dual anode. The performance was compared to that of a cell using a single anode and the same nickel electrode. (The evaluation of the same nickel electrode eliminates any differences in nickel electrode characteristics.)

A second objective of this study was to evaluate the dual anode cell design using thick nickel electrodes for potential pulse power applications. However, only the analysis of a standard thickness (30 mils/0.76 mm) electrode has been completed and is reported herein.

EXPERIMENTAL

Sketches of a conventional nickel-hydrogen cell and the dual anode cell used in this experiment are shown in Fig. 1. The dual anode sketch shows the additional hydrogen electrode and separator placed on top of the nickel electrode. Cell components were 3.5 in. (8.9 cm) diameter pineapple-slice design. The nickel electrode was obtained from the Hughes Aircraft Co. The hydrogen electrodes were obtained from Eagle-Picher Industries. The same nickel electrode was used in both cells. A layered-type separator was used with each design and consisted of one layer of Zircar cloth next to the hydrogen electrode and a layer of radiation-grafted polyethylene film next to the nickel electrode. Voltage leads were spot-welded to the base of each electrode. Following assembly the cells were vacuum filled with 26% potassium hydroxide electrolyte and installed in a boilerplate pressure vessel. The current leads and voltage sensing leads were fed through a Conax fitting mounted in the lid. The vessel was evacuated and then pressurized with 150 psi of hydrogen.

Performance of each cell design was determined with constant current discharges from C/4 to 10C, constant current charges at C/2, pulse discharges at 2C, 4C and 8C and voltage-current relationships for 15-sec charges and discharges at 50% depth of discharge.

RESULTS AND DISCUSSION

The ampere hour (Ahr) capacity of each cell design was determined by discharging the cell at the C/4 rate to 0.1 V. Capacities measured for the single anode cell and the dual anode cell were 1.25 and 1.27 Ahr, respectively. For both designs, however, performance of the cell was based on a capacity of 1.3 Ahr. Charging for all cycles was done at the C/2 rate with a 5% to 10% overcharge. Following all discharges the cell was returned to the same reference point by discharging at the C/4 rate to 0.1 V before starting the next cycle.

Discharge performance at constant current as a function of cell capacity was measured at C/4, C/2, C, 2C, 4C, 6C, 8C and 10C for both cell designs. Voltage profile for the single anode cell is shown in Fig. 2 and for the dual anode cell in Fig. 3. As expected, the discharge amp-hour capacity decreased as the current increased, but both cell designs were similar over the entire range. At the 10C rate the capacity to 0.1 V was 1.09 Ahr for both cells. (Note that the cell voltage was measured at the base of the electrodes and does not reflect voltage losses associated with the current leads and connections when the measurement is taken outside the pressure vessel.)

Comparison of constant current discharges for the two designs at the C and 10C rates are shown in Figs. 4 and 5. At both rates the voltage of the dual anode cell is higher than the conventional single anode cell. The discharge capacities at the C rate were similar (about 1.2 Ahr) for both designs. The 10C discharge capacities were also unaffected by the cell design. The voltage difference between the C rate discharge curves over the entire discharge is 10 to

20 mV, but at the 10C rate the voltage difference increased with the depth-of-discharge. Figures 6 and 7 show the difference in the constant current discharge voltages between the two cells at the midpoint of the discharge and at 75% DOD. At 50% DOD the difference between the dual anode cell and single anode cell was 10 mV at the C rate and 160 mV at the 10C rate. At 75% DOD the dual anode cell C rate voltage was still about 10 mV higher but at 10C the difference between the two increased to 230 mV. These data indicate the dual anode cell has a higher voltage throughout the discharge and has less polarization at the deeper depths-of-discharge than does the single anode cell. The slopes of the middischarge voltage curves were 12.9 mΩ for the dual anode and 26.7 mΩ for the single anode cell. The slopes of the curves in Fig. 7 were 20.1 mΩ for the dual anode and 37.3 mΩ for the single anode cell. For both figures the dual anode cell resistance is about one-half of the conventional cell resistance which is what was anticipated. The change in slope of the single anode cell resistance between 50% DOD and 75% DOD was 10.6 mΩ (37.3 to 26.7), whereas the dual anode cell only changed 7.2 mΩ (20.1 to 12.9).

A comparison of the charge performance at the C/2 rate is shown in Fig. 8. Up to approximately 75% SOC the dual anode voltage was 15 to 20 mV lower than the single anode cell. The rapid rise in the voltage is probably associated with the production of oxygen which was consistent for both designs. The C/2 charge was used as the standard charge rate for the evaluation of the discharge performance. No other charge rates have been investigated.

Another objective of this study was to evaluate the dual anode cell design for pulse power applications. A comparison of the performance of both designs during an 8C standard constant current discharge and an 8C pulse discharge is shown in Fig. 9. During the pulse test the cell was alternately discharged at 8C (10.4 A) for 5 sec then switched to open-circuit for 10 sec until the cell voltage reached 0.1 V. The discharge voltage was taken at the end of the 5 sec discharge period. The standard discharge was a continuous 10.4 A current until the cell voltage reached 0.1 V. The pulse discharge voltage for the dual anode cell was only about 10 mV higher than the voltage obtained during the constant current discharge. However, the pulse discharge voltage for the dual anode cell was about 120 mV higher than the pulse voltage for the single anode cell, indicating a significant decrease in polarization effects with the dual anode design. This figure also shows the pulse discharge voltage of the single anode cell is about 30 mV higher than the constant current discharge voltage. Comparison of the voltage difference between the standard and pulse discharges for both designs demonstrates the significant reduction in polarization in the cell when the second anode is used.

Both designs were also evaluated on pulse discharge at the 2C and 4C rates. Voltage curves were in the same order as the 8C discharges but the differences were less. A comparison of the pulse discharge voltage performance at 2C and 4C for the dual anode cell are compared with the 8C performance in Fig. 10. The improvement in performance of the dual anode cell over the conventional cell is shown in Fig. 11. Midpoint voltages for the pulse discharges are plotted against the discharge rate. At 2C, 4C and 8C rates, the middischarge voltages of the dual anode cell were about 30, 40, and 140 mV, respectively, higher than the single anode cell.

The last test which was used to characterize the performance of the dual anode design was to make short duration charges and discharges at increasing currents while keeping the cell at approximately 50% SOC. After charging to 50% SOC the

cell was charged at the first current for 15 sec, switched to open-circuit for 3 min and 45 sec, and then discharged at the same current for 15 sec followed by another open circuit period. A comparison of the 15-sec charge and discharge voltage performance is shown in Fig. 12. The charge characterization test was terminated after the voltage reached 1.6 V. In order to maintain the 50% SOC condition for the higher current discharges, the cell was charged at the C rate for the time necessary for each succeeding discharge.

The single anode cell reached 1.6 V on charge at 8 A whereas the dual anode cell did not reach 1.6 V until the charging current was 15 A. During the discharge test the single anode cell voltage dropped to 1.0 V at 21 A, however, the dual anode cell voltage did not reach 1.0 V until the current was about 33 A. This test, although not tied to any particular application, demonstrates the improved voltage performance on both charge and discharge for the dual anode cell design.

Summaries of the discharge power obtained from the two cell designs on the constant current and 15-sec discharge tests are shown in Figs. 13 and 14. Figure 13 compares the power from the cell at the midpoints of the constant current discharges. The power outputs, plotted as a function of the discharge current, of the two designs are about the same below the 2C discharge rate (2.6 A) but gradually separate as the discharge current increases. At 13.0 A (10C) the power of the dual anode cell is 18% (15.0 W versus 12.7 W) higher than the single anode cell.

A comparison of the power output as a function of the current of the two cell designs during the 15-sec discharge test is shown in Fig. 14. The single anode cell reached a maximum power of 27 W at about 37 A. The dual anode cell's maximum power was 37 W at about 45 A which is a 37% higher power than the single anode cell. (Since the voltage measurements on these single nickel-hydrogen cells were taken at the base of the electrodes to eliminate voltage losses in the current collectors, these power values should not be used to project performances of higher capacity cells containing multiple cells.)

The results reported in this study were obtained using the same nickel electrode. The experiments were repeated twice, and the results were in agreement. Other types of nickel electrodes and large nickel-hydrogen cell stack sizes need to be evaluated in order to assess the applicability of the dual anode concept.

CONCLUDING REMARKS

The voltage performance of a single IPV nickel-hydrogen cell constructed with a hydrogen electrode on both sides of the nickel electrode was determined and compared to a cell with the conventional design using a single hydrogen electrode. The same nickel electrode was tested in both cell designs. Constant current discharge voltages were compared from C/4 to 10C and 5-sec pulse discharges were compared at 2C, 4C and 8C. Constant current charge performance was compared at the C/2 rate only. Fifteen sec charges and discharges at 50% SOC were used to characterize the cells over a large range of currents and to determine the maximum discharge power of each cell.

In each test the dual anode cell voltage was higher on discharge and lower on charge than the single anode cell. Voltage anomalies at low currents (C/4, C/2) need to be clarified. Further studies with other nickel electrodes and multi-

cell stacks are warranted to determine if the reduction in cell polarizations with the dual anode design justify the additional component weight.

ACKNOWLEDGEMENT

The author would like to acknowledge the assistance of Timothy Ryan and Michael Degen with the experimental work and data reduction for this study.

REFERENCES

1. L. Miller, Proceedings 23rd IECEC, Vol. 2, AMSE, New York, 1988, pp. 489-492.
2. H. S. Lim and S. A. Verzwylt, J. Power Sources, 29 (1990) 503-519.
3. J. J. Smithrick and S. W. Hall, Proceedings 25th IECEC, Vol. 3, AIChE, New York, 1990, pp. 16-21.
4. D. L. Britton, Proceedings 34th International Power Sources Symposium, IEEE, N.J., 1990, pp. 235-238.
5. M. A. Reid, J. Power Sources, 29 (1990), pp. 467-476.

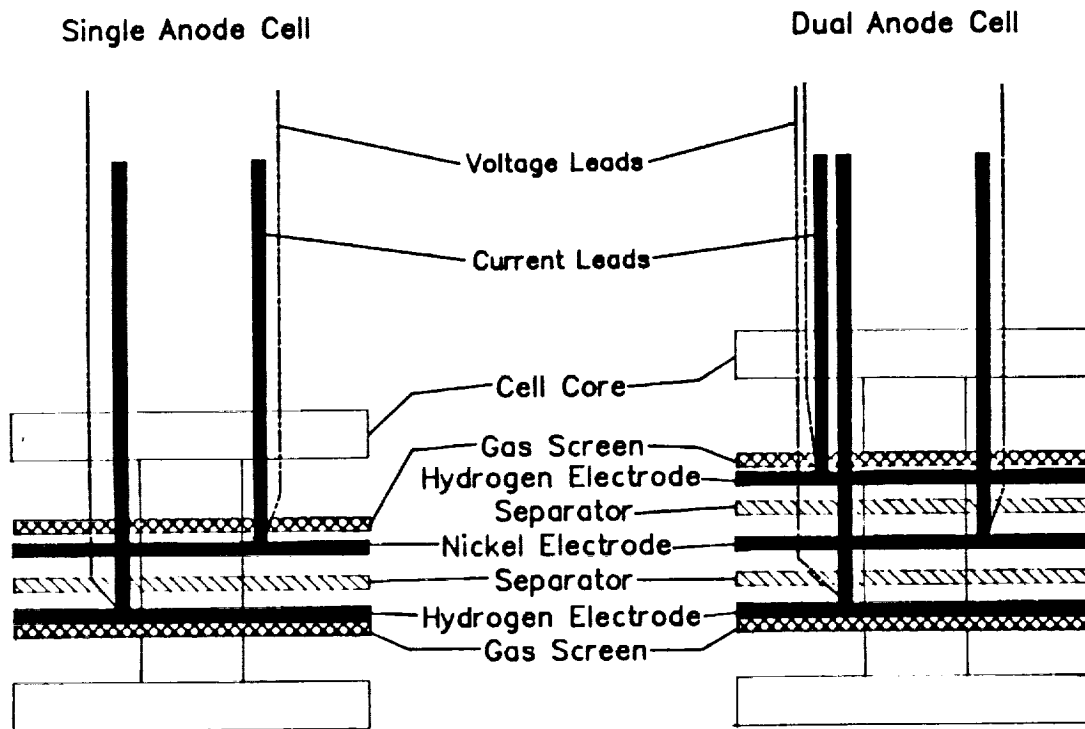


FIG. 1. Schematic diagrams of the single anode and dual anode cells. Electrode area = 50.0 cm².

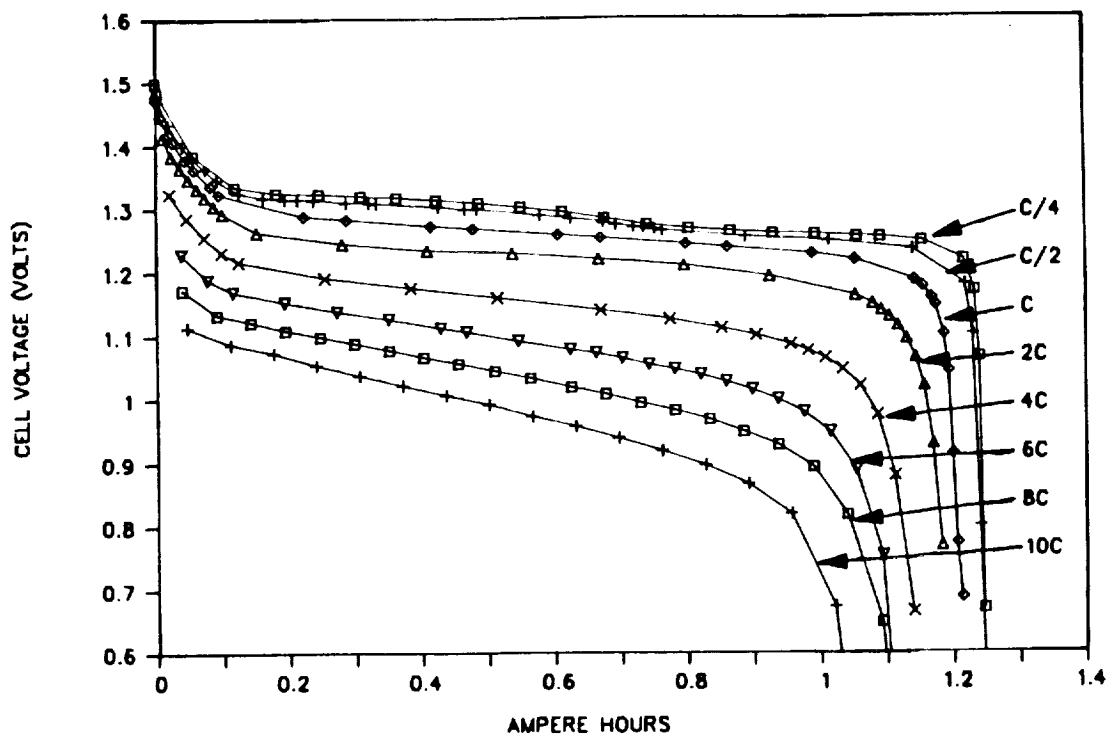


FIG. 2. Constant current discharge voltage profile of the conventional single anode nickel-hydrogen cell. Voltage measured at base of electrodes. $C = 1.3$

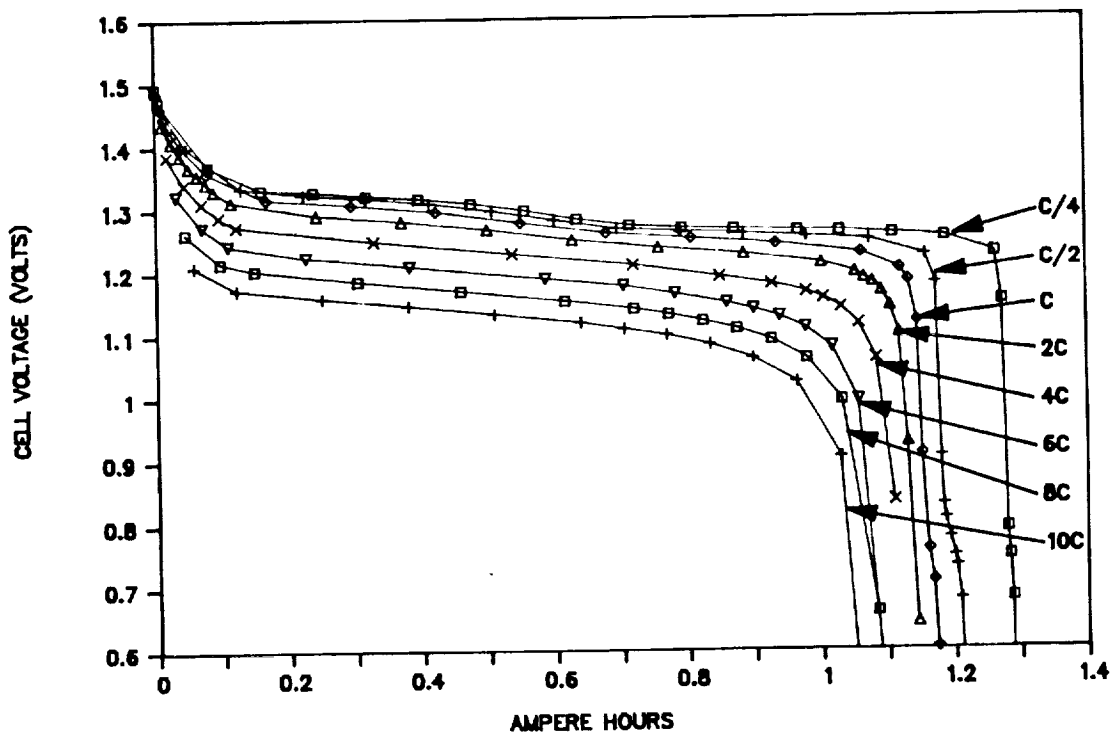


FIG. 3. Constant current discharge voltage profile of the dual anode nickel-hydrogen cell. Voltage measured at base of electrodes. $C = 1.3$

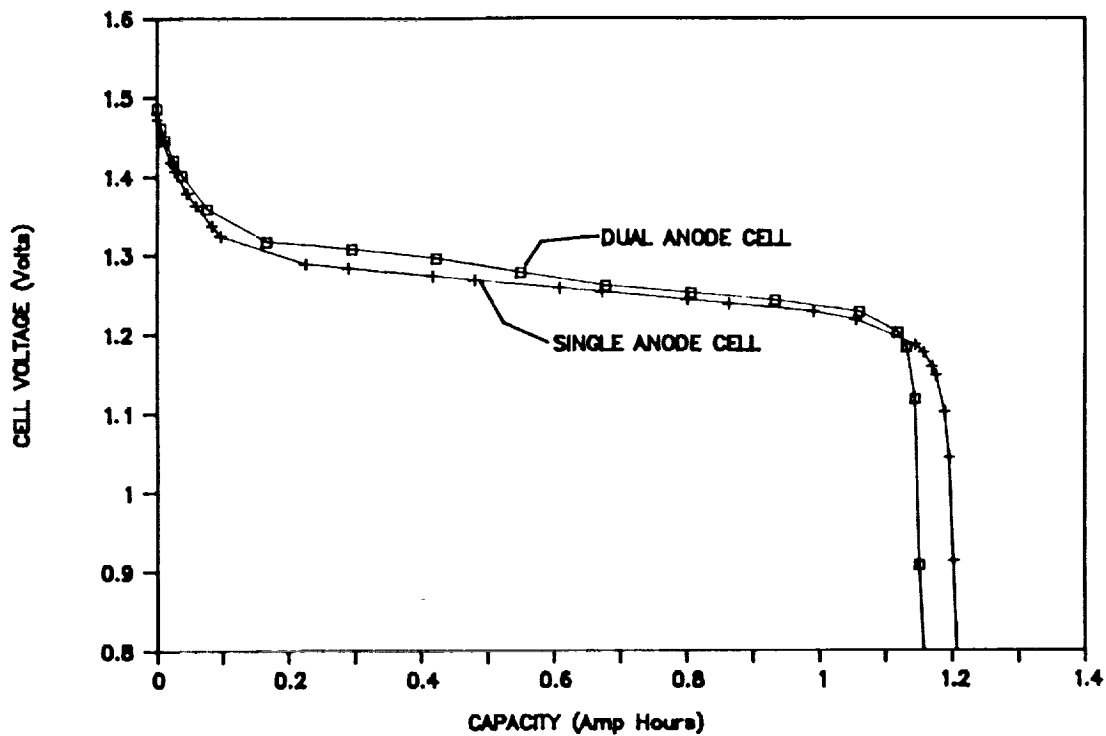


FIG. 4. Comparison of the C rate discharge performance of the single anode and dual anode cells. C = 1.3

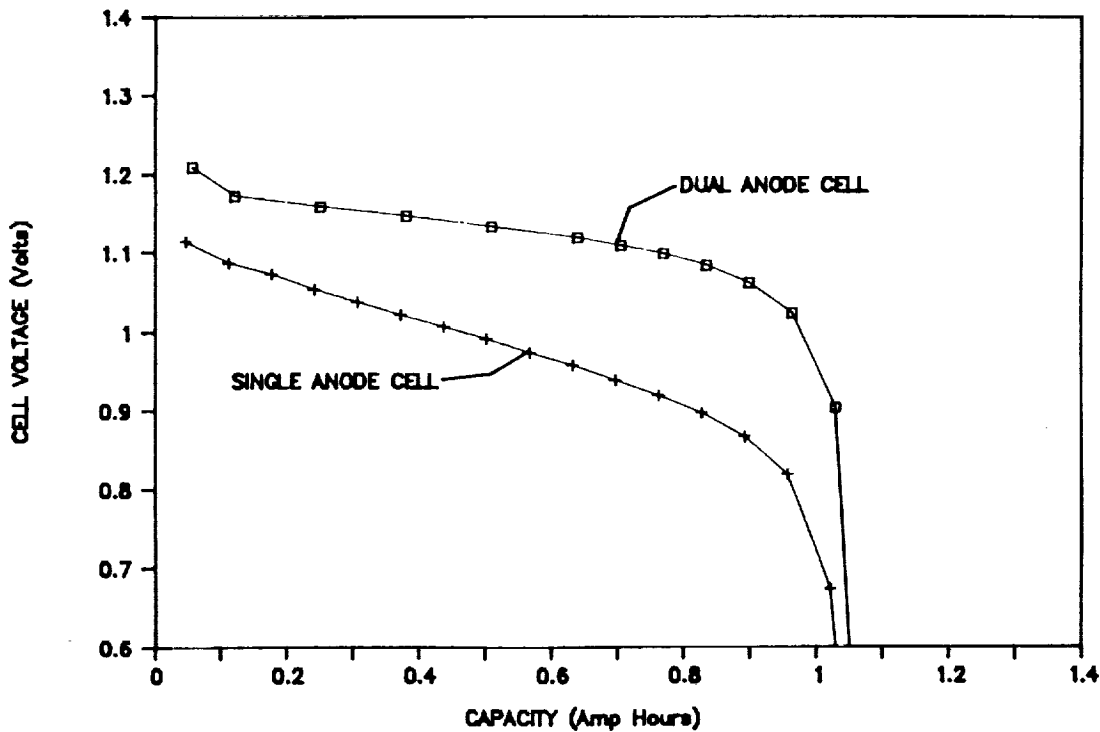


FIG. 5. Comparison of the 10C discharge performance of the single anode and dual anode cells. C = 1.3

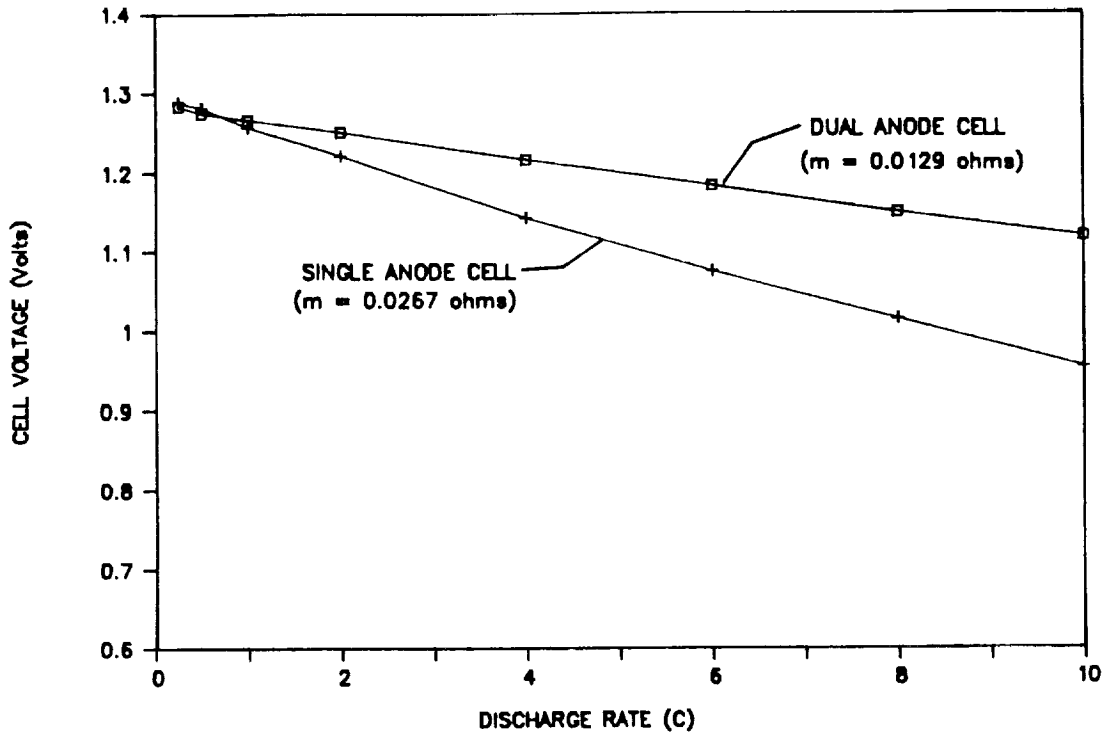


FIG. 6. Plot of mid-discharge cell voltages as a function of discharge rate to compare polarizations of the dual anode and single anode cell designs. $C = 1.3$

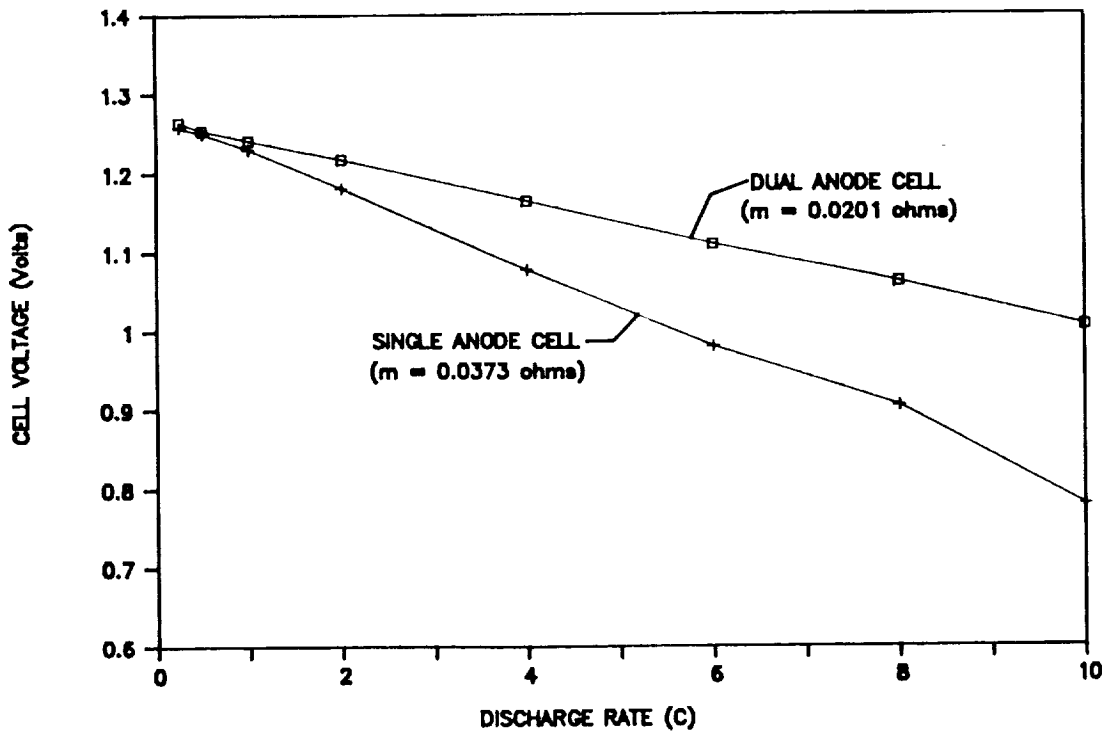


FIG. 7. Plot of cell voltages at 75% DOD as a function of discharge rate to compare polarizations of the dual anode and single anode cell designs. $C = 1.3$

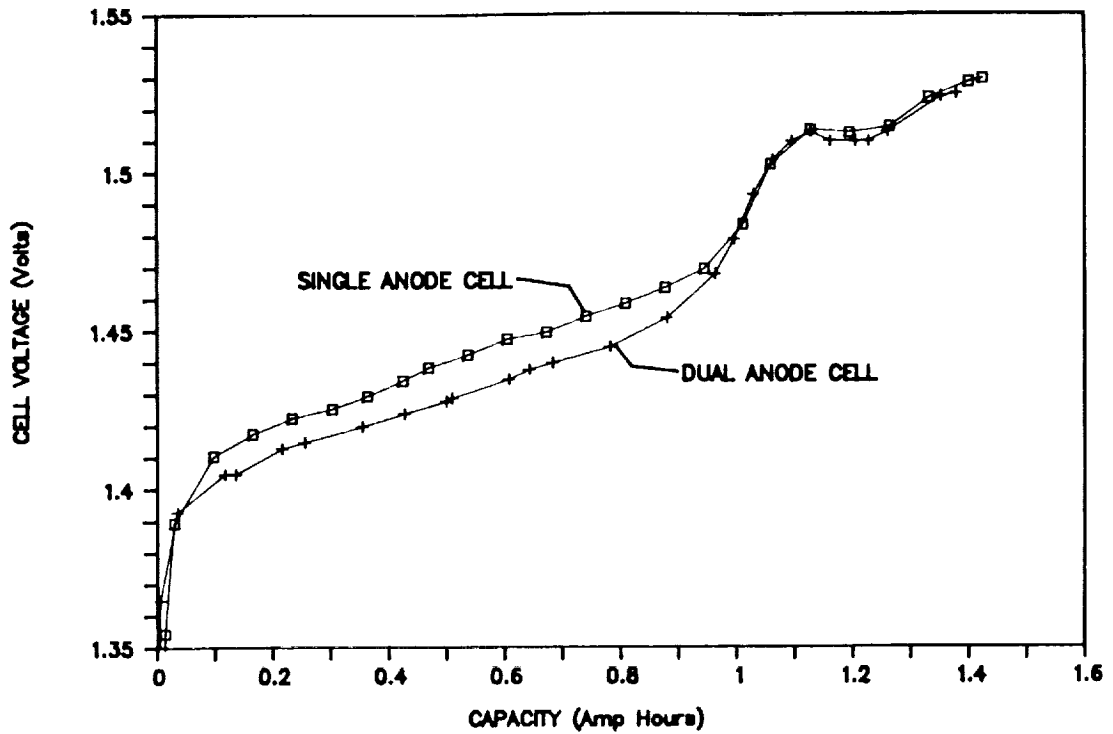


FIG. 8. Charge performance comparison at the C/2 rate. 10% overcharge. C discharge, C/4 drain. C = 1.3

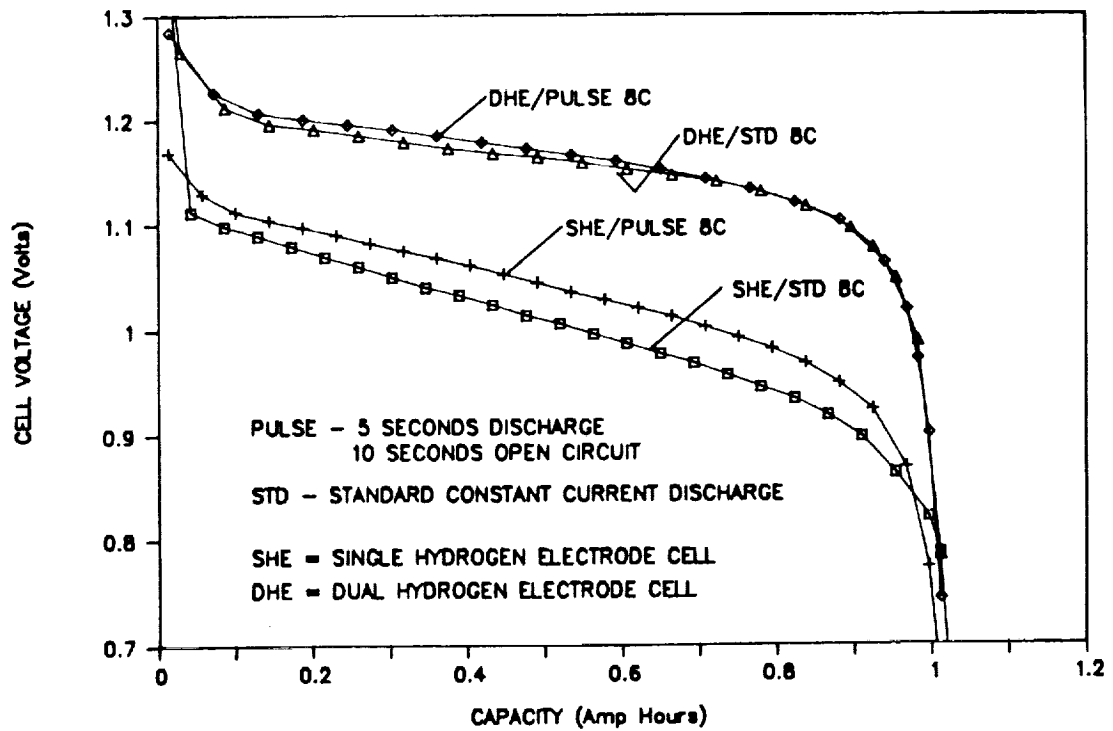


FIG. 9. Comparison of the 8C pulse discharge and 8C constant current discharge voltages. Pulse = 5 seconds discharge, 10 seconds open-circuit. C = 1.3

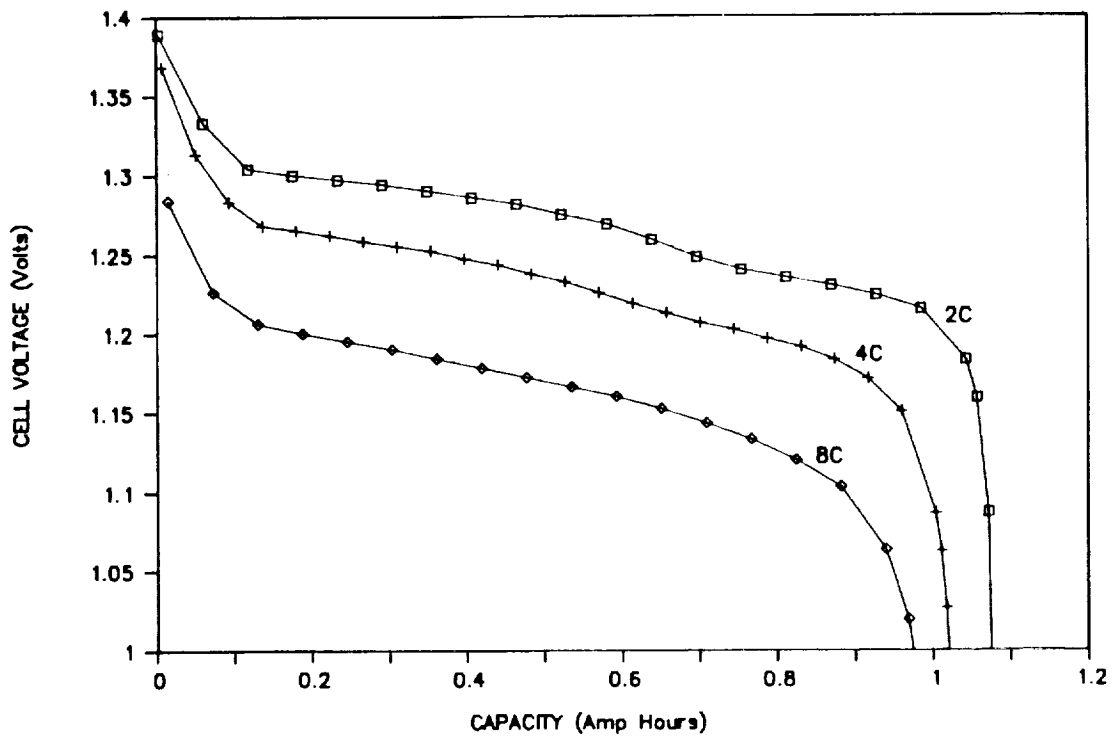


FIG. 10. Pulsed-current discharge voltage profile of the dual anode nickel-hydrogen cell. Voltage measured at base of electrodes. $C = 1.3$

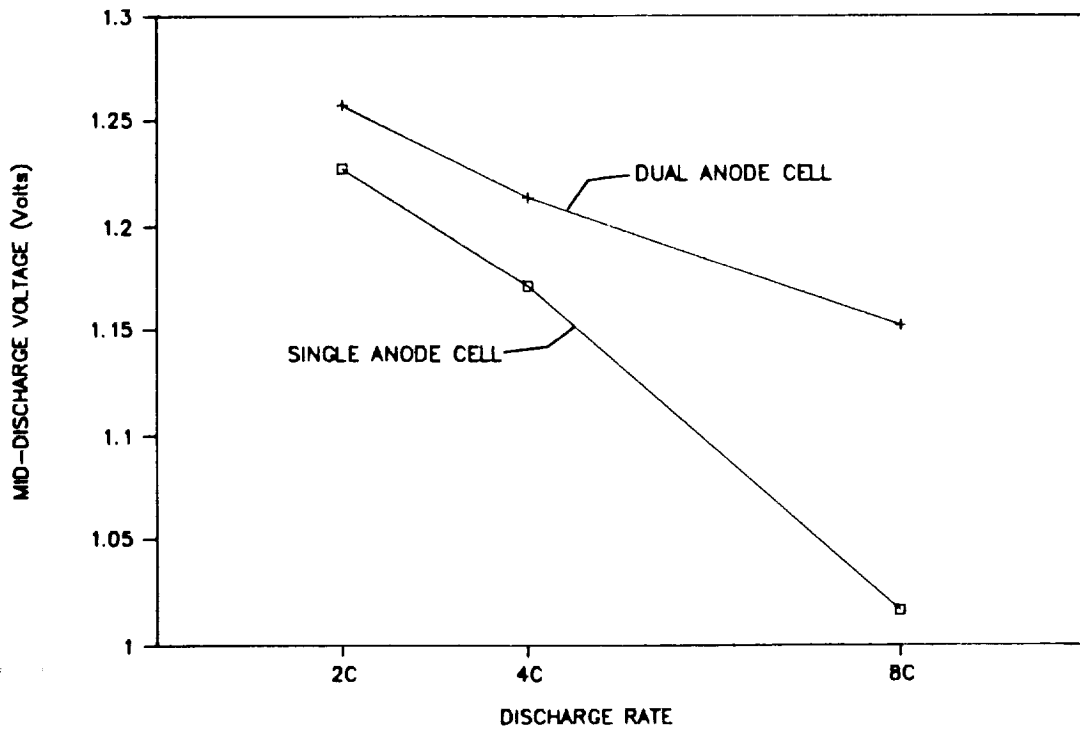


FIG. 11. Comparison of mid-discharge voltages of the single anode and dual anode cells during pulse discharges at 2C, 4C and 8C. $C = 1.3$

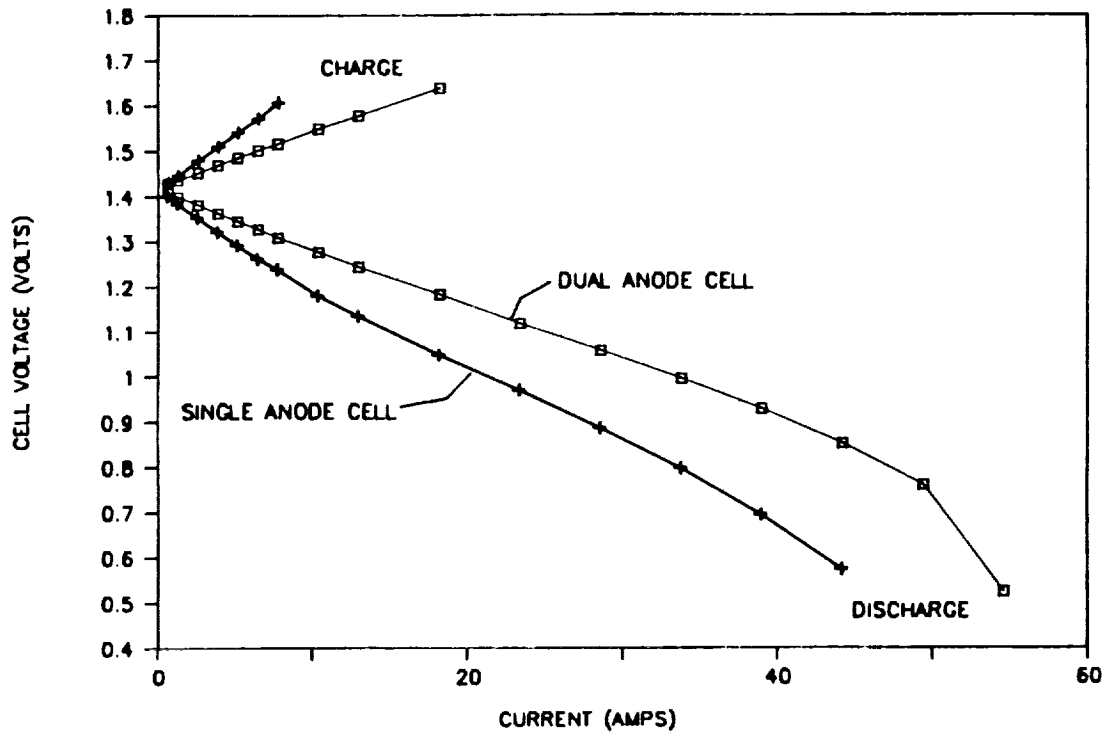


FIG. 12. Charge and discharge polarization measurements at 50% SOC. 15 seconds charge or discharge. Voltage measured at base of electrodes.

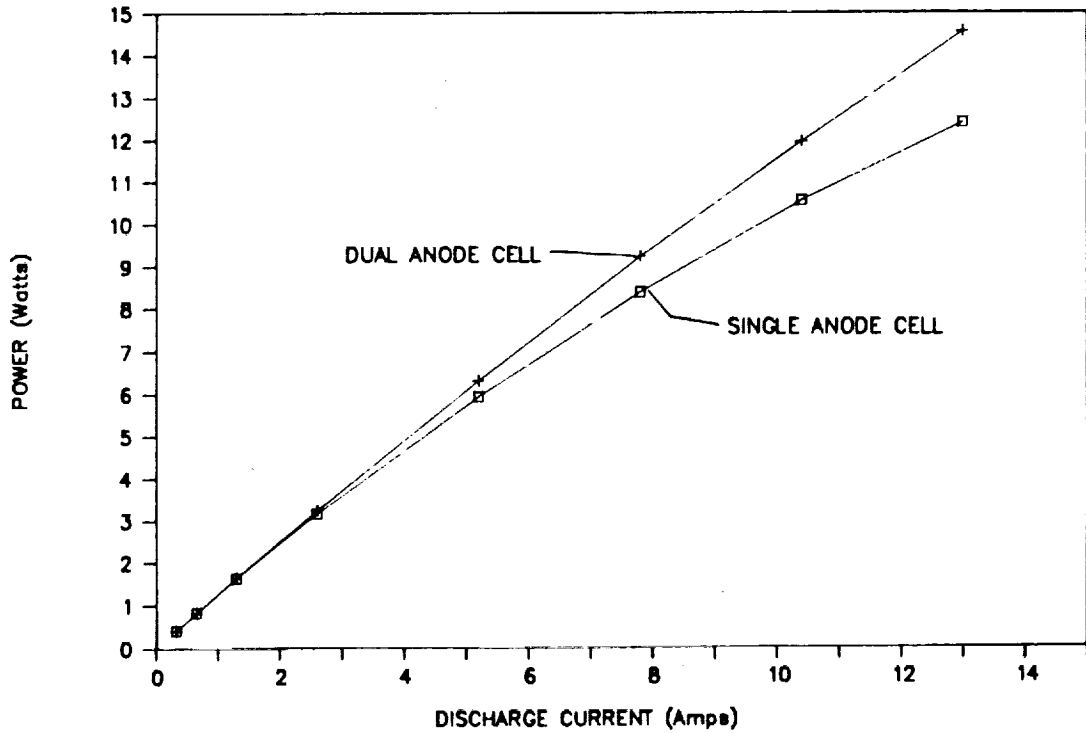


FIG. 13. Comparison of power outputs at 50% DOD during constant current discharges. $C = 1.3$

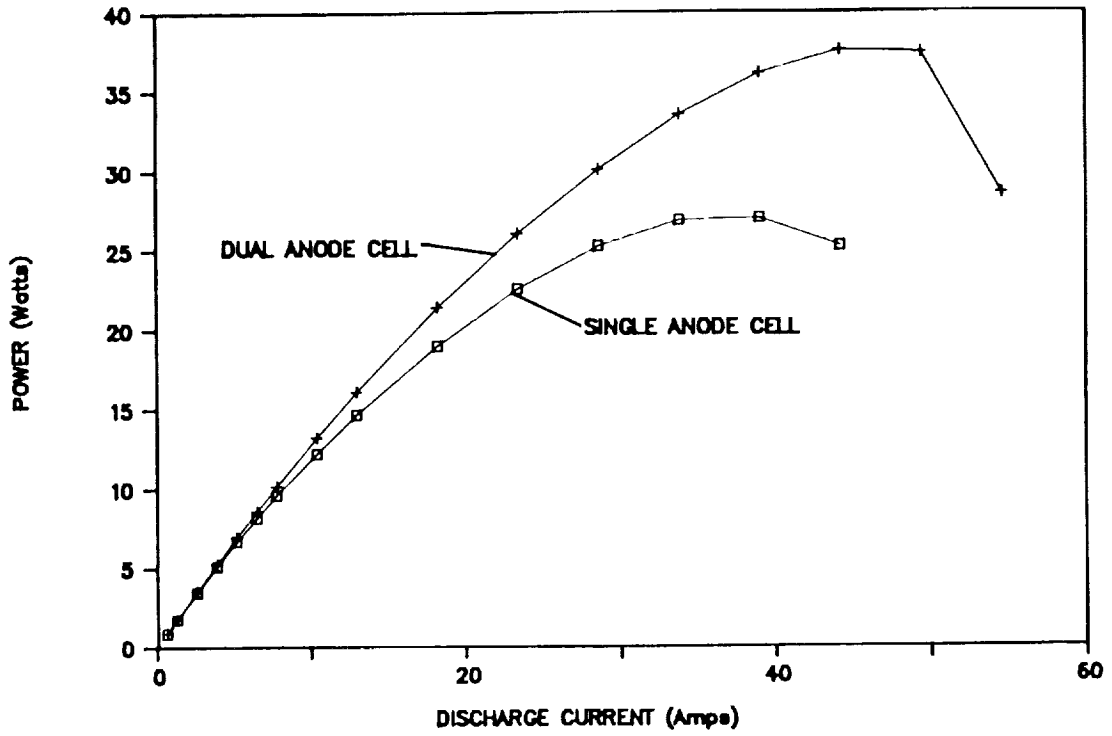


FIG. 14. Comparison of power outputs during discharge polarization test at 50% SOC. $C = 1.3$

MULTIPLE CELL COMMON PRESSURE VESSEL NICKEL HYDROGEN BATTERY

Jeffrey P. Zagrodnik and Kenneth R. Jones
Johnson Controls Battery Group, Inc.
Nickel Hydrogen Battery Division
Milwaukee, Wisconsin

ABSTRACT

Johnson Controls Battery Group, Inc. has developed a multiple cell common pressure vessel (CPV) Nickel Hydrogen battery that offers significant weight, volume, cost and interfacing advantages over the conventional individual pressure vessel (IPV) Nickel Hydrogen configuration that is currently used for aerospace applications. The baseline CPV design was successfully demonstrated through the testing of a 26-cell prototype, which completed over 7,000 44% depth-of-discharge LEO cycles at COMSAT Laboratories. Two-cell boilerplate batteries have now exceeded 12,500 LEO cycles in ongoing laboratory tests. CPV batteries using both nominal 5" and 10" diameter vessels are currently available. The flexibility of the design allows these diameters to provide a broad capability for a variety of space applications.

KEY FEATURES OF THE JOHNSON CONTROLS CPV DESIGN

Nickel Hydrogen batteries are well established as an energy storage subsystem for commercial communication satellites. The standard design has been the Individual Pressure Vessel (IPV) which provides an independent vessel for each cell of the battery. The comparative advantages of a Common Pressure Vessel (CPV) design configuration, in which many series connected cells are contained in a single vessel, are widely recognized. These include higher specific energy, higher system energy density, simplified interfacing, and reduced cost as compared to the IPV (1). However, historical concerns related to electrolyte and thermal management had previously prevented the introduction of a reliable CPV design.

Johnson Controls has successfully developed a patented (2) CPV battery design which overcomes the historical concerns. A radial heat fin provides a pathway for heat transfer from the center of each cell to the pressure vessel wall. Since the metal fins make direct contact with the vessel, they actually provide an improved thermal interface as compared to the IPV design where heat must be transferred either through the polymeric wall wick or through a hydrogen gap in order to pass from the cell to the vessel wall.

The heat transfer interface at the exterior of the vessel is simplified since only one vessel is used for a multicell battery. Since IPV design specific energies are often reported without including their thermal baseplate, there is an additional specific energy advantage for the CPV which might not be readily apparent from a direct comparison of reported specific energies.

The CPV's vessel is electrically neutral so no insulating layer is required on the outside of the vessel. This allows a direct metal to metal contact between the outer vessel wall and the mounting bracket, further enhancing heat transfer. In an IPV, the vessel wall is electrically live and must be insulated from the mounting bracket. Prior to launch condensation can occur on the outside of the IPV vessels creating a possible shorting path between the IPV cells.

Although thin-walled polymeric cell container called an electrolyte containment system (ECS) addresses the issue of electrolyte management in the CPV configuration. The thermally sealed ECS isolates the electrolyte within each cell. An intercell connect between each of the series connected cells employs a specially designed compression seal to prevent electrolyte bridging between cells. Examination of the seals removed from the 26-cell Prototype #1 battery after 7,400 cycles showed no evidence of any leakage.

A hydrogen vent sealed onto the ECS face of each cell allows hydrogen to pass into the vessel plenum from the cells during charge and vice versa during discharge. The vent is designed to prevent wetting with electrolyte and to ensure recombination within a given cell of any oxygen that is generated within that cell during overcharge. This prevents the development of electrolyte imbalances between cells during extended cycling.

INITIAL PROTOTYPE DESIGN

As an initial demonstration of the capabilities of the CPV design, a 26-cell 22 amp-hour prototype was fabricated in a joint effort with COMSAT Laboratories in 1988 (3). The CPV prototype is shown in relation to its IPV counterpart in Figure 1. This battery was composed of two 13-cell half-stacks which are connected in series within the single common vessel to provide a nominal 32 volts. The 10" diameter cells have a semicircular geometry and employ a double tab design to enhance current distribution, as shown in Figure 2.

The half-stacks were inserted into two fixed heat fin cavities (Figure 3) which each contain 13 slots, one for each of the 26 cells. The cells are slipped into the fixed cavity prior to the addition of electrolyte. Upon addition of electrolyte, the asbestos separators in the cells swell providing the desired cell compression and an intimate thermal contact between the cell face and the heat fin. Heat generated in the cell passes axially through the cell face to the heat fin, then radially through the heat fin to the vessel wall. It is the direct thermal contact between the heat fin and the vessel wall that provides a thermal advantage over the IPV design which provides no direct radial pathway for heat conduction to the vessel. It is believed that this thermal advantage will translate to extended life in LEO applications. In GEO applications, where long life is not required, additional improvements in specific energy can be achieved due to the improved thermal pathway.

The two half-stacks for the prototype battery were inserted into a hydroformed Inconel 718 vessel cylinder/dome section. Springs pushed the half-stacks outward against the vessel wall, maintaining the intimate contact between the heat fin cavity and the vessel wall. After insertion of the half-stacks a second dome was welded in place using the same general weld ring design approach that is applied in the IPV vessels.

INITIAL PROTOTYPE TESTING

The Prototype battery was put on a real time LEO life test at COMSAT Laboratories. Over 7,000 44% depth-of-discharge (DOD) cycles were completed at 10°C. Voltage performance was relatively stable over the first 6,400 cycles, prior to the rapid voltage degradation which ultimately caused the battery to reach the 1.0 volt/cell battery failure criteria (Figure 4).

Subsequent destructive physical analyses (DPA) showed that some of the cell ECS's had been damaged at the time of insertion into the fixed heat fin cavity, leading to electrolyte leakage from the cells. The resulting drying out of the positives and separators is believed to have caused the voltage decline and failure of the battery. All cell components, including the negative electrodes were in excellent physical condition. No pinholes or other signs of popping were observed on the negative electrodes. No signs of blistering or other physical degradation were observed on the positives. In retrospect, the ability to complete over 7,000 LEO cycles with a battery which was leaking electrolyte from the onset of testing provides testimony to the resilience of the CPV design.

Two 2-cell laboratory test batteries of the same baseline design (4) continue on a 44% DOD LEO life test, one each at Johnson Controls and COMSAT. They have now exceeded 9,000 and 12,500 cycles, respectively with no significant performance degradation.

FEATURES OF IMPROVED LOOSE HEAT FIN CPV DESIGN

A new loose heat fin design was developed to overcome the problems encountered with insertion of the cells into the fixed heat fin cavity. The cell design was also modified by providing a double ECS with a staggered vent pathway to further enhance the electrolyte management reliability. These approaches were introduced using a 5" diameter vessel, circular cell component design. The circular cell with its loose heat fin is shown in Figure 5. The cells and heat fins are assembled into a stack using a special alignment fixture. The ten cell stack, shown in Figure 6, has a 9.6 Ah capacity, is 9.7" long and weighs 3 kg. A 22-cell version offers a 13.4 Ah capacity is 20.6" long, and weighs 7.9 kg. In general, the higher the capacity and/or voltage, the better the specific energy.

The 5" cell stack is also inserted into a cylinder, but in this case two separate end domes and weld rings are welded in place. This approach allows an unlimited vessel length for design flexibility. Although the cell stack for the 22-cell battery is only 9.7" long, the vessel length is 20.6" to provide the required void volume to maintain a 700 psi maximum operating pressure. Significant improvements in energy density can be achieved by using a thicker, up to 0.060 inch, Inconel 718 shell to allow higher operating pressures.

GENERAL DESIGN CHARACTERIZATION

A computer model is used to help optimize battery design parameters in the initial design stages for a new battery. The model defines optimum design parameters including vessel diameter, positive electrode thickness, number of modules per cell, battery length and weight, given input on the desired battery voltage and capacity. Several design curves for common aerospace design ranges have been developed using this model. Examples are provided in Figures 7-9 for a 22-cell LEO battery in a 5" diameter vessel, a 22-cell LEO battery in a 10" diameter vessel and a 26-cell GEO battery in a 10" diameter vessel. These curves can be used to obtain an initial estimate of the available specific energy and length for a variety of designs. Such estimates serve as a convenient starting point for more detailed design analyses.

OTHER APPLICATIONS

The core CPV design concept has been expanded to provide a family of CPV batteries (Figure 10) for a variety of uses including aerospace, aircraft starting, and terrestrial applications. The combined volume offered by this array of markets provides the potential to eliminate product consistency problems related to intermittent production schedules, minimize the use of batch processing techniques, and allow the introduction of statistical process control (SPC) into the component fabrication processes. These factors will result in a higher level of quality, improved product consistency, and ultimately lower cost than is presently achieved in the IPV Nickel Hydrogen battery industry.

The reduced cost provided by the CPV configuration coupled with other cost reducing design refinements developed under contract to Sandia National Laboratories (5) have made the system viable for a number of terrestrial applications. Among these is a 2 kWh battery designed for photovoltaic applications. This battery employs a composite fiber-wound vessel design. Four 2-kWh prototypes are presently undergoing photovoltaic tests, two each at facilities in New Mexico and Florida (4).

Aircraft starting battery designs also use the fiber-wound vessel approach, but employ a carbon filament to enhance heat transfer and minimize weight. Initial tests suggest that the CPV battery will provide performance equal to or better than Nickel Cadmium in this application. The CPV battery will also provide a reliable measurement of state-of-charge and significantly reduced maintenance. In addition to life-cycle cost savings, the limited maintenance requirements would free aircraft designers to locate the batteries in a remote area since accessibility will no longer be a primary concern. A 20-cell aircraft starting battery prototype is presently being fabricated for test by the U.S. Air Force.

CONCLUSION

In summary, a family of CPV battery designs have been developed for a wide variety of applications. Aerospace designs are presently available in 5" and 10" diameter vessels. Although the database is still limited, tests to date indicate that the significant advantages of the CPV design can be realized in a reliable package.

Johnson Control's present aerospace CPV designs cover a wide range of voltages, 12 to 100 volts, and capacities, 10 to 125 ampere-hours. Vessel diameters have been limited to 5" and 10" diameter versions to date, although a 3.5" diameter design is being advanced to optimize the configuration for battery capacities below 10 ampere-hours.

REFERENCES

1. James Dunlop and Richard Beauchamp, "Making Space Nickel/Hydrogen Batteries Lighter and Less Expensive," AIAA/DARPA Meeting on Lightweight Satellite Systems, Monterey, CA, August 1987, NTIS No. N88-13530.
2. U.S. Patent No. 4,957,830.
3. Marty Earl, James Dunlop, Richard Beauchamp, Jack Sindorf and Ken Jones, "Design and Development of an Aerospace Ni/H₂ Battery," 24th Intersociety Energy Conversion Engineering Conference, August, 1989.
4. Jeffrey Zagrodnik and Kenneth Jones, " Development of Common Pressure Vessel Nickel/Hydrogen Batteries," 25th Intersociety Energy Conversion Engineering Conference, August, 1990.
5. Richard Beauchamp and Jack Sindorf, "Cost reductions in the Nickel/Hydrogen Battery," Journal of Power Sources, 1988, Issue 22.

ORIGINAL PAGE
BLACK AND WHITE PHOTOGRAPH



Figure 1: 26-cell CPV Prototype Battery and IPV Counterpart

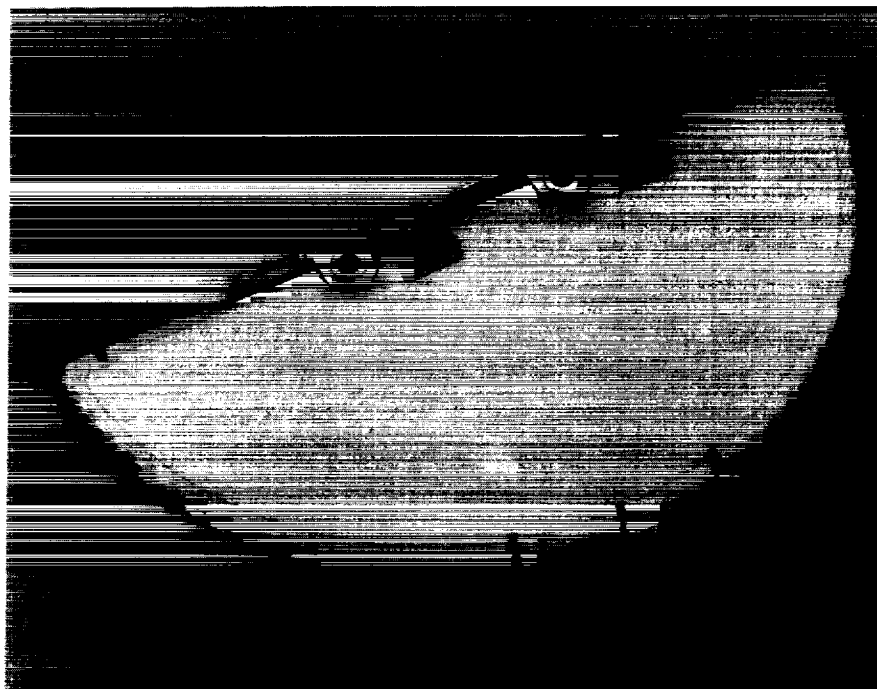


Figure 2: 10" Diameter Semicircular Cell

ORIGINAL PAGE
BLACK AND WHITE PHOTOGRAPH

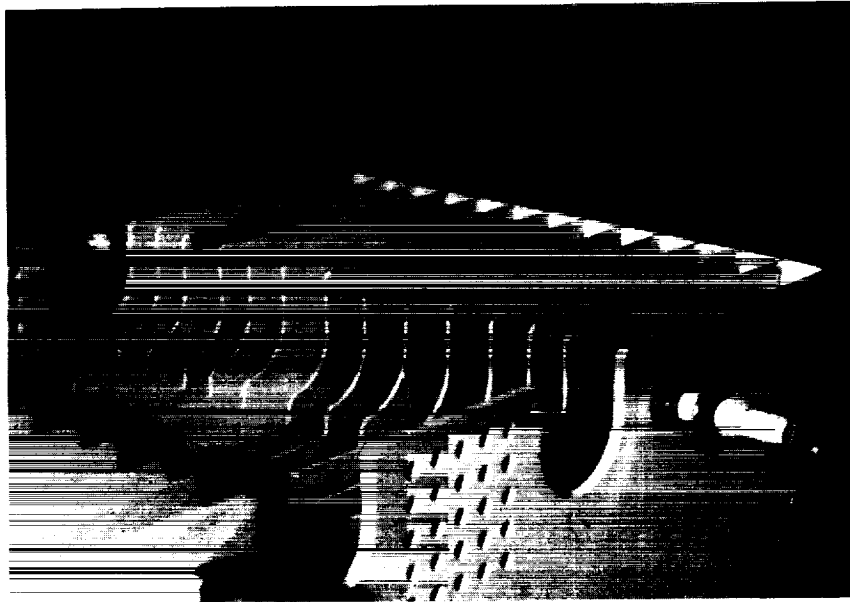


Figure 3: 13-Cell Half-Stack Fixed Heat Fin Cavity

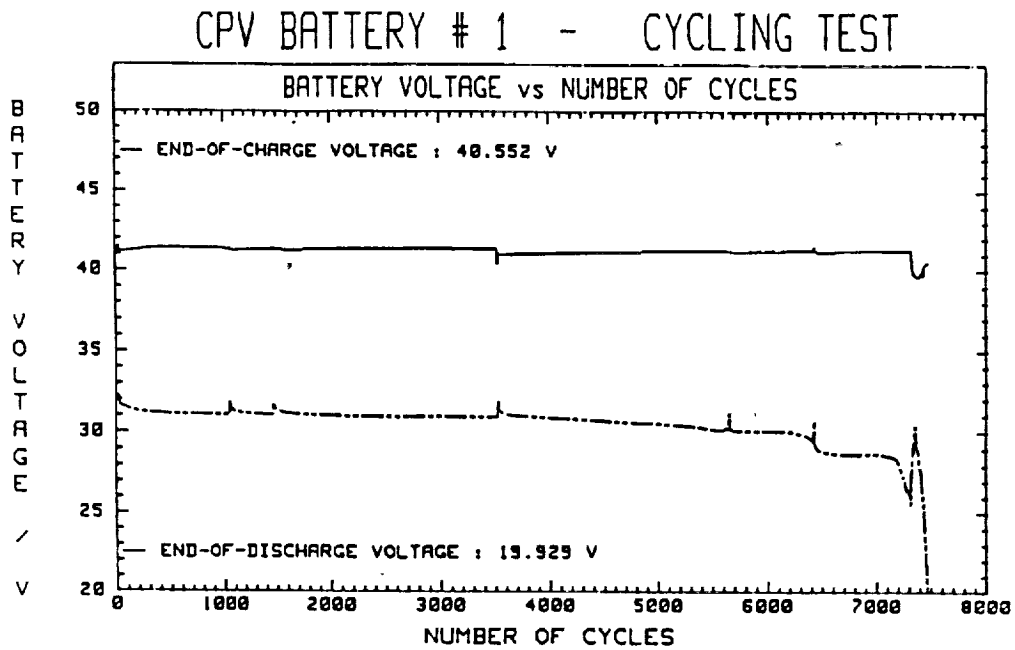


Figure 4: CPV Prototype #1 - Life Cycle Test

ORIGINAL PAGE
BLACK AND WHITE PHOTOGRAPH

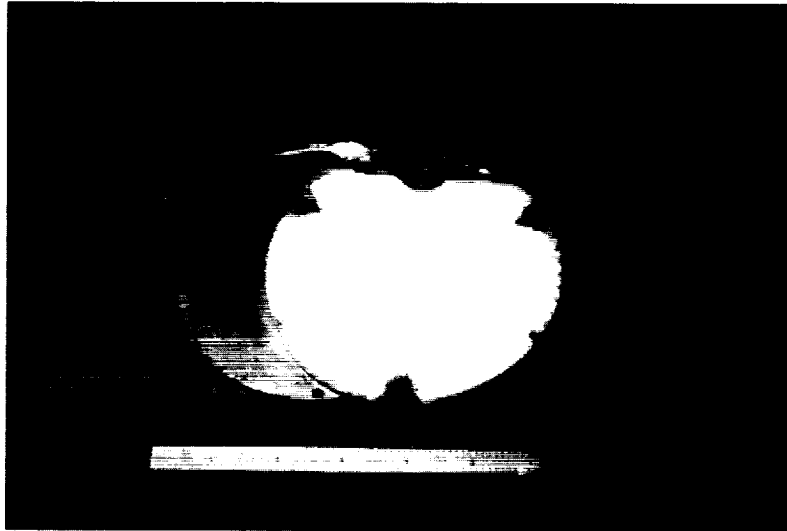


Figure 5: 5" Diameter Circular Cell and Loose Heat Fin

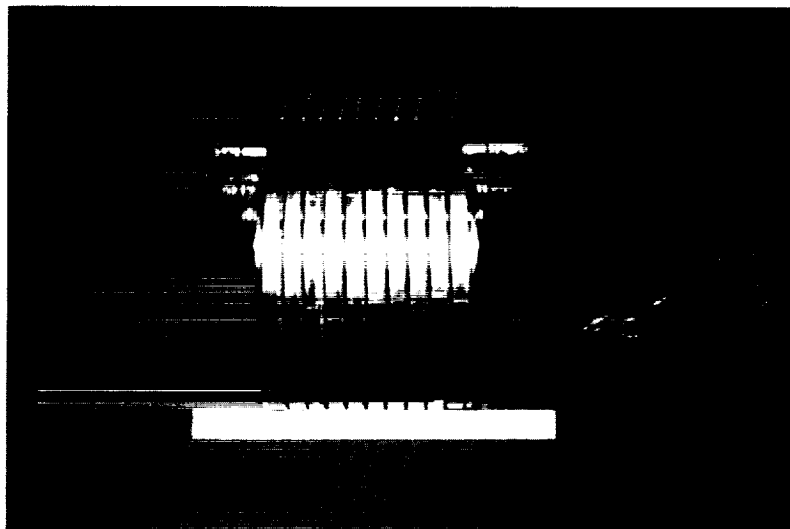


Figure 6: 5" Diameter 10-Cell Stack

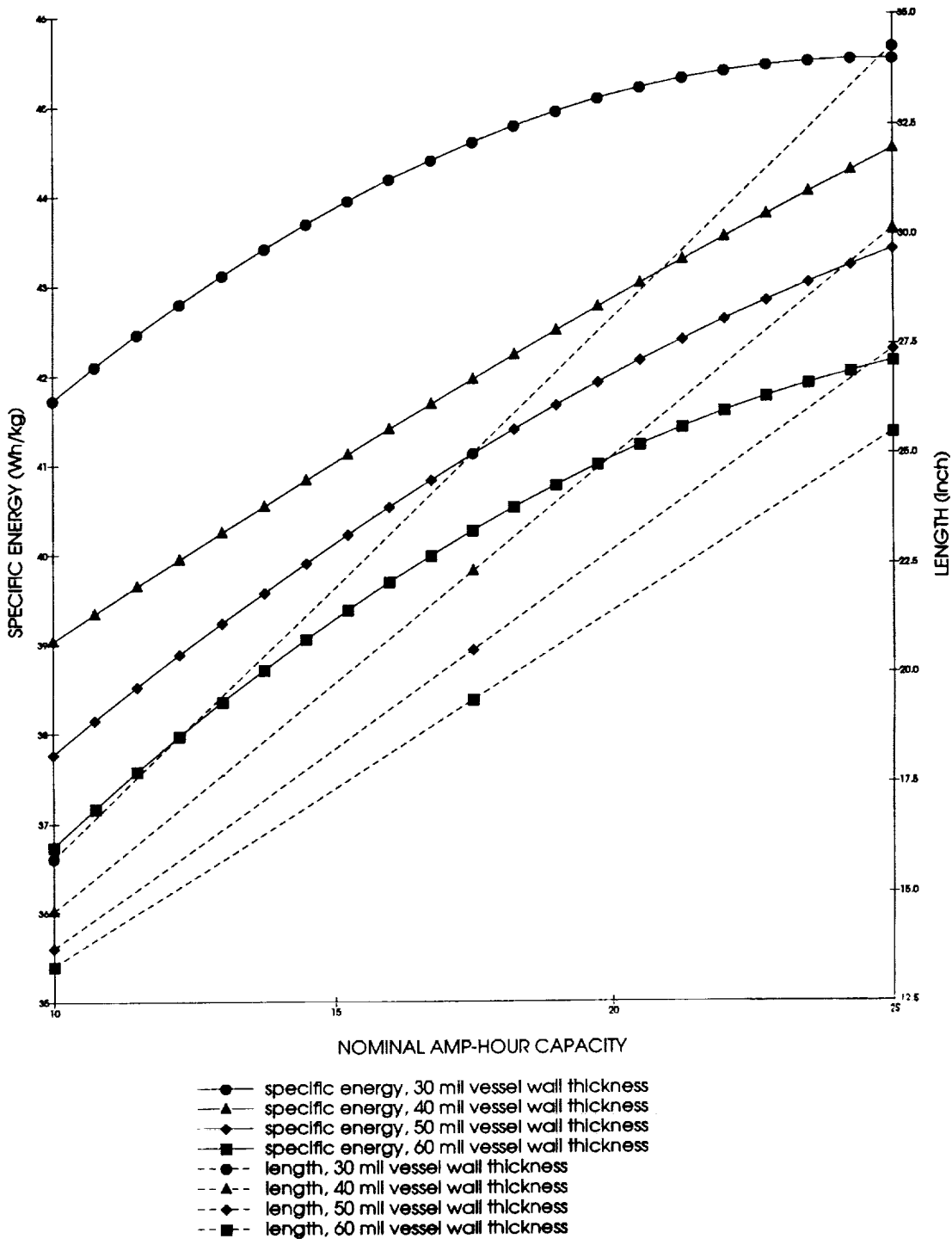


Figure 7: Design Curves for a 22-Cell LEO CPV Nickel Hydrogen Battery in a 5" Diameter Vessel

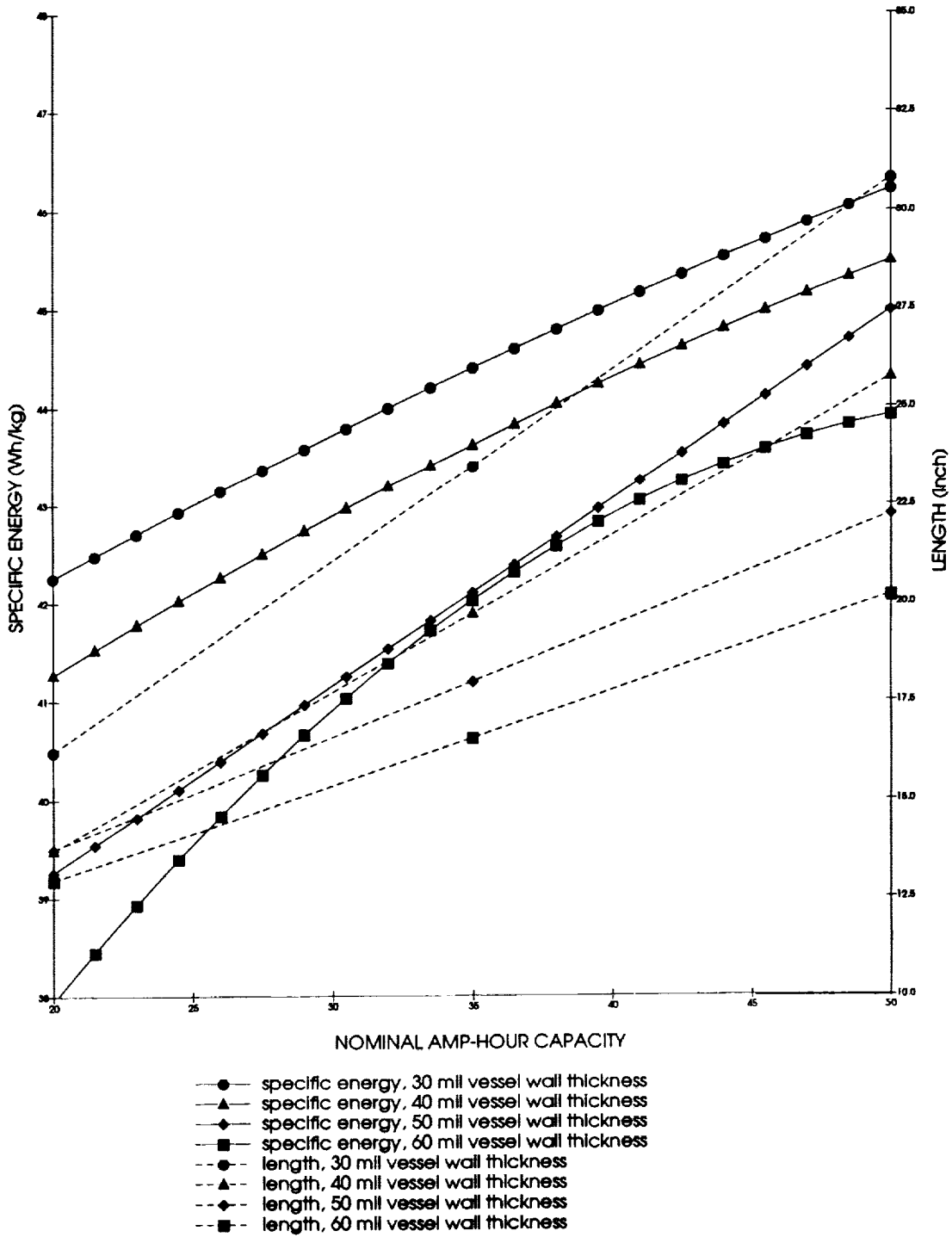


Figure 8: Design Curves for a 22-Cell LEO CPV Nickel Hydrogen Battery in a 10" Diameter Vessel

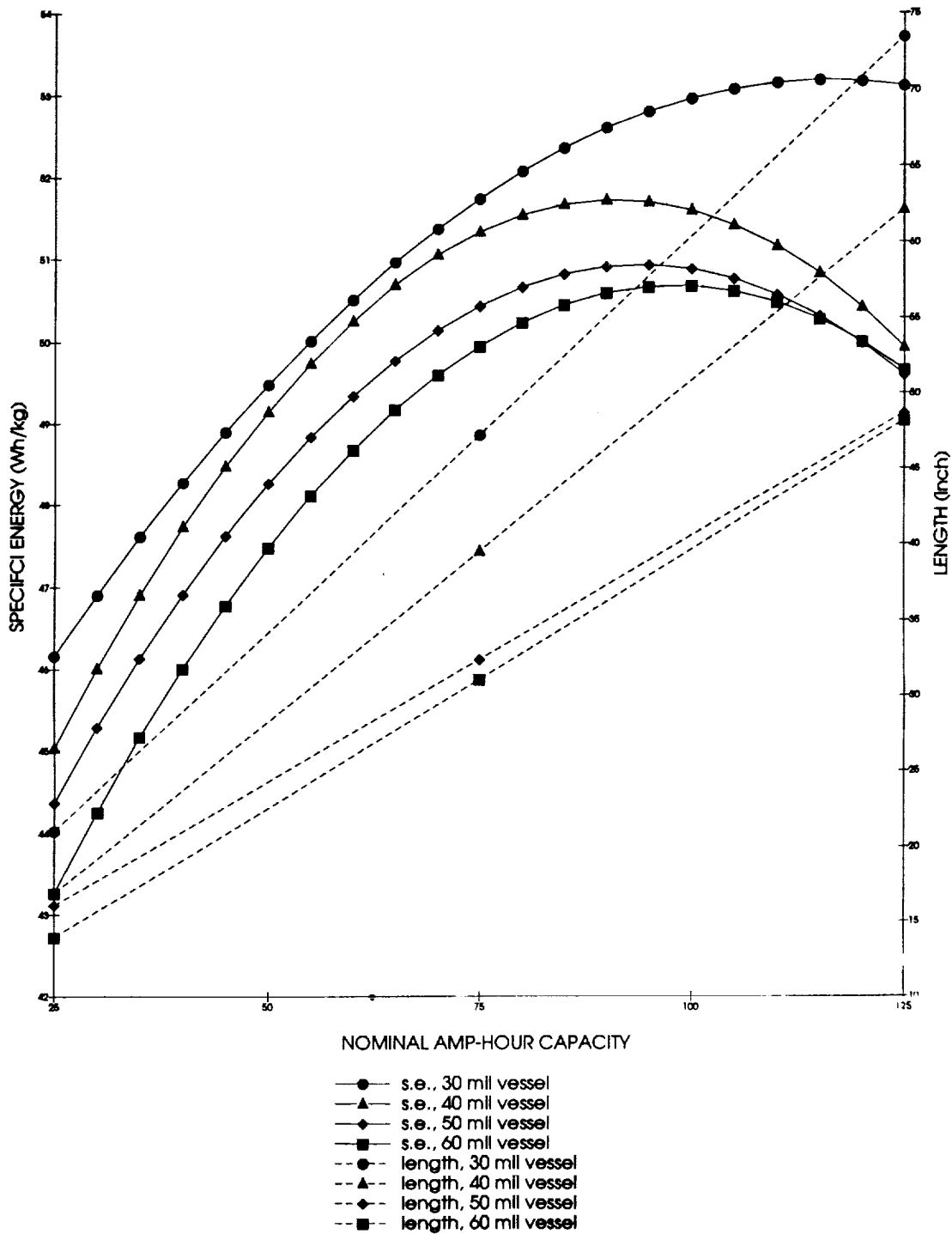


Figure 9: Design Curves for a 26-Cell GEO CPV Nickel Hydrogen Battery in a 10" Diameter Vessel

ORIGINAL PAGE
BLACK AND WHITE PHOTOGRAPH

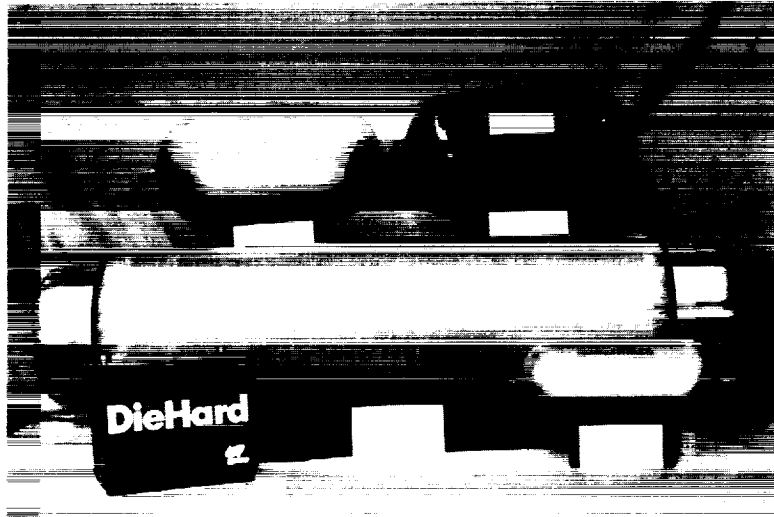


Figure 10: Family of CPV Batteries for Multiple Applications

Clockwise from Upper Left: 26-Cell, 22 Ah GEO Battery
20-Cell, 50 Ah Aircraft Starting Battery
10-Cell, 160 Ah Terrestrial Battery
22-Cell, 13 Ah LEO Battery
Conventional Lead Acid Starting Battery

SMALL CAPACITY, LOW COST (Ni-H₂) DESIGN CONCEPT FOR COMMERCIAL, MILITARY AND HIGHER-VOLUME AEROSPACE APPLICATIONS

James R. Wheeler, William D. Cook, and Ron Smith
Eagle-Picher Industries, Inc.
Joplin, Missouri 64801

Abstract

Nickel-Hydrogen (Ni-H₂) batteries have become the technology of choice for both commercial and defense-related satellites in geosynchronous orbits. Their use for low-earth-orbit (LEO) applications is not as advanced, but seems just as inevitable because of their inherent advantages over nickel-cadmium batteries. These include superior energy density, longer cycle life, and better tolerance to over-charge and reversal. Ni-H₂ cells have the added advantage in both construction and operation of not presenting the environmental possibility of cadmium pollution. Unfortunately, but necessarily, the design of these cells has been driven to high cost by the sophistication of the satellites and their uses. Now, using most of the same concepts but less costly materials and techniques, a low-cost, small cell design has been developed. Combined with the concept of the common pressure vessel, this new design promises to be ideal for the "small-sat" and commercial markets which, increasingly, are calling for large numbers of less-expensive satellites.

Introduction

The development of Ni-H₂ cells in capacities of 20 ampere-hours (AH) or less has been delayed because of the initial demand for development of the technology for larger satellites. Now, however, much of the same technology can be applied to smaller cells. Two cell design are manufactured at Eagle-Picher which are tailored to the specific requirements of the small satellite, not only in terms of power and volume, but also in terms of economic feasibility. These designs are based upon proven manufacturing processes and component heritage, and therefore retain the reliability and performance advantages of their predecessors. Details of these two designs are described herein.

Background and Forecast

Nickel-Hydrogen batteries are well-established as the technology of choice for geocentric satellite applications. For example, there are now approximately 30 operational satellites presently flying nickel-hydrogen batteries. Eagle-Picher has achieved more than 48 million fault-free cell hours of operation for Ni-H₂ power in orbit. Mid- and Low-orbit

(LEO) applications for Ni-H₂ batteries such as military programs and the Hubble Space Telescope are just now entering service. Both commercial and government programs have required extensive development efforts to ensure reliability and optimization of weight and performance.

While these more expensive systems continue to advance, it is not too soon to exploit this technology. In fact, the need for smaller and cheaper satellites and batteries appears to be accelerating with the burgeoning communications business. Direct broadcast satellites, dedicated phone services and government concepts such as Brilliant Pebbles and Brilliant Eyes, and many others demand just such development. Coupled with this demand are increasingly practical methods of launch such as rail-guns and the recently-successful Pegasus aircraft platform. These should go far to diminish some of the constraints on launching large numbers of less-expensive satellites.

RNH-5-1 Design Concept

There are several areas of construction which elevate the cost of production:

- Close-tolerance mechanical part fabrication
- Electrodes of exacting specification
- Pressure vessels with Mil-Spec requirements
- Labor-intensive construction

The new prototype design has incorporated improvements in these and other areas in order to reduce cost and ease of assembly while maintaining the necessary performance and long life. This represents Phase I of the development. These cells have not, however, been optimized for mass. That will be pursued in the near future in a subsequent phase.

Calculations indicate that the energy efficiency will be superior to present technology. Please see Figure 1 for a table of energy comparisons between present systems and a hypothetical, optimized two-cell CPV unit. Please note that the table does not reveal the principal advantages of a CPV design, i.e., that when built into a battery there are only half as many intercell connectors to contribute to battery mass, and that the footprint of the battery will occupy only half the

**Cell Energy Weight
Efficiency Comparison
WH/LB**

| Manufacture | 5AH | 10AH | 15AH | 20AH |
|------------------------|-------|-------|-------|-------|
| Equivalent Sealed Lead | 9.25 | 10.14 | 10.50 | 10.74 |
| EP Sealed Lead | 9.10 | 9.45 | 9.87 | 11.41 |
| EP NiCad | 9.27 | 14.55 | 12.77 | 10.00 |
| EP NiH ₂ * | 14.00 | 16.67 | 19.74 | 22.52 |

* Rated @ 10°C, C/2 Discharge

EP 4/23/90

FIGURE 1

area of one made with IPV cells. The operational feasibility of two-cell CPV modules has already been established ⁽¹⁾.

For a cut-away view of the 5 AH CPV module, see Figure 2. This unit contains two cells of equal size mounted in tandem fashion. All of the cell internals are attached to a header, or base plate, which constitutes the principal structural component. The header contains both terminals, the electrolyte filling port, and the mechanical attachment stud for the cell stack assembly. Therefore several machining operations are consolidated in one piece. Cell activation is accomplished with automatic equipment through a small hole in the header. This will be subsequently sealed by insertion of a metal ball. This sealant method was successfully developed and tested at over 2,000 psi for a different type of pressurized cell. Those cells are presently in production with well over a million cells produced.

5AH CPV

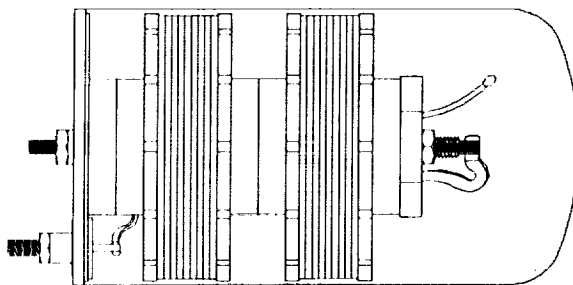


FIGURE 2

Negative electrodes are constructed on less-expensive nickel substrates and have a reduced quantity of platinum catalyst which, tests show, does not degrade performance but which substantially reduces cost. The positive electrodes are de-

signed to be impregnated on a new, automated impregnation line which minimizes human handling. This not only reduces time, but handling damage as well.

Because all components are assembled on the header as a base plate, construction is simplified. Further, the basic design is rugged for improved resistance to launch-vibration damage and can be made even more so by optional internal bracing. This bolsters the inherent advantage of smaller mass which, in itself, makes the unit more vibration resistant. This is an obvious complement to recent innovations in less-expensive launch methodologies. The basic design has the flexibility to incorporate IPV (individual pressure vessel) or CPV arrangements and can vary in size from 5 to 20 AH's in capacity. When stacking is complete, the pressure vessel is simply slid over the cell stack assembly and mated to the header.

The pressure vessel is die-formed of stainless steel. It is electron-beam welded to the header. Due to the thickness and edge design of the header however, it can be easily arc-welded instead and that would reduce welding cost.

Prototype Operation

As Phase I, several dozen prototype modules were constructed to develop the smaller size and less-expensive materials. Five units of the most recent design iteration are undergoing electrical testing at the time of this writing. These units are designed to operate at a maximum pressure of 375 psig. Operation, as expected, conforms to the very good performance previously experienced with 40 AH CPV modules ⁽¹⁾. Unlike those modules these do not have a Teflon inner coating. However, the activation process was effective in overcoming the effects of electrolyte bridging. If desired for added assurance however, the Teflon coating could be easily added. It is also notable that the capacity-retention characteristics of two-module CPV cells are no different from those of IPV cells ⁽¹⁾. Figure 3 is a photograph of the prototype modules on test and of the preliminary Phase II design. Electrical discharge characteristics at different current densities, and pressures are shown in Figure 4.

Phase II is the weight-optimization phase. Modules for this are being built at the time of this writing (April '90) and the results should be available in the future.

The prototype modules described herein offer a significant improvement in ease of manufacture of small inexpensive nickel-hydrogen cells or CPV modules. Significant cost savings are realized from a combination of manufacturing methods and design improvements. This concept has the potential to reduce the cost of cells by a factor of 70% or more. The attributes which make Ni-H₂ superior to Ni-Cd

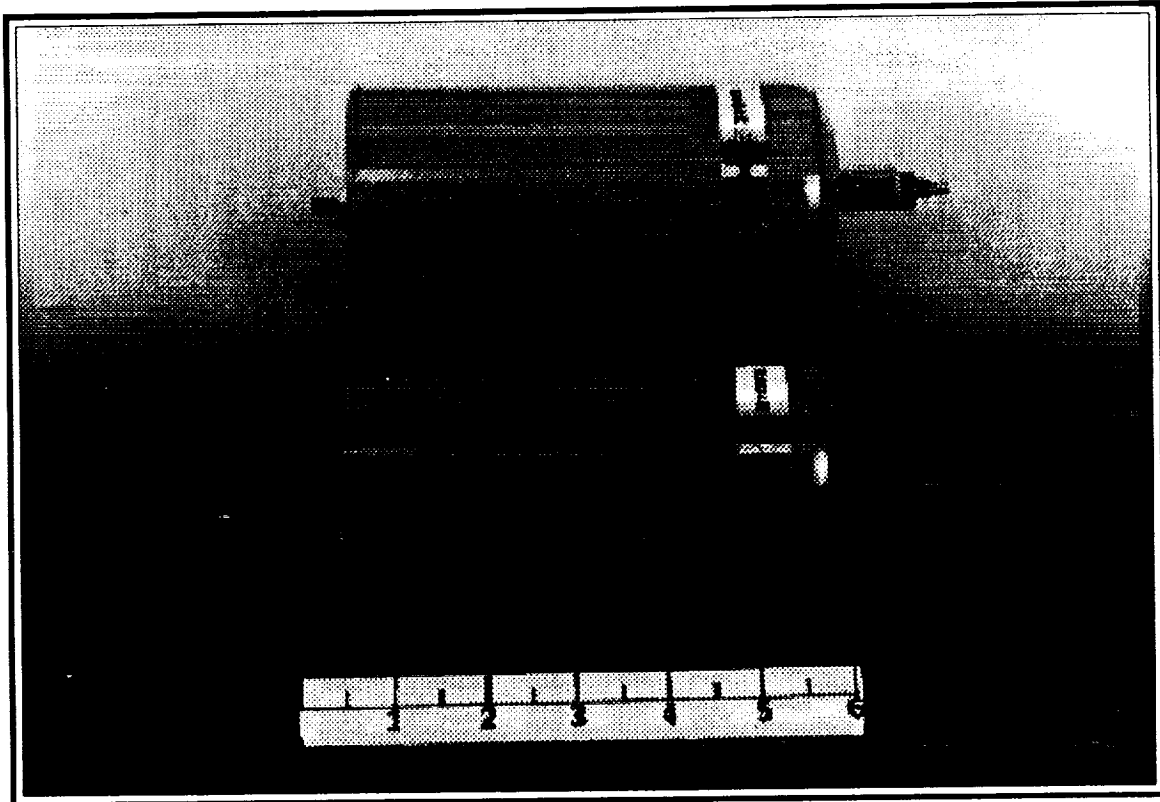


FIGURE 3

and sealed lead acid batteries, i.e. higher energy density, longer cycle life and better tolerance to overcharge and reversal, will now also become cost effective for applications such as small satellites and remote power systems which require long life (2 to 20 years) and maintenance-free operation.

For terrestrial applications the small Ni-H₂ module is less toxic in nature than Ni-Cd's, both in production and operation. Naturally the cell operating pressure can be adjusted by design as desired: higher for space use and lower for less weight-sensitive terrestrial applications.

As for use in space, the fortunate availability of CPV design at this time is especially beneficial because of the weight savings of battery-packaging. Halving the number of inter-cell connectors, and the half-size footprint, both serve to make this battery even more ideally-suited to smaller-diameter, smaller throw-weight launch vehicles.

RNH-12-1 Design Concept

Another design concept which is suited for use in the small satellite is Eagle-Picher's RNH-12-1, a 12 ampere-hour common pressure vessel cell. This cell design has been

manufactured, tested, and delivered to Intraspace Corporation (North Salt Lake City, Utah) for use as a power source on a SPINSAT (Special Purpose Inexpensive Satellite) mission. The SALT spacecraft, designed to carry an altimeter, has a mission life specification of three years.

The RNH-12-1 is a standard 3.5 inch diameter common pressure vessel cell, with two 12 amp-hour stacks connected in series, as depicted in the accompanying sketch, Figure 5. The CPV design offers significant advantages for this battery configuration which are of particular value to the small spacecraft. By eliminating half the number of units which would be required to construct an equivalent power system of IPV (individual pressure vessel) units, the CPV design provides a 30% improvement in specific energy, a 39% improvement in energy density, and a 9.9 pound reduction in overall mass.

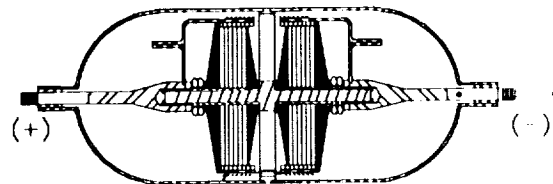
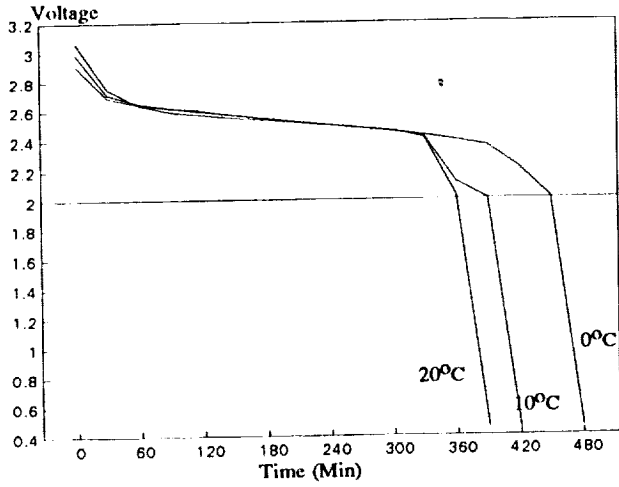


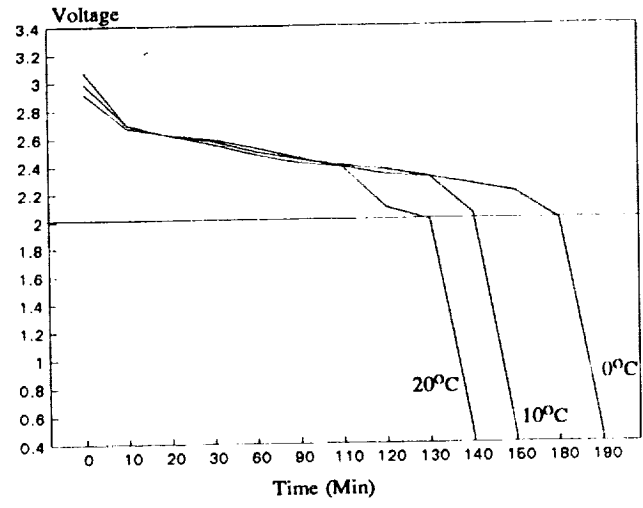
Figure 5

FIGURE 4

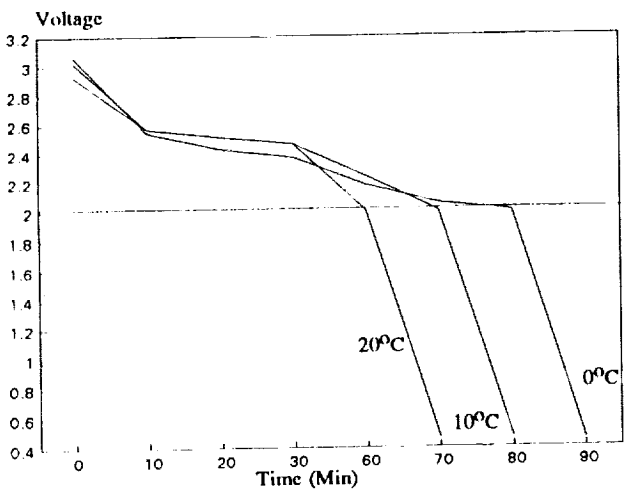
**5 AH CPV CELL
Discharge 1.1A**



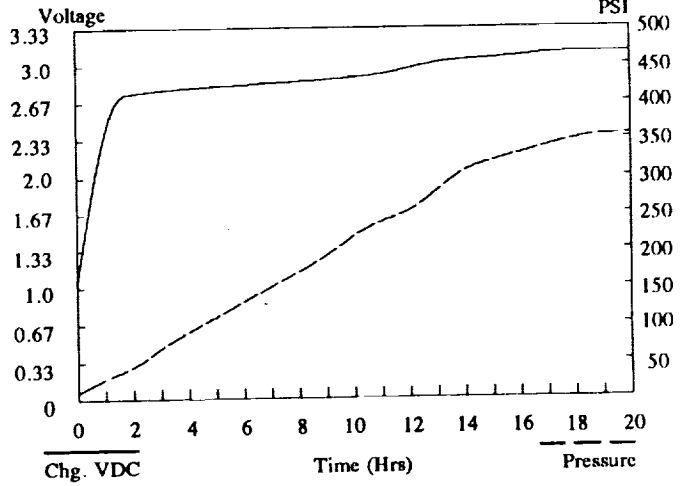
**5 AH CPV CELL
Discharge 2.75A**



**5 AH CPV CELL
Discharge 5.5A**



**5 AH CPV CHARGE VOLTAGE/PRESSURE
C/10 CHARGE 0°C**



Using this concept, sizes up to 30 AH are obtainable. This cell features performance-proven components which have been used in the manufacture of over 14000 nickel-hydrogen cells at Eagle-Picher. Several of the key components are described herein.

A high mechanical-strength nickel slurry sinter positive electrode is used. The plate is manufactured to a thickness of .030 inches and loaded by an aqueous impregnation process.

The negative electrode used is the standard catalyzed nickel substrate collector with a Teflon film barrier backing. The catalyst is a fuel cell grade platinum mixture.

The separator is 10 mil thick and die-punched in the same profile as the electrodes with provision for electrolyte redistribution.

An Inconel 718 pressure vessel is used, hydroformed in the standard domed cylinder configuration with axial terminal ports and a flame-sprayed ceramic wall wick (reservoir) on the inner surface. The pressure vessel is hermetically sealed at the girth using an electron beam weld and meets the requirements of MIL-STD-1522A, having a burst test strength in excess of 5 times the maximum expected operating pressure of the unit at full state of charge.

The RNH-12-1 CPV is fitted with an aluminum thermal sleeve/flange as shown in Figure 9 which provides a path for heat dissipation and serves as an interface for installation into the power system.

A select number of the cells were delivered with cell pressure

| Characteristic | RNH-5-1 (CPV) | RNH-12-1 (CPV) |
|-----------------------------------|------------------------|------------------------|
| Cell Diameter | 2.51 in. | 3.51 in. |
| Overall Length | 5.5 in. | 9.0 in. |
| Cell Mass | 1.1 lbs | 2.25 lbs. |
| Maximum Operating Pressure (MEOP) | 350 psig | 480 psig |
| Safety Factor | 5:1 | 5:1 |
| Capacity | | |
| @ 10°C to 1.1V | 6.3AH | 15AH |
| Nominal Voltage | 2.5V | 2.5V |
| Specific Energy | 14.3WH/lb. | 16.6WH/lb. |
| Energy Density | 0.69WH/in ³ | 0.81WH/in ³ |
| Max. Charge Voltage | 3.2V | 3.2V |

Small Satellite Cell Features
Figure 6

monitors attached to the surface of the vessel which provide an electronic signal that indicates the state-of-charge for the battery as shown in Figure 9. The unit consists of four self-temperature-compensated strain gages connected in a Wheatstone bridge configuration which is calibrated prior to cell activation.

RNH-12-1 Testing

Twenty RNH-12-1 cells (Lot 1) were tested and found to be compliant with all the requirements of the SALT detail specification. Tests were designed which would evaluate the cell's Coulombic efficiency, voltage characteristics, and capacity, as well as tolerance of environmental conditions (random vibration and thermal cycling tests).

The cell is proven capable of maintaining full state-of-charge using a 1.05 charge/discharge ratio in a range between 5 and 80% depth of discharge. Reference Figures 7 and 8.

10°C Charge at 1.2 Amps
RNH-12-1 Cells

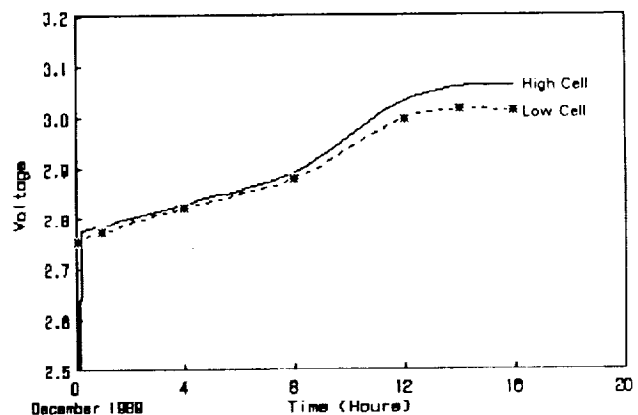


Figure 7

10°C Discharge at 6 Amps
RNH-12-1 Cells

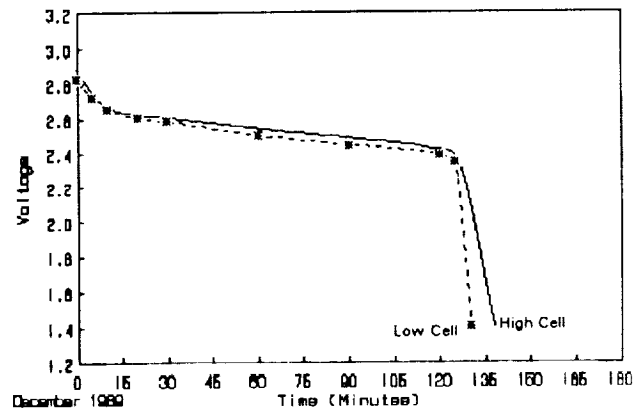


Figure 8

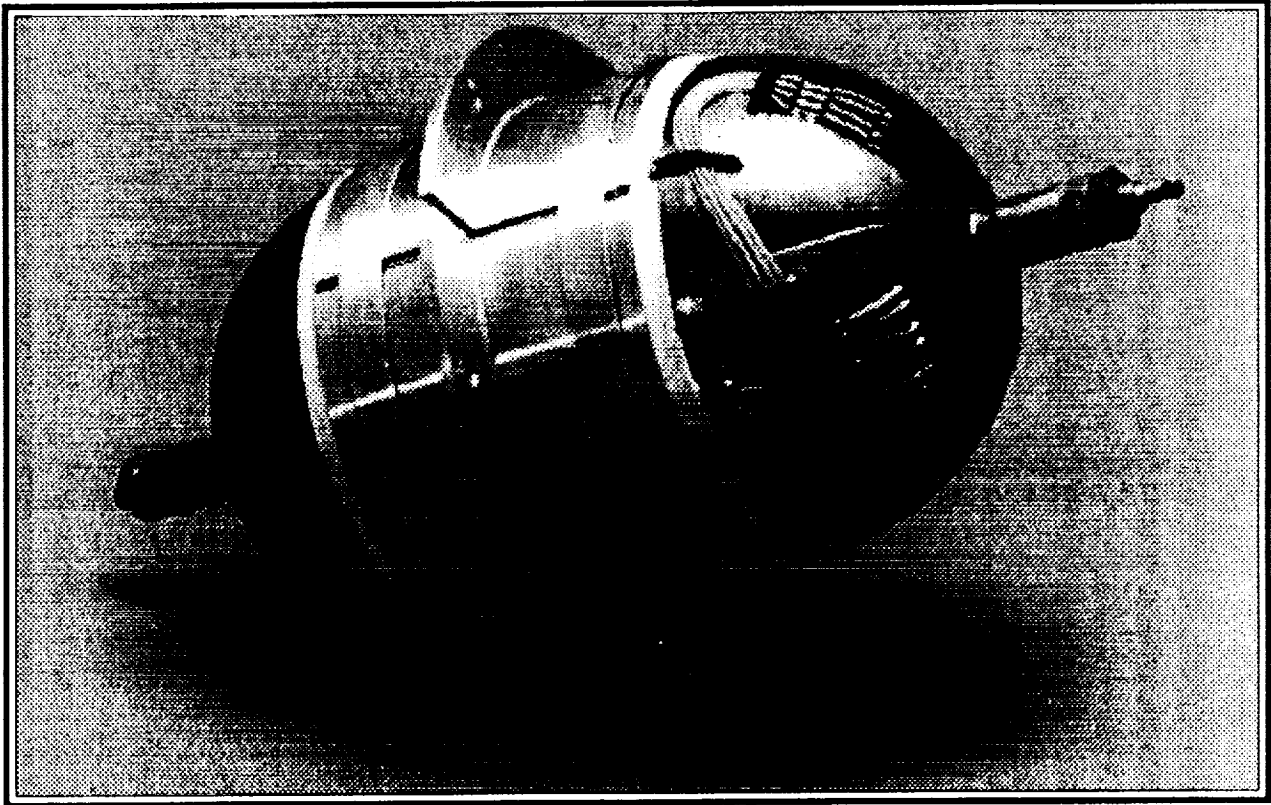


Figure 9
RNH-12-1
With Strain gage and Mounting Flange

Voltage characteristics for the CPV cell are easily predicted by doubling the normal voltage values of an IPV cell at any point during the electrical cycle. The CPV cell design has shown through demonstration that plate-to-terminal current paths are adequate to avoid IR drop which would affect cell voltage.

Qualification units from Lot 1 of the RNH-12-1 cells were subjected to random vibration levels up to 18.5 grms in each of the three axes with no evidence of subsequent performance degradation. Similarly, no difference in performance was seen during or after a thermal exposure test, where the cells were subjected to 8 temperature cycles between -15°C and $+35^{\circ}\text{C}$.

Post-Storage Testing

At the time of delivery for RNH-12-1 Cell Lot 1 (January 1990) the residual units were placed in refrigerated storage (approximately 0°C) in the fully discharged open-circuit condition. Following an approximate 5 months of such

storage a standard capacity check was performed (at 10°C) and the results indicated no performance degradation secondary to storage. In fact, capacities for the two cells which were tested were slightly improved from the pre-storage acceptance tests results.

| | Acceptance Testing | Post-Storage Testing |
|--------|-----------------------|-------------------------|
| S/N 10 | 13.5 AH | 15.0 AH |
| S/N 22 | 13.7 AH | 15.1 AH |

References

- (1) James R. Wheeler, Burton M. Otzinger, "Common Pressure Nickel-Hydrogen Battery Development, Proceedings of the 24th Intersociety Energy Conversion Engineering Conference (August 1989), Vol. 3, pp. 1381-1386.

ORIGINAL PAGE IS
OF POOR QUALITY

SODIUM - METAL CHLORIDE BATTERY RESEARCH AT JPL

B.V. Ratnakumar, A.I. Attia, and G. Halpert
Jet Propulsion Laboratory
California Institute of Technology
Pasadena, California 91109

Sodium - metal chloride batteries have certain distinct advantages over sodium - sulfur batteries such as increased safety, inherent overcharge capability and lower operating temperatures. Two systems, i.e., Na/FeCl₂ and Na/NiCl₂, were developed extensively elsewhere and evaluated for various applications including electric vehicles and space. Their performance has been very encouraging and prompted a detailed fundamental study on these cathodes here at the Jet Propulsion Laboratory. A brief review of our studies on these new cathode materials is presented here. The initial efforts focussed on the methods of fabrication of the electrodes and their electrochemical characterization. Subsequent studies were aimed at establishing the reaction mechanism, determining the kinetics and identifying the rate-limiting processes in the reduction of metal chloride cathodes. Nickel chloride emerged from these studies as the most promising candidate material and was taken up for further detailed study on its passivation - a rate limiting process - under different experimental conditions. Also, the feasibility of using copper chloride, which is expected to have higher energy density, has been assessed. Based on the criteria established from the voltammetric response of FeCl₂, NiCl₂ and CuCl₂, several other transition metal chlorides were screened. Of these, molybdenum and cobalt chlorides appear promising.

INTRODUCTION

The disclosures by Coetzer et al^(1,2) on the use of transition metal chlorides in chloroaluminate melts as positive electrodes in rechargeable sodium batteries have generated a wide interest on the sodium-metal chloride battery systems at various laboratories around the world⁽³⁻⁶⁾. These battery systems have attractive electrochemical characteristics such as high voltages, high energy and power densities and a long cycle life. Besides, some of the problems often encountered with the sulfur cathode in Na/S batteries are noticeably absent in these systems, making them viable alternatives to Na/S batteries in several applications.

The advantages stem mainly from the way these systems are configured: A Na/MCl₂ cell consists of a solid (insoluble) transition metal chloride in NaAlCl₄ electrolyte separated from the anode (molten sodium) by a Na⁺ ion conducting solid electrolyte (beta" alumina ceramic). Some of these

advantages are : 1) about 100° lower operating temperatures, 2) reduced corrosion by the catholyte, 3) increased safety during internal shorts or thermal excursions, 4) tolerance to overcharge and overdischarge and 5) ease of fabrication in the discharged state with little elemental Na. Not surprisingly, sodium - metal chloride batteries, aided by the above attractive features are being considered for various applications including load leveling and electric vehicles. Both Na/FeCl₂ and Na/NiCl₂ batteries have been developed in 40 - 100 Ah size for electric vehicles application⁽⁷⁾. Further, Na/NiCl₂ batteries are currently being successfully evaluated for GEO and LEO space applications⁽⁸⁾.

Considering the promise the Na-MCl₂ battery systems hold for space applications, a program has been initiated at the Jet Propulsion Laboratory to evaluate these systems for NASA's future missions. The program has hitherto focussed on gaining a fundamental understanding of the electrochemistry of the metal chloride cathodes to augment the developmental effort being pursued elsewhere in the U.S. and other countries. In this paper, a brief review of such studies carried out on different metal chlorides is presented.

EXPERIMENTAL

Various methods of fabricating the metal chlorides electrodes have been examined. These methods include 1) hot pressing powders of NaCl and a transition metal with a Teflon binder (stable below 250°C) to obtain electrodes in the discharged state; (2) impregnation of a metal chloride in a sintered matrix of the same or nobler metal; and 3) cosintering of pressed powders of NaCl and a transition metal at 800°C under argon atmosphere for 6-8 hours to obtain the electrodes in the discharged state. The impregnation method has the advantage of providing a suitable morphology for extended cycle life, i.e., the active material is pocketed in the pores of the plaque as in Ni-Cd batteries. In the cosintering method, however, oxidation of the grid is likely as well thus reducing its mechanical integrity during cycling. For the single electrode studies aimed at obtaining fundamental understanding of the metal chloride cathodes, the metal chloride is formed on the metal wire electrode from an in-situ oxidation in the electrolyte. Other experimental conditions are similar to those reported in our earlier communications⁽⁹⁻¹⁴⁾.

RESULTS AND DISCUSSION

Before embarking on the detailed fundamental studies, initial experiments were focussed on the electrochemical characterization of the metal chlorides, i.e., mainly on the discharge behavior, rechargeability, rate - limiting processes etc. Three metal chlorides. FeCl₂, NiCl₂ and CuCl₂ have been chosen for these studies. As mentioned above, FeCl₂ and NiCl₂ have been extensively developed elsewhere. Copper chloride, on the other hand, hasn't been studied much and was included in this program with an expectation that its voltage (as well as energy density) would be higher than FeCl₂ and even NiCl₂.

CHARGE - DISCHARGE BEHAVIOR

The charge - discharge curves of FeCl_2 electrodes, formed by cosintering of Fe and NaCl, and NiCl_2 and CuCl_2 electrodes formed by impregnation (Figs. 2-5 in Ref.9) illustrate the high coulombic yields and good reversibility of these cathodes. Both FeCl_2 and NiCl_2 have flat charge - discharge curves in the range of current densities studied (1-8 mA/cm^2). Copper chloride, on the other hand, exhibits a higher voltage than FeCl_2 and NiCl_2 but sloping charge - discharge curves, suggesting the possible formation of monovalent copper during reduction of CuCl_2 . CuCl_2 appeared to be chemically stable in NaAlCl_4 electrolyte, which is an essential requirement for a successful operation of the metal chloride cathode in the above sodium batteries.

POLARIZATION STUDIES ON SINTERED ELECTRODES

DC linear polarization studies were performed on the sintered metal chloride electrodes to determine the exchange current densities for their reduction (Fig. 7 in ref. 9 and Fig. 1 in ref. 10). The exchange current densities are in the range of 1-2 mA/cm^2 for NiCl_2 and FeCl_2 and 0-1 mA/cm^2 for CuCl_2 . The values are in good agreement with those derived from the potentiodynamic polarization data. The potentiodynamic polarization curves also show mass transfer effects, evident from limiting currents, in the reduction of metal chlorides. Furthermore, the Tafel plots of NiCl_2 and CuCl_2 contain discontinuities during reduction, which, in the case of CuCl_2 , may be due to the possible formation of monovalent copper. In the case of NiCl_2 , these discontinuities may be attributed to a kinetic effect (described later on as passivation) by the discharge products, especially NaCl. Due to these kinetic effects, the NiCl_2 electrode exhibits lower exchange currents at lower states of charge.

AC impedance studies on FeCl_2 and NiCl_2 reveal a single charge transfer step with exchange current densities comparable to those derived from DC polarization data. The complex impedance plots of CuCl_2 , on the other hand, contain a second relaxation loop especially at lower potentials which may be related to the formation of monovalent copper during the reduction of CuCl_2 .

SINGLE - ELECTRODE STUDIES

Single electrode studies were performed on transition metal wire electrodes in NaAlCl_4 electrolyte with an aluminum reference electrode (1.643 V vs. Na) and a nickel foil counter electrode in a pyrex cell. These studies were aimed at verifying the reversibility, establishing the reaction mechanisms, determining accurately the rate parameters and identifying the rate limiting processes in the electrode reactions⁽¹¹⁾. These studies broadly include cyclic voltammetry, dc polarization and ac impedance.

The cyclic voltammograms of Ni (Fig. 1) consist of sharp and symmetric peaks both during oxidation and reduction, implying a high degree of reversibility for this system. A single peak is observed during oxidation as well as reduction with a peak splitting close to 48 mV expected for a two-electron reaction, which is consistent with the phase

diagram of NiCl_2 , Ni and NaCl . The peak current varies linearly with the square root of scan rate implying mass transfer control over the reaction. The above voltammetric behavior is explained in terms of deposition of the oxidation product, by virtue of its insolubility in the electrolyte, over the electrode manifesting itself in a mass - transfer limited situation. From the slope of the peak current against (scan rate)^{1/2}, the diffusion coefficient for Ni^{++} ions across the layers of NiCl_2 deposited was estimated as $4.5 \times 10^{-8} \text{ cm}^2/\text{s}$. The cyclic voltammograms of Fe (Fig. 2) have symmetric, but broad peaks splitting into two peaks at slower scan rates. The peak splitting is 84 mV, which is expected for two single electron transfer steps reported to be apart by 12 mV in the reduction of FeCl_2 . The peak currents once again vary linearly with the square root of the scan rate suggesting mass transfer controlled kinetics. The diffusion coefficient for Fe^{++} across FeCl_2 layers on the electrode was estimated from the slope of peak current against (scan rate)^{1/2} to be $5.2 \times 10^{-8} \text{ cm}^2/\text{s}$. The voltammograms of Cu show expected higher voltages, but also poor reversibility evident from smaller reduction peaks. Also, the voltammograms contain two peaks; the products formed in the second step possibly monovalent copper, appear to be soluble in the electrolyte. This is further confirmed by the presence of dissolved copper in the electrolyte of a Na-CuCl_2 laboratory test cell, especially when the charging is extended beyond (2.83 V vs Na) the first step. The reversibility of CuCl_2 improves if the oxidation is limited to the first step⁽¹²⁾

From the cyclic voltammetric behavior of FeCl_2 and NiCl_2 , certain criteria have been established to predict the feasibility of using a metal chloride as cathode material in sodium batteries⁽¹³⁾. These criteria include a low oxidation current subsequent to the peak, implying low solubility for the chloride, and symmetry in shape and size between the oxidation and reduction peaks even at low scan rates. Using these criteria, several transition metal chlorides including vanadium, cobalt, chromium, manganese, molybdenum and silver have been screened. Cobalt (Fig. 3) and molybdenum (Fig. 4) appear to meet those requirements, with the latter also showing promise as a stable current collector for FeCl_2 and NiCl_2 electrodes.

DC micropolarization studies carried out on NiCl_2 and FeCl_2 wire electrodes gave more accurate exchange current densities of 0.73 and 0.43 mA/cm^2 respectively. Potentiodynamic polarization curves of NiCl_2 exhibit 'passivation' akin to reactive metal anodes, i.e., the current rises sharply and falls down subsequently (Fig.5). This passivation behavior is attributed to the deposition of NaCl formed during reduction on the electrode surface causing significant ohmic polarization at such sites. This is in fact responsible for the 'segmented' Tafel behavior observed with sintered NiCl_2 electrodes. This aspect is addressed in more detail later on. The current - potential curve of FeCl_2 shows reduced passivity as compared to NiCl_2 , probably due to the intermediates formed during reduction being less resistive than NaCl .

The exchange current density derived from the ac impedance data of FeCl_2 is $0.66 \text{ mA}/\text{cm}^2$, in agreement with the values obtained from dc data. Furthermore, the diffusion coefficient calculated from the Randles' impedance plot for Fe^{++} ions across FeCl_2 is 4.4×10^{-8} as compared to 5.2

$\times 10^{-8}$ cm²/s derived from cyclic voltammetric data. The ac impedance (Nyquist) plot of NiCl₂ is similar to that of a passive system, e.g., iron in sulfuric acid, with the relaxation loop bending inward towards the imaginary axis at low frequencies. This characteristic profile (Fig. 6) of the Nyquist plot may serve as a qualitative index for the onset of passivation of NiCl₂.

PASSIVATION OF NiCl₂

From the single electrode studies, NiCl₂ emerged as the candidate cathode material for further study due to its near-ideal reversibility, high exchange currents, simple reaction mechanism free of intermediates and superior electrochemical characteristics. However, NiCl₂ shows a tendency to passivate during reduction at high current densities, which warrants a proper design of electrode geometry to achieve high power densities. A detailed study on the passivation has been carried out under different experimental conditions⁽¹⁴⁾.

DC micropolarization curves obtained at different states of charge show increasing polarization resistance at low states of charge, implying lower exchange currents. The open - circuit potential, on the other hand, remains the same (Fig. 7). This decrease in the exchange current is explained in terms of a progressive reduction in the active (non-passive) electrochemical area due to deposition of the reduction product NaCl on the electrode. Potentiodynamic polarization curves (Fig. 8) at different states of charge also demonstrate the increasing passivation at lower states of charge as is evident from a sharp decrease in the current at overpotentials exceeding 100 mV.

AC impedance measurements carried out at different states of charge also gave lower exchange currents (Fig. 7) at lower states of charge, in agreement with the results obtained from linear polarization. Also, at lower states of charge, the Nyquist plots exhibit the typical profile characteristic of a passive system, wherein the capacitive component bends inward towards the imaginary axis at low frequencies. AC impedance plots obtained at different electrode potentials suggest that at lower (reduction) potentials, i.e., ≤ 950 mV vs Al, the electrode tends to passivate, as is evident from the characteristic shape of the Nyquist plot. The exchange current appears to decrease with a decrease in electrode potential until 950 mV vs Al after which the electrode has a high impedance due to passivation.

CONCLUSIONS

Transition metal chlorides have several attractive features and are viable alternatives to sulfur as positive electrodes in sodium batteries. Our initial studies on metal chloride cathodes were focussed on the methods of fabrication and electrochemical characterization including discharge behavior, rechargeability etc. Detailed fundamental studies carried out in single-electrode configuration gave useful information on the reaction mechanisms, rate parameters and rate-limiting processes. NiCl₂ emerged from our studies as the candidate cathode material for further study and development for NASA's requirements, whereas copper chloride appears to be chemically unstable during extended charge. Among

various other metal chlorides screened, cobalt and molybdenum are likely to be successful as cathodes with the latter also having a potential as a stable current collector for NiCl₂ electrodes. The passivation of NiCl₂, a rate limiting phenomenon, increases at lower states of charge but can be alleviated by a proper electrode design or, as our recent studies show, by increasing the operating temperature to around 275°C. Higher operating temperatures also improve the kinetics, the exchange current increasing by 10% for each 10°C rise in temperature.

ACKNOWLEDGEMENTS

The work described here was carried out at the Jet Propulsion Laboratory, California Institute of Technology, under contract with the National Aeronautics and Space Administration. This program is sponsored by the Office of Aeronautics and Space Technology, Code RP.

REFERENCES

1. J. Coetzer, J. Power Sources, 18, 377 (1986).
2. J. Coetzer, R. J. Bones, R. C. Galloway, D. A. Teagle and P. T. Moseley, U.S. Pat. 4,546,055 (1985).
3. R. J. Bones, J. Coetzer, R. C. Galloway and D. A. Teagle, J. Electrochem. Soc., 134, 2379 (1987).
4. R. M. Dell and R. J. Bones, Bull. Electrochem., 4, 319 (1988).
5. R. J. Bones, D. A. Teagle, S. D. Brooker and F. L. Cullen, J. Electrochem. Soc., 136, 1274 (1989).
6. P. A. Nelson, J. Power Sources, 29, 565 (1990).
7. J. L. Sudworth and R. N. Bull, Proc. DOE/EPRI Beta Battery Workshop VII, 53-1, Toronto (1988); J. L. Sudworth, R. C. Galloway and R. N. Bull, Proc. DOE/EPRI Beta Battery Workshop VII, 52-1, Toronto (1988).
8. B. Hendel and G. Dudley, NASA Aerospace Battery Workshop, Huntsville, AL., Dec. 4-6 (1990).
9. S. Di Stefano, B. V. Ratnakumar and C. P. Bankston, J. Power Sources, 29, 301 (1990).
10. B. V. Ratnakumar, S. Di Stefano and C. P. Bankston, Proc. 24th Intersoc. Energy Conversion and Eng. Conf. (IECEC), Vol. 6, p. 2921, Washington, D.C., August 6-11, 1989.
11. B. V. Ratnakumar, S. Di Stefano and G. Halpert, J. Electrochem. Soc., 137, 2991 (1990).
12. B. V. Ratnakumar, A. I. Attia and G. Halpert, Abst. # 8, 177th Electrochem. Soc. Meeting, Montreal, Canada, May 6-11 (1990).
13. B. V. Ratnakumar, A. I. Attia and G. Halpert, J. Electrochem. Soc. 138, 883 (1991).
14. B. V. Ratnakumar, A. I. Attia and G. Halpert, Proc. 34th Intl. Power Sources Symp., pp 17, June 25-28 (1990).

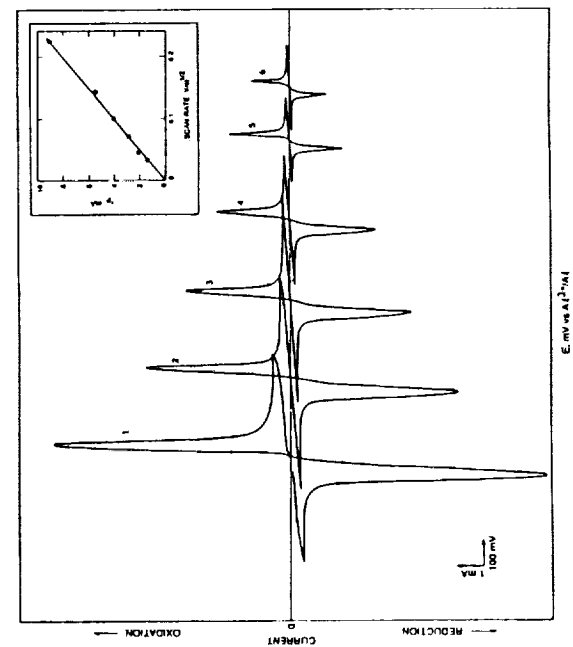


Fig. 1. Cyclic voltammograms of Ni electrode (area: 0.06 cm²) in NaAlCl₄ at 220°C at different scan rates of 1.) 50, 2.) 20, 3.) 10, 4.) 5, 5.) 2, and 6.) 1 mV/s. Peak current varies linearly with the square root of scan rate.

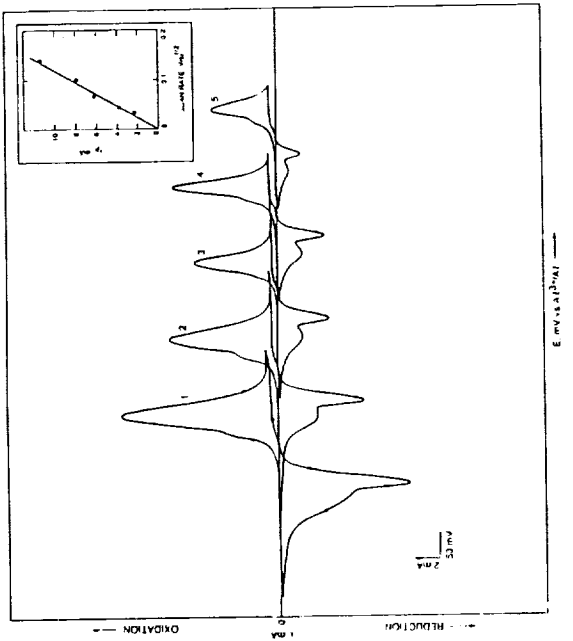


Fig. 2. Cyclic voltammograms of Fe electrode (area: 0.05 cm²) in NaAlCl₄ at 220°C at scan rates of 1.) 20, 2.) 10, 3.) 5, 4.) 2, and 5.) 1 mV/s. Scale on the y axis is 1 mA/cm (reduced to half) for curves 4 and 5. Peak current is again proportional to the square root of the scan rate.

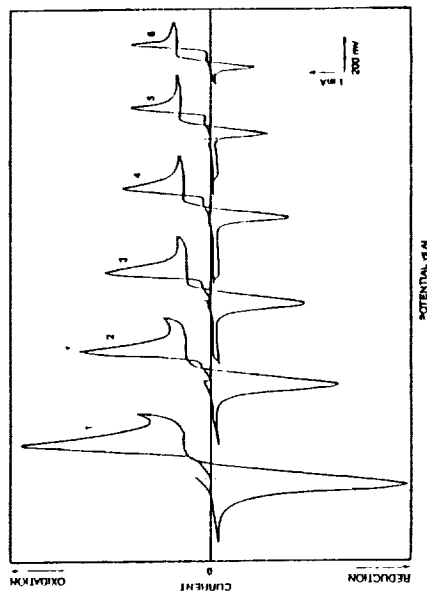


Fig. 3. Cyclic voltammograms of Co (E₀: 870 mV vs. Al) in NaAlCl₄ at 250°C at different scan rates of 1.) 50, 2.) 20, 3.) 10, 4.) 5, 5.) 2, and 6.) 1 mV/s.

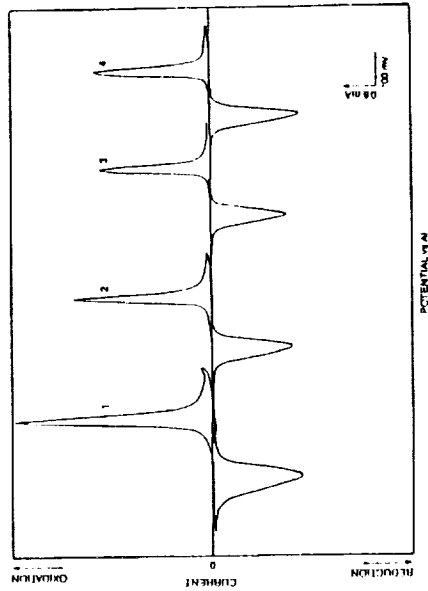


Fig. 4. Cyclic voltammograms of Mo (E₀: 997 mV vs. Al) in NaAlCl₄ at 250°C at different scan rates of 1.) 50, 2.) 20, 3.) 10, and 4.) 5 mV/s (Scale on the y axis is doubled for curve 4).

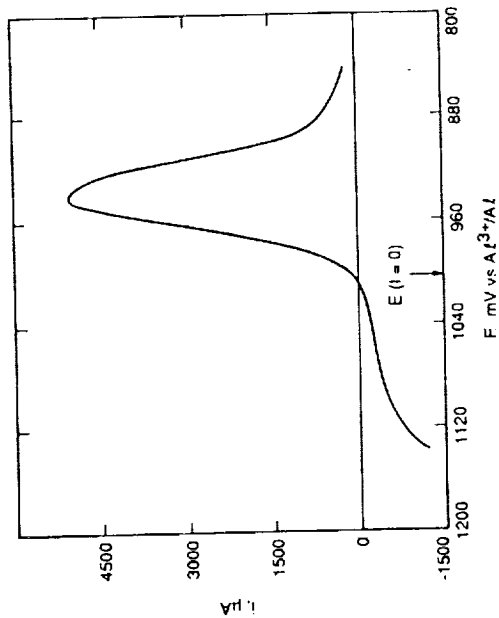


Fig. 5. Typical potentiodynamic polarization curve of NiCl_2 in NaAlCl_4 melt at 250°C at 1 mV/s , illustrating its tendency to 'passivate' during reduction.

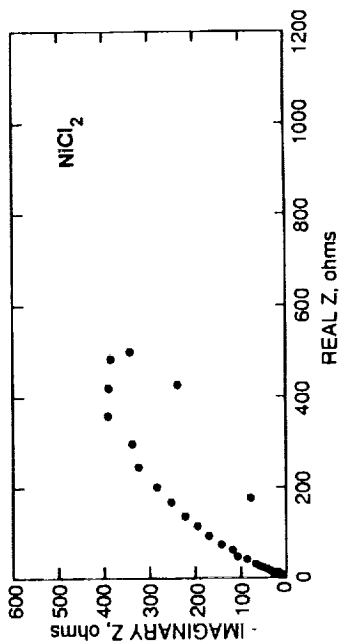


Fig. 6. Nyquist impedance plot of NiCl_2 in NaAlCl_4 at 250°C in the frequency range of 10^3 - 10^2 Hz and at an ac amplitude of 5 mV .

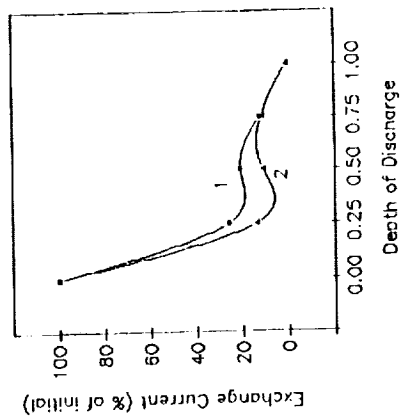


Fig. 7. Decrease in the exchange currents, derived from 1) dc linear polarization and 2) ac impedance data, with the state of charge of NiCl_2 cathode in Na/NiCl_2 cell at 230°C .

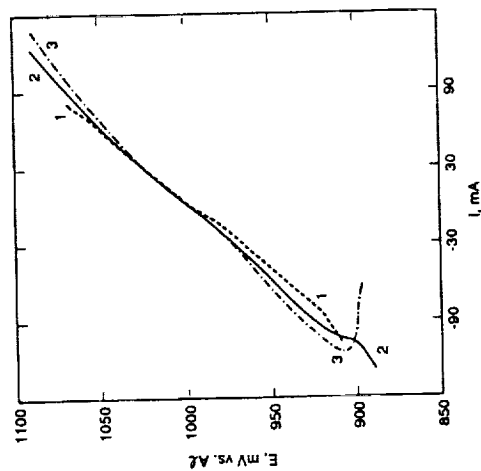


Fig. 8. Current-potential curves of NiCl_2 electrode in Na/NiCl_2 cell at 230°C at a slow scan rate of 0.5 mV/s and at different states of charge of 1.) 0.75 , 2.) 0.5 , and 3.) 0.25 .

ADVANCES IN Li-TiS₂ CELL TECHNOLOGY

S. Surampudi, D.H. Shen, C.-K. Huang, F. Deligiannis,
A. Attia, and G. Halpert
Jet Propulsion Laboratory
California Institute of Technology
Pasadena, California 91109

ABSTRACT

JPL is involved in a NASA sponsored program to develop ambient temperature secondary cells for future space missions. After several years of research on various cathode materials, Titanium Disulfide (TiS₂) was selected in view of its intrinsic reversibility and high faradaic utilization. In the last two years, the efforts were focussed on improving the cycle life of the system and developing 1 Ah cells. Several approaches including the use of mixed solvent electrolytes, the operation of cells at low temperature, and the cycling of cells under different voltage limits, were initially examined to improve the cycle life performance of the Li-TiS₂ system. Spiral wound 1 Ah cells fabricated incorporating the improvements from the above studies have delivered more than 600 cycles at 50% DOD. Work is in progress to identify alternate anode materials that can improve the cycle life of the cells to 1000 cycles at 50% DOD. This paper summarizes the advances made in the Li-TiS₂ technology at JPL since 1989.

INTRODUCTION

Ambient temperature secondary lithium batteries have a number of intrinsic advantages such as higher energy density, longer active shelf life, lower self discharge, etc. over the conventional Ni-Cd, Pb-Acid, and Ag-Zn batteries. The pay-offs are 2-3 fold increase in energy storage capability and a longer active shelf life of 5 to 10 times that of Ni-Cd.

Under a NASA OAET sponsored program, Jet Propulsion Laboratory (JPL) is developing ambient temperature secondary lithium cells for future space applications. The main objective of the program is to develop ambient temperature secondary lithium cells with greater than 100 Wh/kg specific energy while delivering 1000 cycles at moderate depths of discharge (50%) by 1995. Some of the projected space applications of these batteries are for planetary rover, planetary spacecraft/probes, astronaut equipment, and Geo-Syn-Spacecraft.

After a detailed examination of various cathode materials, TiS₂ was selected in view of its intrinsic reversibility and high faradaic utilization (1). The state-of-art Li-TiS₂ cells have a limited cycle life performance (100-200 cycles at 100% DOD), and the cells were found to lose capacity on cycling (2). The capacity loss is found to be

mainly due to the increased cell polarization with cycling. This increased polarization is understood to be due to the electrolyte degradation with cycling. Hence any approach, that can reduce the electrolyte degradation and/or improve electrolyte stability towards lithium will result in improved cycle life. A number of approaches such as the use of mixed solvent electrolytes, the operation of cells at low temperature, and the cycling of cells under different voltage limits, were examined to improve the cycle life performance of the Li-TiS₂ system. Spiral wound 1 Ah cells were fabricated incorporating the improvements from the above studies. The cells have delivered more than 600 cycles at 50% DOD. Other approaches are required to achieve the goal of 1000 cycles. Lithium alloys and intercalation compounds have lower reactivity towards organic electrolyte than the elemental lithium (3). The use of these materials as candidate anode materials can result in improving the cycle life performance of the cells. A number of lithium alloys and intercalation compounds are being evaluated as candidate anode materials. This paper summarizes these advances made at JPL since 1989 in Li-TiS₂ technology .

MIXED SOLVENT ELECTROLYTES

The limited cycle life performance of the ambient temperature Li-TiS₂ cells is mainly due to the high reactivity of the organic electrolyte towards lithium and cathode material(4). JPL used 1.5M LiAsF₆/2-MeTHF as bench mark electrolyte for secondary Li-TiS₂ cells. Use of additive and co-solvents were investigated to improve the stability of THF, 2-MeTHF, and dioxolane electrolytes. The additives and co-solvents investigated were 2-methyl furan (2-MeF), ethylene carbonate (EC), propylene carbonate (PC), and 3-methyl sulfolane (3-MeS). A number of electrolytes with different combinations of additive and co-solvents were evaluated for their stability towards lithium by open circuit stand, AC impedance spectroscopy, and microcalorimetry methods (5). Three electrolytes were selected for detailed assessment in view of their improved stability and conductivity. The selected electrolytes are 1.5 M LiAsF₆ EC/2-MeTHF, 1.5 M LiAsF₆ THF/2-MeTHF/2-MeF, and 1.5 M LiAsF₆ dioxolane/2-MeF. The cycle life performance of the experimental cells(150mAh) activated with these electrolytes is given in Figure 1. The cells activated with 1.5 M LiAsF₆ EC/2-MeTHF and 1.5 M LiAsF₆ THF/2-MeTHF/2-MeF electrolytes showed higher cathode utilization and minimum capacity decline compared to the cells activated with 1.5 M LiAsF₆ dioxolane/2-MeF and 1.5 M LiAsF₆ 2-MeTHF bench mark electrolytes. The rate capability, operating temperature range, and safety of the cells are presently being evaluated. Final selection of the electrolyte will be made based on the results of these studies.

LOW TEMPERATURE OPERATION

The reactivity of the organic electrolyte towards lithium can be reduced by operating the cells at low temperature. It was felt that the reduced reactivity of the electrolytes at low temperature can result in improved cycle life performance (6). In the present investigation, we have

evaluated the influence of temperature on the stability and lithium cycling efficiency of the electrolytes.

The electrolyte investigated are: THF, EC/THF, 2-MeTHF, EC/2-MeTHF, THF/2-MeTHF, and EC/THF/2-MeTHF. All the electrolytes contained 1.5M LiAsF₆. The stability of the electrolytes at three different temperatures (10°, 25° and 70°C) was evaluated by open circuit stand test method. Results of these studies are summarized in Table I. Some of the important observations are: 1) the electrolyte showed higher stability towards lithium at 10°C, 2) the reactivity of electrolyte towards lithium increased with temperature, 3) 2-MeTHF electrolytes exhibited higher stability towards lithium compared to THF electrolytes, and 4) addition of EC improved the stability of THF, 2-MeTHF, and THF/2-MeTHF electrolytes. From these results, it was expected that cycling of the cells at low temperature may result in improved cycle life performance.

Cycle life performance of the cells activated with these six electrolytes was evaluated at 10° and 25°C. These two temperatures were chosen to verify the hypothesis of benefits of low temperature cycling. Sealed 150 mAh experimental Li-TiS₂ cells were cycled by constant current method between 1.7V and 2.7V. The current densities were 2 and 1 mA/cm² for discharging and charging respectively. Cycling efficiency of lithium in various electrolytes was determined from the cycle life data. The lithium cycling efficiency/figure of merit (FOM) was calculated using the relationship:

$$F.O.M._{Li} = \frac{\text{Total Accumulated Discharge Capacity}}{\text{Theoretical Li Capacity}}$$

Lithium cycling efficiency (FOM) in these electrolytes at 10° and 25°C is given in Table II. From the results it can be observed that no significant difference in FOM was observed by cycling cells at 10° and 25°C.

The lithium cycling efficiency results are not in agreement with the prediction of the open circuit stability stand tests. This is probably due to the fact that the open circuit stand test can only provide qualitative information about the reactivity of the electrolytes towards passivated lithium. During cycling, finely divided lithium is formed and the reactivity of the electrolytes towards the freshly formed lithium deposits is significantly higher.

OPERATING VOLTAGE LIMITS

It is known that at voltages lower than 1.5 V, the salt, LiAsF₆, undergoes reduction and at voltage higher than 3 V, some solvents undergo oxidation. Thus, the degradation of the electrolyte can be minimized by selecting optimum cycling limits (end of charge and discharge voltages). To investigate this phenomenon, 1 Ah Li-TiS₂ cells obtained from a commercial source were cycled under three different voltage regimes (1.7-2.7V, 1.9-2.7 V, 1.9-2.5V). These cells were

activated with 1.5 M LiAsF₆ 2-MeTHF/THF/2-MeF. Cycle life performance of these cells under three different voltage regimes is given in Figure 2 (7). From the results, it can be observed that the cycle life performance of the cells is significantly dependent on the cycling voltage limits. The lower voltage limit seems to have higher influence on the cycle life performance. Detailed cycling studies are needed for each electrolyte to identify the optimum operating limits and the degradation mechanisms involved.

1 Ah CELL DEVELOPMENT

Experimental cells (150 mAh) were used until 1989 for the performance evaluation of electrolytes and cathode materials. Spiral wound 1 Ah cells were developed in 1990 for design optimization studies and performance evaluation of components. These cells had an electrode capacity ratio of 6:1 (Li:TiS₂) and were activated with 1.5 M LiAsF₆ EC/2-MeTHF electrolyte. This electrolyte was selected in view of its higher stability and lithium cycling efficiency compared to the other mixed electrolytes investigated at JPL. The cycle life performance of the cells at 50% and 100% DOD was evaluated at C/10 charge and C/5 discharge. The cells had delivered more than 600 and 350 cycles at 50% and 100% DOD, respectively (Figure 3&4). Even though the cycle life performance of these cells is attractive for many commercial applications, it is still inadequate for space applications. Alternate anode materials are being examined to achieve the desired cycle life performance goal.

ANODE MATERIALS

Lithium alloys and intercalation components have lower reactivity towards organic electrolytes than the elemental lithium(3). The use of these materials as candidate anode materials can result in improving the cycle life performance of the cells. Further, the use of lithium alloy anodes may also improve the safety of the cells.

A suitable lithium alloy anode material must have several desirable properties such as high Li diffusivity, low equivalent weight (molecular weight/no. of Li reversible), high reversibility, and low voltage (E° vs. Li). In addition, the material must have good thermal and chemical stability in the cell environment. Detailed analysis of the variables that control the specific energy of the Li alloy-TiS₂ system resulted in establishing selection criteria. The equivalent weight and voltage (vs. Li) of the alloy must be less than 60 gm/eq. and 200 mV, respectively, to achieve a practical specific energy of 70-80 Wh/Kg. The equivalent weights of different alloys were calculated assuming that 80% of the lithium in the alloy is available for reaction. This assumption was made because of the lack of actual experimental data in the literature. The properties of several lithium alloys and the corresponding theoretical specific energy of the Li alloy-TiS₂ system are summarized in Table III. Among the various alloy systems examined, the Li-Si and Li-Cd alloys were only found to satisfy the above criteria. The Li-Al

alloy, with a voltage higher than 200 mV vs. Li, has a theoretical specific energy of more than 300 Wh/Kg because of its lower equivalent weight. In practical cells, Li-Al, Li-Si and Li-Cd alloys are projected to provide greater than 75 Wh/Kg (1/4 of theoretical). Li-C, Li-Pb, and Li-Sn appear to be the next best among the alloys considered.

Li-Al, Li-Cd, Li-Pb, Li-C, Li-Si, Li-Sn materials were evaluated for the stability, and reversibility. The stability of the alloys was evaluated by microcalorimetry and open circuit voltage measurement techniques. Among the alloy materials examined Li-Si and Li-Cd were found to be unstable towards 1.5M LiAsF₆/EC+2-MeTHF electrolyte. The usable capacity and reversibility of the remaining four alloy materials were evaluated in experimental cells by galvanostatic cycling. The realizable specific energy of the Li alloy-TiS₂ system was also calculated. The results of these studies is summarized in Table IV. From the results it can be observed that Li-Al and Li-C alloys are the only materials that can be considered for further evaluation in view of their reversibility and higher specific energy. Detailed assessment of these materials in experimental Li-alloy/TiS₂ cells is in progress.

CONCLUSIONS

Several approaches were examined to improve the cycle life of ambient temperature secondary Li-TiS₂ cells. Some of the important findings of the study are: 1) Li-TiS₂ cells activated with 1.5 M LiAsF₆/EC+2-MeTHF electrolyte showed improved cycle life performance compared to the cells activated with other mixed solvent electrolytes investigated 2) The cycling of the cells at low temperature did not result in improving the cycle life of the cells and 3) Charge and discharge voltage limits were found to have significant influence on the cycle life of the cells. Spiral wound 1 Ah cells activated with 1.5 M LiAsF₆/EC+2-MeTHF electrolyte have delivered more than 600 cycles at 50% DOD. Work is still in progress to improve the safety and cycle life performance of the cells through the use of alternate anode materials.

ACKNOWLEDGEMENTS

The work described here was carried out at the Jet Propulsion Laboratory, California Institute of Technology, through an agreement with the National Aeronautics and Space Administration. The authors would like to thank E. Davies and D. Perrone for their assistance in the cell assembly and testing.

REFERENCES

- (1) S. Subbarao, D. H. Shen, F. Deligiannis, C.-K. Huang and G. Halpert, J. Power Sources, 29 (1990) 579 - 587.
- (2) S. Subbarao, D. H. Shen, C.-K. Huang, F. Deligiannis, G. Halpert and E. Peled, Proceedings of the 34th International Power Sources Symposium, 1990, p. 98.

- (3) Y. Geronov, P. Zlatilova, R. V. Moshtev, J. Power Sources, 12 (1984) 145.
- (4) V. R. Koch, Advances in organic electrolytes for rechargeable lithium batteries, 4th Int. Seminar on Lithium Battery Technology and Applications, Deerfield Beach, FL, March (1988).
- (5) D. H. Shen, S. Subbarao, F. Deligiannis, C.-K. Huang and G. Halpert, Proceedings of the Symposium on Lithium Batteries, ECS Fall Meeting 1990, Edited by S. Subbarao, V. R. Koch, B. B. Owens and W. H. Smyrl, Proceedings Vol. 90-5, p. 114 (1990).
- (6) D. H. Shen, S. Subbarao, C.-K. Huang, F. Deligiannis and G. Halpert, Proceedings of the 34th International Power Sources Symposium, 1990, p. 90.
- (7) C.-K. Huang, S. F. Dawson, D. H. Shen, F. Deligiannis, S. Subbarao and G. Halpert, Proceedings of the Symposium on Lithium Batteries, ECS Fall Meeting 1990, Edited by S. Subbarao, V. R. Koch, B. B. Owens and W. H. Smyrl, Proceedings Vol. 90-5, p. 42 (1990).

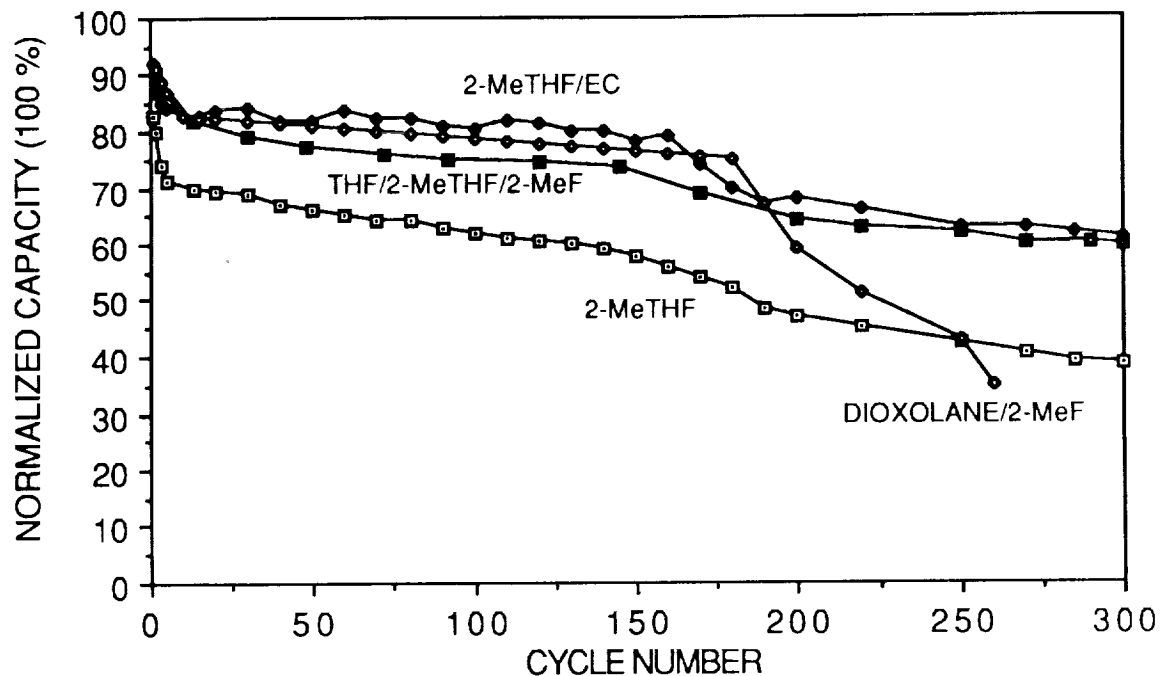


FIGURE 1. Cycle Life Performance of Experimental Cells Activated with Mixed Solvent Electrolytes

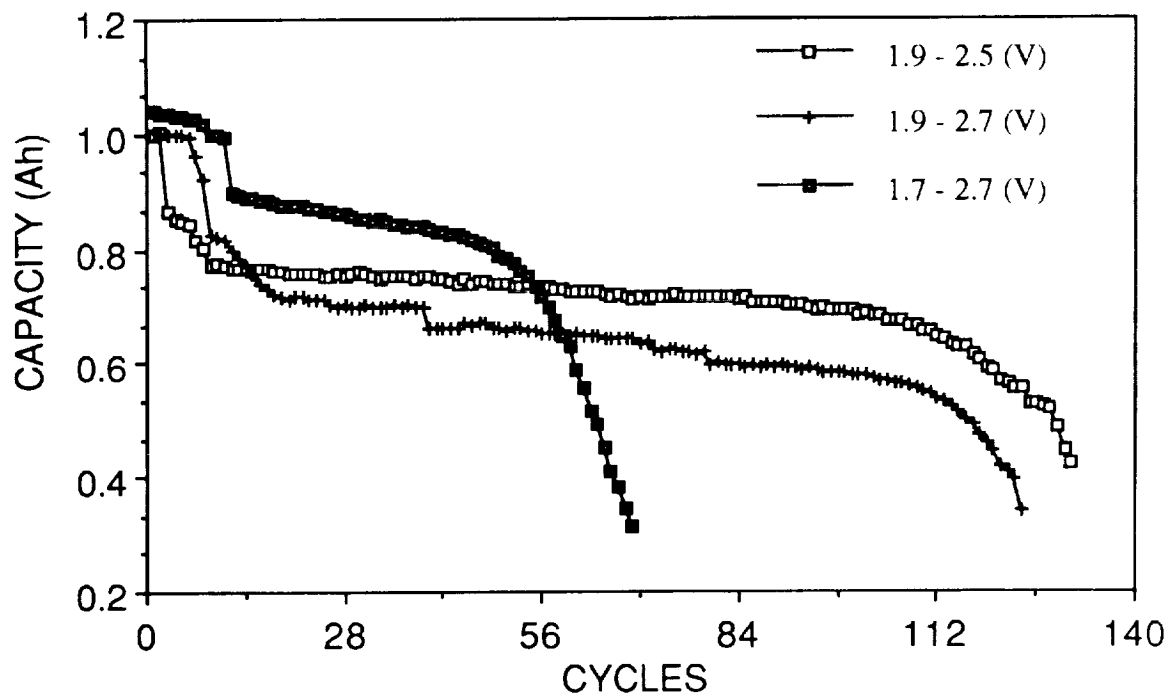


FIGURE 2. Cycle Life Performance of Li-TiS₂ Cells Operated under Different Voltage Limits.

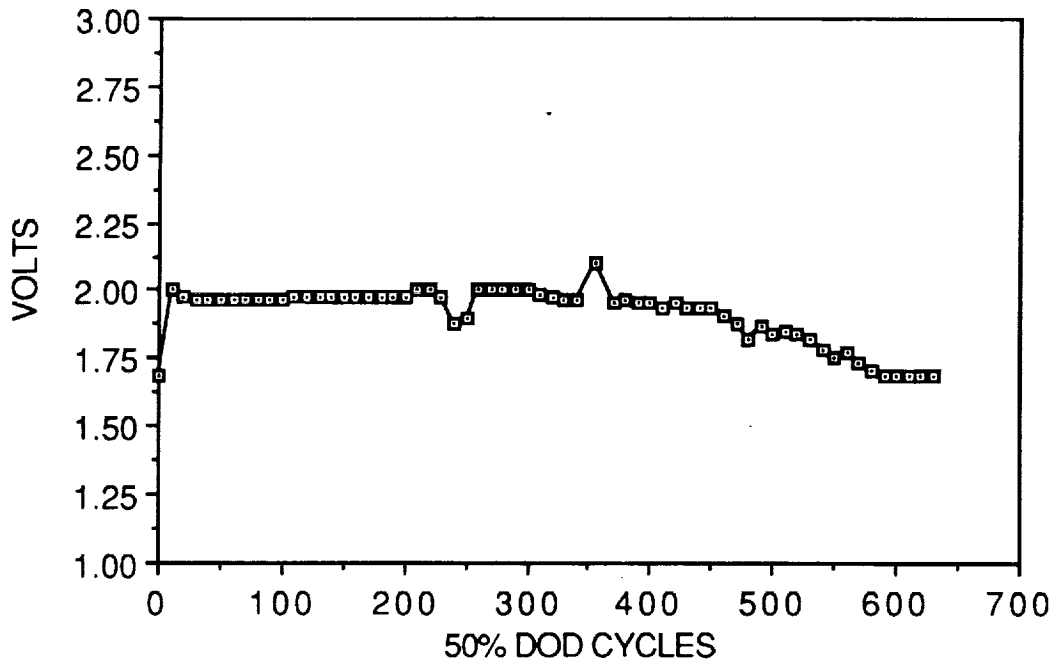


FIGURE 3. Cycle Life Characteristics of 1 Ah Li-TiS₂ Cell at 50% DOD

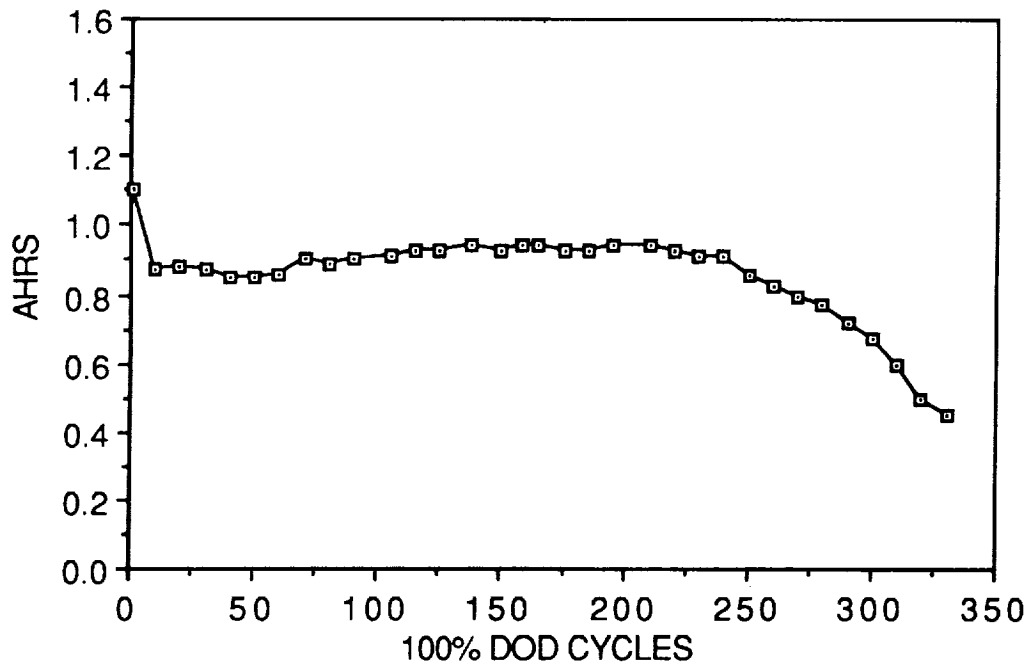


FIGURE 4. Cycle Life Characteristics of 1 Ah Li-TiS₂ Cell at 100% DOD.

TABLE I. Effect of Temperature on the Stability of Electrolytes Towards Lithium (Open Circuit Stand Test Results)

| Electrolyte | <u>10°C</u> | | <u>30°C</u> | | <u>70°C</u> | |
|----------------|------------------|--------------|------------------|--------------|-------------------|--------------|
| | <u>Li</u> | <u>ELEC.</u> | <u>Li</u> | <u>ELEC.</u> | <u>Li</u> | <u>ELEC.</u> |
| THF | <u>BRN</u> | LT YEL | <u>DRK BRN</u> | BRN ppt | <u>DRK BRN</u> | BRN ppt |
| EC+THF | <u>S*</u> | C | <u>BRN SPOTS</u> | C** | <u>BRN SPOTS</u> | BRN |
| 2-MeTHF | <u>S</u> | C(ppt) | <u>S</u> | C | <u>BLK STRIPE</u> | LT YEL. |
| EC+2-MeTHF | <u>S</u> | C | <u>S</u> | C | <u>S</u> | C |
| THF+2-MeTHF | <u>BRN SPOTS</u> | LT YEL | <u>DRK BRN</u> | YEL | <u>DRK BRN</u> | YEL. ppt |
| EC+THF+2-MeTHF | <u>S</u> | C | <u>S</u> | C | <u>BRN SPOTS</u> | LT YEL. |

* S: shining

** C: clear

TABLE II. Effect of Temperature on the Lithium Cycling Efficiency

| <u>ELECTROLYTE</u> | <u>FIGURE OF MERIT (FOM)*</u> | |
|--------------------|-------------------------------|-------------|
| | <u>10°C</u> | <u>25°C</u> |
| THF | 3.3 | 3 |
| EC+THF | 4.6 | 4 |
| 2-MeTHF | --- | 29.5 |
| EC+2-MeTHF | 32 | 38.5 |
| THF+2-MeTHF | 5.1 | 4.5 |
| EC+THF+2-MeTHF | 7.4 | 7.6 |

* $F.O.M._{Li} = (\text{Total Accumulated Discharge Capacity}) / (\text{Theoretical Li Capacity})$

TABLE III. Properties of Alternate Li Anode Material (Theoretical)

| <u>Material Type</u> | <u>E vs. Li (mV)</u> | <u>M.W. (g/mole)</u> | <u>No. of Li Reversible</u> | <u>Specific (Wh/Kg)</u> |
|-----------------------|----------------------|----------------------|-----------------------------|-------------------------|
| Li | 0 | 6.941 | 1 | 472 |
| β -LiAl | 385 | 35.32 | 1 | 312 |
| Li _{1,1} Zn | 191 | 73 | 0.6 | 220 |
| Li _{4,3} Sn | 411 | 148.5 | 2 | 243 |
| Li _{4,5} Pb | 388 | 238.4 | 3.5 | 254 |
| Li _{2,85} Cd | 140.6 | 132.2 | 2.6 | 322 |
| Li _{0,15} C | 200 | 13.05 | 0.15 | 255 |
| LiAlMn | 386 | 36 | 1 | 311 |
| LiAlCr | 386 | 36 | 1 | 311 |
| LiAlCdPb | 200 | 96.5 | 1 | 247 |

TABLE IV. Properties of Alternate Li Anode Material (Experimental)

| <u>Material Type</u> | <u>Stability*</u> | <u>Ave. E vs. Li (mV)</u> | <u>No. of Li** Reversible</u> | <u>Specific Energy (Wh/Kg)</u> |
|-----------------------|-------------------|---------------------------|-------------------------------|--------------------------------|
| Li _{1,2} Al | good | 380 | 0.9 | 300 |
| Li _{2,85} Cd | poor | 0 | --- | --- |
| Li _{3,0} Pb | good | 449 | < 1.5 | 167 |
| Li _{0,13} C | good | 200 | < 0.08 | 186 |
| Li _{4,4} Si | poor | --- | --- | --- |
| Li _{2,5} Sn | good | 520 | < 1.0 | 171 |
| Li _{0,5} Zn | good | 256 | < 0.12 | 62 |

* Microcalorimetric and OCV measurements.

** Galvanostatic cycling studies.

REPORT DOCUMENTATION PAGE

Form Approved
OMB No. 0704-0188

Public reporting burden for this collection of information is estimated to average 1 hour per response, including the time for reviewing instructions, searching existing data sources, gathering and maintaining the data needed, and completing and reviewing the collection of information. Send comments regarding this burden estimate or any other aspect of this collection of information, including suggestions for reducing this burden, to Washington Headquarters Services, Directorate for Information Operations and Reports, 1215 Jefferson Davis Highway, Suite 1204, Arlington, VA 22202-4302, and to the Office of Management and Budget, Paperwork Reduction Project (0704-0188), Washington, DC 20503.

| | | | | |
|---|---|--|---|--|
| 1. AGENCY USE ONLY (Leave blank) | | 2. REPORT DATE September 1991 | 3. REPORT TYPE AND DATES COVERED Conference Publication | |
| 4. TITLE AND SUBTITLE Space Electrochemical Research and Technology | | | 5. FUNDING NUMBERS WU-506-41-21 | |
| 6. AUTHOR(S) | | | | |
| 7. PERFORMING ORGANIZATION NAME(S) AND ADDRESS(ES) National Aeronautics and Space Administration Lewis Research Center Cleveland, Ohio 44135-3191 | | | 8. PERFORMING ORGANIZATION REPORT NUMBER E-6089 | |
| 9. SPONSORING/MONITORING AGENCY NAMES(S) AND ADDRESS(ES) National Aeronautics and Space Administration Washington, D.C. 20546-0001 | | | 10. SPONSORING/MONITORING AGENCY REPORT NUMBER NASA CP-3125 | |
| 11. SUPPLEMENTARY NOTES | | | | |
| 12a. DISTRIBUTION/AVAILABILITY STATEMENT Unclassified - Unlimited Subject Category 44 | | | 12b. DISTRIBUTION CODE | |
| 13. ABSTRACT (Maximum 200 words) This document contains the proceedings of NASA's third Space Electrochemical Research and Technology (SERT) Conference, held at the NASA Lewis Research Center on April 9-10, 1991. The objective of the conference was to assess the present status and general thrust of research and development in those areas of electrochemical technology required to enable NASA missions into the next century. The conference provided a forum for the exchange of ideas and opinions of those actively involved in the field, in order to define new opportunities for the application of electrochemical processes in future NASA missions. Papers were presented in three technical areas: the electrochemical interface, the next generation in aerospace batteries and fuel cells, and electrochemistry for nonenergy storage applications. This document contains the abstracts of the papers presented. | | | | |
| 14. SUBJECT TERMS Electrochemistry; Batteries; Fuel cells | | | 15. NUMBER OF PAGES 252 | |
| | | | 16. PRICE CODE A12 | |
| 17. SECURITY CLASSIFICATION OF REPORT Unclassified | 18. SECURITY CLASSIFICATION OF THIS PAGE Unclassified | 19. SECURITY CLASSIFICATION OF ABSTRACT Unclassified | 20. LIMITATION OF ABSTRACT | |

